Chemical bonding in metal-organic frameworks from fundamentals to design principles

Bristow, Jessica

Award date:
2016

Awarding institution:
University of Bath

Chemical bonding in metal-organic frameworks: from fundamentals to design principles

submitted by

Jessica K. Bristow

for the degree of Doctor of Philosophy

of the

University of Bath

Department of Chemistry

Oct 2016

Summary

Society is now dependent on the continued development and access to modern technology. Materials science therefore stands at the forefront of resolving and tuning functional materials properties, and designing technologies to improve our health, economy and environment. The content of this thesis covers a wide range of methods and approaches for understanding the chemical complexities, and tuneable properties of a unique subset of materials named metal-organic frameworks.

The number of available precursor components for synthesising MOFs has led to a plethora of possible final crystal structures, with vast differences in observed material properties. The use of computational approaches in the prediction of potential functional frameworks, and also for resolving the origin behind observed phenomena, is essential for directing further work in the field.

Work in this thesis includes the parameterisation of an approach that would allow a large-scale and cheap screening procedure of the thermodynamic properties of MOFs. Other work in this thesis includes the calculation of defective framework structures and the thermodynamics associated with their formation. Defects that occur in MOFs, when compared to inorganic binary materials such as oxides, can be considered as severe and non-dilute. The concentration and distribution of potential defects and the stability of the framework as a function of these factors, is a poorly understood area in the research field of MOFs. Finally, interfacing MOFs with surfaces is a relatively new approach for designing functional devices for applications such as gas absorption and photovoltaics. In this thesis we calculate interface binding sites and energetics of adhesion of an archetypal example of a MOF interfacing a metal oxide.

Each approach and direction taken in the work forming this thesis were taken to resolve the theory behind observed phenomena in experiments, and to provide a platform for investigating the potential material properties of yet unsynthesised MOFs.

I have many people to thank for supporting me and working with me throughout my PhD. Firstly, a massive thank you to my supervisor Aron Walsh, who has never doubted my abilities and has supported every idea and piece of work that I have undertaken for 5 years - couldn't of asked for a better boss! A heart felt thank you also goes to Julian Gale, who not only supplied a massive push behind the biggest projects in my PhD, but who is also the kindest and most supportive academic that I have had the privilege of meeting and knowing.

When it comes to the Walsh group, we are each unique and brilliant in our own ways, which has made the last 5 years with both past and present members an enjoyable and stimulating environment. A special thank you must go to the downstairs office, in particular to Lora who always knew when a trip to the bar was necessary, and to Jonathan who always has time to help and advise but is also a good friend.

Some more personal thank you messages also need to also be given. Thank you to my family for their relentless support and their ability of making a non-converging system seem a lot less important than I initially thought. Thank you to my housemate and friend Caroline, who has not only acted a spider catcher backup but has also given me the best memories of Bath, and thank you to Jess for putting up with me as a friend for all of these years! I would not of had such a fun filled time in Bath if it were not for my lovely neighbour and friend Ant, who is the soppiest but most supportive friend I could possibly ask for, always keeping a smile on my face. Thank you to Si for his directness and honesty and keeping the thesis on track and for being an irreplaceable cinema companion.

Finally, thank you to everyone in Australia who made my two internships the best experience of my life, particularly to Raffaella and Marco for being absolutely lovely and for making me feel so welcome both times.

Publications during the course of the PhD

7. Compositional control of pore geometry through steric interactions in a multivariate metal–organic framework series

   Laura K. Cadman, Jessica K. Bristow, Harry Wright, Davide Tiana, Mary F. Mahon, Aron Walsh, and Andrew D. Burrows., To be submitted.

6. Distribution and electronic structure of missing-linker defects in the UiO-66 metal-organic framework

   Katrine L. Svane, Jessica K. Bristow, Sarah Clements, Julian D. Gale and Aron Walsh, To be submitted.

5. Chemical bonding at the metal-organic framework / metal oxide interface: simulated epitaxial growth of MOF-5 on rutile TiO_2

   Jessica K. Bristow, Keith T. Butler, Katrine L. Svane, Julian D. Gale and Aron Walsh, Chemistry of materials, Chem. Sci, manuscript under review.

4. A general forcefield for accurate phonon properties of metal-organic frameworks

   Jessica K. Bristow, J. M. Skelton, Katrine L. Svane, Aron Walsh and Julian D. Gale, Phys. Chem. Chem. Phys., (2016), DOI:10.1039/C6CP05106E.

3. Compositional control of pore geometry in multivariate metal-organic frameworks: an experimental and computational study

   Laura K. Cadman, Jessica K. Bristow, Naomi E. Stubbs, Davide Tiana, Mary F. Mahon, Aron Walsh, and Andrew D. Burrows., Dalton Trans. 45.10 (2016): 4316-4326.

2. Free energy of ligand vacancy formation in the metal-organic framework UiO-66

   Jessica K. Bristow, Katrine L. Svane, Davide Tiana, J. M. Skelton, Julian D. Gale and Aron Walsh, J. Phys. Chem. C., 120.17 (2016): 9276-9281.

1. Transferable Force Field for Metal-Organic Frameworks from First-Principles: BTW-FF

   Jessica K. Bristow, Davide Tiana, and Aron Walsh, J. Chem. Theory Comput., 10.10 (2014): 4644-4652.

Contents

List of Figures

List of Tables

Chapter 1

Introduction

1.1 Motivation for materials science

The degradation of the environment and the politics of the world around us makes it difficult to briefly summarise the motivation for developing sustainable materials and the importance of research into materials science. Three main challenges facing our environment can be highlighted as the most applicable for justifying materials development: global warming, extensive production of waste and the energy deficit.

The concept of global warming is that the temperature of the Earth will increase with increasing concentrations of greenhouse gases, which have high infrared absorption capacity, such as carbon dioxide (CO_2). Svante Arrhenius, often referred to as the founder of physical chemistry, is famous for the Arrhenius equation relating the activation energy and rate constant of a process. Arrhenius is lesser known for developing the theory of why ice ages occur, and in doing so was the first known scientist to propose the greenhouse effect. In 1886, Arrhenius calculated the arithmetic progression of carbon dioxide levels due to human activities, and the effect on the global temperature this has and will continue to have.[1] Over a century later, using the same laws as derived by Arrhenius, we continue to monitor the increase in both CO_2 concentration in the atmosphere and average global temperature. In the late 1950's Charles Keeling[2], empirically measured the atmospheric CO_2 levels on a monthly basis. Records show a constant increase in values measured from the late 50's to the present day, confirming predictions made over a century ago.[3]

A record value for atmospheric levels of CO_2 was measured in November 2015 at the Mount Loa Observatory, the location of the first measurement as made by Charles Keeling. The current concentration of atmospheric CO_2 has exceeded 400 ppm, an increase of almost 100 ppm since the first measurement made. The consequence of increasing CO_2 concentrations and global temperature are severe and has already lead to many environmental disasters such as: melting icecaps, flooding, violent weather conditions, extinction of species and loss of biodiversity. Increasing human population, indus-

Figure 1-1: Low Earth orbit (left) of man-made space debris orbiting the Earth, modelled by NASA in 2015.[4] Landfill waste in London, UK[5] (right).

trial revolutions and the high consumerism of modern lifestyles are all facilitating the rapid increase in CO_2 levels.

The effects that humans have had on the Earth far exceeds the described atmospheric pollution. The production of waste, both industrial and individual is beyond comprehension. It was calculated by the world bank that in 2012 the world produced over 1.18 trillion kg of waste, with 59% sent to landfill and not recycled.[6] This total weight would roughly approximate to the equivalent of 93,000 Shard buildings in London or 22,000 Sydney harbour bridges. Figure 1-1 shows that the waste produced by humans is not only affecting the land and sea of the Earth, but also surrounds the planet. Hundreds of thousands of pieces of man made space debris and human waste orbit the Earth, making each new space adventure more challenging.

Finally, the population of the Earth this year in 2016 has exceeded 7.4 billion people. Energy is required for both feeding and sheltering each person, but also to ensure industrial growth for employment and consumerism. Methods for generating energy often require fossil fuels. Fossil fuel reserves are non-renewable and an unreliable source to base future prosperity on. Renewable sources such as the sun, water, wind and heat offer a clean alternative to the burning of fossil fuels and consequent production of waste greenhouse gases. Materials development to enable the substitution of fossil fuels for renewable sources is needed to offset the higher costs often associated with clean technology. Whilst little evidence currently exists that we are nearing the point where fossil fuels will completely run out, air quality and the continued need for energy is the current motivation for developing renewable technology. Countries that are currently within an industrial revolution such as China, India and Africa are dependent on the use of fossil fuels. The repercussion for such dependence has been immediately evident in China, whose air quality mimics that of London, UK in 1952 in the era of the great smog. We are currently facing an energy deficit, where the energy produced is much lower than the demand of the population. The further development of sustainable and renewable materials to contribute to energy production is critical and already overdue.

Human contribution to waste and environmental effects such as global warming are indisputable. One way to reduce the impact as a species that we have on the planet is to develop new materials with

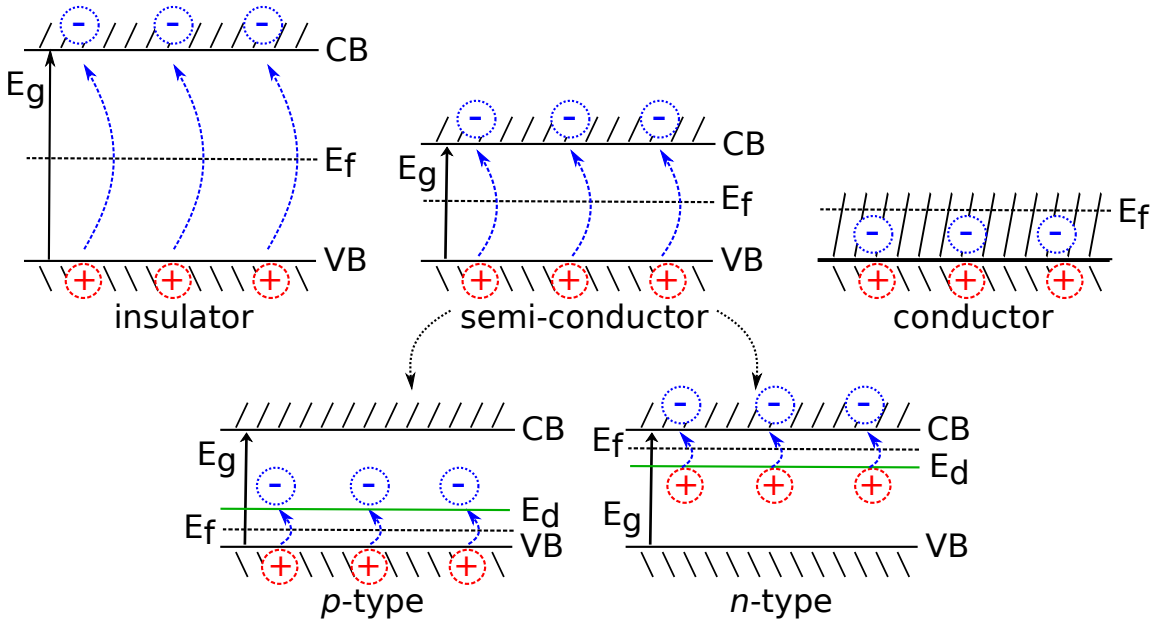

Figure 1-2: Representative bandstructures of insulators, semi-conductors (undoped, *n* and *p*-type) and conductors. Plotted are the valence band (VB), conduction band (CB), optical band gap (E_g), Fermi-level (E_f) and defect level (E_d). Image is reproduced from the given reference.[7]

a reduced environmental footprint. Thus, materials chemistry stands at the forefront of adapting the current way we as humans use and dispose of materials to maintain and improve current lifestyles.

The remainder of the introduction to this thesis will cover the electronic, mechanical and vibrational properties of solid-state materials, and introduce metal-organic frameworks (MOFs) as novel materials, which display a broad range of functional properties making them suitable for many sustainable and renewable applications.

1.2 Electronic structure of materials: metals, semiconductors and conductors

The response of materials to light and heat differs according to their intrinsic electronic structure. Materials are distinguished as insulators, semi-conductors or metals according to the band structure theory. When forming a 3D solid periodic material, discrete energies of molecules and individual atoms are no longer distinguishable, and continuous bands of allowed energy states are formed. Electron occupation of the bands obeys the Pauli exclusion principle, whereby electrons of opposite spins are paired in each molecular orbital, and the occupation distribution obeys Fermi-Dirac statistics.

The energy separation between the highest occupied crystalline orbital (HOCO), known as the

valence band, and lowest unoccupied crystalline orbital (LUCO), known as the conduction band, is defined as the optical band gap. The magnitude of the band gap varies according to the electronic configuration of the atoms forming the solid. It is the variation in band gap that defines a material as an insulator, semi-conductor or metal, thus allowing the response of a material to light and heat to be rationalised (Figure 1-2).[8]

Insulators have a fully occupied valence band and unoccupied conduction band, separated by an energy >3 eV. Insulators are ineffective for electronic conduction due to the absence of electron mobility in fully occupied bands. Intrinsic semi-conductors have band gaps <1 eV and at 0 K behave as if they were insulators. With increasing temperatures, electrons can occupy the conduction band, allowing electronic conductivity from thermal excitations. Additional energy states can also be inserted into the band gap of a semi-conductor or insulator, increasing the probability of electron occupation of the conduction band. Additional energy levels are present either due to extrinsic doping, such as the incorporation of transition metal colour centres, or by intrinsic defects such as the movement of the atoms off lattice sites into interstitial space.[9] Greater detail on electronic conductivity and defects in crystals will be discussed later. Finally, metals posses no band gap between filled and empty states and electrons can be thought of as 'free' or delocalised across multiple states.[10,11]

A concept in band structure theory for rationalising the electronic conductivity and response to light of a material is the Fermi-level. The Fermi-level is hypothetical, and is derived as a reference for a material from Fermi-Dirac statistics (Equation 1.1), where, ε is the energy of a state, μ the chemical potential and k_B the Boltzmann constant.

$$f(\varepsilon) = \frac{1}{e^{((\varepsilon-\mu)/k_B T)} + 1} \tag{1.1}$$

The solution of the Fermi-Dirac function gives each state, depending on its energy and chemical potential, a probability for occupancy at thermal equilibrium at a defined temperature. The Fermi-level (E_f) of a material is the state that has a 50% probability (*i.e.* when ε=1 to give $f(\varepsilon)$=0.5) of being occupied at thermal equilibrium. The notion of the Fermi-level is a convenient method for depicting and rationalising the electronic and optical properties with temperature based on the probability of conduction band occupation.[12]

As shown in Figure 1-2, the Fermi-level of a metal resides within the band of delocalised states produced by the absence of a band gap. For an insulator and undoped semi-conductor, the Fermi-level resides within the band gap. At 0 K in both insulators and semi-conductors the Fermi-level is located half way between the HOCO and LUCO bands. For extrinsically doped semi-conductors, where electron or hole donors are added to the material, the position of the Fermi-level changes.[13] For an example of a doped semi-conductor we can consider the most popular example, silicon. As a semi-conductor silicon has an optical band gap of 1.1 eV and in its non-defective form the Fermi-level will be half way between the valence and conduction bands at 0 K. The addition of an electron donor such as phosphorous, forms an *n*(negative)-type semi-conductor and additional bands are inserted into the

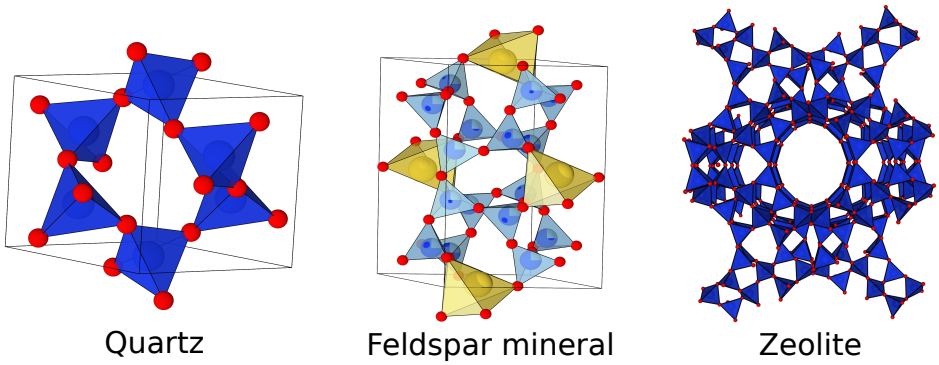

Figure 1-3: The crystal structures of quartz (left), a feldspar mineral containing partial occupancy of the Al/Si sites (blue) with charge compensation cation (yellow) (centre) and a neutral zeolite structure formed of SiO_2 tetrahedra (right).

band gap near the conduction band. The Fermi-level will now be closer to the conduction band, and charge carrier separation and mobility is increased due to a greater probability of electrons being promoted to the conduction band from the new defect states. The addition of a hole donor (or electron withdrawing) species, such as boron in silicon, forms a *p*(positive)-type semi-conductor. In this case, additional defect bands are inserted near the valence band edge, and the Fermi-level shifts near to the valence band.[14] The increased probability of lower energy transitions between the valence band and defect state increases charge carrier separation and mobility. Doping semi-conductors is therefore a method to increase charge carrier mobility and is often used in photovoltaic and thermoelectric devices to increase the efficiency of the device.[15] In the same approach insulators can be doped to produce semi-conducting properties. Additional defect levels inserted into the band gap not only change the conductivity properties but also the frequencies of light absorbed, and therefore the colour of the material.

1.3 Porous materials

1.3.1 Quartz, feldspars and zeolites

Quartz is the ground state structure of a naturally forming mineral of SiO_2 with hexagonal symmetry. Each silicon 4+ cation is in tetrahedral coordination with four oxygen anions. Quartz is the second most common naturally forming mineral in soil due to its stable periodic motif. Quartz in its mineral form is densely packed and does not possess inherent micro porosity, but adsorbs water molecules at exposed surfaces. Porosity can be induced through treatment processes on amorphous polymorphs of SiO_2. These polymorphs are used as drying agents due to their high capacity for water absorption.

Feldspars are minerals that also contain SiO_2 tetrahedra with identical connections but 25% of all Si cations are replaced by Al^{3+}, hence their name: aluminosilicates. The described cation substitution ren-

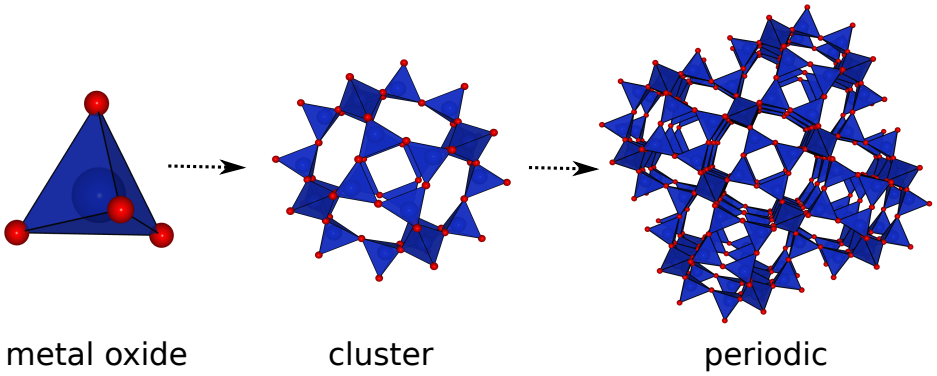

Figure 1-4: The formation of periodic zeolites *via* the coordination of metal oxide tetrahedra.

ders a negative charge on the unit cell, which is compensated by a metal cation such as Ca^{2+}/Na^{+}/K^{+}. The comparative stability of quartz and feldspars does not reflect the fact that the latter is the most common mineral in soil. Due to the removal of the charge compensating cation with exposure to water, feldspars show reduced stabilities and are therefore susceptible to weathering.[16]

Quartz and feldspar minerals have no micro-porosity but do possess mesoporosity. It is reported that natural samples of both minerals contain between 4-19% porosity, with the pores measuring between 2-300 nm in diameter. Such macro-porosity allows a low volume of gas and water absorption throughout bulk samples, but both quartz and feldspar cannot be formally defined as porous materials.[17]

Zeolites are a family of naturally forming minerals that possess the same chemical composition as quartz and feldspars but are defined as porous. A comparative depiction of quartz, a feldspar mineral and a zeolite structure are shown in Figure 1-3. Zeolites are inorganic porous materials formed of a range of cations in tetrahedral coordination with oxygen anions (Figure 1-4). Traditionally zeolites, as initially reported by Hey[18] and Smith[19], were formed of aluminosilicate tetrahedra, but more recently zeolites have been synthesised with a variety of metal cations in differing oxidation states such as Ti^{4+} and Fe^{3+}.[20] zeolites, unlike quartz and feldspars, crystallise to form interconnected cages of metal oxides, which are separated by vacant channels also referred to as pores. If charge compensation cations are required for charged frameworks, it is in these pores that the additional cations will be located. Zeolites are stable materials that are naturally forming, but can also be synthesised by self-assembly methods from precursor molecules (Figure 1-4). It has been reported that by varying the ratio of Si:Al, the stability of zeolites in differing pH environments can be tuned. Those with a greater silicon content show resistivity to degradation after heating in water/ammonia solutions with an alkaline pH, whilst those with a greater aluminium content show resistivity to degradation in neutral aqueous solutions.[21]

Zeolites are defined as molecular sieves owing to a distribution of pore sizes between different crystalline forms. It is their inherent porosity that makes zeolites suitable for a range of applications including gas separation and absorption, chemical sensors, catalytic reaction chambers[22–24], electrodes[25,26],

electrical insulators[27], separation membranes[28,29] and novel reaction-diffusion devices. The stability with temperature of zeolites differs according to the crystal symmetry and final packing density. It has been reported that most zeolites are stable up to approximately 550-600 K, above which amorphous structures can crystallise. Between 750-850 K polymorphs of SiO_2 can form and the integrity of the zeolite structure is lost with de-alumination.[30,31]

1.3.2 Covalent-organic frameworks

Covalent organic frameworks (COFs) are formed of purely organic components that stack and interact to create rings, stacks and sheets that self-assemble into 3D periodic motifs with intrinsic porosity. As their name would suggest, COFs are mainly formed of covalent bonding between organic ligands. The organic ligands comprising their structure require binding atoms/groups to create extended interactions, common groups include direct ester connections (C-O-C), boronate ester groups (B-O-B), triazinegroups ($C_3H_3N_3$) and imine groups (R_2C=NR). COFs are generally synthesised *via* dehydration reactions to create extended networks,[32,33] with pore sizes ranging between 0.5 - 4.0 nm in diameter. Each structure can contain more than one pore size, and therefore more than one internal chemical environment. COFs often have between planes/sheets vdW interactions that allow layers of organic ligands to stack on top of each other, which in many cases is the origin of 3D porosity.

There are three main applications for COFs: gas absorption, heterogeneous catalysis and photoconduction. COFs absorb "green" fuels such as H_2 and waste gases such as CO_2, with binding sites across aromatic rings. The capacity of COFs for volumetric gas uptake of both CO_2 and H_2 has been shown to be comparable to common metal-organic frameworks (MOFs), further details on which will be given later.[34] A noteworthy example of heterogeneous catalysis in COFs was reported by Ding *et al.* who reported the coordination of a catalytically active Pd molecule between nitrogen binding atoms in a COF.[35] It was demonstrated that catalytic activity was not altered by binding the catalyst to the framework.[32]

1.3.3 Porous liquids?

A novel breakthrough in 2015 offers an extension to solid state porous materials. James *et al.* reported a "porous liquid" with vacant internal pores that displayed exceptional methane solubility properties.[36] Solid organic cages were dissolved in a bulky 15-crown-5 solvent such that only 12 solvent molecules were needed to dissolve each cage in solution. Other solid cages dissolved in more common less bulky solvents such as DMF require thousands of solvent molecules per cage. The large size of the chosen crown ether solvent prevents it accessing the internal pore aperture of the organic cage, resulting in the solvent interacting around the external surface. The solution with dissolved organic cages and crown ether solvent flows as if it were liquid, and dissolved internal pores of the organic cage remain unoccupied by solvent, hence the naming; porous liquid.

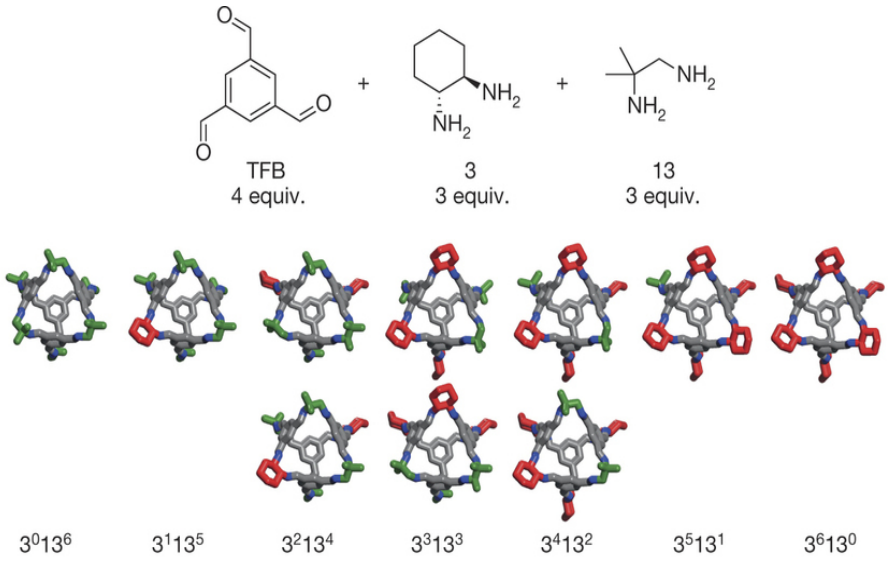

Figure 1-5: Cage structures forming the porous liquid from two different diamines: dimethyl (green) and cyclohexane (red). Figure edited from the given reference.[36]

Each organic cage comprising the "porous liquid" is formed of differing concentrations of two diamines: dimethyl and cyclohexane, which coordinate to the base trialdehyde (TFB) ligand (Figure 1-5). The authors report the advantage of such materials to be that liquids are easier to integrate into an existing industrial plant for gas separation and absorption. The disadvantages of these materials are that the volumetric uptake of gas, such as methane, is lower than solid state materials and that vast quantities of solvent required has a negative environmental impact.[36]

1.3.4 Molecular crystals

Molecular crystals can be formed purely of organic components or both organic and inorganic components and often possess intrinsic porosity with extended periodic structures. The distinction of molecular crystals from COFs and MOFs is that the structure is formed of molecular fragments that are not formally covalently bonded to each other. Instead, the extended structure is connected by van der Waals and charge interactions between the molecular fragments within the crystal.[37] Iron spin cross-over systems are common examples of inorganic molecular crystals (Figure 1-6).[38]

Although many molecular crystals contain a distribution of pore sizes, these are often smaller than are observed in zeolites and MOFs. Also, the stability of the structures, owing to weak intermolecular interactions, is reduced when compared to other solid state materials.

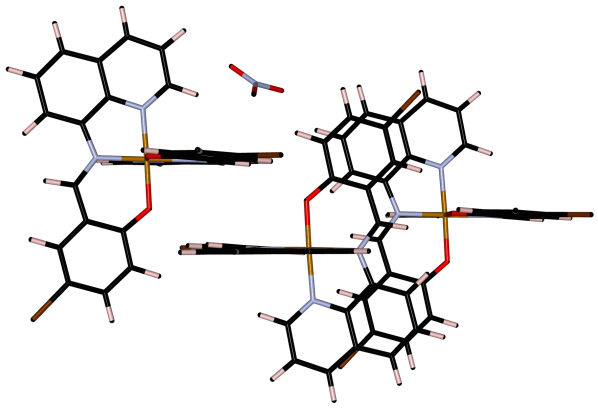

Figure 1-6: The structure of an Fe(III) spin cross over system $[Fe(qsal\text{-}Br)_2]NO_3$.[39] Shown are two molecular fragments of the same chemical formulae and a solvent molecule.

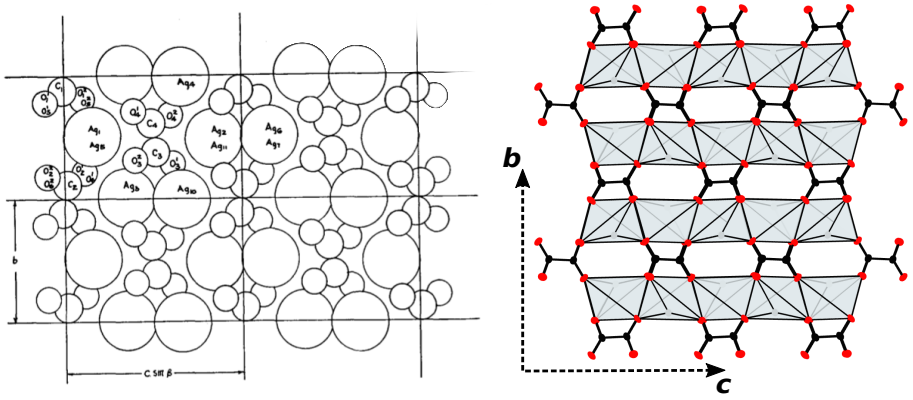

Figure 1-7: Crystal structure of silver oxalate ($Ag_2C_2O_4$) as published in Griffith 1943[41] (left) and remade to highlight the layers of metal nodes and ligand molecules (right).

1.4 Hybrid porous materials: metal-organic frameworks

1.4.1 Discovery and development

MOFs are porous materials formed *via* coordination bonding between organic ligands and metal cations (Figure 1-8). MOFs have extended periodic structures and unlike molecular crystals, MOFs do not possess unbonded molecular fragments. Frameworks of identical composition can crystallise in different forms with unique symmetries, these forms are referred to as topologies. The final topology of a MOF will not only depend on its composition, but also on experimental conditions such as the choice of solvent and temperature. Methods to define the topology of a MOF will be discussed later. MOFs are unparalleled by other porous materials, possessing structural diversity, tunability and functional properties with reasonable reported stabilities.[40]

The first MOF to be reported and recognised as a 3D porous material was silver acetate (Figure

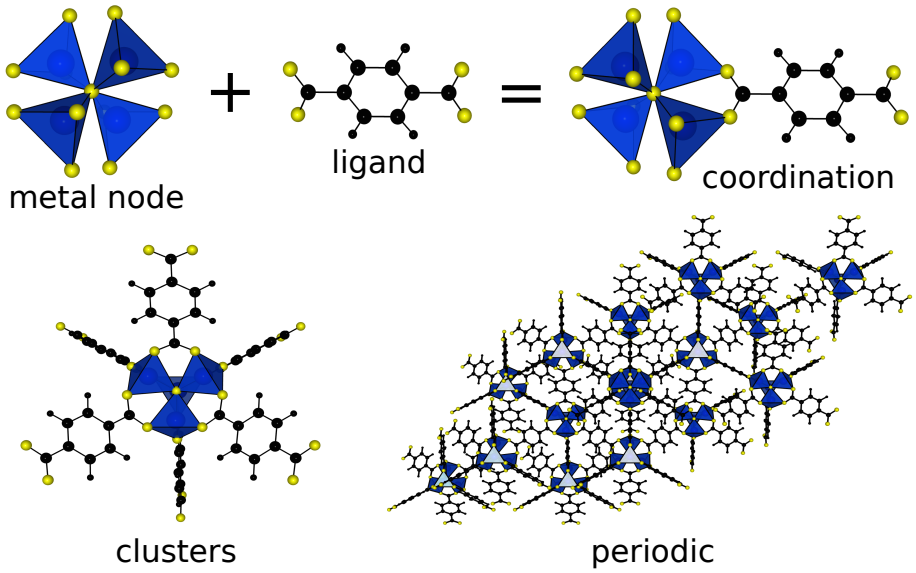

Figure 1-8: The formation of MOFs *via* the coordination of metal nodes and ligands. Clusters further aggregate to form an extended periodic structure (as labelled).

1-7). In 1943 Griffith[41] noted when resolving its crystal structure that "These chains appear to be held together by longer silver-oxygen bonds to form the three-dimensional structure." By publishing this statement Griffith was the first to recognise a 3D periodic motif comprised of both organic and inorganic building blocks. These motifs are now referred to as MOFs or coordination polymers.

The most commonly referred to and researched MOF is MOF-5 (as pictured in Figure 1-8). MOF-5 has a structural formula, $Zn_4O(BDC)_3$, and is formed of $[OZn_4]^{6+}$ metal centres coordinated to 1,4-benzenedicarboxylate (BDC) linkers $(O_2C–C_6H_4–CO_2)^{2-}$ to create a cubic porous framework.[42] The synthesis of MOF-5 was first reported in 1999 by Yaghi *et al.*[43] and was ironically referred to as "exceptionally stable", ironically because MOF-5 is now considered to be one of the least stable MOFs, with decomposition observable after 24 hours of air exposure. The synthesis of MOF-5 by the group of Yaghi pioneered the initial extensive research into the applications that MOFs would be suitable for. The number of MOFs that have been synthesised and characterised to this day is over 50,000. Some examples of MOF structures are given in Figure 1-9, which highlight the variation in crystallised topologies.

1.4.2 Topologies and characterisation

Designing versatile and functional MOFs is a complex and time consuming process. Metal identity and geometry are the first considerations when designing a MOF. Many metals have high associated coordination numbers and variable geometries, resulting in a range of densities, pore sizes and thermodynamic stabilities when forming a periodic framework. Valence occupation of the metal determines

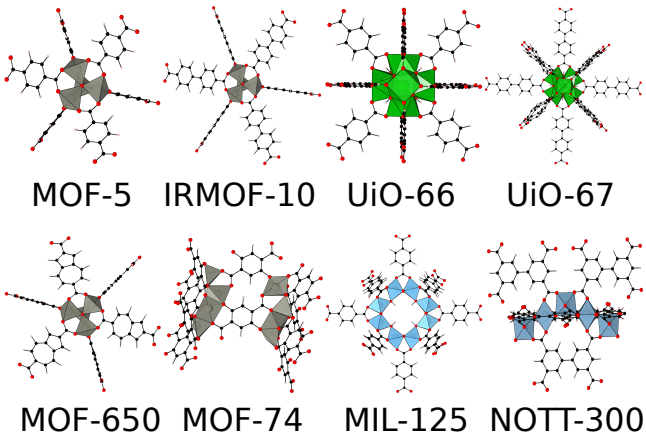

Figure 1-9: A range of metal-organic frameworks with different connectivities and topologies. Metal nodes include Zn (silver), Al (grey), Zr (green) and Ti (blue).

not only the final geometry around the metal but also magnetic and electronic properties that a framework containing the metals is likely to possess. Copper in the +2 oxidation state is d^9, and due to to Jahn-Teller distortions, Cu^{2+} often adopts a distorted octahedral geometry where the axial bonds are elongated.[44] Such a bonding is common in Cu paddle-wheel MOFs (*e.g.* HKUST-1) where axial ligands are often loosely bound solvent molecules. Long range interactions between the electronic spins on neighbouring Cu cations often results in a coupling and pairing of neighbouring spins and an anti-ferromagnetic spin ground state.[45] Metal geometry and coordination is particularly important for catalysis, where catalytic activity can be affected by the reactivity of the active site. Typical metals composing MOFs are Fe, Cr, Co, Mn, Zn, Al, Cu and Mg.[46–48]

A ligand within a MOF must contain a binding site, which can donate electron density to the metal forming a bonded network. The variation in available ligands is vast and includes aromatic groups, redox active and radicals. Ligands are not always used as inactive/inert building blocks, but also themselves contribute to the electronic structure of a MOF. Indeed, the addition of substituents onto the typical BDC ligand has been shown to modulate the fundamental band gap of photoactive MOFs such as MIL-125.[49,50] Other properties such as gas absorption and thermodynamic stability are also affected by ligand identity.[51–53]

The manner in which metal and ligand components combine to form a periodic crystal controls the final symmetry of the synthesised MOF. The word "topology" is used to describe such underlying symmetry within MOFs. Multiple examples of the variation in topologies produced by different metals and ligands are given in Figure 1-10.[54]

Assigning a topology is comparable to allocating MOFs into families with similar bonding connections. An alternative mathematical method for assigning the symmetry of a MOF, is to formally classify each MOF according to a net. Nets are three letter codes that assign a crystallographic classification

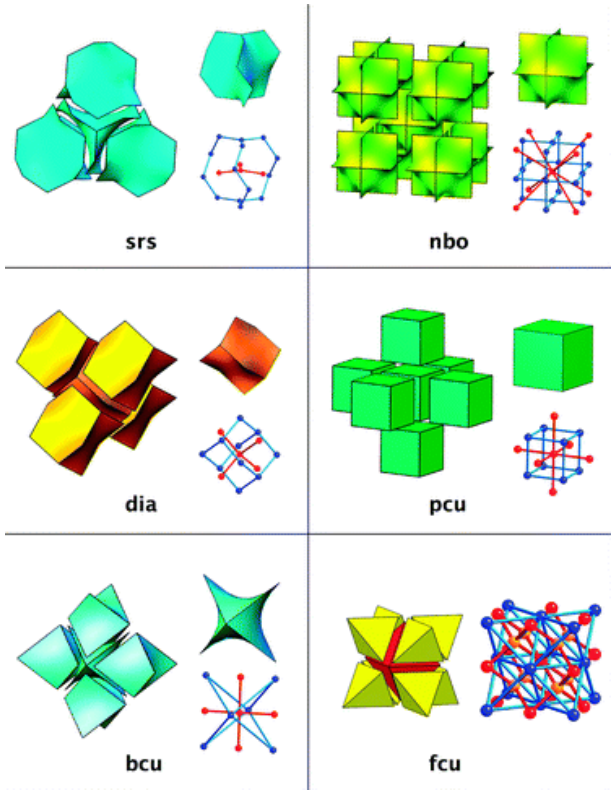

Figure 1-10: Numerous examples of MOF topologies labelled with their associated nets notation. Ball and stick representations are given with symmetry building blocks.[55]

based on the symmetry operations present in each framework. A net is therefore a graph that is applied to the surface of the primitive unit cell of a material, with the vertices (v) of the graph being the atoms and bonds the edges (e). The graph is applied to the primitive unit cell and the genus (g), which is a description of the number of vertices in the unit cell, is derived with the formulae:

$$g = 1 - v + e \tag{1.2}$$

The net of the MOF in question is then assigned based on the genus and metal node shape. Note that the metal node shape refers to the entire secondary building unit (SBU) rather than each individual metal centre. For example, for MOF-5 the geometry of each metal is tetrahedral but the shape of the metal node, which consists of four Zn metals and one inorganic oxygen, is octahedral. The net code assignment of MOF-5 is therefore **pcu**. See Table 1.1 for further examples and assignments. Nets were initially assigned to zeolites and quartz and therefore typical symbols include **sod** from the zeolite, sodalite, and **qtz** from quartz.[56,57]

Additional notation is then used to further describe the assigned net and occurs after the assigned code *e.g.* **dia-n**, where **n** can be **a**, **b**, **c**, **d**, **e**, **f, g, x** ***etc.***. A brief description is given in Table 1.2 of

Table 1.1: The most common nets to describe the topology of MOFs. Given is the space group associated with the nets, the number of vertices in the primitive cell, the genus of the net, metal node shape and examples of MOFs with the given nets.[55,58]

Net	Space group	No. of vertices	Genus	Metal node shape	MOF example
srs	$I4_132$	1	3	trigonal	$Ni(D\text{-}cam)(H_2O)_2$[59]
dia	Fd-3m	1	3	tetrahedral	ZIF-8/ZIF-67[60]
nbo	Im-3m	1	4	square planar	MOF-505[61]
pcu	Pm-3m	1	3	octahedral	MOF-5[62]
tbo	Fm-3m	2	11	square planar	HKUST-1[63]
fcu	Fm-3m	1	6	cubooctahedron	UiO-66[64]
bcu	Im-3m	1	4	cubic	$[Co_2(OH)_2(pmc)_4]$[65]

each additional notation.[57] More than one additional notation may apply to a structure.

When considering the composition of a MOF, it is the intended application that will dictate the choice of metal/ligand. Final crystal topology is difficult to control and is often dependent on synthesis and crystallisation conditions. The Reticular Chemistry Structure Resource is a database that reports g and v for each MOF topology.[66]

1.4.3 Post-synthetic modifications and defects

Post synthetic modification of MOFs allows a more diverse range of properties to be afforded. Common methods of modification are to either substitute an additional group onto a ligand or to remove a ligand completely (Figure 1-11). Additional methods include varying synthesis conditions such as solvent identity and temperature, substituting the metal in the framework, cross-linking ligands by a bridging molecule and interpenetrating multiple frameworks. The purpose of modifying the structure of a MOF is to tune the electronic and mechanical properties, *e.g.* band gap modulation, water and thermal stability, and also, in extreme examples, to change the ground-state topology.

An example of changing the electronic properties of a MOF by changing the solvent in the reaction was reported by Mallick *et al.* The authors report Mg-NDI, a MOF containing Mg^{2+} metal centres and fluorescent naphthalenediimide (NDI) ligands to act as a chemical sensor to different absorbed solvent molecules, with vibrant colour changes within seconds of molecule exchange. Final colour was found to be dependent on the polarity of the absorbed molecule (Figure 1-12). Measured band gaps were shown to increase with increasing polarity from 1.63 eV for Mg-NDI, 1.87 eV for Mg-NDI-DMA (where, DMA is dimethylacetamide) to 2.06 eV for Mg-NDI-EtOH (where, EtOH is ethanol). An analysis of UV-vis spectra identify a shift in a shoulder peak associated with the intermolecular electron-transfer transition from solvent to ligand. The electronic properties of the ligand allow Mg-NDI to act as a cheap visual sensor to small molecules, which may allow the material to be used in

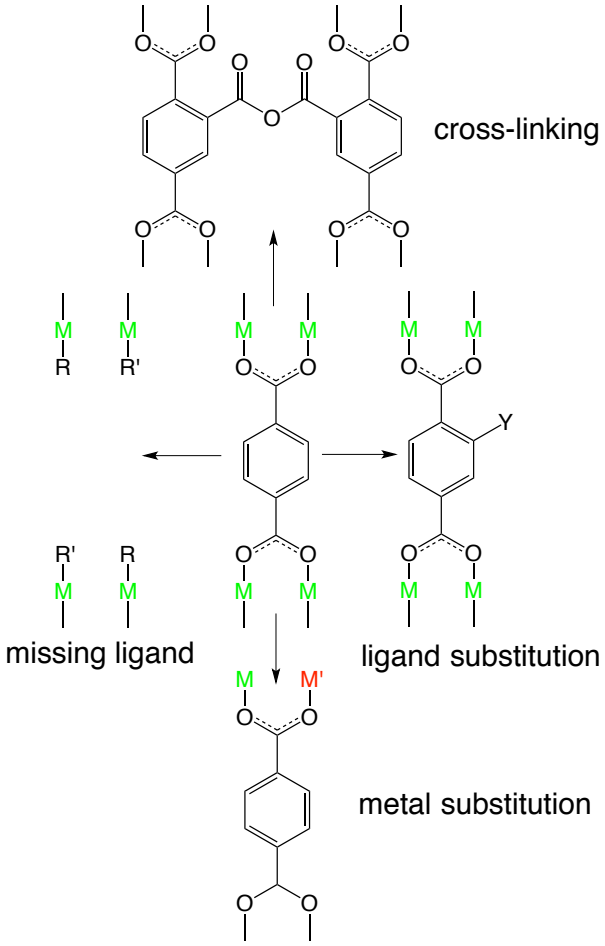

Figure 1-11: Methods to post-synthetically modify a MOF by removing linkers, changing chemical substituents on the ring, changing the metal, and cross-linking the ligands. R represents a neutral capping molecule, R' a -1 charged capping molecule, Y represents an additional substitute *e.g.* Br, I, CH_3 *etc.* and M represents a metal. Image is edited from the following reference.[67]

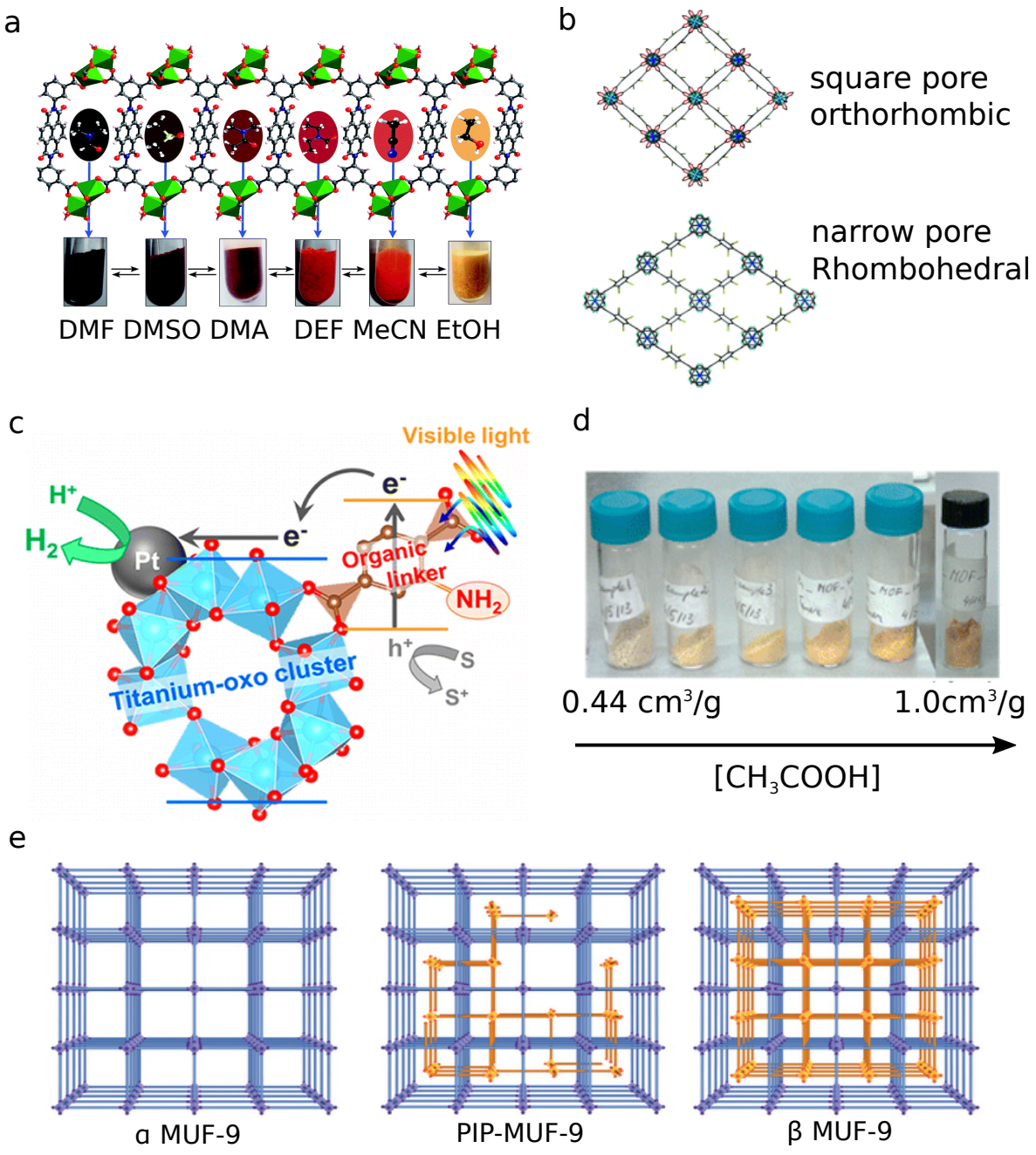

Figure 1-12: Schematic of a) Band gap modification of Mg-NDI by identity of solvent,[68] b) square pore and narrow pore forms of DMOF-1,[69] c) visible light absorption of MIL-125,[70] d) band gap modification of UiO-66 with increasing concentration of acetic acid modulator,[71] and e) MUF-9 framework with differing concentrations of interpenetration.[72]

Table 1.2: Additional notation to further describe a net of a material.[55,58]

Notation	Description
a	Augmented net, the vertices are replaced by a group of vertices *e.g.* Substituting one metal centre for a cluster of multiple metals within the same topology
b	Binary version of the net *e.g.* uni-nodal net with just one vertex
c	Concatenated net *e.g.* two nets crystallising as interpenetrated structures
d	Dual net *e.g.* Natural tilting of the net
e	Edge net *e.g.* putting new vertices in the middle of the edges of the original net
f,g *etc.*	The original net is 'decorated' by replacing a vertex with multiple vertices
x	Extended coordination, Multiple descriptions of the topology *e.g.* The vertices of a nearest neighbour unit connects to an alternative topology description.

applications such as sensing pharmaceutical molecules in waste water.[68]

An alternative method for modulating the band gap of a MOF is to substitute the ligand in the system. This can be done with minimal strain on the framework, for example by the addition of a halogen group onto a ligand. Similar size substitution allows a simple exchange in solvent with the new precursor ligand in solution. Substitution can be conducted in a manner that leaves a mix-ligand MOF product or a complete substitution affording a new MOF. Either product may crystallise in a different symmetry to the original substituted MOF, allowing access to new mechanical and electronic properties.

A recent joint experimental and computational publication by Cadman *et al.*[69] reports different ground state topologies for a MOF named DMOF-1 with varying ratios of BDC-X:BDC, where X is a halogen substitutent. DMOF-1 is formed of Zn^{2+} centres and BDC and diazabicyclo[2.2.2]octane (DABCO) ligands with the structural formula $Zn_2(BDC)_2(DABCO)$.[73] DMOF-1 crystallises in an Orthorhombic symmetry with square pores, at certain ratios of substituting BDC for BDC-X, where X = Cl, Br and I, the structure instead crystallises in a rhombohedral symmetry with narrow pores. DMOF-1 with 100% BDC is a flexible MOF and can "breathe". Breathing is a way to describe a variation in pore shape by a flexing of ligand-metal-ligand angles at the metal centres.[74] The consequence of this is that with small temperature and pressure changes, the internal pore space and underlying symmetry of the MOF can change. Flexible MOFs can be used for applications such as directed drug delivery in the body. The ability to control such a structural change in DMOF-1 *via* the addition of a halogen allows

the structure to be "locked" into different topologies with different pore shapes. The relative energies between the square and narrow pore structures determine the ground state and thermodynamic stability of each topology.

The electronic structure of a material can also be modulated by the substitution of a ligand. It has been demonstrated that the addition of an electron donating group onto BDC in MIL-125, a MOF containing Ti^{4+} metal centres, increases charge separation between ligand and metal with exposure to light. Subsequent photo-generated electrons result in the reduction of Ti^{4+} to Ti^{3+}. Photoactivity is not common for a MOF but could lead to applications such as active layers in photovoltaic devices.[75]

The notion of defects was first described for inorganic materials such as metal oxides. Materials do not form perfect crystals, where all available lattice sites are symmetrically filled above 0 K. Instead, throughout a material such as a metal oxide, atoms can be missing or displaced from a lattice site. The crystal must remain neutral for defects present to be stable. When considering defects in a MOF, a similar concept can be applied. Instead of missing anions, the ligand as the negatively charged component of the framework, could also be missing (Figure 1-11). Charge compensation could be served either by additional capping molecules (when synthesised in solution) or by metal cation vacancies. The removal or absence of a ligand is an extreme example of a defect in the structure and is likely to cause a significant disruption to the local bonding and stability. Experimental evidence of this defect is reported for MOFs such as UiO-66, where the high coordination of the metal prevents structural instability following ligand removal. The phenomena referred to as the "missing linker" is supported by a measured increase in surface area and catalytic activity.[76–78]

Interpenetration of multiple frameworks during crystallisation, has until recently been viewed as an unwanted side effect that reduces internal pore volume and surface area. Recently, Telfer *et al.* reported a MOF named $[Zn_4O(rac\text{-}1)_3]$ (also called MUF (Massey University Framework)), formed of Zn^{2+} centres and biphenyl-4,4'- dicarboxylic acid (H_2BPDC) with a phenyl-substituted diazocine bridge (rac-1). The extent of interpenetration can be controlled by reaction time. Three different crystal structures were accessible during synthesis: α-MUF-9 with no interpenetration, PIP-MUF-9 with partial interpenetration and β-MUF-9 with double interpenetration (Figure 1-12 e). The ligand is chiral, *i.e.* it is non-super imposable on its mirror image form, resulting in a random occupation of enantiomers throughout the structure and observable colour change in the sample.[72] Tuning the degree of interpenetration can therefore tune the frequency of light absorbed and molecular absorption properties.

Finally, cross-linking ligand molecules in a MOF has been shown to alter absorption and storage properties of molecules within the pores. Clay *et al.*[79] reported that UiO-66 crossed-linked by acetic anhydride molecules $(CH_3CO)_2O$) can store a greater volume of polar molecules such as water. Hydrogen bonding between anhydride molecules and absorbed water increases the capacity of the MOF for water absorption. The authors also show the MOF to possess a three-fold increase in proton conductivity if the additional carboxylic acid molecules do not bridge across the MOF pore, but remain

protonated carboxylic acid molecules. Applications proposed for such a system include water storage, electric dehumidifiers, and thermal batteries.

1.4.4 Epitaxial growth on surfaces

The epitaxy of a metal-organic frameworks on a surface such as a binary oxide (Figure 1-13) is chemically complex and involves multiple considerations. Firstly, the termination of a MOF is difficult to experimentally characterise and may depend on the synthesis conditions such as pH, humidity and temperature. Attfield *et al.* report high resolution atomic force microscopy amplitude images of HKUST-1; a Cu^{2+}/BTC (where, BTC is the 1,3,5-benzenetricarboxylate ligand) containing MOF.[80] Crystal growth regions at fractures in the crystals allowed the authors to identify, by measuring step height of crystal spacing, that a ligand (111) termination was present, which leaves one BTC ligand uncoordinated to a Cu center. Independently, Schmid *et al.* report a theoretical investigation predicting the surface termination and resolving the growth mechanism of HKUST-1.[81] Both Attfield and Schmid propose the same surface termination of HKUST-1. Such agreement between experiment and computational further supports the accuracy and viability of modern computations.

It has been demonstrated that MOFs can be grown on a variety of different surfaces including on plastic bottles formed of PET $(C_{10}H_8O_4)_n$), the principle component of which is the BDC ligand, commonly incorporated into many MOF frameworks.[83] Deleu *et al.* reported the growth of thin films of UiO-66(Zr^{4+}/BDC) and MIL-53(Al^{3+}/BDC) on partially depolymerised surfaces of PET with the plastic bottle itself being the synthesis reactor. The versatility of MOFs and their growth onto surfaces extends to binary materials such as oxides, chalcogenides and selenides.

Growth of MOFs on surfaces is affected not only by substrate identify but also the preparation of the surface prior to interfacing and the method of interfacing the two materials. The self-assembly of MOFs on surfaces is a powerful route for the fabrication of functional layered devices. The most popular method for MOF synthesis is a solutional layer-by-layer approach also referred to as a solvothermal process, where a MOF is seeded with precursors in a heated solvent solution. Early approaches for growing MOFs on surfaces was therefore to dip a chosen substrate into precursor solutions, until a given film thickness had been achieved.[85,86] Beton *et al.* report Atomic Force Microscopy images during the growth of HKUST-1 on an Au substrate.[87] Reported is the film thickness as a function of dipping cycle of the substrate into both metal and ligand precursor solutions. Growth is confirmed by an increasing film thickness with each dipping cycle.

Other methods for the epitaxial growth of MOFs on surfaces include electrochemical deposition[88,89], contact printing[90,91], inkjet coatings[92] and spray coatings[82]. Ameloot *et al.* and Ritala *et al.* independently report the gas phase deposition of ZIF-8 (Zn^{2+}/me-IM) (where, me-IM is the 2-methylimidazolate ligand) and MOF-5 (Zn^{2+}/BDC) onto surfaces.[93,94] Gas phase deposition allows greater control over uniformity and thickness for device manufacturing. The authors report the growth of thin films of MOFs using chemical vapour deposition (CVD) and atomic layer deposition (ALD)

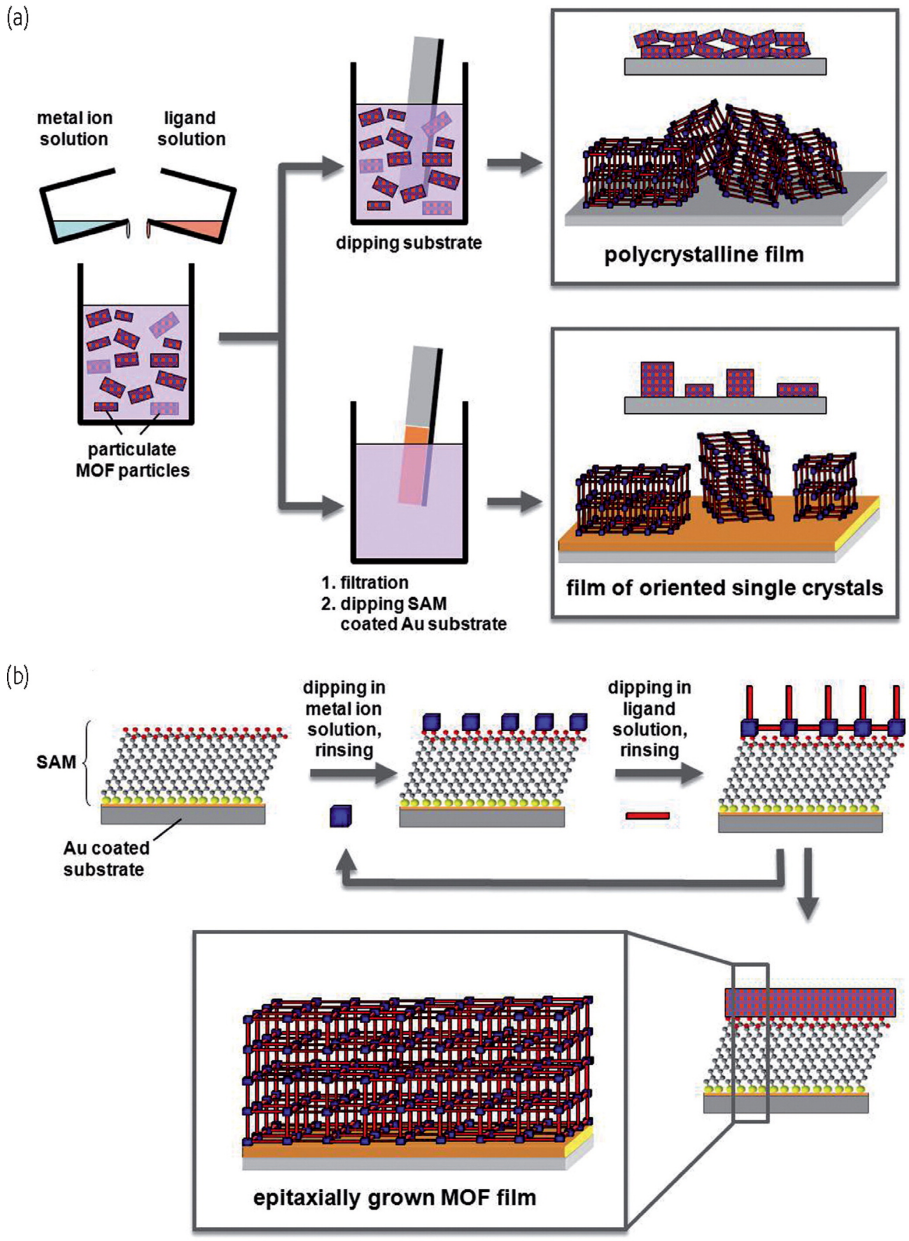

Figure 1-13: Methods for growing thin films of MOFs on surfaces. a) The growth of a MOF crystals on a clean Au surface (above), and the growth of MOF crystals on a SAM-terminated Au surface, with the removal of excess MOF crystals in solution (below). b) Layer-by-layer growth of a SURMOF on a SAM functionalised Au coated substrate.[82]

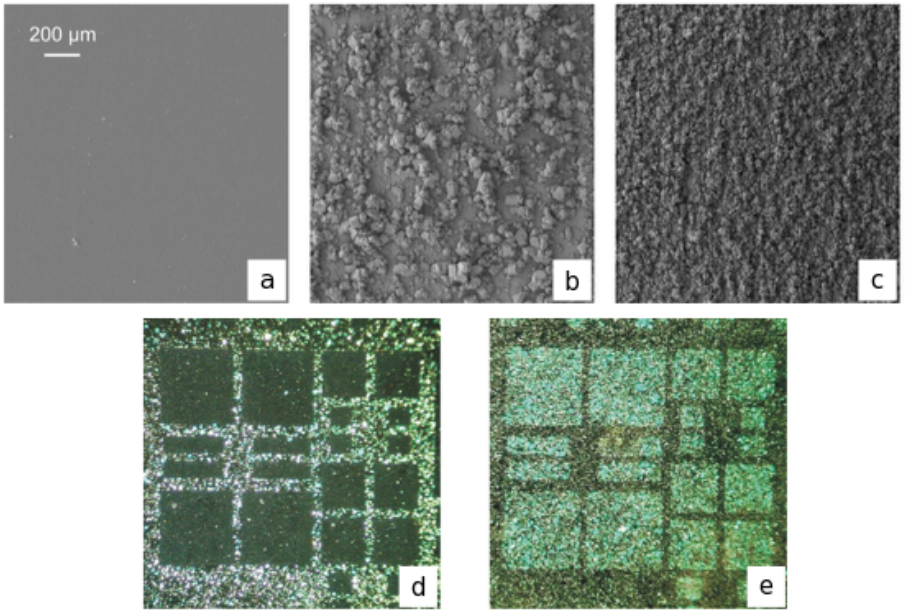

Figure 1-14: SEM images of $[Cu_3(BTC)_2]$ grown on a) bare α-SiO_2 (solvothermal) b) bare Al_2O_3 (solvothermal) c) bare Al_2O_3 (ALD) and optical images of d) "positive" CF_3/COOH SAM functionalised α-SiO_2 e) "negative" COOH/CF_3 SAM functionalised SiO_2. Image is from the given reference.[84]

methods. The ability to grow thin films of MOFs with gas phase deposition is a significant advance in the field of making functional devices. Fischer *et al.* reported the difference in film thickness of $[Cu_3(BTC)_2]$ grown on SiO_2 and Al_2O_3 surfaces with solvothermal and ALD methods (Figure 1-14).[84] An increased film thickness and density was observed on Al_2O_3 surfaces when deposition was achieved *via* ALD (Figure 1-14 c) rather than solvothermal routes (Figure 1-14 b). An absence of growth was observed on α-SiO_2 wafers in identical solvothermal experimental conditions (Figure 1-14 a)), suggesting a chemical incompatibility between the two surfaces of the materials.

In addition to directly interfacing two surfaces, preparing the substrate surface with a functionalised monolayer, such as a long-chain hydrocarbon with charged terminating groups, *e.g.* -COOH and -CF_3^-, allows greater control over self-assembled growth. Indeed, to our knowledge, one of the first reports of growing thin films of MOFs was by Shekhah *et al.*[95] The authors report the growth of MOF-5 on -COOH and -CF_3^- functionalised Pd and Au (111) metallic surfaces. Self-assembled organic monolayers (SAMs), which terminate with the -COOH and -CF_3^- groups, were previously known for their ability to bind metallic clusters from solution.[96] The authors extended this concept, contacting MOF-5 with the functionalised surfaces during crystal growth, thus creating a surface coverage of a MOF on a functionalised metallic surface. MOF thin films grown on functionalised surfaces are referred to as SURMOFs, and the approach is seen as advantageous to interfacing two clean cleaved surfaces as quality and uniformity of the final films is improved with templated and directional growth.

More recent reports of the growth of SURMOFs involve chemical systems with increased complexity for example Liu *et al.* report the growth of the two enantiomers of a chiral MOF with the chemical formulae of $[Zn_2((+)cam)_2(DABCO)_n]$((+)cam = (1R,3S)-(+)-camphoric acid) on MHDA (16-mercaptohexadecanoic acid) and pyridyl terminated PPMT ((4-(4-pyridyl)phenyl)methanethiol) SAMs on a Au surface. A preference for growth of either enantiomer was demonstrated, allowing the authors to separately analyse the properties of two enantiomers of the MOF. As previously stated, Fischer *et al.* report unsuccessful growth of $[Cu_3(BTC)_2]$ on bare α-SiO_2 wafers (Figure 1-14 a)). However, the authors demonstrate that growth is possible on α-SiO_2 if the surface is first functionalised with neutral terminating SAMs such as COOH or negative terminating SAMs such as CF_3^- groups (Figure 1-14 d) and e)).[84]

1.4.5 Applications of MOFs

Catalysis

The use of metal centres to accelerate the rate of chemical reactions was first proposed for homogeneous catalysis. Due to low catalyst recovery, metals were then adhered to solid substrates initialising heterogeneous catalysis. An alternative option to adhering the catalyst onto a substrate is to use porous materials such as MOFs where the active site on the metal is incorporated within the solid framework (Figure 1-15). Catalysis in a MOF was first reported by Fujita *et al.* in 1994.[97] The MOF consisted of near square planar geometry of the Cd^{2+}, Cu^{2+} or Zn^{2+} metal centres with 4,4-bipyridine ligands. This 2D structure is formed *via* π-stacking of the net structure. Axial vacancies on the metal centres render an active site for catalysis.

Pore size, shape and MOF composition all dictate the activity of the metal centres as catalysts. The ability to tune the internal vacant volume of MOFs allows selectivity over what molecules are favoured for absorption. Selectivity leads to control over reaction pathways for conversion of reactant molecules within the structure of a MOF. It is this control that has lead to the industrial use of MOFs in catalytic reactions when a specific product is required. Multiple examples exist of catalysis reactions within a MOF, these include[99]:

- Cyanosilylation of aldehydes ($[Cd(bpy)_2](NO_3)_2)$])[97]
- Huisgen 1,3-dipolar cycloaddition of alkynes and azides ($[Cu(2\text{-}PYMO)_2]$, $[Cu(IM)_2]$, $[Cu_3(BTC)_2]$ and [Cu(BDC)])[100]
- Heck coupling reaction ($Cr_3(F,OH)(H_2O)_2O[(O_2C)\,C_6H_4\,(CO_2)]_3 \times nH_2O$ (n = 25) and [Cu(BDC)] respectively)[101,102]
- Ring opening of epoxides ($[Cu(2\text{-}PYMO)_2]$ and $[Co(PhIM)_2]$)[103]

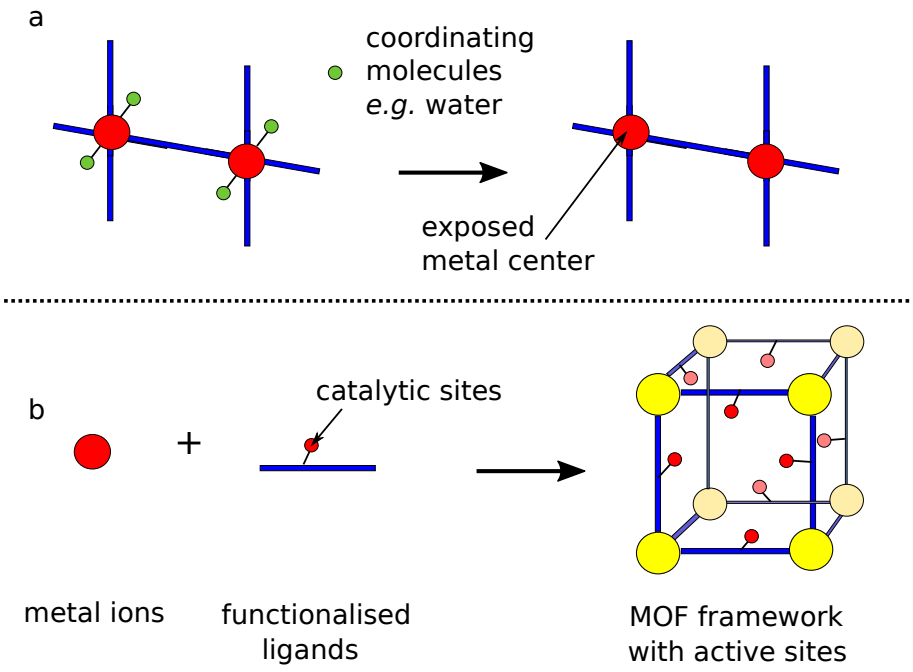

Figure 1-15: Methods for conducting catalysis using MOFs by a) removing coordinated molecules to render active sites, and b) incorporating catalytically active molecules onto the framework. Image edited from the given reference.[98]

- Oxidation and reductions of hydrocarbons (Mn(porphyrin)@[$In_{48}(HImDC)_{96}$] and [$In_2(OH)_3(BDC)_{1.5}$] respectively)[104,105]

- Friedel-Crafts alkylation ([$Zn_4O(BDC)_3$] and [$Zn_4O(NDC)_3$])[106]

Further details, such as yields, mechanism, MOF structures and turnover will not be detailed here, but some appropriate references have been given. There are several advantages of conducting catalytic reactions in a MOF, these are: a reduction in the number of synthesis steps, a greater catalyst recovery, reduction in solvent use and a faster reaction processing time. Often identical activity is seen in comparison with the isolated metal center homogeneous catalysts, particularly for Cu containing MOFs such as the previously described HKUST-1.[107] MOFs can therefore be considered as 'green' catalysts. Most commonly, catalytically active MOFs are synthesised with vacant metal sites for the appropriate coordination of reactants to occur. Other post synthetic modifications including addition of metals to the ligands and supported nanoparticles have also been shown to allow catalytic activity in MOFs (Figure 1-15).[98–100]

More recently, chiral selective MOFs with catalytic activity have been synthesised.[98] Synthesising specific enantiomer products with high yields is particularly important in the medicinal industry. When incorporated into a medicinal product, one enantiomer is often pharmaceutically active whilst the other is either inactive or toxic. Stereoselective synthesis of compounds often consists of expensive purification and separation steps. The use of MOFs as catalyst 'chambers' for stereoselective compound synthesis may reduce costs associated with such productions. Reagents are selected to produce chiral pockets within a pore, which often favour binding to a particular enantiomer over another. The first MOF reported that was capable of stereoselective catalysis was $Cd^{2+}(APD)(NO_3)_2H_2$.OEtOH (where, APD is 1-hydroxy-3-amino-propilydenediphosphonic acid).[108] Alternative production methods exist such as using homo-chiral reagents and influencing reaction kinetics of enantiomeric pair formation. High yields have been reported with $< 10\%$ of unwanted enantiomeric excess. The disadvantage of these MOFs is associated with poor thermal and water stability. Many of the reported catalytically active MOFs also decompose and deform with solvent evacuation; reaction conditions are therefore mild. Reaction times are often days/weeks to obtain a final product in a high yield ($> 50\%$).[98]

Gas absorption and separation

The ability to store a gas is a crucial consideration mainly for removal and separation of waste gases and the development of clean fuel technology such as hydrogen storage. In order to absorb a gas a material must contain sites/features for interactions between the gas and the host material to occur. For gas-absorption to be reversible, physisorption, where weak long-range interactions occur between adsorbent and adsorbate is favoured over chemisorption, where formal chemical bonds form between species. Recent publications have reported favoured binding sites of gases in a MOF.[42,109,110]

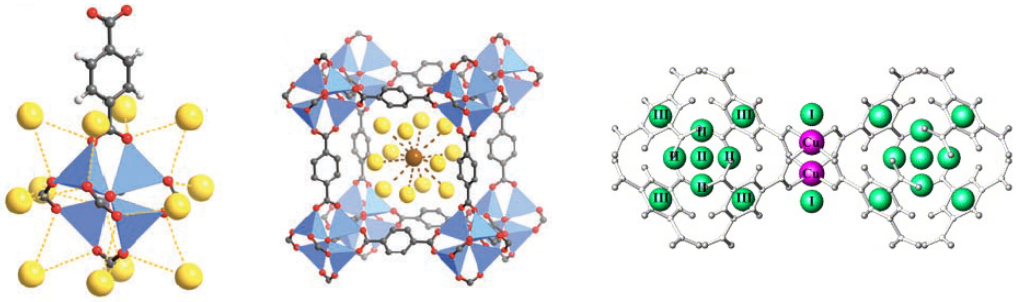

Figure 1-16: Shown are Ar (yellow sphere) absorption sites in MOF-5 (left and centre) and H_2 absorption sites in HKUST-1 (right). Note that for the centre image first and secondary layer absorption is depicted.[110,111]

The question of what is the principle component of a MOF that increases gas storage capabilities is not as simple to answer as one would initially assume. Firstly, it has been shown that gas absorption sites are located at the metal-organic interaction, at the aromatic ring on the ligands, and at the metal node sites (Figure 1-16). Absorption site preference will depend on the composition and topology of the MOF but also the identity of adsorbate. HKUST-1, has vacant metal sites due to labile coordination of water in the axial positions of the pseudo octahedral node. These sites are favoured for absorption owing to stronger interactions forming with the framework (Figure 1-16). Gases such as H_2 bind at the axial positions where the interaction between the species would be greater. Techniques such as inelastic neutron scattering and computational modelling are often used to identify favourable binding sites in MOFs.[42,112–114]

Regardless of composition, initial data for the wt% uptake of hydrogen gas remain low. For example measurements have been reported for MOF-5 of 1.3 wt% H_2 uptake at 77 K and 1 atm pressure.[115] For other topologies such as HKUST-1 an uptake of 4 wt% H_2 at 15 K and 1 bar pressure was measured.[111] The wt% for gases such as CO_2 is much higher (48.0 wt%) measured at 14 bar and 298 K for MOF-5, however higher pressures are often required.[116] The record CO_2 uptake within mild environmental conditions for MOFs is dominated by two structures; Mg/DOBDC (Mg/MOF-74) (8.7 wt% at 298 K, 1 atm)[117] and SIFSIX compounds.[118] Mg/DOBDC, also known as MOF-74, is formed of Mg^{2+} metal centres and 2,5 - dihydroxylateterephalic acid ligands in a five coordinate geometry. It is reported that the hydroxylate group of the DOBDC ligand and the high ionicity of the metal centres both contribute to stronger electrostatic interactions between metal/ligand and CO_2.[117,119]

SIFSIX compounds have been recently reported by the group of Zaworotko *et al.* and have unique compositions. Formed of di-nitrogen linear ligands, hexaflouride(Si, Ti and Sn)$^{2-}$ ligands and Zn^{2+}/Cu^{2+} metal node. The selectivity for and uptake of CO_2 are reported to exceed all those previously reported, with measured values of approximately 11.0 wt% at 298 K, 1 atm. Concatenated or interpenetrated structures within the SIFSIX series, where two frameworks have crystallised within each other, are

shown to absorb additional CO_2. Additionally, SIFSIX structures are hydrophobic and thermally stable up to between 550 - 600 K. The authors report synthesising these SIFSIX compounds to be within the "sweet spot" for gas absorption in MOFs. More specifically, SIFSIX topologies provide intermediate accessible surface areas, a range of pore sizes, strong electrostatic interactions, low processing costs, high reproducibility and high stability.[118]

Drug delivery and molecular sensing

Directed and controlled drug delivery is necessary for the treatment of many diseases including cancer and chronic pain relief. Porous polymer materials such as silica are already used for drug delivery across the body. Recently, MOFs have been proposed as selective porous materials capable of high wt% uptake of pharmaceutical molecules. Prior to the consideration of a MOFs ability to absorb pharmaceutical molecules for drug delivery, the toxicity of potential frameworks for such an application must be measured. The most common MOFs currently considered for drug delivery contain iron metal centres, which have the highest probability of being biocompatible.[120–122] Gref *et al.*[120] report Fe(III) containing MOFs with a hydrophilic aliphatic linker, fumarate (MIL-88A), a hydrophilic aromatic linker, benzene tri-carboxylate (MIL-100) and a flexible MOF formed of BDC ligands, MIL-53. *In vivo* experiments show no long-term enlargement of livers in rats with no detection of the components of the MOFs within 3 months. Furthermore, the authors report no immune or inflammatory reactions suggesting no toxicity effects. The capacity of the MOFs for the anti-tumoural drug, Busulfan (Bu), was then investigated. MIL-100 was measured to uptake 25.5 wt%, MIL-53 14.3 wt% and MIL-88A 8.0 wt%, in comparison to the polymer nanoparticles currently used for cancer treatment, which can uptake 5-6 wt% of Bu.[123] MIL-100(Fe(III)), with vacant pore volumes measuring 8200 and 12700 $Å^3$, can therefore hold five times more Bu than materials already in use. The authors also show that there is a loss of crystallinity of MIL-100 after three days incubation at 37°C. Slow release for directed drug delivery may therefore not be possible with this particular MOF. MIL-101 (Cr(III) and Fe(III)) possess the same symmetry as MIL-100 but instead of BTC contains BDC ligands. Huxford *et al.*[124] report MIL-101 (Fe, Cr) to maintain crystallinity for 6 days at 37 °C, suggesting it to be more stable than MIL-100(Fe) for use in the body. A comparison of uptake for the anti-inflammatory drug Ibuprofen between MIL-100(Cr(III)) 0.347 g Ibuprofen/g MOF, MIL-101(Cr(III)) 1.376 g Ibuprofen/g MOF and MIL-53(Cr(III)) 0.220 g Ibuprofen/g MOF also indicates MIL-101 as a strong candidate for drug delivery.

MOFs have also been used for tracking the delivery of Pt(IV)-containing anti-cancer molecules. Amino nano MIL-101(Fe(III)) was synthesised and grafted with a florescent molecule and a Pt(IV) drug, which were both adhered onto the amino group on the MOF. Such a system allows real time tracking of drug release of the anti-cancer drug.[124] Results indicate a large release of drug within days of ingesting the hybrid MOF material and no indication of further release after 1 week.[124] MOFs can therefore not only be used for drug delivery, but also as sensors for resolving where the drugs were released in the body and across what time period.

With extensive evidence for bio-compatibility and high capacity for pharmaceutical drug uptake, there is strong potential for MOFs to be used for drug delivery. Extensive further testing on toxicity in the human body and material ability to deliver controlled dosages to specified areas is required. New pharmaceutical materials often take between 5-10 years of development and testing before human trials are allowed to progress and the drug or drug delivery method is widely available.

Electrical conductivity

The mechanism behind electrical conductivity differs depending on whether the material in question is an insulator, semi-conductor or metal. The complexity of understanding these mechanisms renders a need for models.

Electrical conductivity in metals is the easiest to envision. The Drude model approximates conductivity in such materials by considering the nuclei as frozen charges with only electron movement possible. In reality electron-electron interactions should be considered, but this is not taken into account within the Drude model. Essentially, in a metal we consider the electrons to flow through the material, scattered only by classical interactions with positively charged nuclei. Electronic conductivity is measured as the movement of charge per unit time across a given area. A simple relationship between electrical conductivity (σ), and charge-carrier mobility (μ) exists:

$$\sigma = ne\mu, \tag{1.3}$$

where, n is the number of free electrons per unit volume and e is the charge of an electron. Typical electrical conductivities of monovalent metals range between 10^7 - 10^8 Scm^{-1}.

Electrical conductivity in non-metals can be induced through ionic conductivity but this can no longer be associated with the Drude model as previously described. In some materials, charged ions can hop across vacant lattice sites (vacancy defects) or diffuse into the space between lattice sites (interstitial defects). Temperature, defect concentration and electrical conductivity are all proportional; in contradiction to the Drude model for metals. An activation barrier must be overcome to allow the ions to migrate through the material and induce electrical conductivity. For materials used in fuel cell solid-state devices, where the movement of ions allows energy production, calculating and lowering these activation energies is critical for device performance.

The composition of the HOCO orbitals often show density located on the metal and LUCO on the ligand, and are often semi-conductors or insulators. To our knowledge a metallic MOF has yet to be reported. The occurrence of electrical conductivity in MOFs, particularly in those that contain large pores, is rare. Several prominent examples will be detailed here, but the field of understanding and developing electrical conductivity in MOFs is barely explored.

One such MOF reported for its electrical conductivity properties is formed of units of $\mathrm{Cu[Ni(PDT)_2]}$. The ligand comprising this structure is redox active, incorporating the described approach to enforce

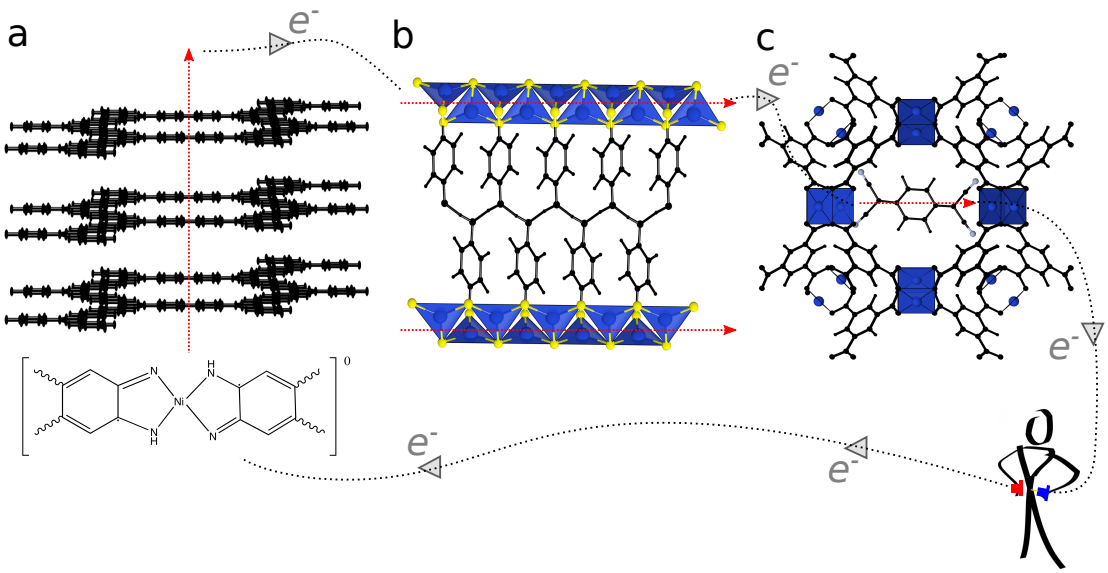

Figure 1-17: Conductivity mechanisms of electronic conductivity in MOFs, a) between 2D sheets, shown is a typical COF/MOF 2D structure with the repeat unit of $Ni_3(HITP)_2$ underneath, which possesses the same 2D structure b) along inorganic 1D layers, shown is the structure of Cu(HT) and c) delocalisation of charge density along a redox active, conjugated guest molecules, shown is a TCNQ molecule in HKUST-1 (note that the position of TCNQ is not converged in the depiction).

carrier movement. Conductivity of this MOF was measured at 1×10^{-8} Scm^{-1} at room temperature. In comparison, a similar 1D coordination polymer (Ni phenyl-1,2,4,5-tetrathiolate), which has a measured of 2×10^{-3} Scm^{-1} at room temperature. It seems that 3D coordination polymers have yet to be made into functional conductive materials.[125] A descriptive article has recently been published analysing the de-localisation of charge density between multiple metals and $C_xH_yS_4$ ligands in a similar 1D coordination polymer. The computational approach of Tiana *et al.* concluded the use of softer elements in the ligands to lower the band gap energy and the choice of metal to be crucial in determining the composition of the HOCO and LUCO orbitals.[126]

Two MOFs far exceed all others reported for electrical conductivity. $Ni_3(HITP)_2$ (Figure 1-17) recently reported by Sheberla *et al.*, where HITP=2,3,6,7,10,11-hexaiminotriphenylene[127] and Cu(HT) (Figure 1-17) reported in 2010 by Low *et al.*[128], where HT=4-hydroxythiophenolate. Both structures have 2D connectivity forming layered sheets. The Ni and Cu metals in the respective MOFs both have near square planar geometry with vacant axial sites available for further coordination. $Ni_3(HITP)_2$ has been described as an analogue to graphene as it has a dense, electron rich aromatic ligand. Unlike graphene each unit as indicated in Figure 1-17 contains a radical as a neutral molecule. Deposited films on a quartz substrate were measured to possess conductivities of 40 Scm^{-1} at room temperature for $Ni_3(HITP)_2$. The record conductivity of a MOF, however, belongs to Cu(HT), bulk electrical conduc-

tivities on pelletised powder samples were measured at 120 Scm^{-1} (room temperature). As a relative comparison ITO is one of the best conducting oxides, which is often used as a light absorbing layer of solar cells. ITO has a conductivity ranging between 400-600 Scm^{-1} depending on the sample preparation during synthesis. The potential for further MOFs with functional electrical conductivities to be predicted/synthesised is therefore promising.

Other attempts at including conjugated, redox active molecules into the framework of COFs to make organic conductive coordination polymers have been made by Cai *et al.*.[129] The authors report the inclusion of a tetrathiafulvalene molecule (TTF) as a ligand into the framework of a COF. Delocalisation of electronic density between the 2D layer is confirmed with UV-vis-IR and electron paramagnetic resonance spectra, and the reported electrical conductivity value was 2.8 x 10^{-3} Scm^{-1}.

Some of the highest recorded electrical conductivities of MOFs, other than Cu(HT) and $Ni_3(HITP)_2$, are achieved by inclusion of redox active, conjugated guest molecules into the pores. Talin *et al.* report the inclusion of 7,7,8,8-tetracyanoquinododimethane (TCNQ) as a guest molecule in the Cu containing framework: HKUST-1. Thin films of HKUST-1 without TCNQ inclusion are reported to possess electrical conductivity values of 10^{-8} Scm^{-1}. The authors report a six order magnitude increase of measured electrical conductivity for thin films of HKUST-1 with TCNQ inclusion, with a measured electrical conductivity value of 0.07 Scm^{-1}.[130] Hendon *et al.* report the composition of the frontier orbitals with TCNQ inclusion in HKUST-1, and show the LUCO to be formed of delocalised density across the TCNQ, thus shifting the predicted optical band gap from 3.5 eV for HKUST-1 to 1.4 eV for HKUST-1 with TCNQ inclusion.[45] The delocalisation of electronic density across the TCNQ molecule explains the origin of the observed increase in electrical conductivity of HKUST-1 with TCNQ inclusion. TCNQ is a molecule known to form conductive materials, and is often used in conductive organic thin films, with typical conductivity values ranging from between 10^{-3}-10^{2} Scm^{-1}. One system known to produce the highest electrical conductivities when forming a 2D network with TCNQ is TTF, hence the interest of using these molecules to induce conductivity in MOFs.[131,132]

The examples described above show that there are three primarily methods for inducing electrical conductivity in MOFs, as depicted in Figure 1-17, and that functional inherent electrical conductivity values in 3D frameworks are yet to be reported. The primary origins conductivities in MOFs are between conjugated layers in 2D MOFs and COFs (as is the case for $Ni_3(HITP)_2$), along inorganic layers in 2D and 3D MOFs and COFs, as is the case for Cu(HT), and finally, by introducing a redox active, conjugated guest molecule.

1.4.6 Material challenges

MOFs are materials that possess potential for a large range of applications. There are however multiple considerations that are preventing commercialisation of MOFs for certain applications. Firstly, the solution processing method by which many MOFs are synthesised is a small-scale batch method, which is difficult to scale up. The volume of solvent and time needed for crystallisation renders the production

of MOFs in kg scale batches expensive and time consuming. Recent reports have suggested successful synthesis of a variety of MOFs in flow rather than batch production, which would reduce the environmental impact of the process.[67] Many MOFs are also sensitive to synthesis condition, with small changes in temperature and precursor concentrations resulting in different topologies with different mechanical and electronic properties.[133] A recent article by Zheng *et al.*[134] shows the vast difference in crystal topologies with time during the formation of the cubic MOF-5. This article highlights how different approaches to synthesis can affect the quality and topology of a MOF sample.[134]

Once synthesised, the stability of the MOF and maintaining the integrity of the framework is a further consideration. MOFs can be reactive in air and samples often degrade within weeks of synthesis, at extremes, MOFs can degrade within hours. Stability of the framework can be improved as previously discussed. One must however consider that for some applications MOFs would ideally replace inorganic binary oxides. Binary oxides such as TiO_2 and Al_2O_3 can be placed in full exposure to air with no evidence of degradation for centuries. With this in mind, the stability of MOFs is a challenge that remains and will continue to be a limitation for use in many theoretically proposed applications. Further issues relating to stability included high reactivity with water, which leads to framework collapse. The stability of MOF-5 with exposure to air has been extensively studied. One such study by Long *et al.*[135] shows the initial loss of crystallinity by comparing the broadness and number of peaks in recorded XRD spectra, as a function of time the structure is exposed to air. The authors show evidence for a small loss of symmetry after 12 hours, with evident loss after 24 hours at room temperature and standard pressure. A further comparison of measured gas uptake and Brunauer Emmett Teller (BET) surface area supports the degradation of the framework. MOF-5 has also been predicted to collapse under conditions with greater than 4% water by mass.[136]

The final consideration associated with the stability of MOFs is structural changes with temperature and pressure. One primary application for MOFs is gas storage. Sustainable gases such as H_2 are often stored under high pressure conditions to increase storage capacity. With many MOFs undergoing phase changes, amorphisation and collapse with pressure and temperatures above 700 K, MOFs must be used in industry under relatively moderate conditions. Binary oxides however remain stable above temperatures of 1000 K and under extreme pressure conditions. Examples of MOFs do exist where the described structural instabilities do not apply, but in general, the coordination of metal and ligand renders an inherent structural weakness leading to instability in extreme environments.

1.4.7 Sustainability of MOFs

MOFs are considered as sustainable materials that possess large potential to contribute to numerous fields of materials chemistry. The applications of MOFs and how they contribute to sustainable chemical technologies has been detailed previously. One challenge that faces the ability to define MOFs as sustainable is the method of synthesis. Although a low cost route in terms of energy requirement, solution processing, commonly used for MOF synthesis, uses vast volumes of solvents. The method is also

slow, often taking a few days for crystal growth. Scaling up synthesis procedures have therefore always been an environmental issue with many solvents being toxic. MOF Technologies is a company who supply some MOFs on an industrial scale for applications such as waste gas removal and separation. They have developed a novel solid state method for the synthesis of MOFs that uses "mechanochemistry".[137] The process involves continuous agitation of the precursor powders for between seconds and minutes depending on desired product crystal sizes. Scaling up using this procedure has been successful and has allowed the company to commercialise (the selling of) MOF samples, which are available in masses ranging from grams to kilograms. Other approaches for the sustainable synthesis of MOFs includes using microwave technology.[138]

1.5 Thesis format

The format of this thesis in presented in four chapters, the content of which covers the work undertaken throughout my three year PhD position.

Chapter 3 presents work on the development of a classical transferable forcefield, capable of accurately predicting vibrational and mechanical properties of MOFs. The parameterisation of the forcefield includes the reproduction of first principles vibrational frequencies for an initial subset of MOFs and compares complex temperature dependent vibrational properties such as the Grüneisen parameter, bulk modulus and thermal expansion coefficient.

Chapter 4 presents work that used both classical and electronic structure methods to analyse the thermodynamics associated with defect formation in a Zr-containing MOF: UiO-66. The defect involves the loss of a finite number of ligand components of the MOF, and can be enforced in the material using different synthesis approaches. We present work on predicting the likely charge capping mechanisms that would occur following ligand removal, and final material vibrational and electronic properties as a function of defect concentration. Following the calculation of symmetry unique configurations for multiple ligand removals, the locality of the defects within the system is discussed.

Chapter 5 presents work with both classical and electronic structure methods on the epitaxial growth of MOFs on surfaces. Work includes a screening procedure to identify lattice mismatch values between a range of MOFs and binary materials such as oxides, chalcogenides and selenides. Following the described procedure, we parameterise a forcefield model from first principles calculations on an archetypal interfacing system between MOF-5 and rutile (TiO_2). Significant results suggest a reconstruction of the oxide surface following the interfacing procedure is thermodynamically favourable.

Chapter 6 presents work on the functional tuneability of the pore-shapes of metal-organic frameworks. The thermodynamics associated with changing the pore geometry and underlying symmetry of a Zn-containing MOF: DMOF-1. Reported is the description of non-covalent and steric interactions in the system with varying concentration of ligand substitutions.

The content of the four results chapters contributes greatly to the understanding of the complex

properties of MOFs and uses a wide variety of theoretical methods from simple classical laws of motion to complex electronic structure theories.

Chapter 2

Theory

2.1 The history of computational modelling

The first computational application of quantum mechanics was modelling of the di-hydrogen molecule in 1927 by Heitler and London.[139] Pauling in 1928[140] continued the work of Heitler and Fritz, reporting the ionisation potential of hydrogen. In this time period it seemed almost infeasible that the Schrödinger equation would ever be applied to systems other than hydrogen or the helium atom due to the expense of integrating the repulsion energy between electron clouds when solving the Schrödinger equation. It was in 1939, when the UK announced war with Germany that the government began to heavily fund scientific research. Computational modelling and computer development was predicted to win the war with technological superiority. It was this decision that initiated a period of rapid improvement of computational resources and allowed the development of computational chemistry. It wasn't until 1955 that the first *ab initio* calculations were realised on more complex diatomic molecules. W. C. Scherr[141] spent two years conducting the first *ab initio* calculation on N_2. By 1966 the calculation was repeated taking just two minutes. The speed up over this 11 year period when comparing the two calculations was by a factor of 525,600. Theories such as Density Functional Theory and Hartree Fock had pre-dated efficient computing resources and it wasn't until the 70's that π-conjugated molecules could be modelled. With each decade the complexity and expense of calculations continues to grow with increasing computational resources. Systems containing hundreds of atoms can now be routinely modelled with *ab initio* methods and those containing hundreds of thousands of atoms can be modelled with molecular mechanics.[142]

2.2 The potential energy surface

In 1935 Eyring proposed the energy landscape of reaction pathways must be considered by a surface that describes the position of the nuclei with energy.[143,144] Features in the surface surrounding the

lowest energy structure would describe the degrees of freedom of the system, with local minima being stable compounds. The theory of Eyring is still critical in describing reaction pathways and locating ground state and transition state structures in both experimental and computational work. Now referred to as the potential energy surface (PES), the variation in energy with differing nuclei arrangements is plotted as a multi-dimensional function with 3N-6 coordinate dimensions, where N>=3. Features of the PES include local minima, which correspond to stable configurations of the system with the global minima corresponding to the ground state structure. Other features include saddle-points, or maxima, which conversely represent unstable transition states between stable configurations.The nature in which the energy of the landscape is calculated differs between computational methods, but the description of the PES remains of fundamental importance when finding stable material configurations.[145] Once resolved, many properties such as dielectric and elastic constants can be derived as a function of this surface plot if the minimum energy structure of a system has been determined. The real potential energy surface is a quantum object, describing and reproducing such an object is complex and requires multiple approximations.

The PES can be explored by mapping out the evolution of the energies and forces of a given system. There are many ways in which the energies and forces can be calculated during energy minimisation, ranging from very accurate and expensive to more approximate but cheaper methods. We now consider some of these methods.

2.3 Energy minimisation

Energy minimisation involves the application of an algorithm to calculate the lowest energy of the system, where the forces acting on all atoms are zero. When considering the PES, atom positions corresponding to zero force on the system correspond to an energy minimum. Energy minimisation often produces the lowest energy system, also called the ground state configuration. However, if a system has a complex PES, with many local minimum surrounding the global minimum, it is common for an optimisation procedure to become "stuck" in a local minimum configuration.

In order to calculate material properties and study a system, the initial structure must be converged with all atoms in their lowest energy ground state positions following energy minimisation. The steepest descent method is the simplest procedure for geometry optimisation, which involves calculating the gradient of the PES between two points following a movement of atom positions. If the move produces a negative gradient, then the produced structure is lower in energy than the previous, and the move was favourable for finding the energy minimum. Movements are continued as an iterative process until any movement results in a positive gradient, meaning a lower energy structure cannot be calculated.[146] The functional for the steepest descent method is given (Equation 2.1).

$$\mathbf{x}_{n+1} = \mathbf{x}_n - \gamma_n \bigtriangledown F(\mathbf{x}_n), n \geq 0 \tag{2.1}$$

where, F($\mathbf{x}_n$) is the energy function, which is defined in a point in space x_n. With each iteration of minimising the total energy a new point ($\mathbf{x}_{n+1}$) in configurational space on the PES is reached as determined by the step spacing between points (γ).

Other more complex methods exist for conducting energy minimisation. For example the Newton-Raphson method, which often requires the least amount of steps but is also the most expensive to calculate per step. With each move this algorithm also calculates the curvature of the potential energy surface, using a second-order Taylor expansion to resolve the ground state structure.[147] Regardless of mathematical approach the principle of geometry optimisation is apparent.

The energy minimisation of a system using the Kohn-Sham equations in DFT follows a procedure of calculating the convergence of the electronic density with each geometry movement. The convergence of electronic density is conducted in cycles when running a calculation; these cycles are called self consistent field (SCF) cycles. The procedure of a SCF cycle is given in Figure 2-1, which describes the iterative process required to satisfy the electronic optimisation criteria of a calculation, whilst minimising the total energy of the system.

2.4 Electronic structure methods

Electronic structure methods are the most expensive methods that implement geometry optimisation to resolve materials properties of a system.

Following the wave-particle duality theory of the electron and other quantum particles, it was clear that classical molecular mechanics (that will be detailed later) was an insufficient approximation for the prediction of electronic properties of a system. Without a defined position or momentum with time, electrons are described by quantum mechanics opposing classical Newtonian theories. Prior to introducing the computational methods used to model electrons, there are fundamental aspects of quantum mechanics that must first be detailed.

2.4.1 The Schrödinger equation

In quantum mechanics, the wave function (Ψ) of a system is a mathematical concept that applies an amplitude of probability to a possible outcome, where the Ψ^2 corresponds to the electron density at a given point in space. The time independent Schrödinger equation[148] gives the relationship between the wave function and the total ground state energy (E) of the system using the Hamiltonian operator ($\hat{H}$):

$$\hat{H}\Psi(\mathbf{r}_i)(\mathbf{r}_j) = E\Psi(\mathbf{r}_i)(\mathbf{r}_j) \tag{2.2}$$

The Hamiltonian operator is mathematical operator, accounting for the kinetic and potential energy of a system:

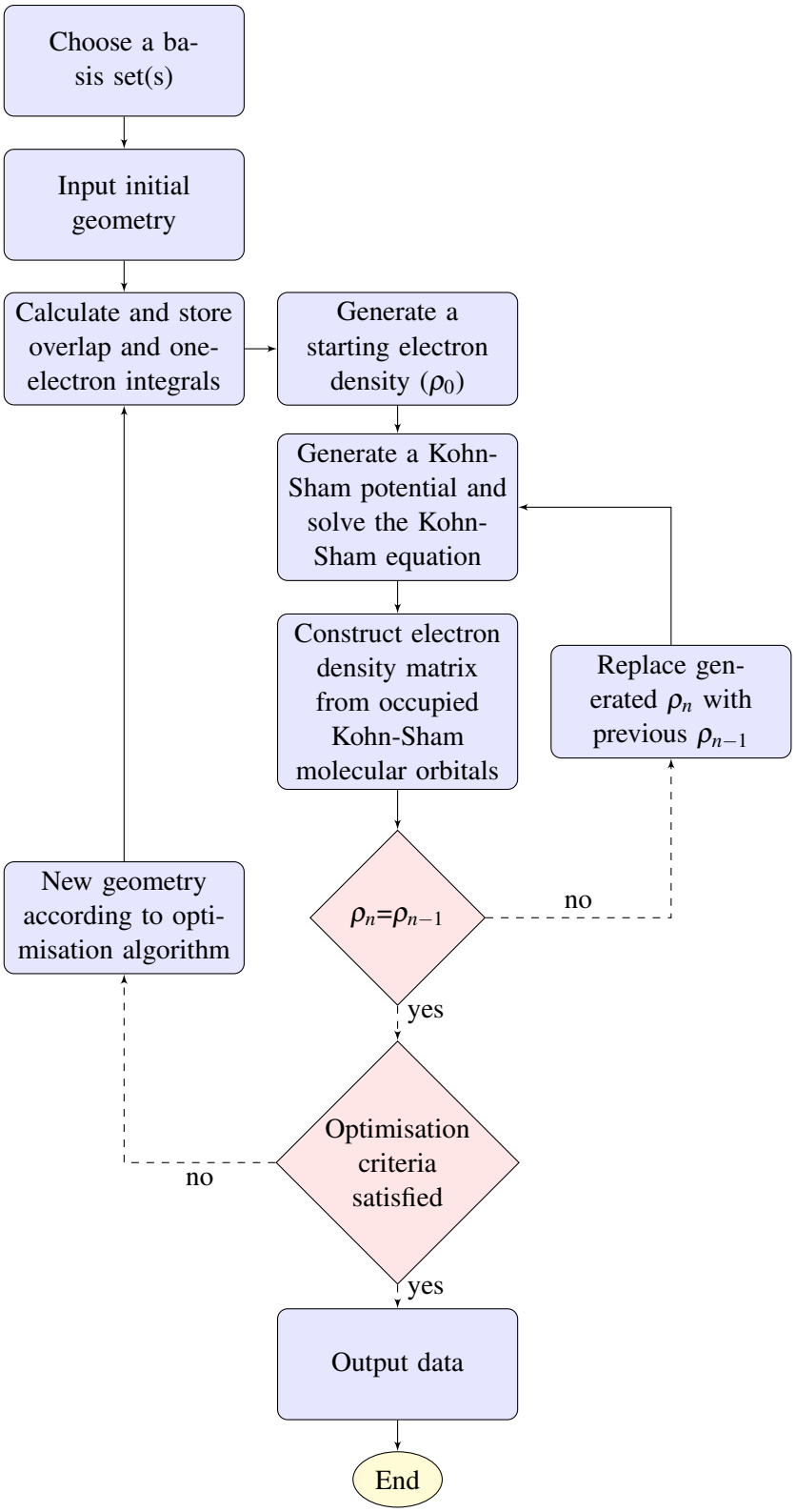

Figure 2-1: Flow chart depicting a SCF approach to energy minimisation when conducting a geometry optimisation with DFT.

$$\hat{H} = -\sum_i \frac{\hbar^2}{2m_e} \bigtriangledown_i^2 - \sum_k \frac{\hbar^2}{2m_k} \bigtriangledown_k^2 - \sum_i \sum_k \frac{e^2 Z_k}{r_{ik}} + \sum_{i<j} \frac{e^2}{r_{ij}} + \sum_{k<l} \frac{e^2 Z_k Z_l}{r_{kl}} \tag{2.3}$$

Where, i and j run over electrons, k and l over nuclei, $\hbar$=h/2π, m_e and m_k are the mass of an electron and nuclei respectively, $\bigtriangledown^2$ is the Laplacian operator, e the charge on an electron, Z is the atomic number and **r** the distance between particles.

The Hamiltonian, as written (Equation 2.3), is formed of five terms that each describe the contribution to the total energy from atomic nuclei and electrons. The first and second terms correspond to the electronic and nuclear kinetic energy, the third term is the nuclear-electron attraction, the fourth is the electron-electron repulsion and finally the firth term is nuclear-nuclear repulsion.

The Laplacian is a differential gradient operator and is given by:

$$\bigtriangledown_i^2 = \frac{\delta^2}{\delta x_i^2} + \frac{\delta^2}{\delta y_i^2} + \frac{\delta^2}{\delta z_i^2} \tag{2.4}$$

Therefore in theory, to calculate the total energy of a system and predict material properties one only needs to solve the Hamiltonian of a system and calculate the wave function.

2.4.2 The Born-Oppenheimer Approximation

In chemical systems, the electrons of an atom move much faster than the nuclei owing to the relative mass of the quantum particles. The Hamiltonian operator, as previously given, considers the mass of both particles. Electronic relaxation can be considered as instantaneous when compared to nuclear movement. Therefore, when conducting a electronic relaxation it is appropriate to consider fixed nuclear positions and decouple the nuclear and electronic energy terms in the Hamiltonian. The decoupling of electronic and nuclear energy terms when solving the Schrödinger equation is called the Born Oppenheimer Approximation, or more formally, the adiabatic approximation.[149,150] The consequence of such an approximation is that the electronic Schrödinger equation can be solved independently:

$$(\hat{H}_{el} + V_N)\Psi_{el}(\mathbf{q}_i;\mathbf{q}_k) = E_{el}\Psi_{el}(\mathbf{q}_i;\mathbf{q}_k) \tag{2.5}$$

where,

$$\hat{H}_{el} = -\sum_i \frac{\hbar^2}{2m_e} \bigtriangledown_i^2 - \sum_i \sum_k \frac{e^2 Z_k}{r_{ik}} + \sum_{i<j} \frac{e^2}{r_{ij}} \tag{2.6}$$

Following each nuclear movement, the electronic Schrödinger equation is solved. Without the consideration of a nuclear-electron coupling term, the cost and complexity of the calculation is reduced. The eigenvalue solutions to the electronic Schrödinger equation are known as electronic eigenvalues. The nuclear-nuclear repulsion term (V_N) is also included to obtain the total electronic energy of the system, E_{el} .

2.4.3 Hartree-Fock

In 1928, two years after the publication of the Schrödinger equation, the Hartree method was published.[151,152] The Hartree method assumes that each electron moves in an average potential (V_{eff}) with the only interaction between electrons being electrostatic. This notion is also called the independent electron approximation. The Hamiltonian of the system is again divided such that each electron is described independently:

$$\hat{H}_{el} = \big[-\frac{\nabla_1^2}{2} + V_{ne}(\mathbf{r}_1) + V_{eff}(\mathbf{r}_1) \big] + \big[-\frac{\nabla_2^2}{2} + V_{ne}(\mathbf{r}_2) + V_{eff}(\mathbf{r}_2) \big] + ... \tag{2.7}$$

Under this consideration the wave function is now given by:

$$\Psi(\mathbf{r}_1, \mathbf{r}_2) = \psi_1(\mathbf{r}_1)\psi_2(\mathbf{r}_2) \tag{2.8}$$

The Hartree method incorporated the SCF approach, where the equations of motion of the electrons are solved iteratively until the lowest energy solution is found. The theory was however unable to describe the anti symmetric nature of the wave function *i.e.* if a transfer of electron was to occur then the sign of the wave function must change. The new electron-electron interaction due to the anti symmetrisation of the wave function is called the exchange energy.[146]

In 1930, Fock reported modifications to the described Hartree method for solving the Schrödinger equation, the new approach was named as the Hartree-Fock approach.[153] To account for the anti-symmetric nature of the wave function the Hartree-Fock method uses a single Slater determinant, which is a determinant of one-particle orbitals, to calculate trial wave functions:

$$\Phi = \frac{1}{(N!)^{1/2}} \begin{vmatrix} \phi_1(\mathbf{r}_1, \sigma_1) & \phi_1(\mathbf{r}_2, \sigma_2) & \phi_1(\mathbf{r}_3, \sigma_3) & ... \\ \phi_2(\mathbf{r}_1, \sigma_1) & \phi_2(\mathbf{r}_2, \sigma_2) & \phi_2(\mathbf{r}_3, \sigma_3) & ... \\ \phi_3(\mathbf{r}_1, \sigma_1) & \phi_3(\mathbf{r}_2, \sigma_2) & \phi_3(\mathbf{r}_3, \sigma_3) & ... \\ . & . & . & ... \\ . & . & . & ... \end{vmatrix},$$

The total energy of the system is calculated iteratively using the variational principle, which states that trial energies must be greater than or equal to the ground state energy. Minimising the trial energies leads to the resolution of the ground state energy and allows the calculation of the potential energy surface.

Owing to the inclusion of Coulomb and exchange integrals from the incorporation of the anti symmetric nature of the wave function and additional considerations such as orbital energies, the Hartree-Fock equation differs from the initial Hartree equation:

$$\hat{F}\psi_i = \varepsilon_i \psi_i \tag{2.9}$$

where, ε is the orbital energy and $\hat{F}$ the Fock operator.

It is the Hartree-Fock equation that is solved *via* the SCF method using a single Slater determinant. The construction of the determinant when calculating the Hamiltonian results in a linear combination of atomic orbitals that allows resolution of the orbital coefficients. The formalism of the Hartree-Fock method results in an exact description of the exchange energy between electrons, owing to the antisymmetric nature of the wave function captured by the determinant method. However, the absence of describing the correlation between electrons results in large overestimations of fundamental band gap energies. [154]

The formalism introduced for the Hartree-Fock method shows no dependence on spin and therefore is known as restricted Hartree-Fock. In 1954, Pople and Nesbet developed the spin unrestricted Hartree-Fock by including the consideration of the two spin states of an electron (α and β, *i.e.* spin-up and spin-down):

$$\begin{aligned} \hat{F}_\alpha \psi_{i\alpha} &= \varepsilon_{i\alpha} \psi_{i\alpha} \\ \hat{F}_\beta \psi_{i\beta} &= \varepsilon_{i\beta} \psi_{i\beta} \end{aligned} \tag{2.10}$$

The spin unrestricted Hartree-Fock method allowed the modelling of open-shell atoms with partially occupied orbitals.

2.4.4 Density Functional Theory

A fundamental concept was missing from the Hartree-Fock theory; the electron correlation. In 1964, Hohenberg and Kohn proposed new approaches that would allow the implementation of a method that would become invaluable for computational prediction of materials properties: density functional theory. [155]

It was realised that a multi-body wave function was frightful to envisage. To avoid calculating such a notion, Hohenberg and Kohn proposed a method to solving the Schrödinger equation by calculating the electron density (ρ) opposing the wave function. It was demonstrated that the electron density could reproduce the wave function and Hamiltonian of a system. The theorem was called the Hohenberg-Kohn existence theory and showed that electron density is a physical quantity, that when integrated over space gives the total number of electrons in a system (N):

$$N = \int \rho(\mathbf{r}) \delta \mathbf{r} \tag{2.11}$$

Hohenberg-Kohn also proposed a free-energy functional that stated that the energy minimisation procedure must abide by the variational principle, which has been previously described. In simplification, the total energy of the system as a function of electron density, which is based on the Born-Oppenheimer approximation can be considered as:

$$E[\rho(\mathbf{r})] = \sum \left(E_{ni}[\rho(\mathbf{r})] + E_{ee}[\rho(\mathbf{r})] + E_{ne}[\rho(\mathbf{r})] + E_{xc}[\rho(\mathbf{r})] \right) \tag{2.12}$$

where, $E_{ni}[\rho(\mathbf{r})]$ is the kinetic energy of non-interacting electrons, $E_{ee}[\rho(\mathbf{r})]$ is the electrostatic repulsion between electrons, $E_{ne}[\rho(\mathbf{r})]$ is the Coulombic attraction between nuclei and electrons and $E_{xc}[\rho(\mathbf{r})]$ (the exchange-correlation functional) describes remaining electronic interactions not currently accounted for. The exchange-correlation functional is the only energy term that is approximated when resolving the total ground state energy.[146]

Kohn and Sham also proposed an energy functional for solving E_{ni}, by considering a fictitious system of non-interacting electrons and resolved the total energy functional in terms of an orbital expression. The final Kohn-Sham equation is given[156]:

$$E[\rho(\mathbf{r})] = \sum_{i}^{N} \left(\left\langle \sum_{i}^{N} (\phi| -\frac{1}{2}\nabla_i^2 |\phi_i \right\rangle - \left\langle \phi_i| \sum_{i}^{nuclei} \frac{Z_k}{|\mathbf{r}_i - \mathbf{r}_k|} |\phi \right\rangle + \sum_{i}^{N} \left\langle \phi_i| \frac{1}{2} \int \frac{n(\mathbf{r}')}{|\mathbf{r}_i - \mathbf{r}'|} \partial \mathbf{r}' |\phi_i \right\rangle + E_{xc}[\rho(\mathbf{r})] \right) \tag{2.13}$$

where, N is the number of electrons. As with Hartree-Fock theory, the consideration of independent electrons in a system allows a Slater determinant method to be used to resolve the eigenvalues of the Hamiltonian. Owing to the functional form of the Kohn-Sham equations the determinant for eigenvalue solutions in DFT is known as the Kohn-Sham Slater determinant method.

The exchange-correlation term (E_{xc}) can be considered as the energy of exchange and movement of electrons in a system, but also contains a classical correction for the self-interaction energy. Self-interaction arises from the classical expression for electron-electron repulsion. In Hartree-Fock theory, where the exchange of an electron is exactly described, there is no self interaction. However, in DFT the exchange-correlation term is not exactly described, and therefore renders a self interaction of the exchanging electron. There is no exact method to calculate the exchange-correlation term in DFT, but there are a wide range of functionals available to approximate this term in different approaches. Consequently, each functional considers the distribution of charge density differently.

$$E_{xc}^{LDA}[\rho_\uparrow, \rho_\downarrow] = \int d^3\mathbf{r} \rho \varepsilon_{xc}^{unif}(\rho_\uparrow, \rho_\downarrow) \tag{2.14}$$

where, the exchange-correlation energy of an uniform electron gas (ε_{xc}), $\rho_\uparrow$ and $\rho_\downarrow$ are the electronic spin densities and $\mathbf{r}$ the positions of the atoms.[157]

$$E_{xc}^{GGA}[\rho_\uparrow, \rho_\downarrow] = \int d^3\mathbf{r} \rho \varepsilon_{xc}^{GGA}(\rho_\uparrow, \rho_\downarrow, \Delta\rho_\uparrow, \Delta\rho_\downarrow) \tag{2.15}$$

where, $\Delta\rho_\uparrow$ and $\Delta\rho_\downarrow$ are the electronic density gradients.[157]

$$E_{xc}^{meta-GGA}[\rho_\uparrow, \rho_\downarrow] = \int d^3\mathbf{r} \rho \varepsilon_{xc}^{meta-GGA}(\rho_\uparrow, \rho_\downarrow, \Delta\rho_\uparrow, \Delta\rho_\downarrow, \Delta^2\rho_\uparrow, \Delta^2\rho_\downarrow, \tau_\uparrow, \tau_\downarrow) \tag{2.16}$$

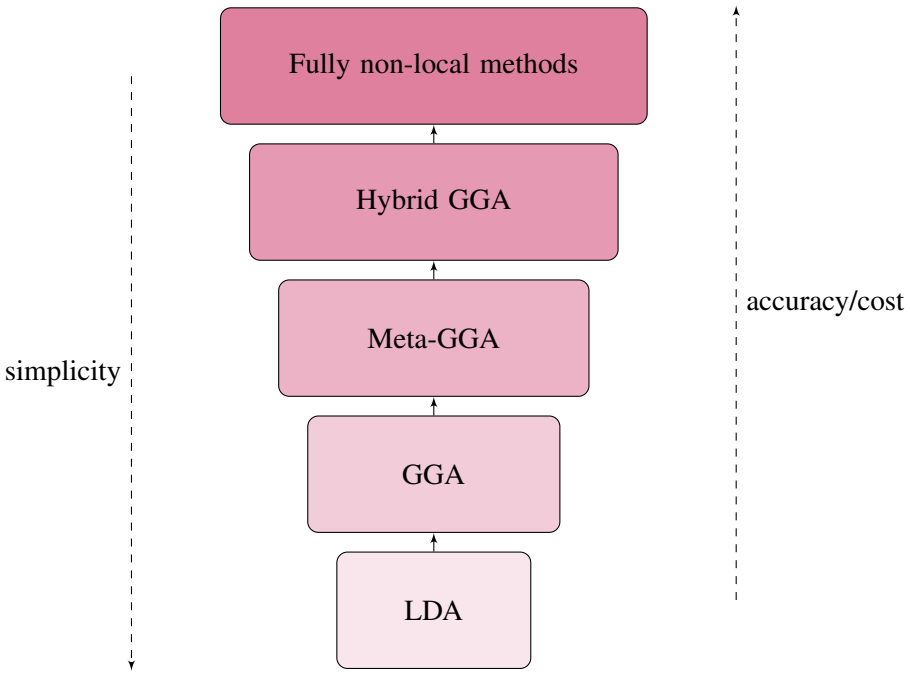

Figure 2-2: Jacob's ladder flow diagram of the cost, accuracy and simplicity of different electronic structure approaches, ranging from local LDA functionals to fully non-local functionals such as random phase approximation methods.

where, Δ^2 is the Laplacian is a mathematical second-order differential operator and the Kohn-Sham orbital (ϕ) kinetic energy densities (τ) are calculated by[157]:

$$\tau_\sigma(\mathbf{r}) = \frac{1}{2}\sum_{i}^{occ} |\Delta\phi_{i\sigma}(\mathbf{r})|^2 \tag{2.17}$$

The appropriate functional for use in DFT calculations will be system and available resources dependent. Many functionals are available within the prominent DFT codes which are based on methods such as: Local Density Approximation (LDA) (Equation 2.14), Generalised Gradient Approximation (GGA) (Equation 2.15), meta-GGA (Equation 2.16) *etc.*[157]

GGA is arguably the most popular method to employ as results often reproduce experimental data and the computations are of reasonable expense.[158,159] GGA considers the gradient of charge density when deriving E_{xc}, allowing properties such as polarisation to be considered. PBEsol is a GGA functional developed by Perdew, Becke and Ernzerhof, which was specifically developed for solids. It has been demonstrated that PBEsol accurately reproduces structural and materials properties of solids including those with large internal vacuums and complex long-range chemical interactions such as MOFs.[160–162]

The Jacob's ladder of exchange-correlation functionals, which was originally presented by Perdew and Schmidt[163] is given in Figure 2-2. Each rung of the Jacob's ladder represents a different exchange-

correlation functional, with their accuracy and computational expense increasing with ascension. The first rung of the ladder is the LDA approach, where systems are modelled as homogenous electron gases and long-range interactions are not considered. The second rung of the ladder is the GGA approach, which includes some long-range interactions by calculating the gradient of electronic density of a system. The third rung is the meta-GGA approach where the curvature of electronic density is calculated, which includes further long-range interactions, thus improving the non-bonding interaction description of the system. The final rung of the ladder are fully non-local exchange-correlation approaches, where the exchange and correlation are exactly described. These are considered the most accurate at describing long-range interactions in a system, but due to their expense, can only model very small molecular systems.

2.4.5 Slater type and Gaussian type orbitals

When calculating the Hamiltonian of a system, the orbital coefficients from the linear combination of atomic orbitals (LCAO) need to be known. The basis set is a mathematical collection of functions that describe each atomic orbital and therefore construct the wave function. There are two main types of basis orbitals used in the LCAO approach: Slater type (STO) and Gaussian type orbitals (GTO).

Slater type orbitals:

$$\chi_{n,l,m}(\mathbf{r},\theta,\psi) = N_{n,l,m,\zeta} Y_{l,m}(\theta,\psi)\mathbf{r}^{n-1} exp^{(-\zeta\mathbf{r})} \tag{2.18}$$

where, n, l and m are quantum numbers, ζ characterises the radial size of the orbital and $N_{n,l,m,\zeta}$ is the normalisation constant.

Gaussian type orbitals:

$$\chi_{a,b,c}(\mathbf{r},\theta,\psi) = N'_{a,b,c,\alpha} x^a y^b z^c exp^{(-\alpha\mathbf{r}^2)} \tag{2.19}$$

where, a, b and c are quantum numbers, which give the angular shape and direction of an orbital and α characterises the size of the orbitals. Changing the exponential form from $\exp^{-\mathbf{r}}$ to $\exp^{-\mathbf{r}^2}$ from Slater to Gaussian orbitals, changes the form of the orbitals to have a Gaussian function, which is more efficient at solving the integration of electronic terms of the Kohn-Sham and Hartree-Fock equations.

A common expression when referring to the convergence of the system is to use a big enough basis set, such that the charge density of a system is appropriately modelled. Different basis sets will apply a different number of basis functions and different cut-off radii of atomic orbital. This concept of convergence refers to the energy of the system not varying with basis set size.

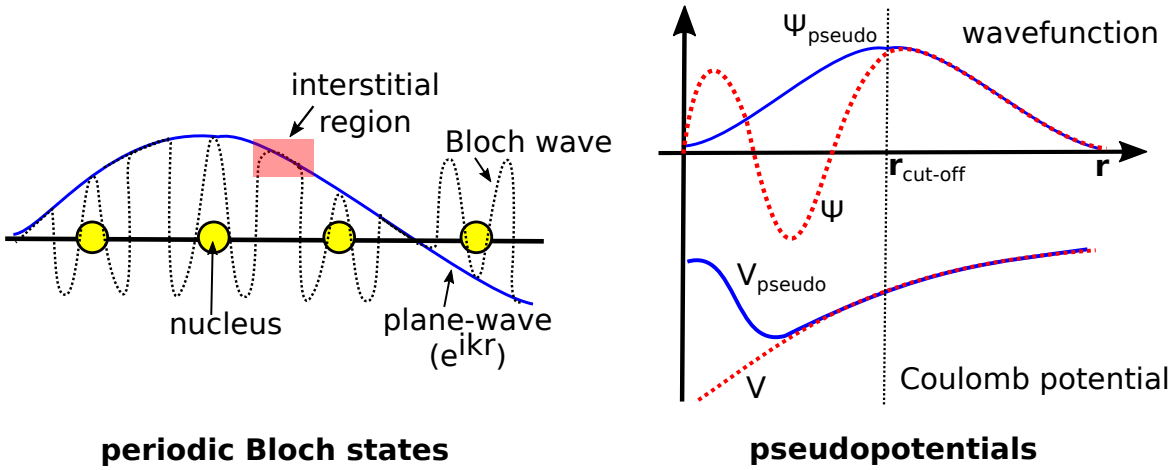

Figure 2-3: Plane wave orthogonal form compared with the Bloch states near nuclei. Highlighted are the interstitial regions between nuclei where the two functional forms match (left). The effect of pseudopotentials on the wave function and Coulomb terms of the system (right). Figure recreated from the given reference.[166]

2.4.6 Plane waves and pseudopotentials

Another basis set method that does not consider atom centred basis sets is the plane wave method. Plane waves are the most popular basis set choice for periodic calculations owing to the simplicity of the functional form. Plane waves are constant frequency orthogonal waves and are used as mathematical expressions to construct the wave function and charge density.[164,165] Mathematically, plane waves are the approximated eigenfunctions of the wave function and so can be used to calculate the Hamiltonian of a system.

Plane waves are expressed mathematically as:

$$\chi(\mathbf{r},\theta,\phi) = Nexp[i(k_x\mathbf{r}sin\theta cos\phi + k_y\mathbf{r}sin\theta sin\phi + k_x\mathbf{r}sin\theta)] \tag{2.20}$$

where, N is a normalisation constant and k_x, k_y and k_z are quantum numbers along the cartesian x, y and z directions.

In 1928 Felix Bloch proposed the theory of electron occupation in bands of a solid material in his PhD thesis. In doing so Bloch also derived a function for applying periodic conditions to a plane wave basis set.[167] Shown in the wave function notation, the plane wave can be considered as the following functional form under periodic considerations:

$$\Psi(\mathbf{r}) = u(\mathbf{r})e^{i\mathbf{kr}} \tag{2.21}$$

where, $e^{i\mathbf{kr}}$ is the plane wave function form and u a periodic potential.

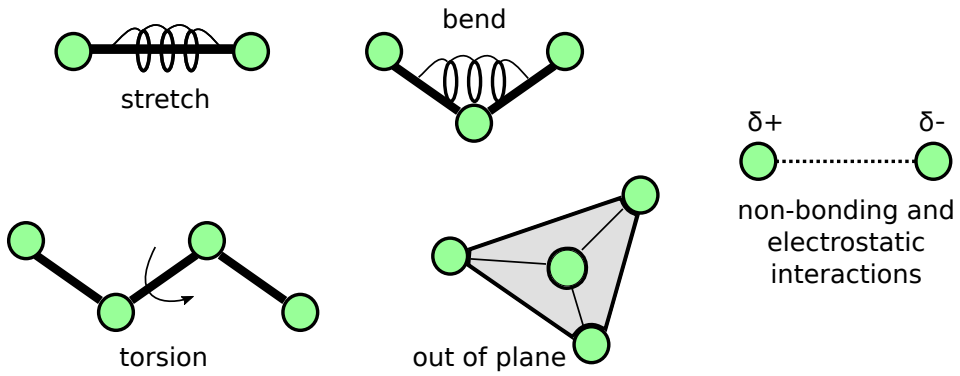

Figure 2-4: Two, three and four-body interactions considered with a forcefield when calculating the total energy of a system.

Many periodic potentials exist with the simplest being a Fourier series. It is shown, however, that near the nuclei of atoms in a system the wave function varies rapidly (Figure 2-3). This variation cannot be accurately captured with the described Fourier series of plane waves. Instead, a method was proposed by Herring in 1940, called the orthogonalised plane wave method (OPW). In the OPW method, Bloch sums of the inner core electrons are subtracted from the plane waves, resulting in only the orthogonalised plane wave form being left to describe the wave function between nuclei (interstitial region), which results in the wave function being constant at the nuclei (Figure 2-3). Pseudopotentials are the effective potentials applied to system to subtract the Bloch states of the wave function from the inner core electrons. The use of pseudopotentials reduces the number of considered electrons in a system, and significantly reduces the computer time of a calculation.[168–170]

2.5 Classical methods: molecular mechanics

A rapid method for the analysis of mechanical and structural properties of materials is to use a classical approach called molecular mechanics.

Molecular mechanics is a method based on Newton's classical laws. Atoms are modelled as hard spheres with associated point charges, which are bonded by harmonic springs with associated force constants. Methods to introduce polarisation effects and charge distribution are available as additional energy descriptions. The principle behind molecular mechanics is to describe bonding and non-bonding interactions in a system as simple analytical functions (Figure 2-4). When sufficiently parametrised, each functional calculates the energy as a consequence to different interactions of connected atoms in the system[171]. Interactions often considered in a bonding forcefield are bond stretching 2-body terms, bond angles 3-body terms, torsion 4-body terms, out-of-plane 4-body terms and non-bonding pair-wise terms.

The functional form for each bonding and many available non-bonding terms are given:

Bond stretching between atom pairs:

$$E_{stretch} = \sum_{stretch} k_{\mathbf{r}}(\mathbf{r} - \mathbf{r}_{eq})^2 \tag{2.22}$$

where, k_r is the force constant, $\mathbf{r}$ the distance and $\mathbf{r}_{eq}$ the equilibrium distance of the bond.

Angle bending between three connected species:

$$E_{bend} = \sum_{bend} k_{\theta}(\theta - \theta_{eq})^2 \tag{2.23}$$

where, k_θ is the force constant, θ is the angle and θ_{eq} the equilibrium angle between three connected atoms.

Torsion angles between four connected connected atoms *i.e.* the angle created between the two planes of bonded pairs (A-B and C-B) when considering an atom connectivity of A-B-C-D:

$$E_{torsion} = \sum_{torsion} \frac{1}{2} V_n[1 + cos(n\Phi - \gamma)] \tag{2.24}$$

where, Φ is the equilibrium phase angle, n is the integer periodicity *i.e.* the number of minima a bond passes through during a 360° rotation, V_n is the barrier height and γ is the phase factor, which gives the minimum of the cosine function.

Out of plane bending describes the energy required to raise a central atom from a planar 4-coordinate system, resulting in an angle (θ) between the plane and raised atom:

$$E_{OOP} = \sum_{OOP} \left(\frac{k}{2}\right) \theta^2 \tag{2.25}$$

VdW (van der Waals) pair-wise non-bonding interactions described as Lennard-Jones [172] and Buckingham [173] potentials. These functions consist of a short-range repulsive ($\mathbf{r}_0^{-12}$ or exponential) and long-range attractive interactions ($\mathbf{r}_0^{-6}$) and are used with a defined cut-off to describe dispersive interactions in the system arising from instantaneous dipoles between nearby atoms.

$$E_{vdW} = \sum_{L-J} \left[\frac{A}{\mathbf{r}^{12}} - \frac{B}{\mathbf{r}^6}\right] \tag{2.26}$$

where, A, B are constants calculated as:

$$A = 4\varepsilon\sigma^{12} \tag{2.27}$$

and

$$B = 4\varepsilon\sigma^6 \tag{2.28}$$

where, ε is the well-depth of the potential energy profile for the bonding interaction *i.e.* the bonding energy and $\mathbf{r}_0$ is the equilibrium distance between particles.

$$E_{vdW} = \sum_{Buckingham} \varepsilon\left(Aexp\left[-B\left(\frac{\mathbf{r}}{\mathbf{r}_0}\right)\right] - C\left(\frac{\mathbf{r}_0}{\mathbf{r}}\right)^6\right) \tag{2.29}$$

Another function for describing the vdW interactions in a system is the non-bonding MM3 Buckingham function.[173] The MM3 Buckingham function form consists of defined constants for A (1.84 $\times$ 10^5), B (12) and C (2.25) and was proposed as a softer energy function to that used in MM2. MM3 has been shown to accurately reproduce hydrogen and carbon positions in many aromatic compounds.[174,175] The advantage of using the MM3 Buckingham function over the Buckingham function is that only two constants (ε and $\mathbf{r}_{ij}^0$) need parametrising, but the exponential repulsive term, which better describes short range interactions, is retained.

$$E_{ij}^{MM3} = \varepsilon_{ij}\left[A\exp\left(-B\frac{\mathbf{r}_{ij}}{\mathbf{r}_{ij}^0}\right) - C\left(\frac{\mathbf{r}_{ij}^0}{\mathbf{r}_{ij}}\right)^6\right] \tag{2.30}$$

The Coulombic non-bonding function additionally describes the non-bonding interactions in a system due to the presence of atomic charges:

$$E_{Coul} = \sum_{Coul} \frac{q_i q_j}{4\pi\varepsilon_0 \mathbf{r}_{ij}} \tag{2.31}$$

where q_i and q_j are the point charges of atoms i and j, respectively, and ε_0 is the vacuum permittivity.

All energy functions are summed into the final energy functional description in which the total potential energy (E) of a system is calculated:

$$E = \sum E^{stretch} + \sum(E^{bend} + E^{stretch-stretch} + E^{stretch-bend}) + \sum E^{oop} + \sum E^{torsion} + \sum(E^{vdW} + E^{Coul}) \tag{2.32}$$

Due to the functional form of the bonding terms, forcefields are often stuck in the harmonic regime, which only describe a bonding interaction accurately if the bond is near its equilibrium position. Further details on the harmonic approximation will be detailed later. As a discussion point, non-bonding interactions can be modelled within an anharmonic regime if Morse functions are used instead of Lennard-Jones or Buckingham functions.[176]

$$E_{Morse}(\mathbf{r}) = D_e(1 - e^{-\alpha(\mathbf{r}-\mathbf{r}_e)})^2 \tag{2.33}$$

where, D_e is the dissociation energy of the bond, which can be calculated using first-principles

methods or experimentally resolved from methods such as measuring heats of formation, and α is the width of the potential energy well.[177,178]

Forcefields are often derived for specific systems and the treatment of these differs depending on the ionicity of the system. For example metal oxides and salts are often formed primarily of ionic interactions and a non-bonding forcefield (vdW and Coulombic energy terms) is sufficient to describe the structure.[179] Organic compounds such as hydrocarbons and proteins are formed primarily of covalent interactions and are therefore often described purely with bonding forcefield parameters.[180] It is clear that a choice is often made between using a bonding or non-bonding forcefield. The advantage of a bonded forcefield is that orbital directional effects are considered. However, the ability to model bond formation and breaking is often inaccurate and requires a non-bonding forcefield. When deriving a forcefield for MOFs the choice between bonding or non-bonding forcefield is no longer available. Consisting of both organic and inorganic components, MOFs need to be described by both bonding and non-bonding potential terms to accurately reproduce structural and material properties. Examples of such forcefields include: Amber, MM3[174], DRIEDING[181] *etc.* Although not specifically derived for MOFs, it has been shown that they can reproduce the organic components of MOFs without the need to reparameterise. It is the inorganic-organic interaction and metal centres of MOFs that often pose the greatest challenge when parameterising MOF forcefields.

2.5.1 Existing forcefields for metal-organic frameworks

A brief summary of prominent reported forcefields for MOFs will be summarised to demonstrate the diversity of existing models.

UFF. The universal forcefield (UFF),[182] first reported by Rappe *et al.* in 1992, is a forcefield with a plethora of parameters for every element in the periodic table, excluding those most recently discovered in 2015. Parametrisation of the UFF involves the consideration of element, hybridisation, connectivity and charges of connected atoms. The UFF considers second, third and fourth order bonding terms such as bond stretching, bending and torsions as typical harmonic oscillators. Non-bonding interactions are treated with Lennard-Jones functions with combination rules for the radii and energy well depth terms. The reported non-bonding function was developed in the Buckingham exponential-6 form:

$$E_{vdW} = Aexp^{-Bx} - C_6/x^6 \tag{2.34}$$

where, the exponential term describes the Pauli repulsion between interacting electron clouds and C_6 attractive term describes the long-range induced dipole-induced dipole dispersive interaction.

Several concepts feature in the UFF that are not common to other forcefields. Firstly, the concept

of a bond radius (r_{ij}) is used to derive final bond strength and length:

$$r_{ij} = r_i + r_j + r_{BO} + r_{EN} \tag{2.35}$$

where, r_i and r_j are the individual atomic radii for bonded atoms, r_{BO} is a bond order correction and r_{EN} is an electronegativity correction. The individual bond radii of each atom is derived to reproduce the natural bond length of the gas-phase diatomic molecules or to reproduce the bond length of a given element with carbon in an experimental crystal structure. The concept of bond order is used to scale final bond lengths and strengths between bonded species by the assignment of a proportionality constant, and are derived from the number of π-electrons in the molecule (*e.g.* benzene consisting formally of 3 double and 3 single C-C bonds has an average bond order of 1.5 per C-C bond). Finally, an electronegativity correction is required to scale the bond lengths and strengths according to the distribution of charge across the bond. The electronegativity correction was derived by O'Keefe and Brese[183]:

$$r_{EN} = r_i r_j (\sqrt{\chi_i} - \sqrt{\chi_j})^2 / (\sqrt{\chi_i} r_i - \sqrt{\chi_j} r_j) \tag{2.36}$$

where, χ_i and χ_j are the electronegativities of atom i and j.

Nuclear effective charges were derived using the charge equilibrium model of Rappe and Goddard.[184]

To derive a partial charge with the charge equilibrium model, the energy of the neutral atom (E_{A0}) must first be calculated *via* a Taylor expansion[184]:

$$E_A(Q) = E_{A0} + Q_A \left(\frac{\partial E}{\partial Q}\right)_{A0} + \frac{1}{2} Q_{A^2} \left(\frac{\partial^2 E}{\partial Q^2}\right)_{A0} + ... \tag{2.37}$$

where, the energy of atom A is E_A and charge of atom A is Q_A.

The same principle is then applied to the atom with formal charges of +1 and -1 with the respective energies ($E_A(+1)$) and ($E_A(-1)$):

$$E_A(+1/-1) = E_{A0} \pm \left(\frac{\partial E}{\partial Q}\right)_{A0} + \frac{1}{2} \left(\frac{\partial^2 E}{\partial Q^2}\right)_{A0} + ... \tag{2.38}$$

The energy of the +1 system is assumed to be the ionisation potential (IP) and -1 system the electron affinity (EA) of atom A (Equations 2.39 and 2.40).

$$\left(\frac{\partial E}{\partial Q}\right)_{A0} = \frac{1}{2}(IP + EA) = \chi_A^0 \tag{2.39}$$

$$\left(\frac{\partial^2 E}{\partial Q}\right)_{A0} = IP - EA = J_{AA}^0 \tag{2.40}$$

The idempotential (J^0_{AA}) is the energy of the Coulomb repulsion between two electrons occupying the same orbital (*i.e.* the self-Coulomb integral). Additional considerations are then employed in the model such as electrostatic balancing and shielding corrections. The partial charges of the system are then derived under the assumption that the chemical potentials (calculated as the derivative of energy with respect to the charge) equalise (Equations 2.39 and 2.40). The described conditions lead to a set of simultaneous equations, which are solved iteratively to assign partial charges (q_A) to each atom in the system, using atom hardness (χ^0) IP and EA values derived from experiment[184,185]:

$$\frac{\partial E}{\partial q_A} = \chi^0_A + \sum_{A=1}^{N} q_B J_{AB} = \chi^0_A + J^0_{AA} q_A + \sum_{B=1;B\neq A}^{N} q_B J_{AB} \tag{2.41}$$

The simplicity of each functional term in the UFF forcefield allows a rapid optimisation of a structure containing any element types. Due to the complex interactions in MOFs, the UFF is unable to accurately reproduce metal-oxygen bond lengths.[186]

UFF4MOF. The UFF4MOF[186] reports eighteen additional parameters to extend the UFF forcefield that are fitted to reproduce the bond lengths between metal and ligand in symmetry representative clusters of MOFs. Retaining the same functional forms of the UFF, parameters for the bond radius, angles, coordination numbers and bond orders between atom types of the elements were refitted to eighteen different atom types in common MOF motifs. Structures considered include the most common $Zn_4O(CO_2)_6$ octahedral node found within the IRMOF-series and the Cu-paddlewheel motif found in a MOF popular for catalysis and gas absorption: HKUST-1. The authors extend the application of the forcefield to reproduce the lattice parameters of nineteen different periodic MOF frameworks, including MOF-5, HKUST-1 and MIL-53 to within a 5% error. Structural properties such as unit-cell parameters and bond lengths are compared to first-principles calculations, but mechanical and thermodynamic properties are not calculated leaving an uncertainty of the applicability of the forcefield for predicting the materials properties of MOFs.

MOF-FF. MOF-FF[187] is a forcefield parameterised to reproduce first-principles structural and vibrational properties of MOFs. The second, third and fourth order bonding terms of the forcefield as were implemented in UFF4MOF (see above) are harmonic functions using force constants taken from the MM3 library of existing forcefield potentials for common hydrocarbons and small molecules.[174] Non-bonding interactions are represented by the MM3 Buckingham function (Equation 2.30). In addition to the MM3 Buckingham form, in MOF-FF the non-bonding interactions also include a dispersion damping term (Equation 2.42) to correct observed over-binding from the attractive r^{-6} term rising faster than the exponential repulsive part at very short distances.

$$E_{ij}^{vdW,MOF-FF} = \varepsilon_{ij}\left[1.85\times10^{5} exp\left(-12\frac{\mathbf{r}_{ij}}{\mathbf{r}_{ij}^{0}}\right) - 2.25\left(\frac{\mathbf{r}_{ij}^{0}}{\mathbf{r}_{ij}}\right)^{6}\left[1+6\left(\frac{0.25\mathbf{r}_{ij}^{0}}{\mathbf{r}_{ij}}\right)^{14}\right]^{-1}\right] \quad (2.42)$$

Parameterisation of ε and $\mathbf{r}_{ij}$ reproduced the interaction energy and bond lengths as predicted by first-principles calculations.

The partial charges used in MOF-FF are derived for each MOF separately using the electrostatic potential (ESP) approach. The ESP method firstly requires a quantum mechanical calculation to generate the electrostatic potentials of the system in bonding regions. Partial charges (q_j) are then varied to reproduce the electrostatic potential (ϕ_{QM}) in regions exceeding the vdW radii (r) for each atom type and the function as given in Equation 2.43 is minimised. In Equation 2.43, the final term ($\gamma(\sum_j q_j - q_{tot})$) is a Lagrange multiplier that ensures charge neutrality of the system.

$$F(q_j) = \sum_{grid}(\phi_{QM}\left((\overrightarrow{\mathbf{r}}_{grid}) - \phi_q(\overrightarrow{\mathbf{r}}_{grid})\right)^2 + \gamma\left(\sum_j q_j - q_{tot}\right) \quad (2.43)$$

The ESP method has been shown to accurately reproduce molecular and surface charges. ESP charges can fluctuate for embedded atoms in a crystalline material leading to unrepresentative charges.[188]

MOF-FF also implements derived partial charges with a Gaussian decay function to dampen electrostatic interactions at short distances and additional Morse functions (Equation 2.33) between metal and ligand with a dissociation energy of 2.17 eV across all metal-oxygen bonding pairs.

Once initial forcefield parameters and charges had been derived, parameters were refitted using a genetic algorithm to reproduce the structure of the periodic frameworks as predicted by first-principles calculations.

The authors of MOF-FF show the forcefield to be capable of accurately reproducing the structure of five clusters representing the symmetry of common MOFs including the octahedral node of the IRMOF-series ($Zn_4O(O_2C_7H_5)_6$), Cu paddlewheel structures such as HKUST-1 ($Cu_2(O_2C_7H_5)_4$) and the Zr UiO-series ($Zr_6O_4(O_2CH)_{12}$). Structural properties such as lattice parameters and bond lengths are presented as further verification of the accuracy of the forcefield. The dependence of MOF-FF on first-principles calculations and also the general complexity of the general form of the forcefield, leaves a poor transferability between structures and a computational expense that may be too great for large-scale screening methods.

QuickFF. Quick-FF reported by Van Speybroeck *et al.* is a program for deriving forcefield parameters for MOFs using first-principles calculations.[189] The forcefields generated with Quick-FF have similar functional form to MOF-FF with bonding terms described by harmonic functions, the MM3 Buckingham or Lennard-Jones function for non-bonding interactions are available and partial charges are derived using the ESP approach with Gaussian charge distribution. Other charge distribution meth-

ods are available including Hirshfeld[190] and RESP[191].

Following the optimisation of a MOF framework with an electronic structure approach, forcefield parameters can be directly extracted from the *ab initio* Hessian for each internal coordinate by the definition of perturbation trajectories across the multi-dimensional PES. The approach for deriving the forcefield parameters involves the evaluation of strain for each degree of freedom and quantifying the strain as a function of trajectory along the potential energy surface, allowing a covalent forcefield energy ($V_{cov}^{FF}(\tilde{q}_n)$) to be calculated and harmonic 2, 3 and 4-body force constants (Equation 2.44) to be derived:

$$V_{cov}^{FF}(\tilde{q}_n) = \frac{k_n}{2}(\tilde{q}_n - q_{n,0})^2 \tag{2.44}$$

where, k_n is the force constant and $q_{n,0}$ the rest trajectory value *i.e.* atomic positions prior to the applied perturbation.

The final trajectories are then fitted to recreate the *ab initio* PES with a refinement included as an error functional due to the approach.

The implementation of Quick-FF through a series of python scripts allows for an easy derivation of forcefield parameters in a form that the authors of MOF-FF have previously shown to reproduce accurate properties of MOFs. The authors report the application of forcefields derived with Quick-FF to frameworks including MOF-5 and show similar results are obtained to those calculated with MOF-FF and structural properties predicted with DFT.[189]

MOF-FF-CGNB One of the most recent advances in the field of transferable MOF forcefields is the development of a coarse grained forcefield, which was reported by Schmid *et al.*[192] The principle of coarse grained modelling is to reduce the number of degrees of freedom in a system by reducing the number of atoms, and grouping these according to chemical environment. The grouped atoms are modelled as one entity and referred to as a pseudo atom. A reduced number of degrees of freedom, leads to cheaper calculations, which allow a transferable application of a forcefield model. Coarse grained models are commonly applied to systems such as proteins, where chemical processes such as protein folding, require coarse forcefield models to reduce complexity.

In MOF-FF-CGNB (metal-organic framework forcefield-coarse grain-non bonding), beads are used to replace individual atoms in a representative system: HKUST-1. Different models are considered for different levels of coarse-graining possible to represent the structure of HKUST-1. The first, referred to as the minimal scheme, places beads at each vertex *i.e.* in the center of each ligand and at the center of the Cu connections in the metal nodes. The second, referred to the intermediate scheme, places a bead at each site of the minimal scheme with an additional location at the carboxylic acid head of the ligand. Finally, there is the building block scheme, where in addition to the beads at the intermediate locations, there is an additional bead on each ligand at the carbon that links the carboxylic acid carbon and remainder of the benzene ring.[192]

The forcefield details remained similar to MOF-FF but required an additional term to account for in plane bending of the square planar metal node in HKUST-1:

$$E^{bend}_{a,coord} = \frac{V_a}{2}\left[1 + cos(4\theta_a + \theta^{ref}_a)\right] \tag{2.45}$$

where, θ_a is the valence angle, θ^{ref}_a is the phase shift and V_a the energy barrier.

The coarse-grain Hamiltonian (H_{cg}) has the dimensions [$3N_b$, $3N_b$], where N_b is the number of beads considered to represent the structure. The Hamiltonian is calculated using a double sided finite difference approach, where all virtual positions of the beads are displaced by a distance, d, in a positive and a negative direction away from the optimised positions. A L-BFGS algorithm is then used to optimise the system under the coarse grain approach.[192]

Additionally, a modified Buckingham term is used for the non-bonding interactions in the system:

$$E^{vdW+C}_{ij} = Ae^{-B(d_{ij}-d^0_{ij})} - \frac{C}{(d_{ij}-d^0_{ij})^6} \tag{2.46}$$

where, d^0_{ij} is an off-set parameter, A and B are repulsive constants and the constant C controls the strength of the dispersive interaction.

MOF-FF-CGNB is shown to accurately reproduce the mechanical and structural properties of two different topologies (**tbo** and **pto**), which are possible with the connectivity of HKUST-1. The level of coarse graining is shown to be be important, and the minimal scheme shown to be insufficient for reproducing the negative thermal expansion properties of HKUST-1. Finally, as the MOF-FF-CGNB could reproduce the bulk elastic properties of HKUST-1, nano-indentation simulations were conducted, where a modelled metallic nano-tip was penetrated into the surface of a constructed supercell. Potential energy of the system was calculated as a function of penetration depth and deformation of the surface layers reported. Coarse-grain methods are appropriate for nano-indentation simulations due to the large system sizes.[192]

MOFomics. The inclusion of MOFomics in this section is questionable as there is no structural relaxation or forcefield implemented, however, the MOFomics program is capable of screening thousands of MOFs for gas absorption properties.[193] The prediction of accurate gas absorption isotherms is currently the most popular use of a forcefield for MOFs, making MOFomics an attractive alternative to deriving forcefields for MOFs for a rapid prediction of such properties.

The process behind MOFomics is simple, and starts with the application of symmetry operations to the experimental coordinates of a crystallographic information file to extract all cartesian coordinates of the atoms in the non-primitive unit cell. Bonds are then identified if the atom distance is shorter than the sum of the covalent radii of two neighbouring atoms. Isolated atom clusters coordinates are removed to desolvate the structures, and partial occupancy disorder removed by favouring atom positions with

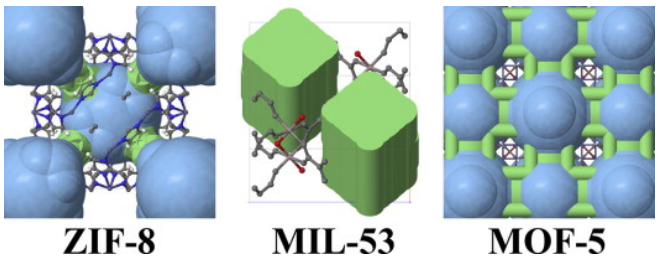

Figure 2-5: Pore systems of ZIF-8 (Zn), MIL-53 (Al) and MOF-5 (Zn) as considered by the approach in the MOFomics program.[193]

higher occupancies and disregarding those of lower occupancy.

Following the preparation of input coordinates, the channels and portals in the structure are identified and characterised. Portals are defined as closed looped paths through the structure with no intersection across atom positions, and channels identified as links between the portals. The vdW radius of the atoms forming the walls of the channels are subtracted from the calculated cylinder volume of void space. A final consideration is the internal volume within cages of the framework. The three-dimensional method of Delaunay triangulation is used to calculate the largest sphere of free-volume in each cage. The combination of calculating the free-volumes of the portals, channels and cages of a MOF allows the internal free-volume and surface area to be calculated. The authors then show the application of MOFomics in characterising and identifying the gas absorption properties of over 800 experimental MOFs and 1600 hypothetical MOFs, and make conclusions of structural features of the MOFs with the volumetric gas uptake capabilities calculated.[193]

MOFomics uses simple mathematical rules to characterise each structure and approximated gas absorption properties. The accuracy is therefore questionable, however, the method has allowed a large-scale screening approach for functional properties of MOFs that may not be possible or as rapid with more complex forcefield models.

2.5.2 Molecular dynamics

The theory behind molecular dynamics is also based on the Newtonian laws of motion and the potential parameters used to compute the forces on atoms remain the same as those used in molecular mechanics. Solving Newton's second law of motion (Equation 2.47) affords the velocity and acceleration of the atoms in a system, allowing the system to progress in time.

$$\frac{\partial^2 \mathbf{x}_i}{\partial t^2} = \frac{F_{\mathbf{x}i}}{m_i} \tag{2.47}$$

where, $F_{\mathbf{x}_i}$ is the force on an atom in a direction ($\mathbf{x}_i$) of a given mass (m_i).

Ensembles

Within MD there are multiple ensembles available within the molecular dynamics method, which apply conditions to the simulations:

NVE Microcanonical NVE ensembles fix the number of atoms, volume and energy of the system throughout the simulation.

NVT Canonical NVT ensembles fix the number of atoms, volume and temperature of the system throughout the simulation. The Nòse Hoover thermostat is the most popular thermostat used to control a predefined temperature of system. A heat bath is applied using a Hamiltonian with an additional degree of freedom.[194–196]

NPT Isothermal-Isobaric NPT ensembles fix the number of atoms, pressure and temperature of the system throughout the simulation. A barostat, in addition to a thermostat, is required to control a predefined pressure throughout the simulation. The Berendsen coupling bath method is commonly employed as a barostat during MD simulations. The Berendsen barostat uses a scaling factor, which is a function of pressure.[197]

Integration algorithms

Integration methods calculate the molecular dynamic trajectories with a predefined time step. A time step is a length of simulation time at which the acceleration and trajectories of the atoms are calculated. To calculate the acceleration and velocities of the atoms at time (t), an algorithm to integrate Newton's equation of motion is required, all algorithms use Taylor expansions:[185]:

$$\mathbf{r}(t+\partial t) = \mathbf{r}(t) + \partial t\mathbf{v}(t) + \frac{1}{2}\partial t^2\mathbf{a}(t) + \frac{1}{6}\partial t^3\mathbf{b}(t) + \frac{1}{24}\partial t^4\mathbf{c}(t) + ... \tag{2.48}$$

$$\mathbf{v}(t+\partial t) = \mathbf{v}(t) + \partial t\mathbf{a}(t) + \frac{1}{2}\partial t^2\mathbf{b}(t) + \frac{1}{6}\partial t^3\mathbf{c}(t) + ... \tag{2.49}$$

$$\mathbf{a}(t+\partial t) = \mathbf{a}(t) + \partial t\mathbf{b}(t) + \frac{1}{2}\partial t^2\mathbf{c}(t) + ... \tag{2.50}$$

$$\mathbf{b}(t+\partial t) = \mathbf{b}(t) + \partial t\mathbf{c}(t) + ... \tag{2.51}$$

where, the velocity ($\mathbf{v}$) is the first derivative, the acceleration is calculated from the second derivative ($\mathbf{a}$), $\mathbf{b}$ is calculated from the third derivative and $\mathbf{c}$ is calculated from the fourth derivative *etc.*

The Verlet algorithm is the most common integration scheme employed within MD. Using both the accelerations and positions of the atoms at time t and time of the previous step, (t - δt) (Equation 2.52), to calculate those at the time of the next step, (t + δt) (Equation 2.53).[185]

$$\mathbf{r}(t-\partial t) = \mathbf{r}(t) - \partial t\mathbf{v}(t) + \frac{1}{2}\partial t^2\mathbf{a}(t) - ... \tag{2.52}$$

$$\mathbf{r}(t+\partial t) = \mathbf{r}(t) + \partial t\mathbf{v}(t) + \frac{1}{2}\partial t^2\mathbf{a}(t) + ... \tag{2.53}$$

The sum of these equations gives:

$$\mathbf{r}(t+\partial t) = 2\mathbf{r}(t) - \mathbf{r}(t-\partial t) + \partial t^2\mathbf{a}(t) \tag{2.54}$$

The velocities at (t + ∂t) can then be calculated by dividing the sum of the functions for (t - ∂t) and (t + ∂t) (Equation 2.54) by $2\partial t$.

The disadvantage of the Verlet algorithm is that it cannot simultaneously calculate positions and the kinetic energy contribution to the total energy. The velocity Verlet algorithm developed by Swope *et al.*[185] evaluates positions, velocity and accelerations simultaneously:

$$\mathbf{r}(t+\partial t) = \mathbf{r}(t) + \partial t\mathbf{v}(t) + \frac{1}{2}\partial t^2\mathbf{a}(t) + ... \tag{2.55}$$

$$\mathbf{v}(t+\partial t) = \mathbf{v}(t) + \frac{1}{2}\partial t[\mathbf{a}(t) + \mathbf{a}(t+\partial t)] \tag{2.56}$$

The positions at (t + ∂t) are then calculated from the velocities and acceleration at time t. Velocities are then calculated at (t + $\frac{1}{2}\partial t$), at which point new forces are calculated from these positions to calculate the accelerations at (t + ∂t). The final step is to resolve the velocities at (t + ∂t), which is done so with the final equation[185]:

$$\mathbf{v}(t+\partial t) = \mathbf{v}(t+\frac{1}{2}\partial t) + \frac{1}{2}\partial t\mathbf{a}(t+\partial t) \tag{2.57}$$

Assigning initial velocities and equilibration

When initially starting a MD simulation, fluctuations in temperature and pressure and unit cell volume can lead to unphysical observation in materials properties. Such fluctuations are due to the manner in which the initial velocities are assigned to the atoms in a system. A Maxwell-Boltzmann distribution of velocities are assigned to each atom randomly, such that each atom is subjected to a different initial thermodynamic temperature.[198] A period of time must be run and disregarded prior to continuing the simulation after randomly assigning velocities in the system. This period of time is called the equilibration time of the simulation. Wild fluctuations in total energy or other properties such as unit

cell parameters should not be observed if the system is at equilibrium. Once at equilibrium, properties of the system in time can be calculated.

2.5.3 Reciprocal k-space

The use of cartesian space for visualising atomic positions is logical, but not efficient for computational modelling. An alternative approach is to use crystal planes with (*hkl*) notion used to describe a plane of the unit-cell of the crystal with respect to the main crystallographic axis. Each crystal plane has an associated unit vector ($\hat{n}_{hkl}$) and spacing between planes (d_{hkl}). For simulations the definition of crystal planes are extended to include a vector definition.[199]

$$\mathbf{G}_{hkl} = \frac{2\pi\hat{\mathbf{n}}_{hkl}}{d_{hkl}} \tag{2.58}$$

$$\mathbf{k} = k_1\mathbf{a}^* + k_2\mathbf{b}^* + k_3\mathbf{c}^* \tag{2.59}$$

The definition of a vector ($\mathbf{G}_{hkl}$) allows each point within the unit-cell to be described by a family of planes in real space (**a**, **b** and **c**) (Equation 2.58), where $\mathbf{a}^* = \frac{2\pi(\mathbf{b}\times\mathbf{c})}{\mathbf{a}.(\mathbf{b}\times\mathbf{c})}$, and $\mathbf{b}^*$ and $\mathbf{c}^*$ are calculated by an iterative procedure. This can be further extended to define a general vector (**k**) in reciprocal space (**k**-space) as a function of lattice lengths opposing crystal planes (Equation 2.59).[199] The use of vectors in reciprocal space allows simulations to consider inverse lattice length, thus reducing the costs of calculations.

$$n(\mathbf{r}) = \sum_{\mathbf{k}=0}^{\infty} n_{\mathbf{k}} exp(i\mathbf{k}.\mathbf{r}) \tag{2.60}$$

Properties such as atomic densities ($n(\mathbf{r})$) in reciprocal space are calculated as Fourier transformations under periodic considerations as a function of the general reciprocal lattice vector, **k** (Equation 2.60).[200]

2.5.4 Band structures

The dependence of electronic (or vibrational) energy as a function of wave vector through the periodic Brillouin zone is called the band structure (Figure 2-6). Visualisation of a band structure is achieved by plotting electronic (or vibrational) energy *vs* wave vector for particular trajectories along high symmetry paths of the Brillouin zone.[201] High symmetry paths will depend on the underlying symmetry of the material, but once plotted the band structure consists of a series of points of allowed energy states (Figure 2-6). The allowed energy states form a continuous band with varying curvature as a function of crystal wave vector. The curvature of a band is also referred to as the dispersion, and contains information on the electron's motion through the Brillouin zone, which is dependent on the crystal potential.

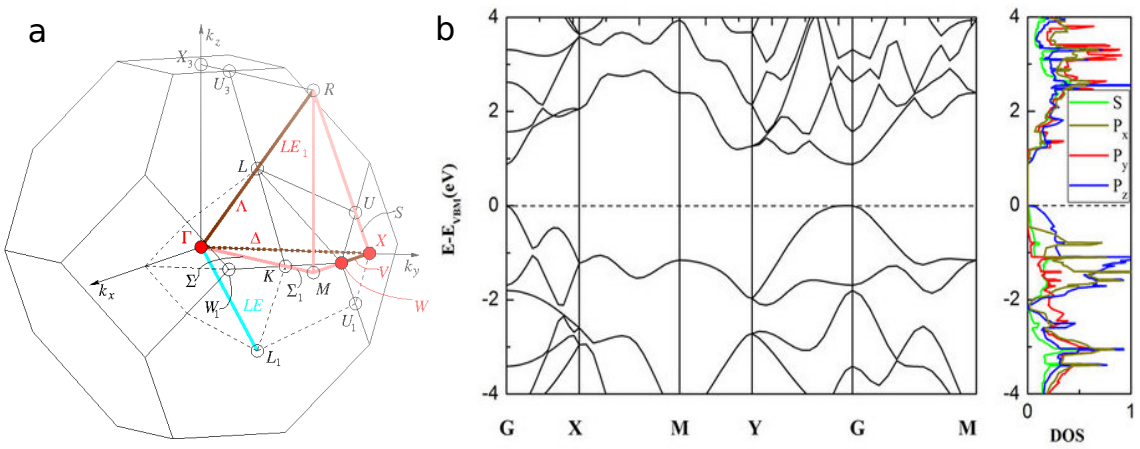

Figure 2-6: a) High symmetry paths in the Brillouin zone of a crystal belonging to the space group number 216. Image was generated using the Crystallographic Bilbao Server.[202] b) Band structure and DOS of black phosphorus, calculated using the PBE functional with the D2 vdW correction using the VASP code.[165,203,204]

A common property derived from the curvature of an electronic band structure is called the effective mass (m_e^*). The "true" mass (m) of a particle such as electron can be calculated with the Newtonian law of motion (F = ma), considering both the force (F) and acceleration (a) of the particle.[205] In a crystal the momentum of a electron moving through the Brillouin is changed by the variation in potential of the changing chemical environment of the crystal.[199] As a consequence, the true mass of the electron may now be considered as an effective mass, which can vary as a function of wave vector (**k**) in the band structure:

$$\frac{1}{m_e^*} = \frac{1}{\hbar^2}\left(\frac{\delta^2 E}{\delta k^2}\right) \tag{2.61}$$

where, E(**k**) is the energy an electron at wavevector **k**.

The calculation of the effective mass of a 1D parabolic band can be simplified (Equation 2.61) to be a function of the curvature of a band.[206] As the approximation is dependent on a parabolic shape of the band, the effective mass should only be derived from the maxima or minima of a dispersed band, and final values will vary with energy ranges sampled.

The inverse relationship between the effective mass and the curvature of a band means that flat bands with little dispersion have a high effective mass. The smaller the value of the effective mass, the greater the acceleration of the electron in the system, suggesting an increase in electrical conductivity in that region of the Brillouin zone. Effective masses are often reported for both electrons and holes (m_h^*). Furthermore a band can possess more than one value of effective mass with different eigenvectors through the Brillouin zone, in this case the lower value of effective mass is referred to as a light electron or hole and greater value as a heavy electron or hole.

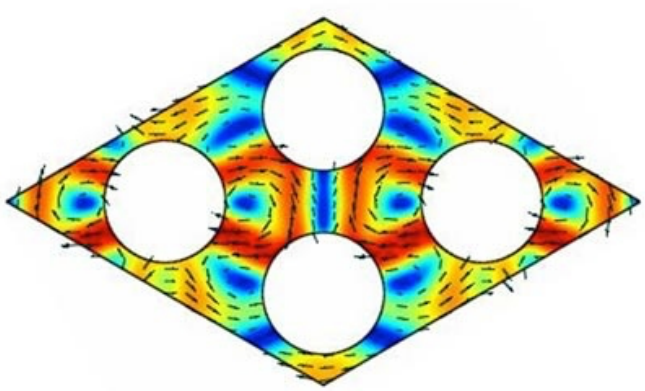

Figure 2-7: Heat travelling through a solid periodic material generated from a computer simulation by Chandler *et al.*[208] Lattice is partitioned by rods (white) to block phonon mobility in distinct regions of the crystal.

2.5.5 Density of states

The electronic density of states (DOS (D(E))) is the number of states (either vibrational or electronic) in an interval of energy that are available for occupation.

$$D(E) = \frac{V_{cell}}{(2\pi)^d} \int_{BZ} d\mathbf{k} \delta(\varepsilon_{i,\mathbf{k}} - E) \tag{2.62}$$

The DOS is calculated *via* the integration in reciprocal-space over the Brillouin zone (Equation 2.62), where V_{cell} is the volume of the unit-cell, $\varepsilon_{i,\mathbf{k}}$ is the energy of an electron (or phonon) as a function of **k**-space, **k**, E is the energy difference between two electrons (or phonons) (E = ε_j - ε_i). An example of a DOS plotted for black phosphorus is given in Figure 2-6.[207]

The DOS can be decomposed into element contributions to the total DOS, allowing a detailed analysis of electronic contributions to be analysed. Furthermore the DOS allows visualisation of the fundamental band gap, which is identified as a gap in the spectra due to an absence of available states.

2.6 Lattice dynamics and phonons

The oscillations/vibrations of atoms in a periodic solid material increase as a function of temperature. A phonon, is a quantum of vibrational energy (hω, where ω is the angular frequency, and h is Planck's constant) and is a quantum particle possessing wave-particle duality properties.

The transport of heat (an example shown in Figure 2-7) through a solid material other than a metal is dominated by the vibrational oscillations of atoms. An analysis of the vibrational properties of a

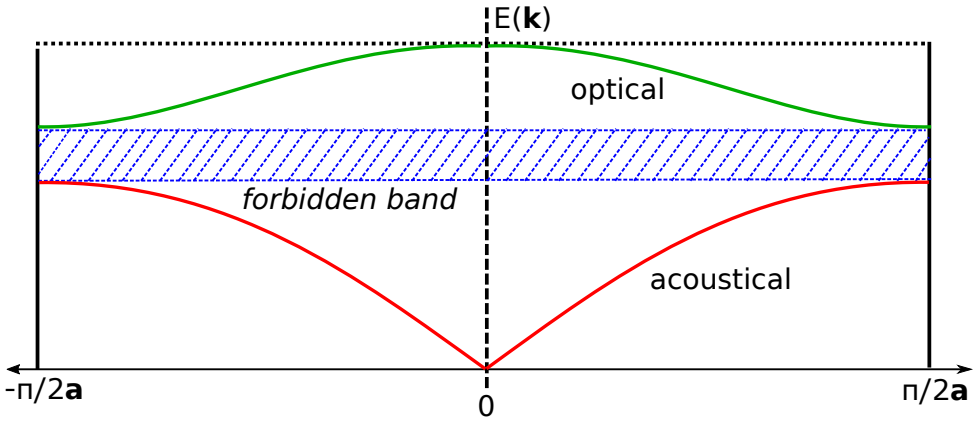

Figure 2-8: Reduced zone representation of phonon band structure plotted as a function of wavevector (**k**). Figure recreate from the given reference.[209]

system is therefore critical in understanding thermodynamic stability and calculating the temperature dependence of material properties.

There are two types of vibrational modes possible in a solid crystal, these are referred to as acoustic and optical modes (Figure 2-8). Acoustic modes correspond to a uniform displacement of the whole crystal in the directions *x*, *y* and *z*. Hence when plotting a phonon bandstructure, which depicts the variation in frequency of a mode as a function of wavevector, three modes are present at 0 energy at the Γ-point. These 0 energy modes are called the Γ-point or acoustic modes, and for a thermodynamically stable structure, should be at the lowest energy. Optical modes correspond to the out of phase movement of oscillating atoms. All modes other than the three described acoustic modes are optical modes of the crystal. The frequency that each mode occurs at depends on the nature of the collective out-of-phase motion occurring in the crystal. As a further consideration a vibrational mode can either propagate transverse (perpendicular) or longitudinal (parallel) to the direction of atom movement.[166,210]

2.7 The harmonic approximation

When considering the interatomic potential (U) between two bonding atoms separated by an interatomic distance (**r**), different approximations are made to simplify modelling the potential energy surface of such a system. In a "real" system an interatomic potential has an anharmonic form with a complex shape (Figure 2-9). Describing the potential energy surface in a functional form for an anharmonic system is complicated. A common approximation to such a description is called the harmonic approximation. The harmonic approximation originates form a Taylor expansion of the interatomic potential (U(**r**)) with small displacements (x) around the minimum at r_0:

$$U = U(\mathbf{r}_0) + \frac{\delta U}{\delta \mathbf{r}}_0 x + \frac{1}{2}\left(\frac{\delta^2 U}{\delta \mathbf{r}^2}\right)_0 x^2 \ldots \tag{2.63}$$

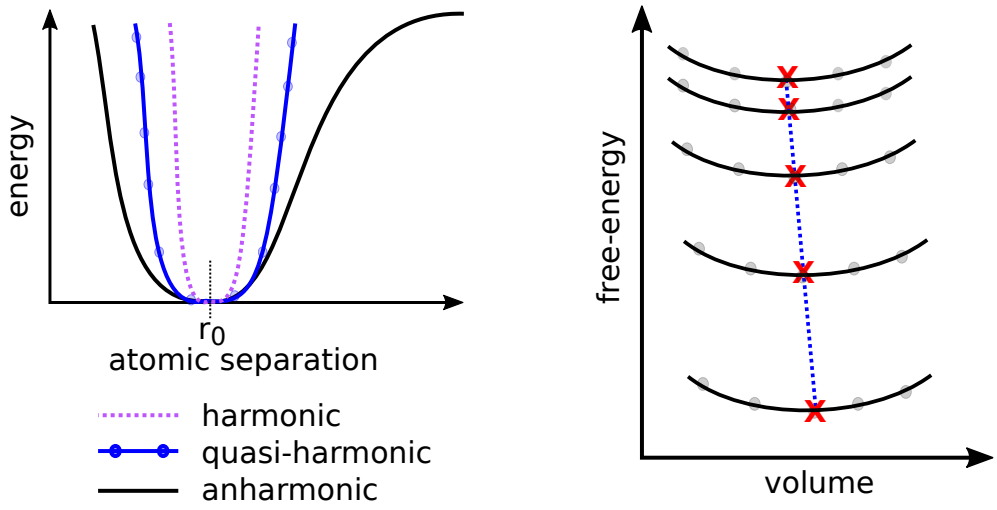

Figure 2-9: Potential energy profiles of a 2-body potential between atoms under the harmonic, quasi-harmonic and anharmonic approximations (left) and Helmholtz free-energy *vs* volume following the fitting of an equation of state (right). Highlighted (blue dotted line) is the shift in minima of free-energy with volume expansion. Figure is recreated from the given reference.[211]

The first term corresponding to the internal energy or lattice energy, is a constant and therefore can be disregarded for lattice dynamics. The second term is the gradient of the interatomic potential and corresponds to a force. Forces are minimised in the configuration at $\mathbf{r}_0$ and so the second term vanishes. The third term $(\frac{1}{2}(\frac{\delta^2 U}{\delta \mathbf{r}^2})_0 x^2)$ is the curvature, or second derivative of the interatomic potential.[212,213] The second-order term is called a force constant and its dependence on the square of the displacement distance results in a parabolic fit to the minimum of interatomic potential surface. Under the harmonic approximation only the force constants are considered when calculating the potential energy of the system (Figure 2-9), hence the approximation's inability to describe an anharmonic potential energy surface. Third-order and higher expansions of the Taylor series are assumed to give a negligible contribution to the total energy and are not included in the harmonic approximation.

2.8 Calculating phonon frequencies and vibrational properties

There are different approaches to calculating phonon frequencies, but the general concept is the same across all methods. The second-order force constants must be calculated from the curvature of the potential energy surface. A dynamical matrix (D), which is a Fourier transformed mass weighted force constant matrix (F), is then constructed to calculate the vibrational frequencies. For periodic materials additional considerations need to be made to ensure the dynamical matrix is a function of a reciprocal lattice vector from the Brillouin zone. This is done by multiplying the dynamical matrix by the phase

factor $\exp^{(i\mathbf{k}r_{ij})}$, where $\mathbf{r}_{ij}$ is the interatomic vector. The dynamical matrix is now a function of lattice vector $\mathbf{k}$ and is referred to with the notation D($\mathbf{k}$). The vibrational frequencies are the square root of the eigenvalues of the dynamical matrix D($\mathbf{k}$).[214,215]

Mathematically, the dynamical matrix is expressed as:

$$D_{i\alpha j\beta}(\mathbf{k}) = \frac{1}{(m_i m_j)^{\frac{1}{2}}} F_{i\alpha j\beta}(\mathbf{k}) \tag{2.64}$$

where,

$$F_{i\alpha j\beta}(\mathbf{k}) = \Sigma_R \left(\frac{\partial^2 U}{\partial\alpha\partial\beta} \right) exp(i\mathbf{k}(\mathbf{r}_{ij} + \mathbf{R})) \tag{2.65}$$

To calculate the vibrational frequencies of phonons in a system there are three main approaches: the frozen phonon method (real space), finite displacement method (reciprocal space) and density functional perturbation theory (DFPT) (reciprocal space). The earliest method for calculating phonon frequencies with *ab initio* methods was the frozen phonon method.[216] The frozen phonon method is a direct method and assumes the eigenvector of the phonon and atomic displacements are frozen. A plot of cohesive energy *vs* amplitude and phonon frequencies could be extracted without force evaluation.[217]

More recent methods for phonon frequency calculation use the fact that the force constants between atoms are dependent on the displacements and forces. The finite displacement method involves displacing all atoms in all directions by given distance and conducting single point calculations on each generated displacement.[213] Crystal symmetry often reduces the number of unique displacements possible. The dynamical matrix of force constants is then constructed and the eigenvalues, of which the coupled vibrational modes of the system are the square root, are calculated by diagonalisation of the matrix.

The final approach detailed here for calculating vibrational frequencies is DFPT (also referred to as the "linear response method"). In DFPT derivatives of the DFT electronic energies with respect to different perturbations are calculated. When calculating properties such as Born charges the perturbation is the application of an external potential.[218] When calculating phonons, however, the perturbation is the displacement of the atoms (as was the case for the finite displacement method).[219] The difference between the finite displacement method and DFPT is the phonon frequencies are directly calculated by direct diagonalisation of the dynamical force constant matrix. The theory is based on the perturbative expansion of the Kohn-Sham energy functional and uses the Hellmann-Feynman approximation, which states the ground state wave function can be used to calculate the first-order correction to the total energy following perturbation.[220]

Classical methods can directly calculate the phonon frequencies through direct diagonalisation of the dynamical matrix using analytical second-order force constants. The square root solutions of the eigenvalues following diagonalising the matrix give the vibrational modes of the collective system.

Once the vibrational frequencies are calculated, using one of the methods that have been described

above, the vibrational partition function (Z^{vib}) can be calculated by summing over each vibrational energy level (U_m^{vib}) of each vibrational mode (m), U_m^{vib} (n,k) = $(n+\frac{1}{2})h\omega(m,k)$.

$$Z^{vib} = \sum_m \sum_k \frac{exp(-h\omega/2k_BT)}{1-exp(-h\omega/2k_BT)} \tag{2.66}$$

To calculate properties such as heat capacities, free-energies and thermal expansion coefficients, vibrational entropy and temperature must be included into the model, which leads to the calculation of free-energy as opposed to internal or lattice energy. Fixing the 0 K unit-cell volume gives Helmholtz free-energies and allowing the unit-cell to relax at a defined temperature leads to the calculation of Gibbs free-energies.

The Helmholtz free-energy (A) is the sum of the total internal energy of the system (U_0), vibrational zero point energy (E_{zp}) and temperature dependent vibrational entropy (TS_V) at constant volume (V).

$$A(T,V) = U_0(V) + E_{zp}(V) - TS_V(T,V) \tag{2.67}$$

and the Gibbs free-energy at constant pressure (P) is given by:

$$G(T,P) = U_0(V) + E_{zp}(V) - TS_V(T,V) + PV \tag{2.68}$$

A simple relationship now exists between Z^{vib} and A:

$$A = -k_BTlnZ^{vib} \tag{2.69}$$

With the Helmholtz and/or Gibbs free-energy of the system calculated, properties such as the heat capacity at constant volume (C_V) can then be calculated:

$$C_V = \sum_m \sum_k w_k k_B \left(\frac{h\omega}{k_BT}\right)^2 \frac{exp(-h\omega/k_BT)}{(exp(-h\omega/k_BT)-1)^2} \tag{2.70}$$

where $w_{\mathbf{k}}$ is the weighting of each **k**-point used to sample the **k**-space.

2.9 Quasi-harmonic approximation

The quasi-harmonic approximation (QHA) is a way to account for anharmonicity of the "real" interatomic potential originating from thermal expansion. The QHA involves minimising the Helmholtz free-energy at constant volume at a given number of lattice expansions and contractions away from the global minimum structure. An equation of state is then fitted across the calculated temperature dependent Helmholtz free energies, which shifts the minimum in Helmholtz energy with volume according to a defined temperature (Figure 2-9). The available equation of states are volume and free-energy dependent, examples include: the Birch-Murnaghan (Equation 2.71), Vinet and Murnaghan equations.

$$P(V) = \frac{3B_0}{2}\left[(\frac{V_0}{V})^{\frac{7}{3}} - (\frac{V_0}{V})^{\frac{5}{3}}\right]\left\{1 + \frac{3}{4}(B_0 - 4) - \left[(\frac{V_0}{V})^{\frac{2}{3}} - 1\right]\right\} \tag{2.71}$$

where, B_0 is the bulk modulus.

The theory is still dependent on calculations conducted under the harmonic approximation, but the consequent volume dependence of vibrational frequencies is considered an anharmonic effect, where the force and displacement of bonds are not linear. The consideration of volume change to the minimum in Helmholtz free-energy with each temperature allows the free-energy to be considered as a Gibbs free-energy. Accurate temperature dependent properties such as the Grüneisen parameter, bulk modulus and constant pressure heat capacity of the system can be calculated using the Gibbs free-energy.

Chapter 3

Transferable forcefield models for MOFs

The continued synthesis of novel frameworks with increasing chemical complexity and multiple energetically accessible topologies has lead to tens of thousands of characterised frameworks. European and government funded databases, such as The Materials Project[221] and Cambridge Structure Database[222], have collated many experimentally characterised and theoretically predicted MOF frameworks and prepared the structures to be "modelling ready" for computations. Modelling ready refers to the removal of thermal disorder in crystallographic files, removal of solvent molecules in the pores and the addition of charge capping molecules/atoms to leave neutral frameworks. Once edited the structures can be modelled, and material properties predicted.

Due to the increasing number of available databases of MOF structures, the application of different modelling approaches in a transferable and scripted manner, to screen through the structures to determine specific material properties, is becoming ever more prevalent in the literature. The most computationally expensive approach for materials screening has been the application of DFT for prediction of electronic structure properties such as fundamental band gap and electronic band structures.[221,223] A vast amount of computational resources are required for electronic structure screening as well as the large requirement of data storage facilities, and although the concept of "big data" storage requirements is not a new concept in computational sciences, it remains a prominent problem in materials screening.

An alternative approach to electronic structure screening, when predicting structural and mechanical properties of materials is to use a cheaper transferable approach, applying simple mathematical models or general forcefield parameters across the database of structures.[224,225] The application of transferable forcefields across databases of MOF structures is a popular approach for the prediction of gas absorption isotherms and elastic constants.[226] Parameterisation of molecular mechanics forcefields is known to produce more accurate structures, but the derivation of such models often renders a forcefield that is too specific to be appropriate for materials screening procedures. Much effort is therefore now spent on "juggling" between accuracy and transferability of forcefield models.

In the two papers presented in this chapter we derive the foundations of two different transferable

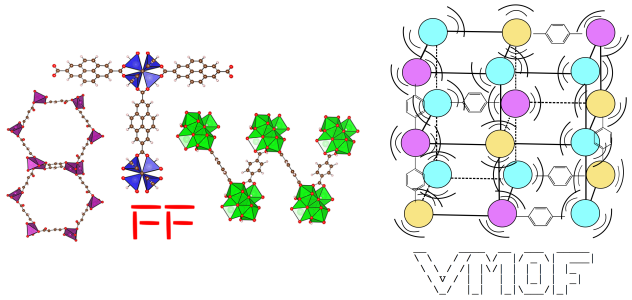

Figure 3-1: Logo of the BTW-FF (left) and VMOF (right) forcefield parameterised to reproduce the structural and mechanical properties of MOFs

forcefields for MOFs: BTW-FF and VMOF (Figure 3-1). VMOF can be considered as an extension to BTW-FF, which was derived to improve the transferability of our parameterised forcefield. In both papers we describe the problems associated with ensuring all parameters remain transferable but also how to ensure the parameters have a physical basis, *i.e.* no force constant has been increased above chemical sense to force a bond length or angle to take the values predicted by first-principles calculations. The intention of both papers is to provide accurate but transferable and easy to use forcefields that can be used by the community for large-scale screening applications.

3.1 Paper 1 - Transferable Force Field for Metal-Organic Frameworks from First-Principles: BTW-FF

The following paper reports the derivation and testing of the BTW-FF forcefield for recreating structural and mechanical properties of MOFs as predicted with first-principles calculations.[227] The forcefield is applied to a subset of six initial structures that possess different bonding connections and pore topologies. A particular discussion point is the distinction between deriving charges for periodic frameworks and for symmetry representative clusters of the materials. Cluster models are commonly adopted for deriving charges as they reduce computational cost, and it is assumed that parameters derived for large clusters would suffice for the periodic motifs. We show by comparing Bader charges for small and large clusters of MOF-5 with the periodic framework, that the long-range interactions of the charged carboxylic acid head groups lead to a systematic error in derived charges of the cluster models. The purpose of the following paper is to discuss the ease of derivation of the forcefield and the accuracy of the properties produced for each topology considered.

In general, the forcefield produces accurate structural, mechanical and vibrational properties of the considered MOFs and was one of the first transferable forcefields published for MOFs, that had been derived for periodic motifs.

3.1.1 Additional ESI

Forcefield parameters

The general format of the BTW-FF forcefield is to use MM3 bonding parameters for the ligands and derive MM3 Buckingham terms for the metal node and interaction between metal and ligand.[174] Additional bonding terms are also used for the interaction between metal and ligand. The explicit functional form of each bonding interaction of the MM3 forcefield is given in the paper. Effective atomic charges are derived using the atoms in molecules theory by Bader.[228,229] When calculating Bader charges, a topological analysis is carried out whereby the first derivatives of charge density is calculated in real space using a first-principles approach, which allows the identification of regions of zero flux, where the gradient of charge density is zero (bond critical points). Bond critical points are defined boundaries where the density in a bond is at its minimum. These are therefore regions where the density associated with each atom type can be defined. Once a region of charge density has been associated with each atom type a numerical value of charge can then be assigned *via* integration methods.

Negative thermal expansion

The increase or decrease of lattice parameters of a solid material with temperature variation is referred to as thermal expansion. For most solids, due to increased amplitude of atom oscillations with increasing temperature, the lattice parameters and volume of the unit cell increase, and is referred to a positive thermal expansion. A rarer phenomenon is the converse scenario and is referred to as negative thermal expansion (NTE) (Figure 3-2).

The term NTE was rarely used between 1960-1990 and the most popular material to be investigated for this property was ZrW_2O_8.[230,231] With the development of perovskites, zeolites and MOFs the number of publications using the term NTE rapidly increased. Thermal expansion can either be described by a linear term (α_L) derived considering the change in lattice parameters (L) or volumetric term (α_V) considering the change in volume (V) of the unit cell with temperature (T):

$$\alpha_V = \frac{1}{V}\left(\frac{\delta V}{\delta T}\right)_p \tag{3.1}$$

$$\alpha_L = \frac{1}{L}\left(\frac{\delta L}{\delta T}\right) \tag{3.2}$$

The extent of thermal expansion in a material is dependent on the strength of bonding interactions within the system. Metal oxides such as ZrO_2 often show little thermal expansion due to strong metal-oxygen bonds.[233]

Several mechanisms have been reported for a range of materials that undergo NTE. The first mechanism to rationalise NTE is often seen in perovskites such as $BaTiO_3$. With increasing temperature the TiO_6 metal polyhedra order, thus decreasing the average Ti-O bond length. Magnetic ordering in

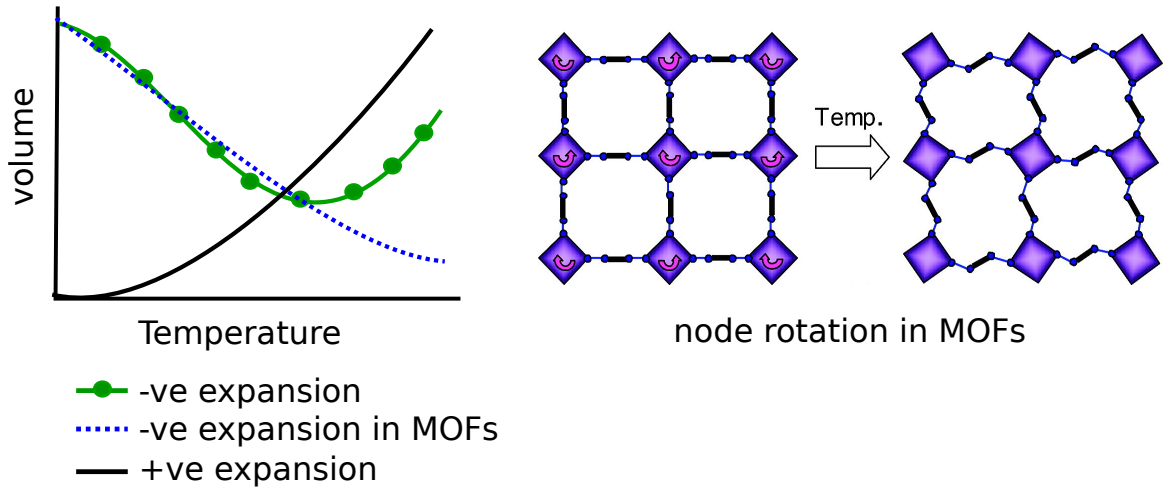

Figure 3-2: Representative thermal expansion profiles of materials (left) and depiction of node rotation with temperature in MOF-C22 (Zn^{2+}/PDC1) that results in negative thermal expansion (right).[232]

perovskites coupled to structural phase changes is the driving force for the ordering. The decreased length of metal-oxygen bonds with increasing temperature results in NTE. Once crystallised into the high temperature cubic phase, $BaTiO_3$ no longer undergoes negative thermal expansion.[234,235] Another origin of NTE occurs in materials such as $LiAlSiO_4$, in which intercalated Li^{2+} cations migrate.[236,237] With increasing temperature, the mobility of the Li^{2+} cations increases, and their distribution through the structure alters such that the lattice contracts. In materials such as $Ta_{16}W_{18}O_{94}$ the origin of NTE is attributed to bulk structure defects *e.g.* grain boundary dislocations.

The most common mechanism for NTE in materials is, however, attributed to transverse vibrational modes. In materials such as zeolites, CuO_2, GaP and InSb, a coupling of transverse vibrational modes and consequent metal polyhedra rotation results in structural phase changes and contraction of the unit cell with increasing temperature.[238,239] The transverse vibrational modes originate from metal-O(or P)-metal connections, where the angle between the connections decreases with increasing temperature, causing a rotation of metal polyhedra and an increase in material density.[230] The majority of described mechanisms result in NTE between particular temperature ranges. As depicted (Figure 3-2), most materials reach a thermodynamic limitation where above a certain temperature, it is no longer favourable for the material to continue to contract and instead unit cell expansion is observed.

Most known MOFs undergo negative thermal expansion, and are therefore unusual materials where examples of positive thermal expansion is rare. MOFs belong to the final discussed mechanism of NTE, associated with transverse vibrational modes. Goddard *et al.* reported modelling a MOF (MOF-C22) that undergoes negative thermal expansion with molecular dynamics simulations.[232] The simulations captured a rotation of metal node coupled to a distortion of ligand out of plane with the unit cell axis (figure 3-2). The described structural distortions were attributed to transverse vibrational modes across

ligand-metal-ligand interactions analogous to those connections in zeolites, CuO_2, GaP and InSb. Another feature of thermal expansion in MOFs is that there is not often a temperature at which the structure would begin to expand following contraction. The poor stability of MOFs with increasing temperature often results in structural decomposition or collapse due to dissociation of the weak VdW interactions between metal and ligand. As depicted (Figure 3-2) the thermal expansion profile of MOFs from experimental and computation work only features NTE. The mechanism proposed by Goddard for NTE has been supported by numerous other investigations, both computational and experimental.[240–242]

Paper correction

A correction to the Buckingham MM3 equation (Equation 2) has been made in the published article:

In article:

$$E_{vdW} = \varepsilon \left[A\exp - B\left(\frac{r_0}{r}\right) - C\left(\frac{r_0}{r}\right)^6 \right] \tag{3.3}$$

Correction:

$$E_{vdW} = \varepsilon \left[A\exp\left(- B\frac{r}{r_0}\right) - C\left(\frac{r_0}{r}\right)^6 \right] \tag{3.4}$$

3.1.2 Forcefield parameter files

The forcefield parameter files can be found as open-source resources at the following Github address: https://github.com/WMD-group/BTW-FF

3.1.3 Personal contribution

My personal contribution to the paper entitled *"Transferable Force Field for Metal-Organic Frameworks from First-Principles: BTW-FF"* included the initial derivation of the BTW-FF forcefield and calculation of structural, mechanical and vibrational properties. DFT calculations for the initial optimisation of the MOF frameworks were conducted by D.Tiana and calculation of effective atomic charges using the Atoms in Molecules theory by Bader was a collective effort between myself and D. Tiana.

3.1.4 Access statement

JCTC Journal of Chemical Theory and Computation

Article

pubs.acs.org/JCTC

Transferable Force Field for Metal−Organic Frameworks from First-Principles: BTW-FF

Jessica K. Bristow, Davide Tiana, and Aron Walsh*

Centre for Sustainable Chemical Technologies and Department of Chemistry, University of Bath, Claverton Down, Bath BA2 7AY, United Kingdom

Supporting Information

ABSTRACT: We present an ab-initio derived force field to describe the structural and mechanical properties of metal−organic frameworks (or coordination polymers). The aim is a transferable interatomic potential that can be applied to MOFs regardless of metal or ligand identity. The initial parametrization set includes MOF-5, IRMOF-10, IRMOF-14, UiO-66, UiO-67, and HKUST-1. The force field describes the periodic crystal and considers effective atomic charges based on topological analysis of the Bloch states of the extended materials. Transferable potentials were developed for the four organic ligands comprising the test set and for the associated Cu, Zn, and Zr metal nodes. The predicted materials properties, including bulk moduli and vibrational frequencies, are in agreement with explicit density functional theory calculations. The modal heat capacity and lattice thermal expansion are also predicted.

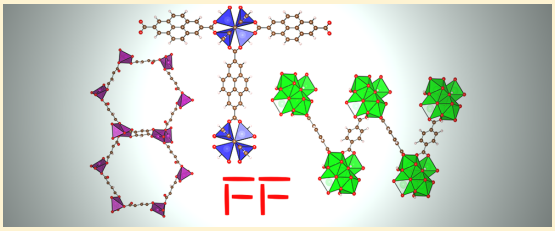

1. INTRODUCTION

Metal−organic frameworks (MOFs), or coordination polymers, are hybrid materials that display a range of unique properties that can be used for a variety of applications ranging from gas storage and catalysis to photovoltaics and drug delivery systems.[1−3] MOFs are formed via the coordination of metals and organic ligands in a self-assembled manner to create an extended crystalline material. The number of possible combinations of building blocks is therefore vast, and the associated crystal structures and properties are often unpredictable. To reduce efforts spent on refining the optimum conditions for the synthesis of a particular MOF, and to identify compositions of particular interest, accurate property predictions from computer simulations would be highly beneficial.

The emerging field of "materials design" has largely been based around the application of modern electronic structure techniques, such as density functional theory (DFT), to predict the structures and properties of new materials.[4−8] Such approaches are appropriate for high-symmetry close-packed inorganic materials but are challenging for the large and complex crystal structures associated with MOFs. For example, a "complex" quaternary semiconductor such as Cu_2ZnSnS_4 can be described using only 8 atoms in its primitive unit cell,[9] while a "simple" MOF can require several hundred atoms. For example, the popular framework MOF-5 has 106 atoms in its primitive cell and 424 atoms in its conventional crystallographic cell. A high-quality calculation of a single MOF poses a heavy computational burden; a large-scale screening is prohibitively expensive.

An alternative to a direct quantum mechanical treatment, which usually involves a self-consistent numerical solution of the Kohn−Sham or Hartree−Fock equations, is the use of an analytical interatomic potential or force field that can describe a range of properties of interest.[10,11] An accurate and transferable force field for MOFs would provide a means of rapidly screening material compositions and properties for particular applications.

A number of initial MOF force fields have been recently reported.[12−16] These have been mainly fitted for specific MOF structures that were highlighted experimentally as possessing functional properties. An example by Vaduyfhuys et al. is a force field for the Al containing MIL-53.[17] One common approximation for MOF potentials, to reduce the complexity of parametrization, is to fix the atom positions within the unit cell. This approach is generally used for probing gas adsorption using Grand Canonical Monte Carlo (GCMC) or Molecular Dynamic (MD) simulations. The advantage is that the intraframework interactions need not be considered, facilitating fast screening,[2,18−23] but materials response functions are not described. As an extension to this approach one can conduct hybrid GCMC and MD calculations to model structural transitions of flexible MOFs.[24−26]

A second approach is to use a generic force field derived for molecules such as proteins, hydrocarbons, and common gases; OPLS-aa (Optimized Potentials for Liquid Simulations—all atom), DREIDING, and MM3 (Molecular Mechanics 3) are examples of these.[27−29] The application of generic force fields

Received: June 13, 2014
Published: August 27, 2014

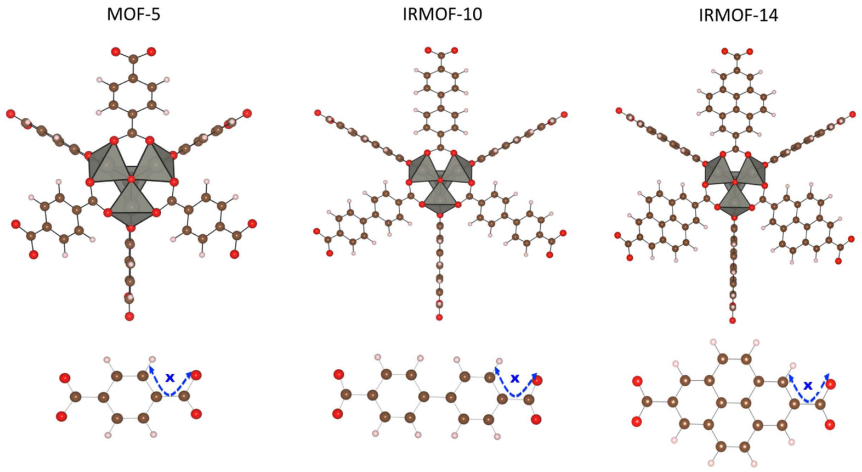

Figure 1. Comparative illustrations of the repeating units of Zn-containing MOF-5, IRMOF-10 and IRMOF-14 with the organic ligands shown underneath each structure. Torsion angle (atom types 170-913-902-912) labeled as **x** has been highlighted.

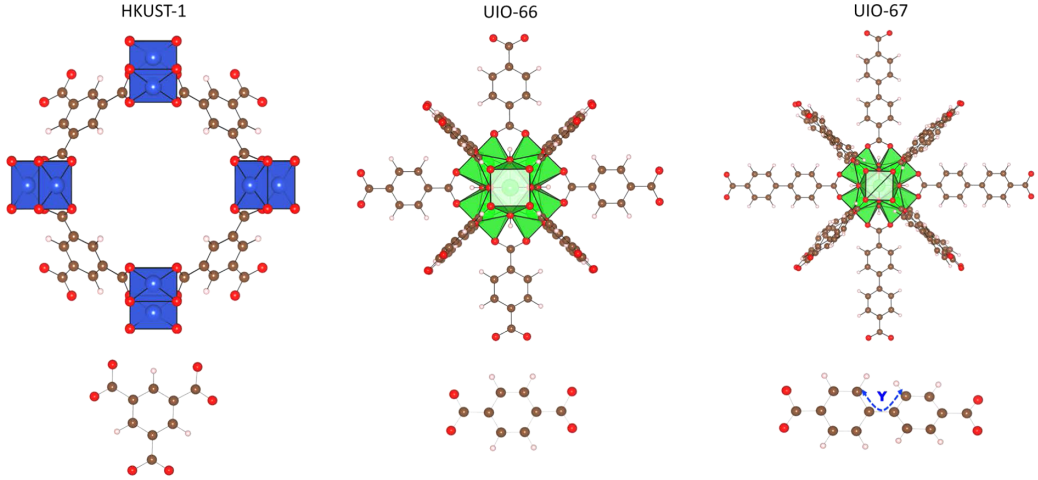

Figure 2. Comparative illustrations of the repeating units of Cu-containing HKUST-1 and Zr-containing UiO-66 and UiO-67 with the organic ligands shown underneath each structure. Torsion angle (atom types 912-903-903-912) labeled as **y** has been highlighted.

to MOFs, which consist of both organic and inorganic components, is highly convenient but approximate. While large-scale screenings can be again performed,[30,31] complex geometries and interactions are often not modeled with quantitative accuracy. Recent progress includes UFF4MOF, an extension of the universal force field (UFF)[30] to describe some common metal−organic framework motifs.[32]

A third common approach to MOF force fields is to construct representative finite clusters (fragments) of the full MOF crystals.[33] The advantage is faster derivation with a reduced number of interaction parameters (and degrees of freedom) in the model. The disadvantage is that the neglect of periodicity and long-range interactions is unphysical and standard mechanical, thermal, and dielectric properties cannot be described in the absence of a sophisticated embedding procedure.

In this paper, we report a force field to describe metal−organic frameworks parametrized by first-principles crystal structures and electron density. The aim is a transferable potential form suitable to describe the majority of ligand and metal combinations for MOFs, including predicting properties of novel compositions. In contrast to the universal force field approach in which general parameters not fitted for MOFs and fixed generic charges are employed, we develop a force field that has been fitted explicitly to the periodic frameworks. Some initial parameters have been refined from existing force fields (MM3 and MOF-FF) and the functional format of MM3 is preserved.[34−36] Ligand and metal interatomic potentials are parametrized and validated across multiple MOF structures and atomic charges are determined based on topological analysis using Bader's atom in molecules theory (AIM)[37] of the equilibrium electron density from solid-state DFT calculations.

2. METAL−ORGANIC FRAMEWORKS

We consider six representative MOFs covering three of the most common isoreticular frameworks: [MOF-5 (Zn_4O-

$(BDC)_3$), IRMOF-10 ($Zn_4O(BPDC)_3$), IRMOF-14 ($Zn_4O(PDC)_3$), UiO-66 ($Zr_6O_4(OH)_4(BDC)_6$), UiO-67 ($Zr_6O_4(OH)_4(BPDC)_6$), and HKUST-1 ($Cu_3(BTC)_2$)], as illustrated in Figures 1 and 2.

MOF-5 was first reported by the group of Yaghi.[38] It is formed of Zn_4O clusters and 1,4-benzenedicarboxylate (BDC) organic ligands. The Zn metal centers are in tetrahedral coordination with respect to oxygen (Figure 1), which is similar to the bulk metal oxide. The crystal structure can be described by its primitive rhombohedral unit cell of dimensions a = 18.289 Å, α = 60.0°. The cubic unit cell of MOF-5 has the associated dimension of a = 25.832 Å and space group $Fm\bar{3}m$.[39] The ligands form the edges of the cubic structure and the metal clusters the corners. Each unit cell contains half the ligand molecules orientated face-on and half rotated 90° into the plane. The structures of IRMOF-10 and IRMOF-14 are analogous to that of MOF-5, differing only in the ligand identity. The organic ligand comprising IRMOF-10 is 4,4′-biphenyldicarboxylate (BPDC), whereas for IRMOF-14 it is pyrene-2,7-dicarboxylate (PDC). The cell parameter for the cubic unit cell of IRMOF-10 is a = 34.281 Å, while IRMOF-14 is a = 34.381 Å.[39]

Beyond the isoreticular Zn-MOFs, UiO-66, UiO-67, and HKUST-1 were also modeled (see Figure 2). UiO-66 is formed of $Zr_6O_4(OH)_4$ clusters 12-coordinated to BDC ligands, such that each Zr ion is in octahedral coordination with capping η^3-OH and η^3-O anions.[40,42,43] The cubic cell dimension for UiO-66, with the space group $F\bar{4}3m$, is a = 20.978 Å.[40] The crystal structure of UiO-67 is similar but composed of the biphenyl ligand (BPDC); the extension is analogous to that of MOF-5 to IRMOF-10. The behavior of the BPDC ligand differs for UiO-67 due to a ligand twist (labeled **y** in Figure 2). First-principles calculations predict the twist across the central carbon atoms connecting the two aromatic rings to be approximately 31°. UiO-67 also has the space group $F\bar{4}3m$, with cell dimension a = 27.094 Å.[40,44] The UiO series is of increasing interest for MOF applications due to their high thermal stability up to 813 K and resistivity to water decomposition.[45]

HKUST-1 differs in relation to the structures previously discussed. Here, the ligand is 1,3,5-benzenetricarboxylic acid (BTC), as shown in Figure 2. This MOF, first reported by Chui et al.,[41] is of interest not only for its high gas storage capacities but also for its unique electronic structure originating from Cu−Cu interactions. The room temperature experimental crystal structure infers metal−metal separation of 2.63 Å. The metal nodes in HKUST-1 are Cu, which are in a square planar coordination resulting in a 3D network with a paddlewheel geometry and three voids of diameters 5, 11, and 13.5 Å, respectively. Each metal center has 4 BTC ligands, with additional water coordination in vertical alignment with the Cu−Cu interaction, resulting in a pseudo-octahedral geometry for hydrated crystals. The water can be removed and/or substituted to further expose the metals.[46,47] In this paper, we will consider only the dehydrated HKUST-1 structure. HKUST-1 has a cubic crystal symmetry (space group $Fm\bar{3}m$) with a lattice dimension of a = 26.343 Å. Table 1 gives a summary of unit cell parameters of each structure described.

Table 1. Experimentally Determined Crystal Structure Parameters of Six Metal−Organic Frameworks[a]

MOF	metal	oxidation	ligand	space group	a (Å)	N
MOF-5[39]	Zn	II	BDC	$Fm\bar{3}m$	25.832	424
IRMOF-10[39]	Zn	II	BPDC	$Fm\bar{3}m$	34.281	664
IRMOF-14[39]	Zn	II	PDC	$Fm\bar{3}m$	34.381	760
UiO-66[40]	Zr	IV	BDC	$F\bar{4}3m$	20.978	456
UiO-67[40]	Zr	IV	BPDC	$F\bar{4}3m$	27.094	684
HKUST-1[41]	Cu	II	BTC	$Fm\bar{3}m$	26.343	576

[a]Oxidation refers to the formal metal oxidation state, while N refers to the number of atoms in the unit cell described.

3. THEORETICAL APPROACH

3.1. Reference Solid-State Electronic Structure Calculations. In order to provide systematic benchmark data, electronic structure calculations for the periodic crystals were performed using DFT as implemented in the VASP (Vienna Ab-Initio Simulation Package) code.[48,49] All calculations were performed using the PBEsol functional,[50] which is a semilocal functional that usually predicts equilibrium structures in very good agreement with experiment; its success for MOFs has been well demonstrated.[3,51] Comparison of different exchange-correlation functionals for a range of materials shows that the structures and frequencies of PBEsol are among the most accurate currently available for solids.[52,53]

The computational setup differed between structures due to variations in the unit cell size. A 2 × 2 × 2 k-point grid was used for the optimization of UiO-66. Due to the larger unit cells of MOF-5, IRMOF-10, IRMOF-14, UiO-67, and HKUST-1, only Γ-point sampling was performed. The quasi-Newtonian relaxation employed for structural optimization was converged to forces of 0.005 eV/Å or lower. A kinetic energy cutoff of 500 eV was employed for the plane-wave basis set. Scalar-relativistic projector-augmented wave (PAW) potentials were used to model the interactions between the core and valence electrons on each atom, with the 3d electrons treated explicitly for Zn. Effective atomic charges for each atom type were derived using the AIM theory on the total electron density (i.e., the sum of the PAW and valence density) for the optimized structure.[54] Vibrational frequencies were calculated with Γ-point sampling of the Brillouin zone using the finite displacement method.

3.2. Force Field Parametrization and Testing. The functional form of MM3 is maintained in our parametrization. Thus, the overall energy expression is

$$E_{\mathrm{MM3}} = \sum E^{\mathrm{str}} + \sum (E^{\mathrm{bend}} + E^{\mathrm{str-str}} + E^{\mathrm{str-bend}}) + \sum E^{\mathrm{opb}} + \sum E^{\mathrm{tor}} + \sum (E^{\mathrm{vdW}} + E^{\mathrm{Coul}}) \quad (1)$$

where str = stretch, tor = torsion, opb = out of plane bend, Coul = Coulomb, and vdW = van der Waals interactions and where the usual bond stretching and bending modes are described, in addition to longer range van der Waals (dispersion) and Coulombic interactions. Nonbonding interactions were calculated using the Buckingham equation:

$$E_{\mathrm{vdW}} = \varepsilon\left(A\ \exp\left[-B\left(\frac{r_0}{r}\right) - C\left(\frac{r_0}{r}\right)^6\right]\right) \quad (2)$$

vdW radii and ε values are given in Table 4. Default values for the A, B, and C constants were used (184000.0, 12.0, 2.25, respectively) as defined in TINKER.

The MM3 force field has been shown to recreate organic systems accurately and, more recently, has been applied to MOF structures.[33−36,55] The TINKER package[56,57] contains the full set of the MM3 force field parameters and has a range of capabilities for crystal structure and property calculations.

Table 2. Comparative Bader Charges Derived for a Small Cluster (SC) (79 Atom, $Zn_4O_{13}C_{42}H_{30}$) and Large Cluster (LC) (328 Atom, $Zn_{32}O_{104}C_{120}H_{72}$) of MOF-5 Compared with Those Derived for the Periodic System Used in the BTW-FF and UFF Models[a]

		Bader charges (au)				
atom type	element	BTW-$FF_{inc.core}$	BTW-$FF_{exc.core}$	SC	LC	UFF
172	Zn	1.281	1.408	1.291	1.291	1.308
913	C (acid)	1.497	2.683	1.558	1.536	1.912
912	C (benz)	−0.053	−0.011	−0.058	−0.055	1.912
902	C ($C-C_{acid}$)	−0.008	−0.007	0.010	−0.003	1.912
170	O (acid)	−1.151	−1.768	−1.195	−1.168	−2.300
171	O (inorganic)	−1.115	−1.336	−1.171	−1.207	−2.300
915	H (H−C)	0.126	0.083	0.090	0.123	0.712

[a]Also given are the periodic charges with and without the inclusion of core density. Charges are given in atomic units.

The XTALMIN program inside of TINKER was used to apply periodic boundary conditions allowing the full crystal to be modeled and optimized. The internal positions are described using connectivity (in the absence of space group symmetry). When considering the interaction between organic and inorganic building blocks both "bonding" and "nonbonding" contributions were included. Atom types were assigned based on the element and the environment of the crystal. The reparameterization of the MM3 force field include the terms describing the carboxylic head and interaction between metal node and ligand. New parameters were also derived for the metal node, particularly for the metal−inorganic oxygen interaction. TINKER default values of the Buckingham potentials were used in association with Coulomb long-range terms to describe nonbonding interactions.

Vibrational frequencies were calculated at the Γ-point using the VIBRATE program, and bulk moduli with the DYNAMIC program in the TINKER package through molecular dynamic simulations. A series of Canonical (NVT) ensemble calculations were employed to fix the unit cell volume at 1 K with negligible kinetic energy contribution. Unit cell volumes were sampled every 0.01 Å for ±1% from the equilibrium volume (V_0). Simulations were run for 250 000 dynamic steps with a time step of 1 fs at 1 atm with an Ewald cutoff of 11 Å. Constant temperature of the system was maintained with a Nosé−Hoover thermostat. The Velocity Verlet algorithm was used to integrate the Newton equations. Average values of the potential energy were taken from the final 50 ps (500 dynamic steps). The bulk moduli (B_0) of each structure was calculated using the isothermal Birch−Murnaghan equation of state (eq 3). Data processing was implemented in Octave using the Asturfit program, which performs a least-squares fit to the Birch−Murnaghan equation of state.[58,59]

$$P(V) = \frac{3B_0}{2}\left[\left(\frac{V_0}{V}\right)^{7/3} - \left(\frac{V_0}{V}\right)^{2/3}\right]\left\{1 + \frac{3}{4}(B_O' - 4)\left[\left(\frac{V_0}{V}\right)^{2/3} - 1\right]\right\} \quad (3)$$

Linear (α) (eq 4) and volumetric (β) (eq 5) thermal expansion coefficients were calculated from a series of anisotropic isothermal−isobaric (NPT) ensemble calculations. The Berendensen bath coupling method was used as a barostat to maintain defined pressures. The temperatures were sampled at 1 K and between 80−500 at 50 K increments with 500 K as an additional temperature point. The program DYNAMIC was used to calculate the average lattice parameters over 50 ps following equilibration for 200 ps.

$$\alpha = \left(\frac{1}{a_0}\right)\left(\frac{\partial a}{\partial T}\right)_P \quad (4)$$

$$\beta = \left(\frac{1}{V_0}\right)\left(\frac{\partial V}{\partial T}\right)_P \quad (5)$$

For isotropic expansion $3 \times \alpha = \beta$; this relationship was used when calculating the volumetric thermal coefficients from the linear thermal coefficients. The value of the lattice parameter a when calculating the linear thermal expansion coefficient was taken as the average of the 298 K MD simulation and $\partial a/\partial T$ is the average slope over the temperature range 80−500 K.

Finally, isochoric heat capacities (C_V) were calculated within the harmonic approximation from the vibrational frequencies of each structure for temperatures ranging between 80 and 500 at 50 K intervals using the standard (Einstein) phonon summation:

$$C_V = \sum_{\omega} k_B \left(\frac{\hbar\omega}{k_B T}\right)^2 \frac{\exp\left(\frac{\hbar\omega}{k_B T}\right)}{\left[\exp\left(\frac{\hbar\omega}{k_B T}\right) - 1\right]^2} \quad (6)$$

3.3. Molecular versus Periodic Charges. One distinction of our MOF potential is the choice of effective atomic charges. When deriving effective charges the core atomic density is often not considered due to the use of a pseudopotential or effective core potential. This leads to a systematic error in the calculation of the atomic surfaces, making bonds appear more ionic in nature.[60] With the PAW method, we can reconstruct the total charge density of the system as a sum of the valence and PAW density. The effective charges derived from topological analysis of charge density for different structural representations of MOF-5, including those of BTW-FF (with and without the core density) are listed in Table 2.

Analysis of data first confirms the importance of including core charges for MOFs. The differences are large, especially for the carboxylic head of the ligand. Second, comparing charges derived from the Bloch states versus finite molecular orbitals, we show that similar results can be obtained when a large cluster is used. In contrast, the standard molecular UFF parametrization has a more ionic description with charges larger in magnitude for all atoms.

4. RESULTS

To begin, topological analysis of charge density of the equilibrium MOF structures from the electronic structure

dx.doi.org/10.1021/ct500515h | J. Chem. Theory Comput. 2014, 10, 4644−4652

Table 3. Atomic Charges Derived *Via* Topological Analysis for Each Atom Type in Each MOF[a]

		effective atomic charges (au)						
element	atom type	MOF-5	IRMOF-10	IRMOF-14	UiO-66	UiO-67	HKUST-1	avg. charges
C (benz)	912	−0.054	−0.046	−0.044	−0.058	−0.060	−0.023	−0.050
C (acid)	913	1.497	1.538	1.538	1.576	1.548	1.540	1.539
C (C_{benz}−C_{acid})	902	0.008	−0.028	0.051	−0.056	0.006	−0.011	−0.008
C (C_{benz}−$C_{benz'}$)	903		−0.012			−0.035		−0.024
O (acid)	170	−1.151	−1.163	−1.156	−1.181	−1.182	−1.091	−1.154
O (inorganic)	171	−1.115	−1.214	−1.224	−1.189	−1.881		−1.186
O (O−H)	75				−1.242	−1.244		−1.243
H (H−C)	915	0.126	0.105	0.092	0.129	0.096	0.158	0.118
H (H−O)	21				0.622	0.623		0.622
metal		1.281	1.295	1.297	2.601	2.610	1.036	1.291 (Zn), 2.605 (Zr)

[a]Atomic charges are given in atomic units and total average charges of all structures are given.

calculations was performed to obtain the effective atomic charges to be used in the force field. The values are presented in Table 3. Comparable charges were derived for MOF-5, IRMOF-10, and IRMOF-14, and also for UiO-66 and UiO-67. The higher charge of Zr is consistent with its higher oxidation state. Similar derived charges for each atom type allowed average charges to be used, resulting in a fully transferable model, analogous to that of an UFF implementation.

The values used for the van der Waals radii and polarizability (ε) parameters describing the nonbonding interactions in each structure are given in Table 4. The derived parameters of Zn and Cu are similar to those derived by Schmid et al.[34] Zr is heavier and its higher oxidation state in UiO-66 results in greater polarizability; hence, its values are larger. The Zr parameters are similar to those already used within inorganic crystals.[61]

Table 4. van der Waals Radii and ε Values Used for the Transition Metals within the MOF Structures[a]

elements	vdW radii (Å)	ε (kcal mol^{-1})
Zn	2.290	0.276
Cu	2.290	0.276
Zr	3.520	0.367

[a]Epsilon refers to the polarizability of the atoms, which is an energy term within the van der Waals function in the MM3 format (eq 1).

The final set of force field parameters to describe all MOFs reported here are included as Supporting Information (SI) and an online repository, which will be updated with future potentials.[62]

4.1. IRMOF Series. The lattice parameter agreement between the equilibrium BTW-FF and DFT (PBEsol) structures is very good (errors of less than 1%). The full internal structural parameter comparison for MOF-5, IRMOF-10, and IRMOF-14 is provided as SI. Atom type assignment is shown in Figure 3.

An interesting observation was made when deriving the potentials for both MOF-5 and IRMOF-10. Initial parametrization resulted in slightly distorted ligand structures with a nonplanar torsion angle occurring between the O-C(carb)-C(phen)-C(phen) (170-3-902-2) (labeled as **x** in Figure 1). For comparison a DFT(PBEsol) calculation was run starting from a 2.73° angle, where the equilibrium structure gave a distortion of 1.04°. Our data suggests that the ground-state of the ligands in MOF-5, IRMOF-10, and IRMOF-14 is slightly distorted, with a space group of lower symmetry than the average one identified at room temperature. This distortion is likely to fluctuate at higher temperatures, with an average structure that is planar (double well potential). The force field parameters presented contain a torsion potential to suppress this distortion and recreate experimental data; however, it can be removed without disrupting the remainder of the framework.

4.2. UiO-Series. Compared to the IRMOF series, the structural fit of UiO-66 and UiO-67 proved more challenging to converge. The equilibrium lattice constants are within 0.51% of the DFT(PBEsol) values. The ligand potentials used to model the IRMOF structures are transferable to UiO-66 and UiO-67 with small errors in bond lengths and angles (see SI). Atom type assignments are shown in Figure 4. The results and the error associated with the Zr−inorganic oxygen bond (2.23 and 2.67% in UiO-66 and UiO-67, respectively) suggest a more robust nonbonding interaction for these bonds may be required to improve the overall accuracy of the models (e.g., higher-order multipoles in the electrostatic summations).

To stress the close relationship between MOF-5 and UiO-66, the ligand potentials for the BDC ligand remained unchanged

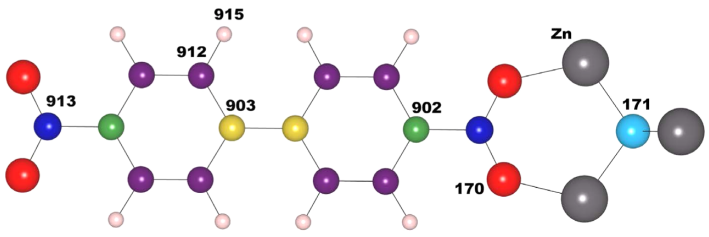

Figure 3. Atom type definitions used for MOF-5/IRMOF-10/IRMOF-14.

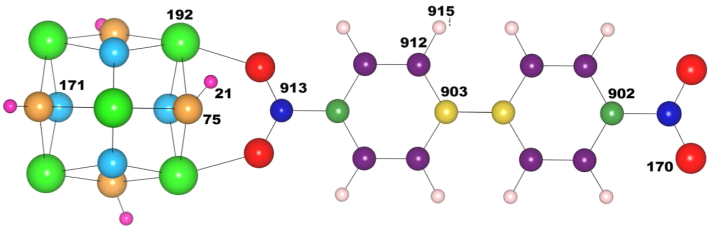

Figure 4. Definition of atom types for UiO-66 and UiO-67.

between the structures. This is also the case for IRMOF-10 and UiO-67. The one exception is that in order to recreate the 31° twist across the central bond of the biphenyl ligand within UiO-67, the applied *k*-force for the torsion (912-903-903-912 atom types) was reduced. The resultant twist of UiO-67 was 32.2°. The Zr potential is fully transferable between UiO-66 and UiO-67.

4.3. HKUST-1. The equilibrium lattice constants of HKUST-1 show errors of less than 0.1%, with the internal structure parameters also well described (see SI). See Figure 5

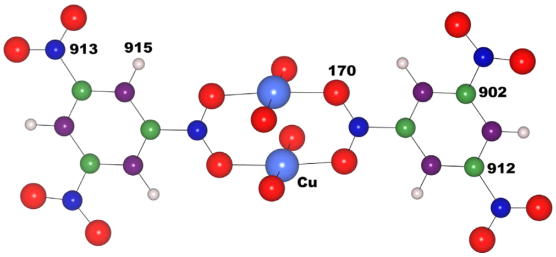

Figure 5. Definition of atom types for HKUST-1.

for atom type assignment. The nature of the Cu−Cu bonding is somewhat in debate; chemically each Cu ion is formally divalent (d^9) and the unpaired spin form open-shell and closed-shell singlets, as well as a (ferromagnetic) triplet state.[63,64] Here, it was necessary to model Cu−Cu as 5 coordinate, that is, bonded to 4 carboxylic acid oxygens in the equatorial positions and 1 Cu in the axial position. Reasonable *k*-force was required to model this metal−metal interaction. Future work could extend these HKUST-1 potentials to include water coordination as described in the introduction of this paper to form a pseudo Cu octahedral environment.

4.4. Property Calculations. To validate the accuracy and transferability of the potential model beyond equilibrium structures, a series of materials property calculations have been performed. We have determined the bulk moduli and vibrational frequencies for each structure using our force field and compared these to available reference data. These properties are extremely computationally expensive to calculate on the DFT potential energy landscape but are straightforward using our potential model.

The calculated bulk moduli are given in Table 5, with the energy/volume curves provided in Figure 6. An excellent agreement with reference values for all structures besides UiO-66 is shown. The trends in the obtained bulk moduli of the MOFs is also consistent with available experimental and DFT calculated values. UiO-66 appears to be an unique case due to the large increase in mechanical strength for UiO-66 when

Table 5. Bulk Moduli of MOF-5, IRMOF-10, IRMOF-14, UiO-66, UiO-67, and HKUST-1[a]

	Bulk moduli (GPa)	
MOF	BTW-FF	Reference
MOF-5	11.95	18.20[65]
IRMOF-10	8.25	6.00[66]
IRMOF-14	8.40	5.90[66]
UiO-66	27.15	41.01[65]
UiO-67	19.15	17.15[65]
HKUST-1	25.05	24.53[65]

[a]Values reported are those using BTW-FF and available reference data from DFT calculations. Reference calculations used Density Functional based Tight Binding (Kuc et al.)[66] and PBE functional (Wu et al.).[65] Note that the bulk modulus is related to the second derivatives of the energy with respect to volume and hence is sensitive to the theoretical approach.

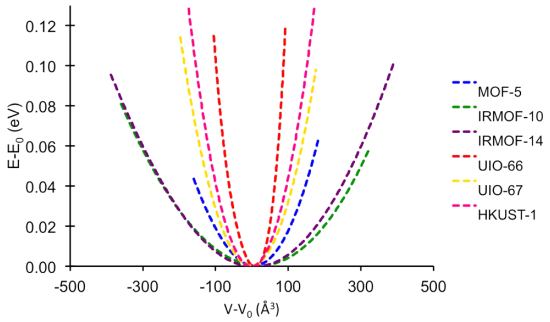

Figure 6. Energy/volume curves for MOF-5, IRMOF-10, IRMOF-14, UiO-66, UiO-67 and HKUST-1, from which the bulk moduli were derived via an equation of state.

comparing this value with the structurally similar UiO-67. To our knowledge, experimental values for the bulk modulus of UiO-66 are not available currently to provide a definitive reference. The large difference between the bulk moduli of MOF-5 and UiO-66 is due to the coordination and oxidation state differences of the metal centers in either structure. In MOF-5 the metals are 4-coordinate and formally Zn^{2+} and in UiO-66 the metals are 6-coordinate with 6 further capping ligands to create a total outer coordination of 12. In addition, the formal oxidation state of the metals in UiO-66 is Zr^{4+}. UiO-66 can therefore be considered as being formed of stronger interactions, which increase the mechanical strength of the material.

It should be noted that the bulk modulus of a material is temperature dependent. Direct comparison with experimental data is therefore not often appropriate when discussing accuracy to athermal calculations.[67] Furthermore, where values

dx.doi.org/10.1021/ct500515h | J. Chem. Theory Comput. 2014, 10, 4644−4652

from other DFT studies are compared, it should be remembered that these values are sensitive to the choice of functional, where the bulk modulus is proportional to the equilibrium cell volume, that is

$$K = -V_0 \frac{\partial P}{\partial V} \tag{7}$$

where standard local and semilocal functionals can produce large errors.

Vibrational frequencies were calculated and compared with those from DFT (PBEsol) (see Figure 7). A generally good

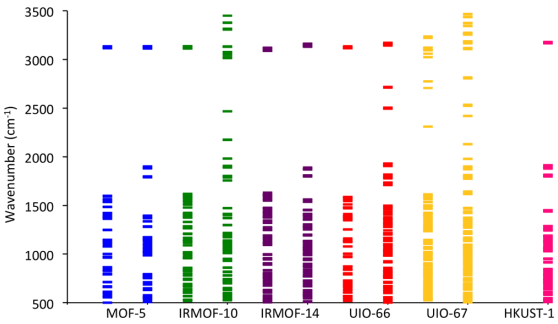

Figure 7. Γ-point vibrational frequencies between 500−3500 cm^{-1} for MOF-5, IRMOF-10, IRMOF-14, UiO-66, UiO-67, and HKUST-1. DFT calculated (left) and BTW-FF calculated (right). Note: DFT (PBEsol) frequencies for HKUST-1 could not be computed owing to the computational expense.

agreement is found for all structures. There are, however, frequencies in the 1900 cm^{-1} to 3000 cm^{-1} range for UiO-67 and IRMOF-10, which are not calculated with DFT. We can assign these anomalous modes to stretches involving the central C−C bond (atom types 903-903). The force constants involving the connection of this central bond were strengthened to prevent the previously discussed carboxylate head twisting distortion occurring. Further additional modes for UiO-67 and also for UiO-66 were predicted by BTW-FF in the same frequency region. Analysis of the associated eigenvectors confirms these to be due to stretching modes within the Zr−O(O−H) (atom types Zr-75) bonds. These bonds have the largest error (2.23% and 2.67% for UiO-66 and UiO-67, respectively, Supporting Information Table S2) when compared to the equilibrated DFT structure. HKUST-1 was not included in the vibrational frequency analysis as the DFT proved to be too expensive to compute due to the larger crystal structure. It should be noted that soft modes associated with the carboxylate torsion of the ligands were present in all cases. This torsion has previously been described and labeled as **x** in Figure 1.

As a further analysis, we compare the vibrational frequencies of the IRMOF and UiO-series with DFT (B3-LYP) data previously reported and analyzed by Civalleri et al. and Valenzano et al. for the respective series of structures (Table 6 and Table 7).[44,68] Assignment of the vibrational frequencies for prominent stretching and bending modes shows an excellent agreement in our reported results using BTW-FF and those from DFT (B3-LYP). This agreement further supports the accuracy of our model.

Occupation of the lattice phonons at finite temperatures leads to changes in the crystal structure parameters. Linear and

Table 6. Assigned Vibrational Frequencies (ω) for MOF-5, IRMOF-10, and IRMOF-14[a]

	ω (cm^{-1})			
description	DFT (MOF-5)	MOF-5	IRMOF-10	IRMOF-14
O_{acid}−Zn−O_{acid} bend	114	111	123	136
Zn−$O_{inorganic}$−Zn bend	136	174	181	178−179
Zn−O_{acid}−C_{acid} bend	263	283	302−305	284
Zn−$O_{inorganic}$ asymmetric stretch	512	497	497−498	493
Zn−O_{acid} symmetric stretch	579	558	544−575	545−565
Zn−O_{acid} asymmetric stretch	606	563−568	590−602	575−590
C_{acid}−O_{acid} symmetric stretch	1421	1394	1471−1473	1355−1382

[a]Reference DFT calculations B3-LYP level of theory in the CRYSTAL code (Civalleri et al.). Reported DFT values are for MOF-5.[68]

Table 7. Assigned Vibrational Frequencies (ω) for UiO-66 and UiO-67[a]

	ω (cm^{-1})		
description	DFT (UiO-66)	UiO-66	UiO-67
Zr−O_{acid} asymmetric stretch	556	558	593
μ_3−O stretch	673	671−672	667−671
O−H bend	771, 814	778−779, 810−812	872
C_{acid}−O_{acid} symmetric stretch	1408	1380, 1408	1363

[a]Reference DFT calculations B3-LYP level of theory in the CRYSTAL code (Valenzano et al). Reported DFT values are for UiO-66.[44]

volumetric thermal expansion coefficients have been calculated to determine the change in unit cell size with increasing temperature. Many MOFs are known to contract with increasing thermal energy due to transverse vibrational modes of the ligands. Details describing the causes of negative thermal expansion in solid materials are detailed in a referenced review.[69] The phenomenon is not to be confused with structural changes that occur following the evacuation of internal solvent molecules.

Negative thermal expansion was calculated for each structure as shown by the thermal expansion coefficients (Table 8). The

Table 8. Calculated Linear (α) and Volumetric (β) Thermal Expansion Coefficients of MOF-5, IRMOF-10, IRMOF-14, UiO-66, UiO-67, and HKUST-1

MOF	α (×10^{-6}) (K^{-1})	β (×10^{-6}) (K^{-1})
MOF-5	−5.27	−15.80
IRMOF-10	−8.11	−24.32
IRMOF-14	−4.95	−14.86
UiO-66	−1.04	−3.11
UiO-67	−2.22	−6.66
HKUST-1	−3.18	−9.53

extent of unit cell contraction with temperature is shown in Figure 8. IRMOF-10 experiences the greatest thermal contraction due to bending modes of the biphenyl ligand. IRMOF-14 and MOF-5, although containing the same metal node as IRMOF-10, have more rigid ligands and therefore contract less with temperature. The UiO series contract the

dx.doi.org/10.1021/ct500515h | J. Chem. Theory Comput. 2014, 10, 4644−4652

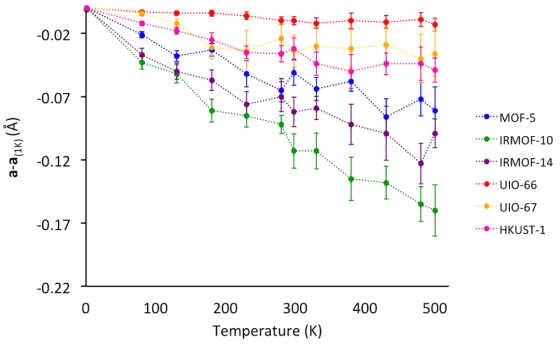

Figure 8. Thermal expansion profiles for MOF-5, IRMOF-10, IRMOF-14, UiO-66, UiO-67, and HKUST-1. In contrast to standard quasi-harmonic approaches, molecular dynamic simulations include high order anharmonicity from phonon−phonon interactions. Shown is the difference in *a* parameter at a given temperature, with respect to the *a* parameter at 1 K. Error bars indicate the variation in the lattice constants at each temperature due to thermal fluctuations.

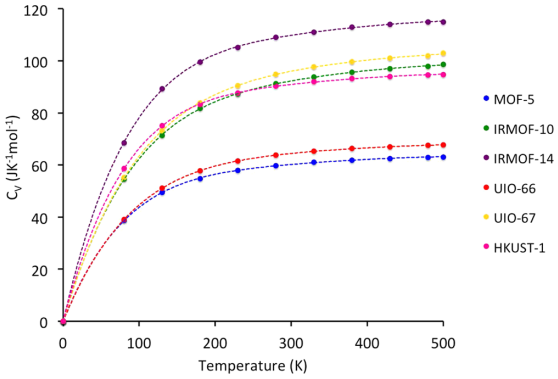

Figure 9. Temperature dependence of the predicted volumetric heat capacities for MOF-5, IRMOF-10, IRMOF-14, UiO-66, UiO-67, and HKUST-1.

least due to the high charge on the Zr metal node resulting in a rigid extended structure. The influence of the charge on the metal is highlighted by the difference in behavior of UiO-67 and IRMOF-10. These structures contain the same ligand, but due to the higher ionicity of UiO-67, soft bending modes of the biphenyl ligand are no longer present. The final structure, HKUST-1 also exhibits very weak negative thermal expansion at high temperatures. A low charge was calculated on the Cu metal centers (Table 3) suggesting that HKUST-1 exhibits harder structural properties due to the rigidity of the tricarboxylate ligand and not increased ionicity. Calculated values are consistent with those previously found from experiment and MD simulations.[70−72]

Finally, volumetric heat capacities were calculated at constant volume from the vibrational frequencies (eq 6) for each structure under the harmonic approximation. The heat capacity describes the energy required to increase the temperature of a material by a given quantity and is determined from the changes in vibrational occupancy with increasing temperature. The values plateau at relatively low temperatures (200−300 K) suggesting low Debye temperatures (Figure 9). Unfortunately, little experimental data is available on the heat capacity of MOFs to date for comparison.

5. CONCLUSIONS

We have parametrized a new interatomic potential to describe the crystal structures and properties of metal−organic frameworks. The force field is shown to accurately reproduce the structural parameters of MOF-5, IRMOF-10, IRMOF-14, UiO-66, UiO-67, and HKUST-1. The ligand parameters are transferable between the Zr and Zn frameworks and are expected to be valid for other systems of interest. Bulk moduli and vibrational frequencies have been calculated and are in agreement with calculations on the DFT (PBEsol) potential energy surface. Finally, we highlighted the importance of periodic boundaries when deriving empirical parameters for MOFs. Future work will concern extending this model to other systems and extending the range of materials response functions that can be calculated for hybrid frameworks.

■ ASSOCIATED CONTENT

Ⓢ Supporting Information

Structural parameters, including bond lengths, angles, and unit cell parameters for each structure. Potential parameter sets and data used to plot modal heat capacities. This material is available free of charge via the Internet at http://pubs.acs.org

■ AUTHOR INFORMATION

Corresponding Author

*Email: a.walsh@bath.ac.uk.

Notes

The authors declare no competing financial interest.

■ ACKNOWLEDGMENTS

We thank Rochus Schmid for providing access to his MOF-FF potential implementation, and Jonathan Skelton for useful conversations and guidance with this work. J.K.B. is funded by the EPSRC Doctoral Training Centre for Sustainable Chemical Technologies at Bath University (Grant No. EP/G03768X/1). D.T. is funded under ERC Starting Grant 277757. A.W. acknowledges support from the Royal Society University Research Fellowship scheme. The work benefits from the high performance computing facility at the University of Bath. Access to the HECToR and ARCHER supercomputers was facilitated through membership of the HPC Materials Chemistry Consortium (EP/F067496).

■ REFERENCES

(1) Millward, A. R.; Yaghi, O. M. *J. Am. Chem. Soc.* **2005**, *127*, 17998−17999.
(2) Bernini, M. C.; Fairen-Jimenez, D.; Pasinetti, M.; Ramirez-Pastor, A. J.; Snurr, R. Q. *J. Mater. Chem. B* **2014**, *2*, 766−774.
(3) Hendon, C. H.; Tiana, D.; Walsh, A. *Phys. Chem. Chem. Phys.* **2012**, *14*, 13120−13132.
(4) Jain, A.; Ong, S. P.; Hautier, G.; Chen, W.; Richards, W. D.; Dacek, S.; Cholia, S.; Gunter, D.; Skinner, D.; Ceder, G. *APL Mater.* **2013**, *1*, 011002.
(5) Wang, C.; Chen, S.; Yang, J.-H.; Lang, L.; Xiang, H.; Gong, X.; Walsh, A.; Wei, S.-H. *Chem. Mater.* **2014**, *26*, 3411.
(6) Frost, J. M.; Butler, K. T.; Brivio, F.; Hendon, C. H.; van Schilfgaarde, M.; Walsh, A. *Nano Lett.* **2014**, *14*, 2584−2590.
(7) Zakutayev, A.; Zhang, X.; Nagaraja, A.; Yu, L.; Lany, S.; Mason, T. O.; Ginley, D. S.; Zunger, A. *J. Am. Chem. Soc.* **2013**, *135*, 10048−10054.

(8) Scanlon, D. O.; Walsh, A. *Appl. Phys. Lett.* **2012**, *100*, 251911.
(9) Jackson, A. J.; Walsh, A. *J. Mater. Chem. A* **2014**, *2*, 7829−7836.
(10) Lewis, G.; Catlow, C. *J. Phys. C* **1985**, *18*, 1149.
(11) Catlow, C.; Guo, Z.; Miskufova, M.; Shevlin, S.; Smith, A.; Sokol, A.; Walsh, A.; Wilson, D.; Woodley, S. *Philos. Trans. R. Soc. A* **2010**, *368*, 3379−3456.
(12) Greathouse, J. A.; Allendorf, M. D. *J. Am. Chem. Soc.* **2006**, *128*, 10678−10679.
(13) Schmid, R.; Tafipolsky, M. *J. Am. Chem. Soc.* **2008**, *130*, 12600−12601.
(14) Salles, F.; Ghoufi, A.; Maurin, G.; Bell, R. G.; Mellot-Draznieks, C.; Férey, G. *Angew. Chem., Int. Ed.* **2008**, *47*, 8487−8491.
(15) McDaniel, J. G.; Yu, K.; Schmidt, J. *J. Phys. Chem. C* **2012**, *116*, 1892−1903.
(16) Greathouse, J. A.; Allendorf, M. D. *J. Phys. Chem. C* **2008**, *112*, 5795−5802.
(17) Vanduyfhuys, L.; Verstraelen, T.; Vandichel, M.; Waroquier, M.; Van Speybroeck, V. *J. Chem. Theory Comput.* **2012**, *8*, 3217−3231.
(18) Yang, Q.; Liu, D.; Zhong, C.; Li, J.-R. *Chem. Rev.* **2013**, *113*, 8261−8323.
(19) Babarao, R.; Jiang, J. *Langmuir* **2008**, *24*, 6270−6278.
(20) Wilmer, C. E.; Leaf, M.; Lee, C. Y.; Farha, O. K.; Hauser, B. G.; Hupp, J. T.; Snurr, R. Q. *Nat. Chem.* **2011**, *4*, 83−89.
(21) Yazaydin, A. O.; Snurr, R. Q.; Park, T.; Koh, K.; Liu, J.; LeVan, M. D.; Benin, A. I.; Jakubczak, P.; Lanuza, M.; Galloway, D. B. *J. Am. Chem. Soc.* **2009**, *131*, 18198−18199.
(22) Sikora, B. J.; Winnegar, R.; Proserpio, D. M.; Snurr, R. Q. *Micropor. Mesopor. Mater.* **2014**, *186*, 207−213.
(23) Fu, J.; Sun, H. *J. Phys. Chem. C* **2009**, *113*, 21815−21824.
(24) Zhang, L.; Hu, Z.; Jiang, J. *J. Am. Chem. Soc.* **2013**, *135*, 3722−3728.
(25) Ghoufi, A.; Maurin, G. *J. Phys. Chem. C* **2010**, *114*, 6496−6502.
(26) Zhang, L.; Wu, G.; Jiang, J. *J. Phys. Chem. C* **2014**, *118*, 8788−8794.
(27) Yang, Q.; Zhong, C. *J. Phys. Chem. B* **2006**, *110*, 17776−17783.
(28) Düren, T.; Bae, Y.; Snurr, R. Q. *Chem. Soc. Rev.* **2009**, *38*, 1237−1247.
(29) Wu, D.; Wang, C.; Liu, B.; Liu, D.; Yang, Q.; Zhong, C. *AIChE J.* **2012**, *58*, 2078−2084.
(30) Rappé, A. K.; Casewit, C. J.; Colwell, K.; Goddard Iii, W.; Skiff, W. *J. Am. Chem. Soc.* **1992**, *114*, 10024−10035.
(31) Haldoupis, E.; Nair, S.; Sholl, D. S. *J. Am. Chem. Soc.* **2012**, *134*, 4313−4323.
(32) Addicoat, M. A.; Vankova, N.; Akter, F. I.; Heine, T. *J. Chem. Theory Comput.* **2014**, *10*, 880−891.
(33) Tafipolsky, M.; Amirjalayer, S.; Schmid, R. *J. Phys. Chem. C* **2010**, *114*, 14402−14409.
(34) Bureekaew, S.; Amirjalayer, S.; Tafipolsky, M.; Spickermann, C.; Roy, T. K.; Schmid, R. *Phys. Status Solidi B* **2013**, *250*, 1128−1141.
(35) Allinger, N. L.; Yuh, Y. H.; Lii, J. H. *J. Am. Chem. Soc.* **1989**, *111*, 8551−8566.
(36) Allinger, N. L.; Li, F.; Yan, L. *J. Comput. Chem.* **1990**, *11*, 848−867.
(37) Bader, R. F. *Acc. Chem. Res.* **1985**, *18*, 9−15.
(38) Li, H.; Eddaoudi, M.; O'Keeffe, M.; Yaghi, O. M. *Nature* **1999**, *402*, 276−279.
(39) Eddaoudi, M.; Kim, J.; Rosi, N.; Vodak, D.; Wachter, J.; O'Keeffe, M.; Yaghi, O. M. *Science* **2002**, *295*, 469−472.
(40) Yang, Q.; Guillerm, V.; Ragon, F.; Wiersum, A. D.; Llewellyn, P. L.; Zhong, C.; Devic, T.; Serre, C.; Maurin, G. *Chem. Commun.* **2012**, *48*, 9831−9833.
(41) Chui, S. S.-Y.; Lo, S. M.-F.; Charmant, J. P.; Orpen, A. G.; Williams, I. D. *Science* **1999**, *283*, 1148−1150.
(42) Cavka, J. H.; Jakobsen, S.; Olsbye, U.; Guillou, N.; Lamberti, C.; Bordiga, S.; Lillerud, K. P. *J. Am. Chem. Soc.* **2008**, *130*, 13850−13851.
(43) Schaate, A.; Roy, P.; Godt, A.; Lippke, J.; Waltz, F.; Wiebcke, M.; Behrens, P. *Chem. Eur. J. A* **2011**, *17*, 6643−6651.
(44) Valenzano, L.; Civalleri, B.; Chavan, S.; Bordiga, S.; Nilsen, M. H.; Jakobsen, S.; Lillerud, K. P.; Lamberti, C. *Chem. Mater.* **2011**, *23*, 1700−1718.
(45) Wiersum, A. D.; Soubeyrand-Lenoir, E.; Yang, Q.; Moulin, B.; Guillerm, V.; Yahia, M. B.; Bourrelly, S.; Vimont, A.; Miller, S.; Vagner, C. *Asian J. Chem.* **2011**, *6*, 3270−3280.
(46) Lin, K.-S.; Adhikari, A. K.; Ku, C.-N.; Chiang, C.-L.; Kuo, H. *Int. J. Hydrogen Energy* **2012**, *37*, 13865−13871.
(47) Gascon, J.; Aguado, S.; Kapteijn, F. *Micropor. Mesopor. Mater.* **2008**, *113*, 132−138.
(48) Kresse, G.; Hafner, J. *Phys. Rev. B* **1993**, *47*, 558.
(49) Blöchl, P. E. *Phys. Rev. B* **1994**, *50*, 17953.
(50) Perdew, J. P.; Burke, K.; Ernzerhof, M. *Phys. Rev. Lett.* **1996**, *77*, 3865−3868.
(51) Hendon, C. H.; Tiana, D.; Fontecave, M.; Sanchez, C.; D'arras, L.; Sassoye, C.; Rozes, L.; Mellot-Draznieks, C.; Walsh, A. *J. Am. Chem. Soc.* **2013**, *135*, 10942−10945.
(52) De La Pierre, M.; Orlando, R.; Maschio, L.; Doll, K.; Ugliengo, P.; Dovesi, R. *J. Comput. Chem.* **2011**, *32*, 1775−1784.
(53) He, L.; Liu, F.; Hautier, G.; Oliveira, M. J.; Marques, M. A.; Vila, F. D.; Rehr, J.; Rignanese, G.-M.; Zhou, A. *Phys. Rev. B* **2014**, *89*, 064305.
(54) Henkelman, G.; Arnaldsson, A.; Jónsson, H. *Comput. Mater. Sci.* **2006**, *36*, 354−360.
(55) Tafipolsky, M.; Amirjalayer, S.; Schmid, R. *J. Comput. Chem.* **2007**, *28*, 1169−1176.
(56) Ponder, J. W.; Richards, F. M. *J. Comput. Chem.* **1987**, *8*, 1016−1024.
(57) Pappu, R. V.; Hart, R. K.; Ponder, J. W. *J. Phys. Chem. B* **1998**, *102*, 9725−9742.
(58) W. Eaton, J.; Bateman, D.; Hauberg, S. *GNU Octave Manual*, Version 3; Network Theory Limited: Godalming, U.K., 2008.
(59) Otero de la Roza, A.; Luaña, V. *Comput. Theor. Chem.* **2011**, *975*, 111−115.
(60) Tiana, D.; Francisco, E.; Blanco, M. A.; Pendás, A. M. *J. Phys. Chem. A* **2009**, *113*, 7963−7971.
(61) Peng, Z.; Ewig, C. S.; Hwang, M.-J.; Waldman, M.; Hagler, A. T. *J. Phys. Chem. A* **1997**, *101*, 7243−7252.
(62) https://github.com/WMD-Bath/BTW-FF; Walsh Materials Design Group: Bath, U.K. (accessed June 11, 2014).
(63) Talin, A. A.; Centrone, A.; Ford, A. C.; Foster, M. E.; Stavila, V.; Haney, P.; Kinney, R. A.; Szalai, V.; El Gabaly, F.; Yoon, H. P. *Science* **2014**, *343*, 66−69.
(64) Butler, K. T.; Hendon, C. H.; Walsh, A. *J. Am. Chem. Soc.* **2014**, *136*, 2703−2706.
(65) Wu, H.; Yildirim, T.; Zhou, W. *J. Phys. Chem. Lett.* **2013**, *4*, 925−930.
(66) Kuc, A.; Enyashin, A.; Seifert, G. *J. Phys. Chem. B* **2007**, *111*, 8179−8186.
(67) Skelton, J. M.; Parker, S. C.; Togo, A.; Tanaka, I.; Walsh, A. *Phys. Rev. B* **2014**, *89*, 205203.
(68) Civalleri, B.; Napoli, F.; Noel, Y.; Roetti, C.; Dovesi, R. *CrystEngComm* **2006**, *8*, 364−371.
(69) Miller, W.; Smith, C.; Mackenzie, D.; Evans, K. *J. Mater. Sci.* **2009**, *44*, 5441−5451.
(70) Han, S. S.; Goddard, W. A. *J. Phys. Chem. C* **2007**, *111*, 15185−15191.
(71) Sun, Y.; Sun, H. *J. Mol. Model.* **2014**, *20*, 1−15.
(72) Lock, N.; Christensen, M.; Wu, Y.; Peterson, V. K.; Thomsen, M. K.; Piltz, R. O.; Ramirez-Cuesta, A. J.; McIntyre, G. J.; Norén, K.; Kutteh, R. *Dalton Trans.* **2013**, *42*, 1996−2007.

3.2 Paper 2 - A general forcefield for accurate phonon properties of metal-organic frameworks

The following paper is an extension to the previous paper, building on concepts of the previous BTW-FF[227] forcefield, a new transferable forcefield, named VMOF, was derived. Several improvements to both the accuracy and transferability were made to the BTW-FF. Firstly, the effective atomic charges that were derived by Bader analysis of the charge density[243–245] using first-principles calculations in BTW-FF, were replaced with Gasteiger[246] charges in VMOF. Gasteiger charges are derived using a pseudo charge equilibrium scheme, where the orbital electronegativity is only partially equalised using an iterative procedure depending on the identity of the nearest neighbour bonding. The advantage of Gasteiger charges over Bader charges is that the Gasteiger charges can be derived using a single processor on a local machine using the GULP molecular mechanics programme.

When deriving VMOF we found imaginary phonons associated with enforcing a planar torsion across the head of the carboxylic acid group (Ocarb-Ccarb-Cbenz-Cbenz). First-principles calculations, as reported in the paper, confirm the phonon instability to be due to this torsion, which following imaginary eigenvectors allowed rotation of the carboxylic acid heads to leave angles ranging from 1-10° in the archetypal MOF-5. Force constants in VMOF for this torsion were derived from first-principles calculations, but all other bonding forcefield parameters remain from the CHARMM library.

MM3 non-bonding parameters are derived by a relaxed fitting procedure to reproduce the bond lengths and mechanical and vibrational properties of an initial subset of MOFs. Furthermore, the MM3 non-bonding parameters are derived with the respective metal oxide included in the fitting procedure, structural, mechanical and vibrational properties were again fitted. The final MM3 parameters are therefore capable of reproducing the bulk materials of the MOFs studied, and of their respective oxides, for example the parameters for MOF-5, which is comprised of Zn metal nodes, can also reproduce the material properties and structure of ZnO. During the fit of VMOF we observed a greater accuracy if the MM3 Buckingham constants, which were originally derived for hydrocarbons,[174] were varied slightly. A full discussion of the change to the MM3 constants is given in the paper.

Other changes to the BTW-FF to derive the VMOF forcefield, include using the CHARMM bonding forcefield parameters opposing those from the MM3 forcefield for BTW-FF. Additionally, the change from using the TINKER[247] programme to using GULP[248,249] for the VMOF forcefield makes the forcefield more accessible, owing to GULP being a more popular programme to use for solid-state materials.

The main focus of the following paper is the accuracy of the vibrational properties, including those calculated using the QHA, thus allowing the consideration of volume change with temperature as an anharmonic effect. It is anticipated that the simplicity of the derivation of VMOF would encourage the community of MOF modellers to use the forcefield, and also would allow for the preparation of a large-scale screening procedure of the vibrational properties of MOFs.

3.2.1 Forcefield parameter files

The forcefield parameter files can be found as open-source resources at the following Github address: https://github.com/WMD-group/VMOF

3.2.2 Personal contribution

My personal contribution to the paper entitled *"A general forcefield for accurate phonon properties of metal-organic frameworks"* included the derivation of the VMOF forcefield and calculation of structural, mechanical and vibrational properties with both DFT and VMOF. Other work done by myself includes structural optimisation with DFT and quasi-harmonic approximation (QHA) calculations with VMOF and DFT QHA calculations on NOTT-300. J.M.Skelton conducted the DFT QHA calculations on MOF-5, IRMOF-10 and UiO-66 and provided python scripts for producing IR and DOS plots and integrating Phonopy with GULP.

PCCP

PAPER

View Article Online
View Journal

Cite this: DOI: 10.1039/c6cp05106e

A general forcefield for accurate phonon properties of metal–organic frameworks†

Jessica K. Bristow,[a] Jonathan M. Skelton,[a] Katrine L. Svane,[a] Aron Walsh*[ab] and Julian D. Gale*[c]

Received 22nd July 2016,
Accepted 30th September 2016

DOI: 10.1039/c6cp05106e

www.rsc.org/pccp

We report the development of a forcefield capable of reproducing accurate lattice dynamics of metal–organic frameworks. Phonon spectra, thermodynamic and mechanical properties, such as free energies, heat capacities and bulk moduli, are calculated using the quasi-harmonic approximation to account for anharmonic behaviour due to thermal expansion. Comparison to density functional theory calculations of properties such as Grüneisen parameters, bulk moduli and thermal expansion supports the accuracy of the derived forcefield model. Material properties are also reported in a full analysis of the lattice dynamics of an initial subset of structures including: MOF-5, IRMOF-10, UiO-66, UiO-67, NOTT-300, MIL-125, MOF-74 and MOF-650.

1 Introduction

Metal–organic frameworks (MOFs), formed from metal cations and anionic organic molecules, are versatile materials with a range of functional properties. There are a vast number of possible candidate structures from known metals and ligands, which may self-assemble into a variety of 3D MOF structures. Developing a cheap, transferable and accurate method for initial property screening of potential MOF candidates for applications such as gas absorption, explosives detection and use in solar energy conversion is therefore desirable to reduce the cost and time of experimental work. Given the tractable, but still computationally expensive, nature of density functional theory (DFT) and higher levels of first principles theory, the development of forcefields capable of reproducing structural, mechanical and vibrational properties of MOFs would be highly advantageous to the large community of computational chemists interested in the thermoelastic properties of MOFs.

A current dilemma for the development of forcefields for MOFs is the choice between transferability and accuracy. Large scale screening procedures offer a powerful tool for guiding experimental work but often involve multiple approximations, creating a level of uncertainty when used to calculate complex properties. *Ab initio* derived forcefields for prediction of charges and force constants offer accurate reproduction of the properties of individual or families of MOFs with similar topologies, but lack transferability. However, one must also consider that the purpose of using a forcefield for materials with large primitive unit cells is to remove the need to conduct expensive higher level calculations in the first place. A final consideration is associated with the diversity of MOFs. Due to differing compositions and topologies, the nature of the interaction between metal and ligand ranges between ionic and covalent. To derive one forcefield capable of reproducing all such interactions is a challenging task.

A vast number of forcefields for MOFs have already been reported; here we give a summary of the most prevalent and recent developments as a brief but broad overview. When parameterising a forcefield for MOFs there are many different approaches one can take. Firstly, existing transferable forcefields, such as CHARMM,[1,2] MM3,[3,4] GAFF[5] and UFF,[6] which have been extensively derived for common organic and, to a lesser extent, inorganic compounds, offer an abundant source of reasonable parameters for the individual components of MOFs. It is therefore only the interaction between metal and ligand for which additional potential parameters must be derived. UFF4MOF[7] is an example of such a forcefield, reported by Addicoat *et al.*, where the forcefield is an extension to the Universal forcefield (UFF). The UFF consists of multiple parameters capable of adequately reproducing the structures of organic molecules and inorganic clusters with little specific fitting. Indeed its incorporation in many user-friendly visualisation programs has increased the popularity of the UFF forcefield over many other more specifically parameterised transferable forcefields such as CHARMM. UFF4MOF employs additional atom types with parameterised valence coordination, equilibrium bond distances, effective charges and bond angles of the UFF to

[a] Centre for Sustainable Chemical Technologies and Department of Chemistry, University of Bath, Claverton Down, Bath, BA2 7AY, UK
[b] Department of Materials, Imperial College London, Exhibition Road, London SW7 2AZ, UK. E-mail: a.walsh@imperial.ac.uk; Tel: +44 (0)1225 385432
[c] Curtin Institute for Computation, Department of Chemistry, Curtin University, PO Box U1987, Perth, WA 6845, Australia. E-mail: j.gale@curtin.edu.au
† Electronic supplementary information (ESI) available. See DOI: 10.1039/c6cp05106e

achieve a more accurate reproduction of the structure of clusters and periodic models of different MOFs. A more specific modification of UFF to reproduce the interaction of IRMOF-10 with CO_2 was reported by Borycz *et al.*[8]

Another approach is to derive bonding force constants and partial charges for each individual MOF using DFT calculations. MOF-FF is an example of a DFT-derived forcefield and was developed by Schmid *et al.*[9] MOF-FF is capable of reproducing the structure and properties of many MOF topologies with initial parameterisation using the MM3 forcefield. The forcefield is then further fitted for individual MOFs based on data obtained from first principles calculations. The transferability for many families of MOFs has therefore not been extensively tested. Quick-FF was published by Van Speybroeck *et al.*[10] and offers a method for rapid application of a forcefield to a MOF based on force constants extracted from a first principles Hessian. Quick-FF is still based on the MM3 non-bonding functional form but bonding parameters must be input by the user for the MOF of interest. The application of Quick-FF to MOF-5 and MIL-53 was reported, and was shown to reproduce both the structural parameters and the breathing behaviour of MIL-53.[10] Here derivation of charges and bonding parameters remains dependent on first principles calculations. BTW-FF, our own previously reported MOF forcefield, which has been shown to reproduce the structure and properties of many different MOF topologies, also used partial charges obtained from DFT, using a Bader analysis of the charge density of each MOF considered.[11]

Finally, large scale screening procedures can be based on a primitive mathematical description of the bonding in a framework or using a transferable forcefield, such as UFF, for all structures. High-throughput computational screening offers a valuable method for an approximate initial analysis of properties such as volumetric gas uptake or surface area. Screening also offers a means of structure prediction for hypothetical frameworks based on possible bonding considerations.[12–15]

Comparisons of forcefields for simple MOFs, such as MOF-5, are now standard practice and offer little evaluation of the difficultly in derivation of the forcefield. Furthermore, the transferability of parameters across variations in the topology and crystallinity are rarely extensively tested. In particular, a recent focus is on defects and disorder in MOFs. Alterations of the frameworks must still render accurate and reliable results with the same forcefield parameters.

We highlight the calculation of phonon properties to be a relatively sparsely populated area of study for MOF forcefields; indeed, many forcefields, including previous work of ours, have merely compared vibrational Γ-point frequencies and plotted IR spectra. Phonon properties are critical for the analysis of dynamic stability, particularly if soft-modes are present, energetic stability (*via* free energies) and finite-temperature properties.[16–20] Calculating phonon properties, such as phonon dispersion curves, with DFT is costly, and is only affordable and practical for specific MOFs of interest. Routine screening of phonon properties for large numbers of MOFs is currently only affordable with forcefield methods. One must also remember that experimental structures are often determined using X-ray diffraction. This can lead to inaccurate structure refinement of hydrogen positions and assignment of space groups that represent average structures. For some MOFs this may lead to loss of information regarding subtle distortions, such as non-planarity of carboxylate groups. Analysing the phonon stability of the structure, particularly for DFT calculations, is expensive and often avoided during electronic structure analysis. A transferable forcefield, not specifically fitted for each individual MOF, may allow small distortions of a framework to be identified, though the extent to which this is possible may depend on whether polarisability is included in the model or not. Optimising MOFs with a forcefield prior to using DFT may therefore be beneficial.

A final note regarding the importance of phonon property calculations is that MOF forcefields are often fitted at 0 K to an experimental structure determined at room temperature. Furthermore, temperature dependent properties (such as bulk moduli) from a 0 K optimisation are also often compared to room temperature experiments. Incorporating the consideration of temperature through free energy minimisation is a desirable alternative solution to having to make such approximate comparisons.

Here we present a new forcefield derived with the intention to bridge the gap between accuracy and transferability, while also incorporating an extensive analysis of phonon properties. The forcefield, named VMOF (vibrational metal–organic framework), is derived with the intention to be transferable, accessible and accurate when reproducing the structure and dynamical properties of MOFs. VMOF is a development of our previously reported BTW-FF forcefield for MOFs. In this paper we report the foundations and derivation of VMOF, along with a comparison of initial structure parameters and mechanical properties calculated for a range of MOFs. The main focus of the paper is then on discussing the accuracy of the forcefield for reproducing phonon properties obtained from DFT. We report densities of states (DOS), infra-red (IR) spectra and temperature dependent thermodynamic properties, such as free energies, vibrational entropy, and constant volume heat capacities. We show this new forcefield to be capable of accurately reproducing properties for an initial subset of MOFs. Finally, we perform quasi-harmonic calculations that, to the best of our knowledge, have not been previously reported for the given structures, and report additional temperature dependent structural properties.

2 Methodology

2.1 First principles reference calculations

Reference quantum mechanical calculations were conducted to have a standard method of validation of the new forcefield. The Vienna *ab initio* Simulation Package (VASP)[21] code was used to perform Kohn–Sham density functional theory (DFT) calculations using the PBEsol exchange–correlation functional.[22] The projector-augmented wave method[23] was used for the interaction between core and valence electrons of all atoms in the system. During optimisation, all forces were converged to values of less than 0.001 eV $Å^{-1}$ with a plane wave basis set

cut-off of 600 eV. Γ-Point sampling of the Brillouin zone was considered sufficient for the MOFs owing to the unit cell dimensions of the systems, excluding MOF-74, which required a 4 × 4 × 4 k-point grid. A D3 van der Waals correction[24] was included and found to be necessary to remove phonon instabilities for some MOF structures. Reference calculations for the binary oxides: ZnO, Al_2O_3, TiO_2 and ZrO_2, were performed with the same convergence criteria in VASP, with the chosen polymorphs being wurtzite, corundum, rutile and baddelite, respectively. The k-point grid and plane wave cut-off were converged separately for each metal oxide, with final values being given in the ESI† along with the optimised unit cell parameters.

2.2 Forcefield calculations

VMOF was derived using the General Utility Lattice Program (GULP) code, which has extensive capabilities suited to both inorganic and organic materials.[25,26] VMOF considers the metal node and organic component as essentially separate entities interacting only by modified MM3 Buckingham potentials, in addition to the Coulomb terms.

$$E_{ij}^{\mathrm{MM3}} = \varepsilon_{ij}\left[A\exp\left(-B\frac{d_{ij}}{d_{ij}^0}\right) - C\left(\frac{d_{ij}^0}{d_{ij}}\right)^6\right] \quad (1)$$

The MM3 Buckingham functional (eqn (1)) form consists of defined constants, A (1.84×10^5), B (12) and C (2.25), and was proposed as a ''softer'' energy function to that used in MM2. MM3 has been shown to accurately reproduce hydrogen and carbon positions in many aromatic compounds.[3,4] The two remaining parameters per atom type, epsilon and the van der Waals radius, were fitted to reproduce phonon stable metal oxide structures by deriving these parameters for both the metal and the inorganic oxygen. The reference to inorganic oxygen here describes oxygen atoms that are coordinated only to metal atoms. Epsilon and van der Waals terms for the carboxylate oxygen and hydroxyl oxygen atom types were fitted in a relaxed fitting procedure to reproduce structural and mechanical properties of all the MOFs being tested. A further feature is the use of combination rules, where; $\varepsilon_{ij} = \sqrt{\varepsilon_{ii}\varepsilon_{jj}}$ and $d_{ij} = \sqrt{d_{ii}d_{jj}}$, to reduce the number of parameters that require fitting, thus increasing the transferability. The long-range cut-off of the MM3 Buckingham potentials was set to 12 Å.

The derivation of parameters for the organic ligands was considered separately. Intramolecular bonding parameters for the ligands are taken directly from the CHARMM library and are implemented as harmonic functions. We consider the intramolecular bonding parameters between neighbouring atoms, angles between three connected neighbours and torsions between four connected atoms. A small modification was made to the CHARMM parameters for the 4-body torsion across the carboxylate head of all ligands considered, the derivation of which will be discussed later.

The total energy (U) can be written as;

$$U = \sum_{\text{bonds}}\frac{1}{2}k_r(r-r_0)^2 + \sum_{\text{angles}}\frac{1}{2}k_\theta(\theta-\theta_0)^2 + \sum_{\text{dihedrals}}\frac{1}{2}k_\Psi[1+\cos(n\Psi+\Psi_0)] + \frac{1}{2}\sum_i\sum_j\frac{q_iq_je^2}{4\pi\varepsilon_0 r_{ij}}$$

where, k_r, k_θ and k_Ψ are interatomic force constants, r the distance between pairs of atoms, θ and Ψ are angles, q represents point charges and ε_0 is the vacuum permittivity. Note that the harmonic bonding terms in GULP possess a multiplication factor of $\frac{1}{2}$, and so CHARMM force constants were appropriately scaled.

The charges of the ligands are derived within GULP using the charge equilibration model of Gasteiger,[27,28] while formal charges are used for the metal nodes and inorganic oxygen atoms. Gasteiger charges were selected since the charges are geometry independent and depend only on connectivity. Whilst other charge equilibration schemes suffer from charge delocalisation errors, Gasteiger charges do not.[28] Initial charge parameterisation involved taking the average charge of each atom type in a subset of common MOF ligands including; 1,4-dicarboxylate (BDC), 1,3,5-tricarboxylate (BTC), 4,4′-biphenyl dicarboxylate (BPDC), 2,6-azulenedicarboxylate (AZ), 4,4′-biphenyl tricarboxylate (BPTC) and 2,7-pyrene-dicarboxylate (PDC). Once derived for a specific atom type, the same charges are used for all the structures modelled. Although Gasteiger charges are approximate, the advantage is that they are efficient to compute and well suited for our purpose.

2.3 Property calculations

2.3.1 Mechanical properties. Bulk moduli (B_0) were calculated from the relevant components of the elastic constant and compliance tensors, which were determined from the analytical second derivatives of the energy with respect to strain on the system. The elastic compliance tensor is just the inverse of the elastic constant tensor. The reported bulk moduli calculated with the forcefield follow the Hill convention, *i.e.* they are the averages of the Reuss and Voigt definitions. First principles bulk moduli for each structure were calculated at 0 K by fitting a third-order Birch–Murnaghan equation of state to energy-volume data calculated at a series of expansions and contractions about the equilibrium structure. For each expansion and contraction the atomic positions were optimised. First principles elastic constants were calculated using the finite differences method to construct the second derivatives of the energy with respect to the atomic positions. Only symmetry inequivalent displacements were considered.

2.3.2 Vibrational properties. IR frequencies and intensities, as well as DOS, were post-processed from both forcefield and first principles methods to apply a consistent broadening factor of 10 cm^{-1} with a frequency sampling resolution of 1 cm^{-1}. First principles calculations of dynamical matrices were performed using density functional perturbation theory within VASP to obtain ε^∞ and phonopy was used to calculate the eigenvalues. IR frequencies and intensities were then plotted with identical resolution and broadening factors.

2.3.3 Lattice dynamics and thermodynamic properties. To calculate the thermodynamic properties, such as Helmholtz and Gibbs free energies, vibrational entropy and volumetric heat capacity, and the dependence with temperature, we use phonopy.[29,30] Phonopy is a python package for setting up post-processing finite-displacement phonon calculations that can be integrated with multiple first principles codes, and includes an extension for the quasi-harmonic approximation. Further details are given in the ESI.†

The quasi-harmonic approximation[31] allows a greater number of thermodynamic properties to be computed along with their temperature-dependence. The practical reality of the quasi-harmonic approximation is to minimise the internal energy at constant volume at a given number of lattice expansions and contractions away from the global minimum structure. An equation of state is then fitted across the calculated temperature-dependent Helmholtz free energies, which changes the minimum free energy volume according to a defined temperature. The temperature dependence of the phonon frequencies is then expressed in terms of Gibbs free energy. The theory is still dependent on calculations conducted under the harmonic approximation, but the consequent volume dependence of the vibrational frequencies is an anharmonic effect. In general it is possible to use the analytical derivatives of the free energy with respect to strain to optimise all cell parameters independently within the ZSISA[32] (zero static internal stress) approximation. While this can be routinely achieved using some forcefield implementations,[33] the requirement to compute third-order derivatives makes this particularly demanding with quantum mechanical approaches.

Throughout the calculation of thermodynamic properties a consistent Brillouin-zone phonon sampling (q-point) mesh of $32 \times 32 \times 32$ was used, with a symmetry tolerance of 10^{-3} Å for determining the space group symmetry during atomic displacement generation.

To remove imaginary modes, observed only during compression in the DFT calculations, the corresponding Hessian eigenvectors were used to displace the atoms, thereby lowering the symmetry, and the structure relaxed accordingly. Removing imaginary modes with the forcefield required the use of a rational function optimisation approach to ensure that the Hessian has the correct final structure after optimisation.

3 Results

3.1 Forcefield fitting

3.1.1 Universal forcefield and metal oxide parameters. When considering the initial derivation of parameters for each metal, besides fitting the epsilon and van der Waals radius for each species, we have also examined the influence of changing the Universal MM3 constants. This was found to be beneficial to the overall quality of the results. After extensive testing, we found that the modification of the MM3 constants by changing the B parameter to 11.5 and C parameter to 2.55, reproduced DFT and experimental structural and mechanical properties of the MOFs and metal oxides more accurately. In support of the modification of the MM3 constants, we report structural and mechanical properties for the binary oxides with the original

Table 1 Comparison of structural and mechanical properties of metal oxides between experiment (exp.) and the VMOF forcefield with modified MM3 parameters (VMOF). Given are the elastic constants (C_{ij}), bulk moduli (B_0), unit cell parameters and metal–oxygen (M–O) bond lengths. All lengths are reported in Å and elastic constants and bulk moduli are reported in GPa. Percentage errors in the cell parameters relative to the experimental values are given in parenthesis under each value reported. DFT values are calculated with the PBEsol functional

	a	b	c	M–O	C_{11}	C_{12}	C_{13}	C_{33}	C_{44}	C_{55}	B_0
ZnO											
Exp.[34]	3.250	3.250	5.207	1.992	209.6	121.1	105.1	210.9	—	42.5	183.0
DFT	3.225	3.225	5.211	1.972	187.8	123.1	108.6	209.0	—	27.9	143.4
% error	(0.77)	(0.77)	(0.08)								
VMOF	3.219	3.219	5.014	1.967	242.6	108.2	100.7	199.2	—	78.4	143.2
% error	(0.95)	(0.95)	(3.71)								
ZrO_2											
Exp.[35]	5.070	5.070	5.070	2.195	533.5	97.9	—	—	64.3	—	243.7
DFT	5.064	5.064	5.064	2.193	575.6	139.8	—	—	80.1	—	279.3
% error	(0.12)	(0.12)	(0.12)								
VMOF	5.123	5.123	5.123	2.218	630.8	131.2	—	—	125.7	—	297.7
% error	(1.05)	(1.05)	(1.05)								
TiO_2											
Exp.[36]	4.594	4.594	2.959	1.980, 1.949	366.0	225.0	—	—	189.0	—	282.0
DFT	4.585	4.585	2.941	1.971, 1.944	274.5	208.8	—	—	236.3	—	251.9
% error	(0.20)	(0.20)	(0.61)								
VMOF	4.414	4.414	3.168	1.980, 1.934	362.4	337.2	—	—	213.7	—	335.1
% error	(3.92)	(3.92)	(7.06)								
Al_2O_3											
Exp.[37]	4.764	4.764	13.001	1.858	497.3	162.8	116.0	500.9	146.8	—	240.0
DFT	4.755	4.755	12.962	1.966	482.2	157.0	121.0	493.3	162.6	—	269.4
% error	(0.19)	(0.19)	(0.30)								
VMOF	4.870	4.870	12.899	1.848	564.3	224.3	152.2	463.3	123.9	—	291.3
% error	(2.23)	(2.23)	(0.78)								

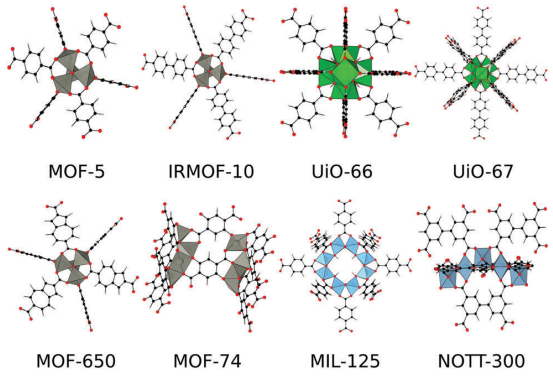

Fig. 1 Structures of MOF-5, IRMOF-10, UiO-66, UiO-67, MOF-650, MOF-74, MIL-125 and NOTT-300. Metal polyhedra are highlighted for Zn (silver), Zr (green), Ti (blue) and Al (grey), with atoms coloured black for carbon, white for hydrogen and red for oxygen. Compositions and symmetries are given in Table 2.

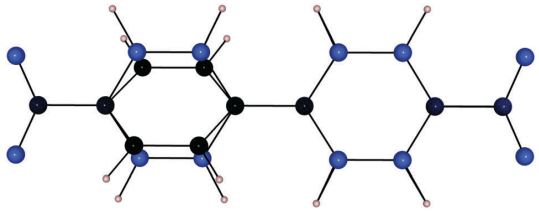

Fig. 2 Overlaid planar (blue) and twisted (black) 4,4′-BPDC ligands showing the change in geometry of the ligand after following the imaginary phonon modes in the initial structure of IRMOF-10.

MM3 constants (see ESI†) and modified constants (Table 1) in comparison with experimental values. Using the original MM3 constants results in large errors for second order elastic properties such as the elastic constants and bulk moduli.

The forcefield model that we have chosen to adopt to increase transferability involves formal charges at the metal node. The unit cell parameters and elastic constants of the metal oxides reproduced by the forcefield are generally reasonable (Table 1), though with a tendency to overestimate the hardness of materials. Formal charge models usually include the shell model for polarisation of the oxide ions, which can effectively soften the mechanical properties, but we maintain the use of a rigid ion model for consistency with the CHARMM parameters for the organic ligands.

A final comparison of the mechanical properties between experiment and DFT further highlights the variation in calculated values of the elastic constants and bulk moduli of the metal oxides (Table 1). The mechanical properties calculated with VMOF remain within a reasonable range with both experiment and DFT values.

3.1.2 Ligand parameters. Force constants for the ligand parameters are taken directly from the CHARMM library. During the derivation of forcefield parameters for the metal nodes, there was one 4-body interaction with the ligand that showed a particular propensity for producing phonon unstable structures if varied. The torsion across the head of the carboxylate groups did not always remain planar during optimisation, and enforcing planarity by increasing the force constant across this bonding connection often rendered structures phonon unstable. We therefore calculated the force constant across this interaction in an isolated BDC^{2-} ligand in the gas phase. The PBE0 functional[38] was used in the NWChem program[39] with the Dunning correlation consistent cc-pVTZ basis sets[40] to fully relax the ligand with a 0 and 90° torsion of the carboxylate heads in relation to the aromatic ring (depicted in the ESI†). We calculate the energy difference between the two configurations to be 0.530 eV. To maintain transferability of the forcefield we assume little variation of this energy would occur across different aromatic dicarboxylate ligands. Therefore, it is this value that the force constant is fitted to for the torsion between O_{carb}–C_{carb}–C_{benz}–C_{benz} for all structures with these atom types.

3.2 Structural properties

Following the derivation of the forcefield parameters, mechanical and vibrational properties have been calculated for eight different MOFs (Fig. 1), representing a range of ligand and metal node types: MOF-5, IRMOF-10, UIO-66, UIO-67, MOF-650, MIL-125 and NOTT-300.

Prior to the calculation of thermodynamic properties, several observations regarding the vibrational stability of IRMOF-10 and MIL-125 were made during optimisation. Firstly, for IRMOF-10 we initially calculated a significant number of imaginary vibrational modes. To relax the structure into the ground-state and remove all sources of instability, all imaginary modes were simultaneously relaxed following an initial displacement along the corresponding phonon eigenvectors. The final structure was re-converged and no imaginary modes were found. We attribute the initial structural instability to the BPDC ligand; following optimisation we observed a rotation about the central C–C bond

Table 2 MOFs modelled with the VMOF forcefield in this work. Given are the metal cations with the corresponding formal oxidation state and the ligands comprising the MOFs, along with the reported space group number and name

Name	Metal	Ligand	Space group
MOF-5 (IRMOF-1)	Zn^{2+}	1,4-Benzene dicarboxylate	225 ($Fm\bar{3}m$)
IRMOF-10	Zn^{2+}	4,4′-Biphenyl dicarboxylate	225 ($Fm\bar{3}m$)
MOF-650	Zn^{2+}	2,6-Azulene dicarboxylate	225 ($Fm\bar{3}m$)
UiO-66	Zr^{4+}	1,4-Benzene dicarboxylate	225 ($Fm\bar{3}m$)
UiO-67	Zr^{4+}	4,4′-Biphenyl dicarboxylate	225 ($Fm\bar{3}m$)
MIL-125	Ti^{4+}	1,4-Benzene dicarboxylate	139 ($I4/mmm$)
MOF-74	Zn^{2+}	2,5-Dihydroxyterephthalic acid	2 ($P\bar{1}$)
NOTT-300	Al^{3+}	3,3′,5,5′-Biphenyltetracarboxylic acid	98 ($I4_122$)

Table 3 Comparison of unit cell parameters (*a*, *b*, *c* with all values in Å) from the VMOF forcefield with those calculated using DFT (PBEsol functional); percentage errors of FF values compared to DFT are given in brackets

Name	DFT unit cell parameters	VMOF unit cell parameters
MOF-5 (IRMOF-1)(Zn^{2+})	25.894, 25.894, 25.894	25.935 (0.16), 25.935 (0.16), 25.935 (0.16)
IRMOF-10 (Zn^{2+})	34.385, 34.385, 34.385	34.417 (0.09), 34.417 (0.09), 34.417 (0.09)
MOF-650 (Zn^{2+})	30.695, 30.695, 30.695	30.766 (0.23), 30.766 (0.23), 30.766 (0.23)
MOF-74 (Zn^{2+})	6.740, 15.142, 15.142	6.764 (0.35), 15.031 (0.73), 15.031 (0.73)
UiO-66 (Zr^{4+})	20.798, 20.798, 20.798	20.909 (0.53), 20.909 (0.53), 20.909 (0.53)
UiO-67 (Zr^{4+})	27.094, 27.094, 27.094	26.878 (0.80), 26.878 (0.80), 26.878 (0.80)
MIL-125 (Ti^{4+})	18.852, 18.843, 17.921	18.859 (0.01), 18.859 (0.08), 18.043 (0.68)
NOTT-300 (Al^{3+})	14.836, 14.836, 11.871	14.862 (0.18), 14.862 (0.18), 11.500 (3.23)

Table 4 Comparison of bulk moduli (GPa) obtained with the VMOF forcefield with those calculated with DFT. DFT bulk moduli were calculated with the PBEsol functional with D3 dispersion correction, by fitting calculated energy/volume curves to a Birch–Murnaghan equation of state with ±3% sampling away from the equilibrium volume

Name (metal)	DFT (GPa)	VMOF (GPa)
MOF-5/IRMOF-1 (Zn^{2+})	16.9	8.8
IRMOF-10 (Zn^{2+})	8.6	5.1
MOF-650 (Zn^{2+})	12.5	6.8
UiO-66 (Zr^{4+})	40.4	19.0
UiO-67 (Zr^{4+})	21.9	11.7
MIL-125 (Ti^{4+})	25.1	18.5
MOF-74 (Zn^{2+})	28.1	14.9
NOTT-300 (Al^{3+})	47.8	25.2

connecting the two aromatic rings. The final torsion across this bond was 30–31° between rings (Fig. 2). We propose that the planar experimental configuration may be a thermally averaged structure, and that the true ground-state actually involves twisted ligands. For IRMOF-10 we calculate the structure with twisted ligands to be 0.275 eV (0.046 eV per ligand) more stable than the planar structure. UiO-67 is formed of the same BPDC ligands, which are experimentally characterised as twisted with near identical angles to those in IRMOF-10 between torsion planes. Electronic structure calculations were recently reported by Hemelsoet *et al.*, highlighting the flexibility of the BPDC ligand in UiO-67. This study reported the difference in relative occurrence

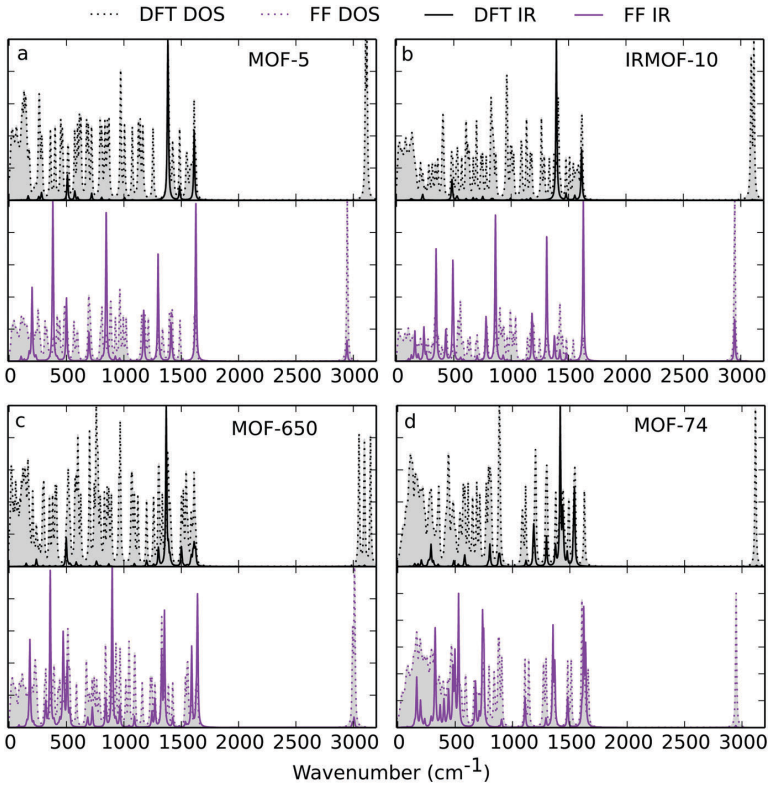

Fig. 3 Overlaid IR spectra and phonon density of states (DOS) calculated with DFT (top, black) and FF (bottom, purple) methods, plotted between 0–3200 cm^{-1} for MOF-5 (a), IRMOF-10 (b), MOF-650 (c) and MOF-74 (d). All spectra are normalised to lie between 0 and 1 and area the under DOS is shaded (grey) for clarity.

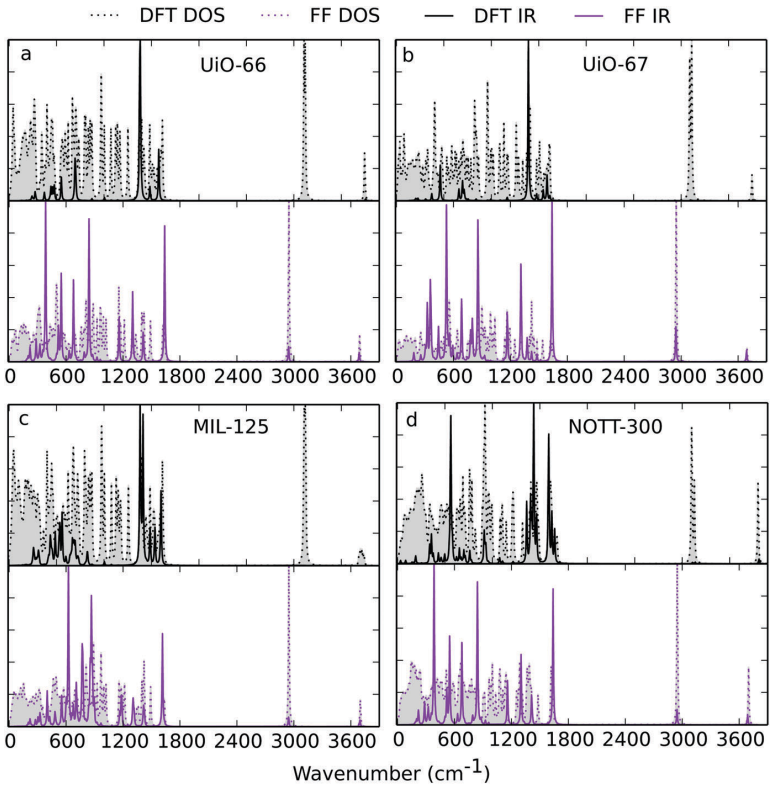

Fig. 4 Overlaid IR spectra and phonon density of states (DOS) calculated with DFT (top, black) and FF (bottom, purple) methods, plotted between 0–3900 cm^{-1} for UiO-66 (a), UiO-67 (b), MIL-125 (c) and NOTT-300 (d). All spectra are normalised to lie between 0 and 1 and area under the DOS is shaded (grey) for clarity.

in torsion angles between the aromatic rings between 0–90° during a molecular dynamics simulation. As IRMOF-10 is formed of weaker intermolecular interactions, an increased flexibility of torsion angles would be expected.[41] Furthermore, we calculate the $BPDC^{2-}$ ligand in the gas phase to possess a torsion angle of approximately 33° in its ground-state configuration (further details in the ESI†).

Similar structural instabilities were observed for MIL-125, which is reported as belonging to the tetragonal space group number 139. Initially we obtained 17 associated imaginary modes, and re-optimised to produce a structure with two imaginary modes. This structure was found to have a broken symmetry with the hydrogen on the hydroxyl groups flipped into the pore of the MOF rather than being held in the pore windows. The remaining two imaginary modes could not be removed with further optimisation, and the calculations became too expensive to continue. However, the lower symmetry structure was 0.407 eV per primitive unit cell more stable, with no external pressure on the cell.

The selected MOFs studied here were chosen to ensure a variety of different topologies and bonding interactions were present, thus testing the broad applicability of the forcefield. The metal cations and ligands comprising these MOFs are given, along with the experimentally determined space groups, in Table 2.

A comparison of optimised unit cell parameters between DFT and forcefield methods are given in Table 3. All structures are reproduced by the forcefield with low errors on the unit cell parameters, thus demonstrating the accuracy of the forcefield and its ability to reproduce different structural features of MOFs, despite the simplicity of its derivation.

3.3 Mechanical properties

Bulk moduli have been calculated with DFT and VMOF to compare the mechanical strength of the materials predicted with the two approaches (Table 4).

The forcefield predicts smaller bulk moduli than DFT. The discrepancy in bulk moduli between DFT and forcefield is likely to be due to an inaccurate description of the long-range dispersion interactions. The converged unit cell volumes calculated with DFT are generally smaller than those predicted with the forcefield, leading to larger bulk moduli. We do, however, highlight that experiment often finds MOFs to have a softer bulk modulus than those predicted with electronic structure methods. Yot *et al.* reported experimental bulk moduli, as measured using high pressure XRD methods, for UiO-66 and

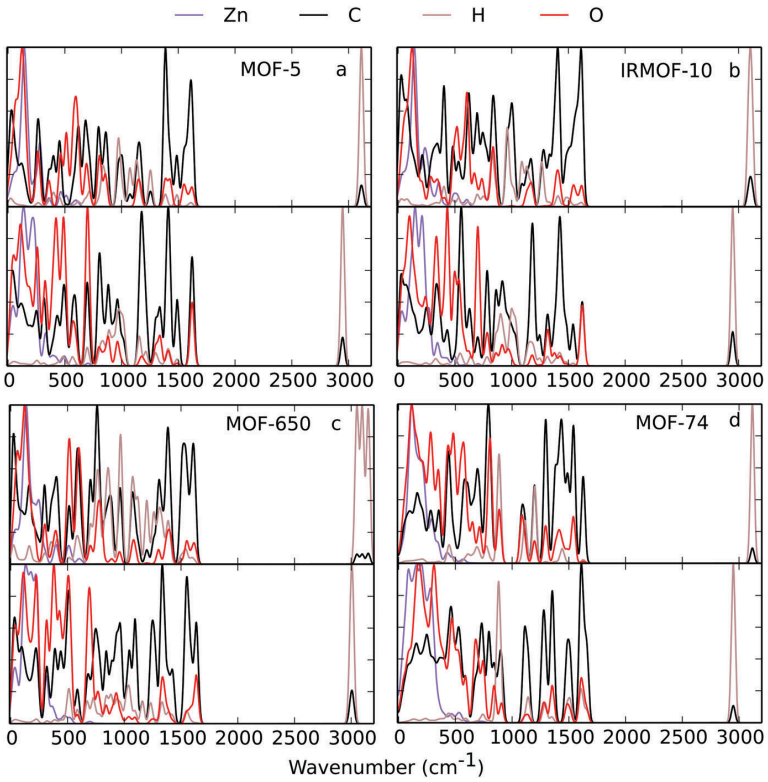

Fig. 5 Partial phonon density of states (PDOS) projected according to the elemental contribution calculated with DFT (top) and FF (bottom) methods, plotted between 0–3200 cm^{-1} for MOF-5 (a), IRMOF-10 (b), MOF-650 (c) and MOF-74 (d). All spectra are normalised to lie between 0 and 1.

MIL-125 to be 17.0 and 10.0 GPa, respectively, which are closer to the forcefield values than those calculated by DFT.[42] The trend in mechanical strength for each framework is the same between the two methods, with increasing mechanical strength from IRMOF-10 < MOF-74 < MOF-650 < MOF-5 < UiO-67 < MIL-125 < UiO-66 < NOTT-300.

Higher charged cations form primarily ionic interactions between metal and ligand. It can therefore be rationalised that UiO-66, UiO-67 and MIL-125 would possess stiffer bulk moduli (greater resistance to compression) than the Zn-isoreticular MOFs, which possess large internal voids and weaker van der Waals interactions between Zn^{2+} and organic ligands.

3.4 Phonon properties

3.4.1 IR spectra. The first approach to assessing the ability of a forcefield to reproduce accurate vibrational properties is to calculate the phonon density of states and the associated IR spectra (weighted by the mode intensities) to ensure the fingerprint of vibrational modes is similar between DFT and forcefield methods. Good agreement is observed between vibrational IR spectra and DOS between DFT (Fig. 3) and the forcefield (Fig. 4). The plots highlight the stability of the modelled MOFs with both methods, but also the small deviation between the two sets of calculated DOS and IR spectra. The biggest discrepancy between VMOF and DFT IR spectra is in the fingerprint (lower frequency region). This is due to the metal–oxygen bond stretching modes, and since IR activity $\propto$ charge $\times$ displacement, the discrepancy is primarily due to the use of formal charges for the metal ions. Importantly, we highlight that the DOS spectra between DFT and forcefield remain comparable, which suggests the use of a formal charge model has had little effect on the forces.

The decomposition of the DOS into elemental contributions is shown in the partial DOS plots (Fig. 5 and 6). Several features are evident in both spectra calculated with DFT and FF methods that are chemically well established. Firstly, the range of modes involving the metal cations all occur at low frequencies ($<$500 cm^{-1}). Also observed in this region for all MOFs is a small contribution from C, H and O from the rocking motions of the ligands. At finite temperature it is these low frequency modes that are populated, and therefore control the MOF dynamics (*e.g.* the shape of the thermal ellipsoid). Therefore, the motions of the MOF will occur primarily at the metal nodes, as well as subtle rotations at the MOF-ligand connections. In the mid-frequency range, between 1300–1500 cm^{-1}, the high contribution of C and O to the density of states is due to motions of the asymmetric and symmetric C_{carb}–O_{carb} stretches of the carboxylate groups in the MOFs. Finally, modes above

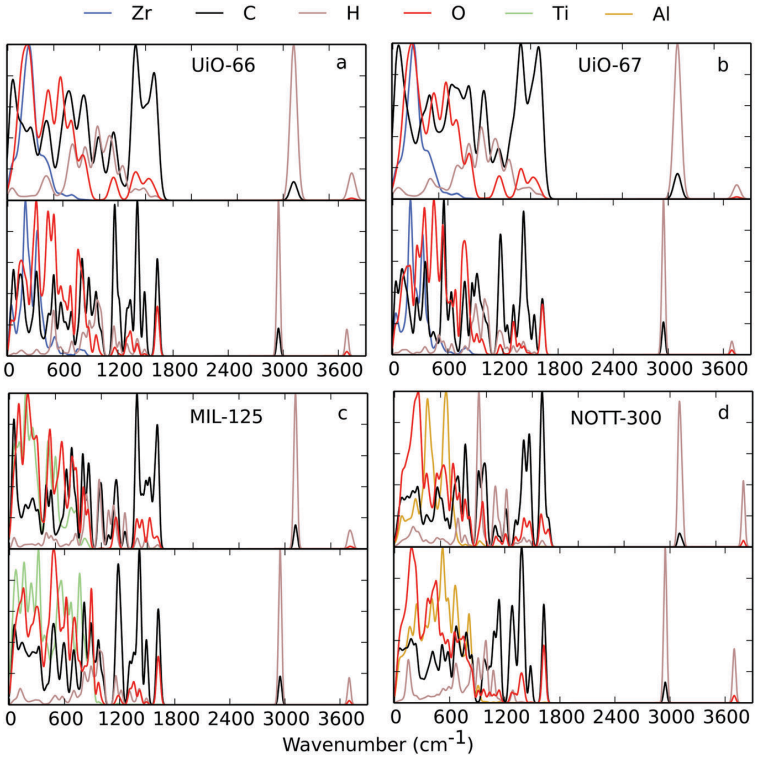

Fig. 6 Partial phonon density of states (PDOS) decomposed according to the elemental contribution calculated with DFT (top) and FF (bottom) methods, plotted between 0–3900 cm^{-1} for UiO-66 (a), UiO-67 (b), MIL-125 (c) and NOTT-300 (d). All spectra are normalised to lie between 0 and 1.

3000 cm^{-1} are associated with C–H and O–H stretches at the ligand and within some metal nodes, respectively. The important conclusion from the density of states plots is that we see good agreement between DFT and forcefield methods, suggesting the vibrational properties of the MOFs are well reproduced by VMOF.

It is common to characterise the vibrational properties of a material by assigning specific IR frequencies. However, we demonstrate that a vast amount of vibrational information is not accounted for by doing this for MOFs. The comparison of DOS and IR spectra show the difference in detail and highlight the importance of considering vibrational modes that are not IR active when parameterising a forcefield. The DOS also shows the significant number of soft vibrational modes that MOFs possess, which give rise to structural instability with temperature and pressure. We note a shift of the frequencies of the C–H stretch between the two methods. As the C–H stretch occurs as one of the highest frequency modes, it is contributing the most to the zero-point vibrational energy and is likely to be the biggest contribution to the C–H stretch calculated error between methods. The reliability of the forcefield is not likely to be affected by the disagreement in zero point energy between the methods for the study of complex processes such as phase changes. It is unclear if it is DFT or the FF model that contains the greatest error on the C–H stretch. The forcefield parameters for the C–H interaction remain unchanged from the CHARMM forcefield and therefore have not been derived specifically for BDC incorporated into a MOF. On the other hand, a scaling factor is often used on the vibrational frequencies in DFT calculations that would have the greatest effect on the stretching mode of the C–H bond. Such scaling factors can correct for anharmonicity, while forcefield parameters can be derived explicitly to reproduce experimental anharmonic frequencies.

3.4.2 Helmholtz free energy. Reproducing accurate relative free energies of a system with temperature is crucial for the prediction of thermodynamic processes such as phase changes and reaction energies for the formation of defects within frameworks, for example in our previous work investigating the ''missing linker phenomenon'' in UiO-66.[43]

The constant volume (Helmholtz) free energy, vibrational entropy and constant-volume heat capacities as a function of temperature are plotted for all MOFs considered with both first principles and forcefield methods (Fig. 7). The forcefield is shown to reproduce the calculated thermodynamic properties from DFT very well. Little deviation across all structures is observed, further supporting that the forcefield can accurately reproduce the vibrational properties of the subset of MOFs studied.

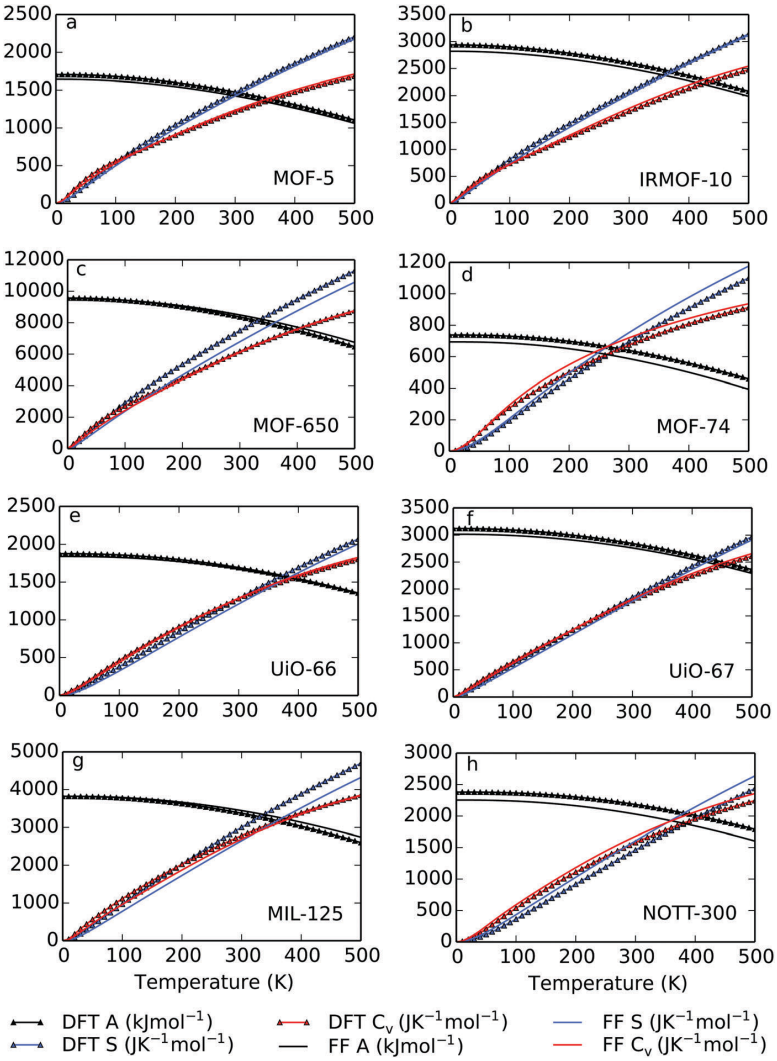

Fig. 7 Comparison of calculated Helmholtz free energy (black), vibrational entropy (blue) and constant volume heat capacity (C_v) (red) of (a) MOF-5, (b) IRMOF-10, (c) MOF-650, (d) MOF-74, (e) UiO-66, (f) UiO-67, (g) MIL-125 and (h) NOTT-300 between DFT (symbol) and FF (line) methods.

3.4.3 Quasi-harmonic approximation properties. Fitting forcefield models to ground state properties of the equilibrium structure does not account for the variation in volume and unit cell shape with temperature. As a method for extending the harmonic model of vibrations, the quasi-harmonic approximation (QHA) allows anharmonicity associated with volume change (thermal expansion) to be considered when calculating structural and thermodynamic properties.

Whilst conducting tests for the quasi-harmonic approximation we noted a particular sensitivity of the fitted forcefield parameters to the free energy equation of state with framework compressions. Consequently, calculated properties varied depending on the volume sampled for the expansions and contractions away from the local minimum structure. For MOF-5 the initial volume sampled was $\pm 3\%$ away from the energy minimum in 0.05% steps. We observed, with both DFT and forcefield methods, that beyond approximately 2% compression multiple imaginary vibrational modes emerged. When following these imaginary modes, a subtle twist at the carboxylate head relative to the benzene ring (approximately 3–5°) was observed. The same observation was made for IRMOF-10, suggesting that with compression "softer" MOFs undergo this subtle rotation of the benzene rings leaving a non-planar torsion between the ring and carboxylate heads of the ligand. We note that we could remove imaginary modes for all structures during compression with the forcefield, but the same process with electronic structure methods became too expensive for IRMOF-10, which possessed 2 imaginary modes at the highest compression of 3%.

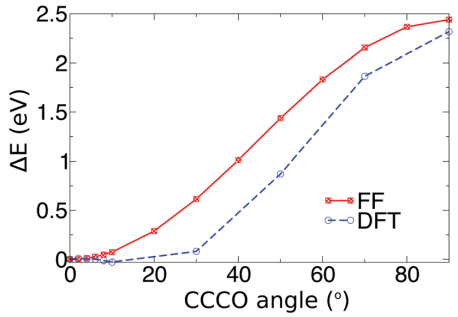

Fig. 8 Energy cost per ligand when rotating all C–C–C–O torsions in the ligands by successive angle increments away from the initial planar 0° structure. Relative energies are reported for both DFT and VMOF.

To investigate this phenomenon further we modelled the same rotation of BDC in MOF-5 away from the initial planar 0° structure. Calculations were conducted on the periodic systems with the VMOF forcefield. To model the same rotation with DFT, we cut a representative cluster with the chemical formula Zn_4O(BDC-H_2). The PBE0 functional was used in the NWChem program with the Dunning correlation consistent cc-pVTZ basis sets.[39,40,44] The rotation leaves the carboxylate heads in the same position in a direct bonding interaction with the metal centres, and only moves the benzene ring; following the rotation, there is a non-planar torsion between ring and carboxylate head (see ESI†). Rotating the ligand in this manner in MOF-5 is shown to cost little energy with both DFT and VMOF up to 10° (Fig. 8). The potential energy surface is shallow, with a 5° change being comparable to k_BT. Therefore it can be expected that the group will be rotationally active at room temperature. We highlight the similarity in the calculated trend between DFT and VMOF for the modelled rotation, supporting our observations of the instability of the planar structure with compression with DFT.

Once the physical significance of structural distortion with compression was investigated, we were able to rationalise trends observed from quasi-harmonic calculations. Due to the expense of the quasi-harmonic approximation calculations with first principles, we report only forcefield thermodynamic properties for UiO-67, MIL-125, MOF-650 and MOF-74 (Fig. 10).

There is a limited amount of data in the literature for experimental verification of the predicted thermal expansion profiles. Our calculated thermal expansion profile for MOF-5 however resembles the profile measured by Zhou *et al.*, where an increasing thermal expansion coefficient is observed above 100 K. At 300 K, Zhou *et al.* measure the thermal expansion coefficient of MOF-5 to be approximately 15×10^{-6} K^{-1}, the corresponding thermal expansion coefficient calculated with VMOF and DFT are 23×10^{-6} and 36×10^{-6} K^{-1}, respectively.[45]

The use of the quasi-harmonic approximation allows the calculation of a more extensive range of properties, such as the Grüneisen parameter, bulk modulus, heat capacity and thermal expansion coefficient, as a function of temperature. For all structures we found that the QHA properties that showed the greatest sensitivity were the bulk modulus and thermal expansion. These properties are derived directly and indirectly from the curvature of the potential energy surface, respectively, and therefore exaggerate the difference between the methods. We highlight that VMOF, which was not specifically parameterised to reproduce negative thermal expansion of MOFs, manages to exhibit this

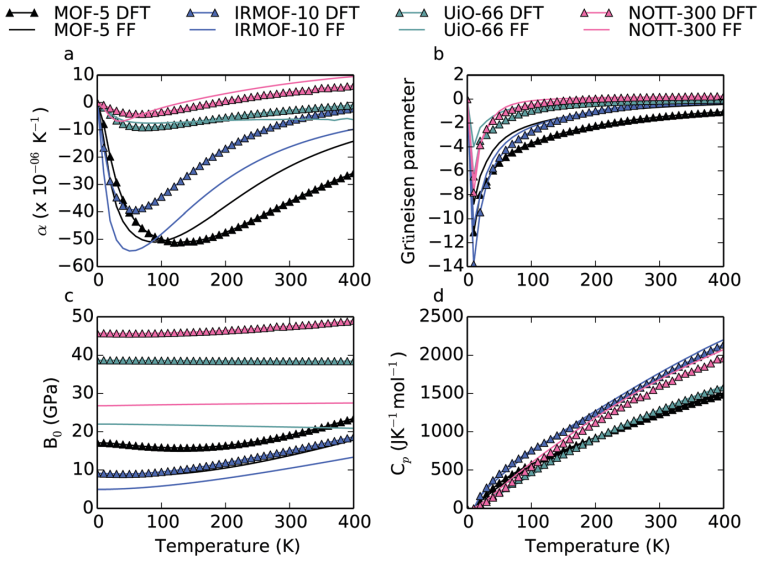

Fig. 9 Comparison of structural and thermodynamic properties as a function of temperature calculated with the quasi harmonic-approximation for MOF-5, IRMOF-10, UiO-66 and NOTT-300 using DFT and the VMOF forcefield (FF). (a) Linear thermal expansion coefficient (b) Grüneisen parameter (c) bulk modulus (d) heat capacity at constant pressure.

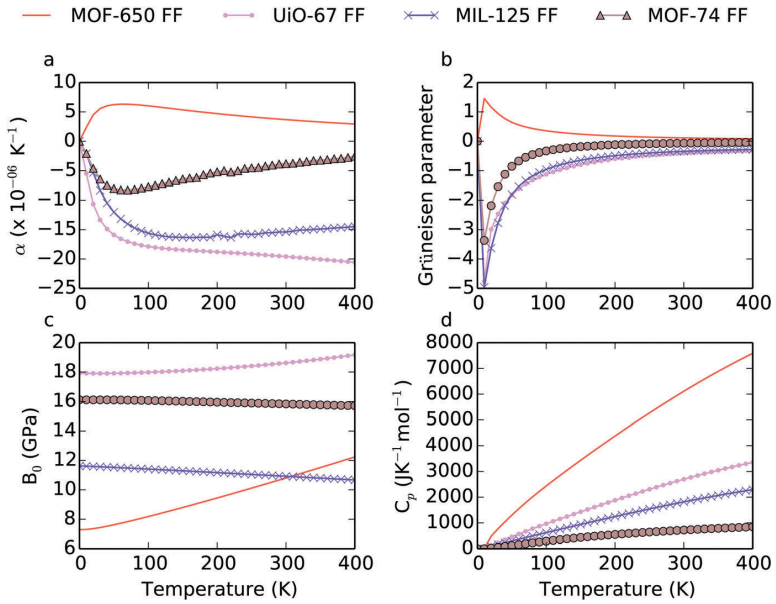

Fig. 10 Structural and thermodynamic properties as a function of temperature calculated with the quasi-harmonic approximation for MOF-650, MOF-74, MIL-125 and UiO-67 using the VMOF forcefield (FF). (a) Linear thermal expansion coefficient (b) Grüneisen parameter (c) bulk modulus (d) heat capacity at constant pressure.

phenomenon and accurately in comparison to DFT for MOF-5, IRMOF-10, UiO-66 and NOTT-300. Due to the expense of the quasi-harmonic approximation calculations with first principles, we report only forcefield thermodynamic properties for UiO-67, MIL-125, MOF-650 and MOF-74 (Fig. 10).

Whilst fitting an equation of state for IRMOF-10, we observed a sensitivity of the calculated properties with DFT to the extent of compression considered. Properties such as the bulk modulus, Grüneisen parameter and thermal expansion were calculated to vary significantly when including high-pressure points (*i.e.* large compressions). We also observed a significant shift in minimum of Helmholtz energy with change in volume at the defined temperatures. Such a shift and variation in calculated properties suggests the zero point energy contribution to have a large effect on the structure.

Several interesting features more specific to each structure are observed from the QHA calculations (Fig. 9 and 10). Firstly, a comparison of thermal expansion coefficients show the vast difference in structural changes with temperature. The "softer" Zn-isoreticular MOFs, such as MOF-5 and IRMOF-10 with both DFT and FF methods, are calculated to possess the largest negative thermal expansion coefficients at low temperature, suggesting the extent of thermal expansion reflects the mechanical strength of the materials. Indeed, the "hardest" MOFs, UiO-66 and NOTT-300, show little variation in thermodynamic properties with temperature. The temperature dependent bulk moduli are shown to differ between DFT and forcefield methods (Fig. 9), following the calculated trend in static bulk moduli. Specifically, VMOF yields softer mechanical properties at finite temperatures than electronic structure methods. We note that the trend and shape of each profile with temperature is reproduced by the forcefield, and that the temperature dependent Grüneisen parameter and heat capacity at constant pressure are reproduced accurately and appear unaffected by the discrepancy in bulk moduli. Due to the accuracy of the quasi-harmonic approximation being restricted to 1/2–2/3 the melting point temperature (depending on the material), we cannot model the full behaviour of the heat capacity at high temperatures. The temperature dependence of the thermodynamic properties of MOF-650 appears to show a significantly different trend to all other structures, which all show similar behaviour. MOF-650 has a large internal void with cell parameters exceeding 30 Å. The azulene ligand comprising MOF-650 is also rigid and would allow little structural flexibility when compared to IRMOF-10, which is of similar size. It is likely to be these two factors that result in positive thermal expansion and Grüneisen parameter at low temperature. Finally, the Grüneisen parameter shows a similar trend for each structure, excluding MOF-650. The increase in Grüneisen parameter with temperature reflects the increase in mechanical strength following contraction of the cell parameters.

4 Conclusions

A new transferable forcefield for metal–organic frameworks named VMOF has been parameterised to reproduce accurate lattice dynamics and phonon properties. Such a forcefield

contributes greatly to the current extensive field of MOF forcefields as it is unique in the number of thermodynamic properties that can be accurately determined in a rapid and transferable manner. For an initial training set of MOFs including MOF-5, IRMOF-10, UiO-66, UiO-67, NOTT-300, MIL-125, MOF-650 and MOF-74 we calculate numerous thermodynamic properties including bulk modulus, free energies and constant volume heat capacities. We further conduct quasi-harmonic calculations and find excellent agreement in thermal expansion, bulk moduli, Grüneisen parameter and heat capacity with temperature between DFT and the newly parameterised forcefield. This now opens the way for the future high-throughput computational screening of materials vibrational properties for a wide range of MOFs.

Data access statement

The VMOF forcefield is available as a library file for GULP from https://github.com/WMD-group/VMOF. A set of raw phonon data and program input/output files are available from https://researchdata.ands.org.au.

Acknowledgements

J. K. B. is funded by the EPSRC (Grant no. EP/G03768X/1). J. D. G. thanks the Australian Research Council for funding under the Discovery Programme, as well as the Pawsey Supercomputing Centre and NCI for the provision of computing resources. A. W. acknowledges support from the Royal Society University Research Fellowship scheme. K. L. S. is funded under ERC Starting Grant 277757 and J. M. S. is funded under EPSRC Grant no. EP/K004956/1. The work benefited from the high performance computing facility, Balena, at the University of Bath, and access to the ARCHER supercomputer through membership of the HPC Materials Chemistry Consortium (EP/L000202).

References

1 B. R. Brooks, C. L. Brooks, A. D. MacKerell, L. Nilsson, R. J. Petrella, B. Roux, Y. Won, G. Archontis, C. Bartels and S. Boresch, *J. Comput. Chem.*, 2009, **30**, 1545–1614.
2 B. R. Brooks, R. E. Bruccoleri, B. D. Olafson, D. J. States, S. Swaminathan and M. Karplus, *J. Comput. Chem.*, 1983, **4**, 187–217.
3 N. L. Allinger, Y. H. Yuh and J. H. Lii, *J. Am. Chem. Soc.*, 1989, **111**, 8551–8566.
4 N. L. Allinger, F. Li and L. Yan, *J. Comput. Chem.*, 1990, **11**, 848–867.
5 J. Wang, R. M. Wolf, J. W. Caldwell, P. A. Kollman and D. A. Case, *J. Comput. Chem.*, 2004, **25**, 1157–1174.
6 A. K. Rappé, C. J. Casewit, K. Colwell, W. Goddard Iii and W. Skiff, *J. Am. Chem. Soc.*, 1992, **114**, 10024–10035.
7 M. A. Addicoat, N. Vankova, F. I. Akter and T. Heine, *J. Chem. Theory Comput.*, 2014, **10**, 880–891.
8 J. Borycz, D. Tiana, E. Haldoupis, J. C. Sung, J. I. Siepmann, O. K. Farha and L. Gagliardi, *J. Phys. Chem. C*, 2016, **120**, 12819–12830.
9 S. Bureekaew, S. Amirjalayer, M. Tafipolsky, C. Spickermann, T. K. Roy and R. Schmid, *Phys. Status Solidi B*, 2013, **250**, 1128–1141.
10 L. Vanduyfhuys, S. Vandenbrande, T. Verstraelen, R. Schmid, M. Waroquier and V. Van Speybroeck, *J. Comput. Chem.*, 2015, **36**, 1015–1027.
11 J. K. Bristow, D. Tiana and A. Walsh, *J. Chem. Theory Comput.*, 2014, **10**, 4644–4652.
12 C. E. Wilmer, M. Leaf, C. Y. Lee, O. K. Farha, B. G. Hauser, J. T. Hupp and R. Q. Snurr, *Nat. Chem.*, 2012, **4**, 83–89.
13 A. O. Yazaydin, R. Q. Snurr, T.-H. Park, K. Koh, J. Liu, M. D. LeVan, A. I. Benin, P. Jakubczak, M. Lanuza and D. B. Galloway, *J. Am. Chem. Soc.*, 2009, **131**, 18198–18199.
14 M. Haranczyk and R. Martin, *J. Phys.: Conf. Ser.*, 2015, 012103.
15 M. V. Parkes, C. L. Staiger, J. J. Perry IV, M. D. Allendorf and J. A. Greathouse, *Phys. Chem. Chem. Phys.*, 2013, **15**, 9093–9106.
16 B. Huang, A. McGaughey and M. Kaviany, *Int. J. Heat Mass Transfer*, 2007, **50**, 393–404.
17 B. Huang, Z. Ni, A. Millward, A. McGaughey, C. Uher, M. Kaviany and O. Yaghi, *Int. J. Heat Mass Transfer*, 2007, **50**, 405–411.
18 H. Babaei and C. E. Wilmer, *Phys. Rev. Lett.*, 2016, **116**, 025902.
19 M. Arnold, P. Kortunov, D. J. Jones, Y. Nedellec, J. Kärger and J. Caro, *Eur. J. Inorg. Chem.*, 2007, 60–64.
20 F. Jeremias, V. Lozan, S. K. Henninger and C. Janiak, *Dalton Trans.*, 2013, **42**, 15967–15973.
21 G. Kresse and J. Furthmüller, *Phys. Rev. B: Condens. Matter Mater. Phys.*, 1996, **54**, 169.
22 J. P. Perdew, A. Ruzsinszky, G. I. Csonka, O. A. Vydrov, G. E. Scuseria, L. A. Constantin, X. Zhou and K. Burke, *Phys. Rev. Lett.*, 2008, **100**, 136406.
23 P. E. Blöchl, *Phys. Rev. B: Condens. Matter Mater. Phys.*, 1994, **50**, 17953.
24 S. Grimme, J. Antony, S. Ehrlich and H. Krieg, *J. Chem. Phys.*, 2010, **132**, 154104.
25 J. D. Gale, *J. Chem. Soc., Faraday Trans.*, 1997, **93**, 629–637.
26 J. D. Gale and A. L. Rohl, *Mol. Simul.*, 2003, **29**, 291–341.
27 J. Gasteiger and M. Marsili, *Tetrahedron*, 1980, **36**, 3219–3228.
28 J. Gasteiger and M. Marsili, *Tetrahedron Lett.*, 1978, **19**, 3181–3184.
29 A. Togo and I. Tanaka, *Scr. Mater.*, 2015, **108**, 1–5.
30 A. Togo, L. Chaput, I. Tanaka and G. Hug, *Phys. Rev. B: Condens. Matter Mater. Phys.*, 2010, **81**, 174301.
31 F. I. Mopsik, *J. Res. Natl. Inst. Stan. A-Phys. Chem.*, 1973, 407–409.
32 N. Allan, T. Barron and J. Bruno, *J. Chem. Phys.*, 1996, **105**, 8300–8303.
33 J. D. Gale, *J. Phys. Chem. B*, 1998, **102**, 5423–5431.
34 R. Ahuja, L. Fast, O. Eriksson, J. Wills and B. Johansson, *J. Appl. Phys.*, 1998, **83**, 8065–8067.

35 G. Fadda, L. Colombo and G. Zanzotto, *Phys. Rev. B: Condens. Matter Mater. Phys.*, 2009, **79**, 214102.
36 Z. Jian-Zhi, W. Guang-Tao and L. Yong-Cheng, *Chin. Phys. Lett.*, 2008, **25**, 4356.
37 J. Gladden, J. H. So, J. Maynard, P. Saxe and Y. Le Page, *Appl. Phys. Lett.*, 2004, **85**, 392–394.
38 C. Adamo and V. Barone, *J. Chem. Phys.*, 1999, **110**, 6158–6170.
39 M. Valiev, E. J. Bylaska, N. Govind, K. Kowalski, T. P. Straatsma, H. J. Van Dam, D. Wang, J. Nieplocha, E. Apra and T. L. Windus, *Comput. Phys. Commun.*, 2010, **181**, 1477–1489.
40 T. H. Dunning Jr, *J. Chem. Phys.*, 1989, **90**, 1007–1023.
41 A. Van Yperen-De Deyne, K. Hendrickx, L. Vanduyfhuys, G. Sastre, P. Van Der Voort, V. Van Speybroeck and K. Hemelsoet, *Theor. Chem. Acc.*, 2016, **135**, 1–14.
42 P. G. Yot, K. Yang, F. Ragon, V. Dmitriev, T. Devic, P. Horcajada, C. Serre and G. Maurin, *Dalton Trans.*, 2016, **45**, 4283–4288.
43 J. K. Bristow, K. L. Svane, D. Tiana, J. M. Skelton, J. D. Gale and A. Walsh, *J. Phys. Chem. C*, 2016, **120**, 9276–9281.
44 D. E. Woon and T. H. Dunning Jr, *J. Chem. Phys.*, 1993, **98**, 1358–1371.
45 W. Zhou, H. Wu, T. Yildirim, J. R. Simpson and A. H. Walker, *Phys. Rev. B: Condens. Matter Mater. Phys.*, 2008, **78**, 054114.

Chapter 4

Defects in MOFs

4.1 Paper 3 - Free energy of ligand vacancy formation in the metal–organic framework UiO-66

In the following paper the defect formation free energies of the missing ligand phenomenon, as depicted in Figure 4-1, in a Zr MOF: UiO-66 are calculated. Following the removal of a BDC ligand, charge compensation must occur to leave a neutral and stable framework. We consider the available anions for charge compensation that would be present in different experimental studies, where an acid modulator is commonly used to increase the concentration of the defect in the system: Cl^-, OH^- and CH_3COO^-. Defect free energies consider a full thermodynamic cycle including solvation free energies of the ligand and charge compensation molecules using a continuum model. Furthermore, the defect free energies are calculated as a function of concentration. In the most extreme cases, 6 missing ligands per unit cell was considered, which corresponds to a defect concentration of 25%. Finally, materials properties with an increasing concentration of missing ligand defects were calculated. The data presented in this paper could be used to characterise the likely concentration of missing linker defects in experiments by comparing measured properties with those calculated and reported in the following paper.

4.1.1 Additional ESI

Forcefield parameters

The forcefield used to model UiO-66 and its defective structures is an initial version of the VMOF forcefield that was presented in paper 2 entitled "A general forcefield for accurate phonon properties of metal-organic frameworks", but the non-bonding interactions in the framework differ considerably from VMOF. The differences between the forcefields will now be highlighted.

The Buckingham[173] non-bonding function (Equation 2.29) was used to describe the attractive and repulsive components, as opposed to the MM3 Buckingham function in VMOF, between metal and

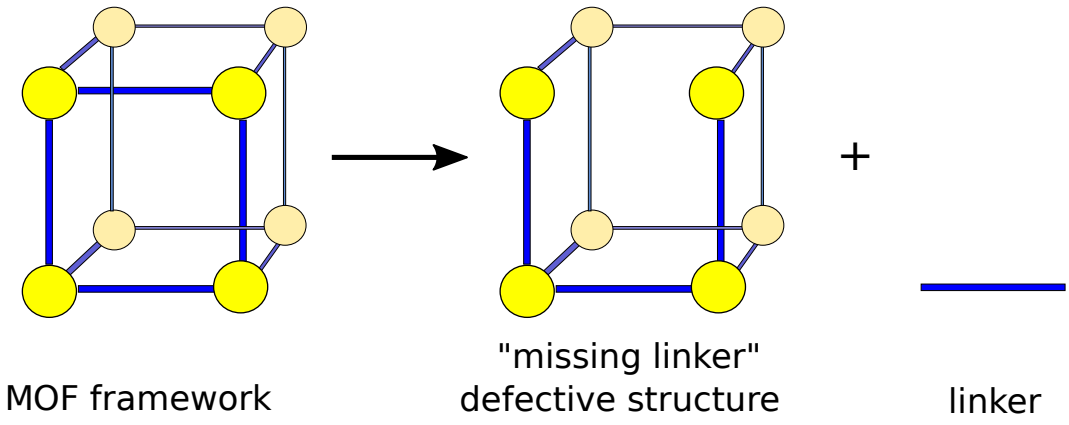

Figure 4-1: Schematic of the formation of the missing linker defects in MOFs.

ligand and within the metal node. Each parameter of the Buckingham function was derived to reproduce structural properties of UiO-66 and the charge capping terminations. Additional non-bonding interactions were needed between some charge capping terminations to prevent unphysical binding when in close proximity. The small repulsive interactions that were added were derived to reproduce first-principles structural data. All new bonding parameters for the charge capping anions were taken from the CHARMM library. All charges were derived with the Gasteiger approach[246], which has also already been described.

The TIP3P model was used for internal forcefield parameters of water (as a neutral capping molecule), with additional non-bonding Buckingham terms to describe the coordination to Zr metal centers. Water models in both classical and electronic structure methods are notoriously difficult to derive, and many models have been parameterised to reproduce different thermodynamic properties or phases of water. TIP3P is a three-point model with partial charges assigned to each atom in the molecule, and was derived to reproduce bulk water at 298 K and 1 atm with a density of 0.997 g/ml. Properties of water that were reproduced when deriving the TIP3P model were the heat of vapourisation of 109.53 kcal/mol and the oxygen-oxygen radial distribution in bulk water from light scattering experiments. A modification was made to the non-bonding Lennard-Jones parameters original[250] TIP3P model in 1996, it is the modified[251] TIP3P model that is used in the following paper.

All other forcefield parameters used are the same as those used for the VMOF forcefield and have already been described. The forcefield itself is specifically derived to reproduce the structural properties of UiO-66 and its defective structures, and is not transferable to other MOF structures.

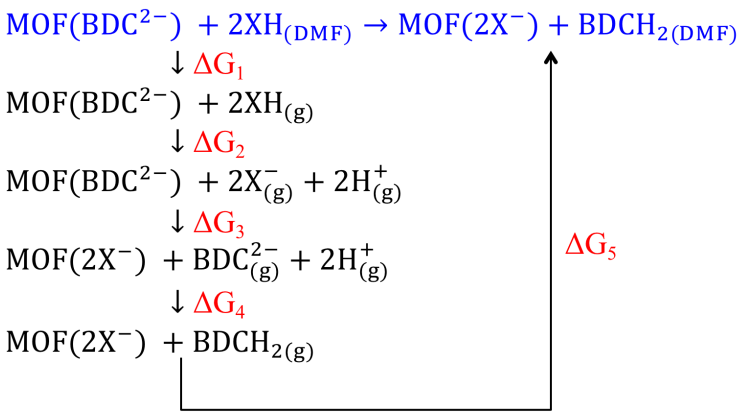

Figure 4-2: Thermodynamic cycle for the removal of 1 BDC ligand from UiO-66, where X is the anion used for charge compensation.

Defect formation energies

The thermodynamic cycle for calculating defect free energies of each ligand removal as considered in the following paper is given in Figure 4-2. The description of each Gibbs free energy value used to calculate the final defect energy of formation are provided in Table 4.1.

Table 4.1: Free-energy components considered to calculate the total defect energy of formation.

Process	Description	Method of calculation
ΔG_1	desolvation of XH	NWChem
ΔG_2	gas phase dissociation of XH	NIST database
ΔG_3	defect formation energy	GULP
	($\Delta G_3 = (G_{perfect} + E_{XH})$ - $(G_{defective} + E_{BDCH2})$)	
ΔG_4	gas phase double protonation of BDC	NIST database
ΔG_5	solvation free-energy of BDC in DMF	NWChem

Continuum models for implicit solvent modelling

To model the interaction of the defect molecules and ligands with DMF solvent, an implicit solvation model, also known as a continuum model, was used. Instead of explicitly modelling solvent molecules in solution, a continuum model replaces the chemical identity of a solvent by embedding the solute molecule in a dielectric continuum of permittivity, ε.[252] The cavity, which is created by the solute molecule in the continuum, has a solvent accessible surface (SAS) that could interact with solvent molecules. The response of a charged solute molecule in a dielectric continuum results in a polarisation of the dielectric medium. The conductor-like screening model (COSMO)[253] is used in the following paper to calculate solvation energies in the dimethylformamide (DMF) solvent. In COSMO the SAS

is constructed approximately by segments, and the polarisation of the continuum is calculated by a scaled-conductor approximation. The electric charge on each in the molecule (q) is calculated with a first-principles approach and therefore the charge on the surface segments, which are a function of the dielectric constant of the continuum (ε) can be calculated:

$$q = \frac{\varepsilon - 1}{\varepsilon + 0.5} \tag{4.1}$$

The dielectric constant can be measured experimentally or calculated with a first-principles approach for different solvents. In the following paper we use the experimentally measured temperature dependent dielectric constant of DMF. Solubility at the infinite dilution limit can then be calculated as the difference in free energy between the the molecule in gas phase and in the continuum model with a given solvent.[253]

The advantages of a continuum model is that solvent-solvent interactions are not considered, which considerably simplifies the solvent model, and that large-scale MD simulations of the movement of the solvent molecules are not needed to calculate free energies of solvation and free-energies.

4.1.2 Forcefield parameter files

The forcefield parameter files can be found as open-source resources at the following address:
https://researchdata.ands.org.au/free-energy-ligand-uio-66/654382

4.1.3 Personal contribution

My personal contribution to the paper entitled *"Free energy of ligand vacancy formation in the metal–organic framework UiO-66"* included the derivation of the forcefield model for UiO-66 and defective frameworks, included charge compensating anions following linker removal. I also used the COSMO continuum approach for calculating the solubility of reference state molecules in solvent and calculated defect free-energies. All structure optimisation on clusters and periodic systems with both DFT and forcefield was carried out by myself, including the calculation of material properties. K. Svane provided the symmetry unique structures of each defect concentration in the cubic unit cell of UiO-66.

4.1.4 Access statement

THE JOURNAL OF PHYSICAL CHEMISTRY C

Article

pubs.acs.org/JPCC

Free Energy of Ligand Removal in the Metal–Organic Framework UiO-66

Jessica K. Bristow,[†] Katrine L. Svane,[†] Davide Tiana,[†] Jonathan M. Skelton,[†] Julian D. Gale,[*,‡] and Aron Walsh[*,†,∥]

[†]Centre for Sustainable Chemical Technologies and Department of Chemistry, University of Bath, Claverton Down, Bath BA2 7AY, United Kingdom

[‡]Nanochemistry Research Institute/Curtin Institute for Computation, Department of Chemistry, Curtin University, P.O. Box U1987, Perth, Washington 6845, Australia

[∥]Global E[3] Institute and Department of Materials Science and Engineering, Yonsei University, Seoul 120-749, Korea

Supporting Information

ABSTRACT: We report an investigation of the "missing-linker phenomenon" in the Zr-based metal–organic framework UiO-66 using atomistic force field and quantum chemical methods. For a vacant benzene dicarboxylate ligand, the lowest energy charge-capping mechanism involves acetic acid or Cl^-/H_2O. The calculated defect free energy of formation is remarkably low, consistent with the high defect concentrations reported experimentally. A dynamic structural instability is identified for certain higher defect concentrations. In addition to the changes in material properties upon defect formation, we assess the formation of molecular aggregates, which provide an additional driving force for ligand loss. These results are expected to be of relevance to a wide range of metal–organic frameworks.

INTRODUCTION

Metal–organic frameworks (MOFs) are materials formed via the coordination of metal centers and organic linkers in three dimensions. The varied chemical compositions and structural topologies of MOFs make them suitable for a broad range of applications including gas storage and separation, solar energy conversion, and heterogeneous catalysis.[1−6]

One MOF that has attracted particular attention is UiO-66 (Figure 1), which was first synthesized by Cavka et al.[7] This material features a high coordination of 12 benzene-1,4-dicarboxylate (BDC) ligands around each Zr^{IV} node and is thermally stable up to 813 K.[8] The internal surface area (800 $m^2\ g^{-1}$) is large with the structure containing both tetrahedral and octahedral cages. Each octahedral cage is edge-sharing with eight tetrahedral cages and face-sharing with eight octahedral cages.[9] The inner-sphere coordination of Zr in UiO-66 is 6, but additional face-sharing oxide and hydroxide ligands lead to an outer-sphere coordination of 12.

Wu et al. and Vermoortele et al. reported a significant internal surface area increase for UiO-66 synthesized with an acidic modulator such as acetic or hydrochloric acid.[10,11] This phenomenon, leading to increased gas storage capabilities with little stability loss, has been attributed to a missing BDC linker from the unit-cell, with a subsequent reduction in coordination of the Zr metal.[9,12,13] The acid modulator has been shown to promote linker removal.[10] Recent reports have focused on the charge-capping mechanism following the removal of the linker. Experimental evidence, such as quantum tunnelling peaks in inelastic neutron scattering, associated with terminating methyl groups, suggest acetic acid becomes incorporated into the framework.[11] The incorporation of Cl^- ions when using HCl has also been suggested.[14] Considering that an excess of $ZrCl_4$ is often used during synthesis and that experimental conditions

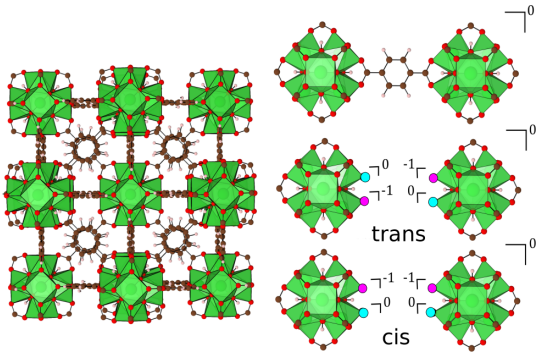

Figure 1. Crystal structure of UiO-66 (left) and locations on the metal node where charge compensating or neutral molecules can bind following BDC linker removal (right). The locations of charge compensating molecules are highlighted in maroon and neutral molecule locations are highlighted in black. Top right shows the BDC linker connection between Zr-metal nodes prior to removal. Centre and bottom right shows the locations considered for charge compensating molecules following linker removal.

Received: February 18, 2016
Revised: April 5, 2016
Published: April 12, 2016

DOI: 10.1021/acs.jpcc.6b01659
J. Phys. Chem. C 2016, 120, 9276−9281

do not completely exclude water, there is an abundance of potential charge-capping ions.

NU-1000[15] is a structurally similar Zr-containing MOF, which is often compared to UiO-66. The Zr node in NU-1000 has the formula $[Zr_6(\eta_3\text{-}O)_4(\eta_3\text{-}OH)_4(OH)_4(H_2O)_4]^{8+}$ and in UiO-66 has the formula $[Zr_6(\eta_3\text{-}O)_4(\eta_3\text{-}OH)_4]^{12+}$. The additional incorporation of four hydroxide and four water molecules in NU-1000 is due to the use of $ZrOCl_2$ as the Zr precursor source, as opposed to the $ZrCl_4$ precursor used to synthesize UiO-66.[15−17]

The fraction of BDC linkers missing from UiO-66 is highly debated. Reports vary from 1−4 vacancies per metal node depending on synthesis conditions; however, all measurements are indirect (e.g., thermogravimetric analysis) and usually yield an average over a large sample volume. Regardless of the method employed, it is clear that the defect concentrations are high and beyond those typically found in crystalline materials.

In this paper, we investigate the free energy of formation of missing ligand defects in UiO-66 using a combination of first-principles and molecular mechanics computational techniques. We consider a range of charge compensating schemes involving commonly used species. The results validate recent experimental observations of high defect concentrations and reveal a thermodynamic driving force for defect aggregation in the UiO-66 system.

METHODOLOGY

The predictive power of computational chemistry applied to metal−organic frameworks is well established.[18−23] Here, we combine empirical and first-principle methods. The analytical force field calculations allow us to probe large and complex defect structures including vibrations and hence calculate the Gibbs free energy of ligand removal. The higher-level density functional theory calculations provide a means of validation, while also giving an estimation of solvation and cluster energies for reaction products that are challenging to compute using empirical interatomic potentials.

Force-Field Calculations. We have considered the cubic unit cell of UiO-66, which contains 24 linkers and 4 metal nodes. Force-field calculations were performed with GULP.[24,25] Parametrisation of the interatomic potential was conducted to recreate the structural and material properties of nondefective UiO-66, including bond lengths, bond angles, phonon frequencies, bulk modulus, and elastic constants. The details of the force field and a comparison of the predicted structure of UiO-66 against experimental data is given in the Supporting Information (SI). The bulk and defective structures were first optimized with respect to the internal energy, and then the free energy of the final structure was calculated including the vibrational entropy. For all defect reactions considered, reactants and products were optimized at constant external pressure, thus providing the Gibbs free energy (ΔG) of reaction.

Density Functional Theory Calculations. Reference solid-state density functional theory (DFT) calculations on the pristine and defective structures of UiO-66 were performed using VASP.[26] These periodic DFT calculations were to provide high-quality fitting data for the force field and to validate the defect structures. The PBEsol functional[27] was used with a plane-wave cutoff of 600 eV and wave functions were calculated at the Γ-point of the Brillouin zone. Projector augmented wave potentials were used to model the interaction between valence and core of all atoms with $4d^25s^2$ as the valence configuration of Zr. Internal forces were converged to less than 0.005 eV/Å. The optimized unit-cell parameters from PBEsol/DFT (a = 20.80 Å and α = 90.0°) reproduce the experimental structure (a = 20.98 Å and α = 90.0°) of UiO-66 to within 1%. Comparisons of the crystal structures produced by DFT and force field methods are given in the SI.

Free energies of solvation for molecular fragments in DMF (dimethylformamide) were calculated with the continuum solvation model, COSMO, in NWChem[28] (cc-pVTZ basis set).[29,30] The self-consistent field energy convergence was set to 10^{-6} Ha and the M06-2X functional,[31,32] which is known to produce accurate thermodynamic properties, was used to obtain geometries. In the solvation model, we used the temperature-dependent experimental dielectric constant of DMF, as reported by Bass et al.[33] Other thermodynamic quantities, such as the energy of protonation of BDC, were taken from the NIST database.[34] Finally, molecular cluster binding energies were calculated with the B3LYP functional.[35] This approach gives a good description of hydrogen bonding interactions at low computational cost. The dielectric constant of DMF at 300 K was used. A single point counterpoise correction for the basis set superposition error (BSSE)[36] was calculated on the converged cluster geometries.

RESULTS

Charge-Capping Mechanism. For a balanced defect reaction, conservation of charge and mass is required. Acetic acid (CH_3COOH) and/or HCl are commonly used as acidic modulators to promote linker removal from the structure. In addition, the commonly used solvent, DMF, and also H_2O can be incorporated. The removal of one BDC linker results in a system with an overall +2 charge and reduces the coordination sphere of 4 Zr centers from 12 to 11. We consider seven capping mechanisms for charge compensation and stabilizing the structure by saturating the coordination of each metal center with a neutral molecule (Table 1).

Table 1. Charge Compensation Models for a Missing Linker from UiO-66[a]

	charged		
model	precursor	anion	neutral
1	HCl	Cl^-	
2	HCl	Cl^-	H_2O
3	CH_3COOH	CH_3COO^-	
4	H_2O	OH^-	
5	H_2O	OH^-	H_2O
6	H_2O	OH^-	DMF
7	HCl	Cl^-	DMF

[a]Given are the charge compensating molecules coordinated onto the two Zr centers, the precursors, and the neutral molecules included in some models to saturate the Zr coordination spheres.

There are two choices for adding the charge-capping and neutral molecules into the structure, labeled as trans and cis in Figure 1. We find the lowest energy arrangement for trans substitution, which can be understood from simple electrostatics, as it maximizes the distance between the charge-capping species, and also steric effects. All results refer to the most stable (trans) configuration.

Defect Formation Energies. The defect free energies as a function of temperature, calculated using mass and charged

DOI: 10.1021/acs.jpcc.6b01659
J. Phys. Chem. C 2016, 120, 9276−9281

balanced chemical reactions, are given in Figure 2. The charge compensating models are detailed in Table 1 and full reactions

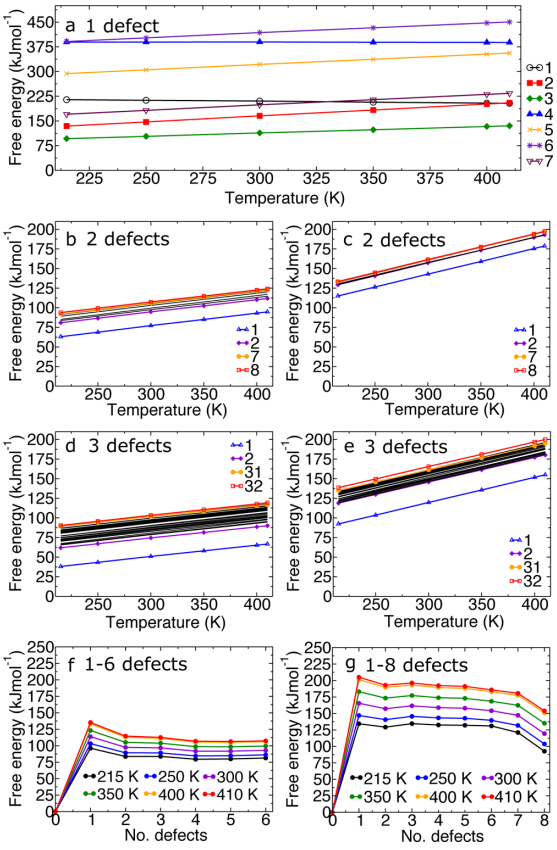

Figure 2. Free energy of defect formation for (a) a single vacancy with a range of capping models (labeled 1−7 corresponding to Table 1). (b,c) Two vacancies with acetate and Cl^-/H_2O capping models. Highlighted are the two lowest and highest energy configurations, all other configurations are shown as black lines. (d,e) Three vacancies with acetate and Cl^-/H_2O capping models. (f,g) removal of 1−8 ligands for the CH_3COO^- and Cl^-/H_2O charge-capping models toward the formation of the ordered vacancy NU-1000 type configuration. All energies are presented per defect and include contributions from the vibrational internal energy and entropy.

are listed in the SI. The reaction energy is sensitive to the charge compensation model. The inclusion of OH^- as a binding ligand is particularly unfavorable. The higher calculated defect energy associated with OH^- is due to the energy required to split its precursor (water) in DMF as a solvent.

The charge-capping mechanisms that had the lowest associated formation free energy were with acetic acid and Cl^-/H_2O. The acetic acid cap was optimized from multiple initial configurations. In each case, the CH_3COO^- ligand converged to a structure with bidentate coordination and identical bond lengths. Little structural distortion or loss of symmetry occurs to the framework of UiO-66 with the incorporation of acetic acid due to it possessing an identical headgroup to BDC. Slight losses of symmetry calculated when using CH_3COO^- as the charge-capping ion are due to the loss of a mirror plane from the introduction of the methyl group. It is therefore the similarity between the chemical structure and solvation energies of the BDC and acetate head groups that makes acetic acid the lowest energy charge-capping mechanism in UiO-66.

Interestingly, we found that binding a Cl^- ion with a neutral molecule had a much lower energy than binding only Cl^- ions. Following the insertion of a monodentate charge-capping ion alone we observed it bridging between two neighboring Zr centers. When water/DMF were introduced, such that the Zr centers remained fully coordinated, the defect energy was lowered. This confirms, as expected, that an undercoordinated metal center is energetically unfavorable. Our findings also suggest that a small concentration of water during synthesis may increase the number of linker vacancies within the material. We found the effect of coordinating DMF as a neutral molecule to have little influence on the defect energy. It can be seen that when comparing the energies for single Cl^- and Cl^-/DMF substitution, DMF, as a neutral coordinating molecule, lowers the defect energy of removing one BDC linker. Note that between 350−400 K, the energies of the respective charge-capping mechanisms cross and the single Cl^- model becomes more favorable than the Cl^-/DMF model, suggesting DMF coordination to be unfavorable at high temperatures.

Multiple Ligand Vacancies. Taking the lowest energy charge-capping mechanisms (CH_3COO^- and Cl^-/H_2O), as identified in Figure 2a, we further investigated the defect energies associated with the removal of additional BDC ligands. We present the defect energies for each of the symmetry unique locations of 2 BDC removals in Figure 2b,c. The details of these configurations are given in the SI. The lowest energy configurations are identified to occur when removing linkers from the faces of the same tetrahedral cage, which also form the vertices of the central octahedral cage. The most favorable position renders one metal node as 10 coordinate and two other metal nodes as 11 coordinate.

For the removal of three BDC linkers, we calculate 32 symmetry unique configurations in a single unit cell. We have calculated the defect formation energy of all configurations for the lowest energy charge-capping mechanisms (CH_3COO^- and Cl^-/H_2O), Figure 2d,e. Each configuration is numbered in order of increasing magnitude of the defect energy, (i.e., configuration 1 has the lowest energy and configuration 32 has the highest). We find a broader distribution of defect energies for the acetate capping than for Cl^-/H_2O. We observe the short-range structural disorder in the acetate configurations, where the acetate molecule points into the pore and does not stay in planar alignment, to be larger with clustered defects due to local interactions and a loss of symmetry. Configuration 1 has the lowest defect energy by 23.8 and 26.5 kJmol^{-1} for the acetate and Cl^-/H_2O capping, respectively, when compared to configuration 2. This configuration corresponds to three BDC linkers being removed from the same tetrahedral cage within the structure with strong local interactions between the defects. In contrast, the highest energy configurations feature parallel vacancies that create a long-range structural instability.

Beyond three ligands, there is a combinatorial explosion and we become limited by our simulation cell size. However, we have considered some representative configurations. For acetic acid, removing four ligands equating to two BDC linkers per metal node has no significant energy penalty (Figure 2f). This result agrees, at least qualitatively, with experiment in that a large increase in surface area can be obtained by using acetic

DOI: 10.1021/acs.jpcc.6b01659
J. Phys. Chem. C 2016, 120, 9276−9281

acid as a modulator to remove linkers from the structure. The removal of five and six linkers from the unit cell results in a small increase in defect energy per linker removal before phonon stability and therefore structural integrity is lost with the removal of 7−8 linkers for acetic acid compensation. For Cl^-/H_2O (Figure 2g), there is a reduction in energy per defect when removing 7 and 8 BDC linkers (i.e., 3.5−4 linkers per metal node), together with a phase change from cubic to monoclinic symmetry, which occurs in a similar manner to the breathing motion of "winerack" MOFs. There is also an increased structural flexibility due to the high number of vacant ligand sites. The predicted phase change occurs at a very high concentration of defects and so may not be experimentally observable. Simulated powder X-ray spectra are given in the SI.[37] The symmetry reduction to monoclinic does not happen in the case of the acetic acid charge cap, because this is a bidentate ligand and the structural integrity of the cubic phase is maintained.

A Boltzmann distribution for two and three linker vacancies shows that 99% of defects will be clustered at 300 K for the acetate and Cl^-/H_2O, respectively. Under equilibrium conditions, a distribution of isolated vacancies is unlikely and a dominant preference for clustered vacancy motifs would be expected, which is consistent with recent X-ray scattering analysis.[38] Furthermore, the dynamic nature of charge capping, including rapid proton transfer has been suggested from very recent simulation studies.[39]

Ordered Defect Structure. A further simulation was performed for the OH^-/H_2O charge-capping system with 8 linkers missing from the cubic unit cell. This corresponds to the node structure of NU-1000, a MOF synthesized from a different Zr precursor. As an analysis of the energy required to form this structure, we repeat the removal of 1−8 linkers in the same manner as previously performed but instead for the OH^-/H_2O charge capping. The final structure is equivalent to NU-1000 and was constructed along the highest symmetry path (the same path as was followed for the acetate and Cl^-/H_2O charge capping). Interestingly, we do not see the same phase change as was observed with the Cl^-/H_2O capping; instead hydrogen bonding between the hydroxyl groups and water maintains the cubic symmetry with only small structural distortions. The defect energy associated with the formation of this structure (8 vacant linkers from the cubic unit cell) is similar to the cost of a single defect (see SI), highlighting the unusual tolerance of UiO-66 for high defect concentrations. We note that the defect energy for this charge capping considers the OH^- capping source to be from the splitting of water. Synthesis methods for NU-1000 involve the use of a Zr−OH precursor, which offers an alternative OH^- source. We therefore highlight the observed trend as being of interest rather than the specific energetics of ligand removal for making a NU-1000 type structure.

Molecular Association in Solution. Because of the high concentration of defects predicted for UiO-66, we should consider processes beyond the typical dilute limit of non-interacting defects. Cluster formation following the removal and subsequent protonation of BDC may occur both in the framework but also between the removed species in the solvent. Possible clusters that may form in solution are depicted in Figure 3. A strong binding energy of −104.7 $kJmol^{-1}$ between two acetic acid molecules and one BDC-H_2 linker has been calculated (Figure 3f).

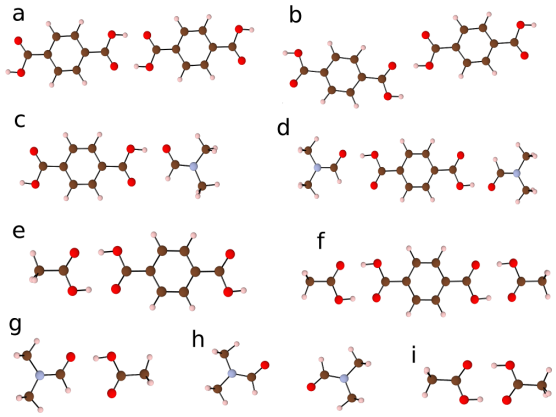

Figure 3. Equilibrium geometries of molecular clusters for which binding energies are given in Table 2.

Formation of molecular clusters in solution may provide an additional driving force for BDC linker to leave the UiO-66 framework when this acid is used as a modulator. Other clusters considered are shown to have a weaker binding energy between components (Table 2). Experimental evidence has been reported that even when synthesized without an acidic modulator UiO-66 can possess the missing linker defect at a low concentration. A contributing factor may be the strong calculated binding energy (−75.3 $kJmol^{-1}$) between DMF and BDC-H_2 (Figure 3d). The formation of this cluster can provide a thermodynamic driving force for a reduced number of linkers to be incorporated into the framework during the formation of UiO-66. The values reported are qualitative because hydrogen bonding between the solvent and molecule is not described in a continuum model. An explicit solvent model could provide a more accurate description of aggregate formation in future studies.

Table 2. Binding Energies (after BSSE Correction) of Molecular Clusters Shown in Figure 3 Formed Following Linker Removal from UiO-66 at 300 K (in DMF Solvent)

cluster				ΔE ($kJmol^{-1}$)
a	BDC	BDC		−47.6
b	BDC	BDC		−22.5
c	BDC	DMF		−29.5
d	BDC	DMF	DMF	−75.3
e	BDC	CH_3OOH		−52.8
f	BDC	CH_3OOH	CH_3OOH	−104.7
g	CH_3OOH	DMF		−38.3
h	DMF	DMF		−4.7
i	CH_3OOH	CH_3OOH		−56.1

Spectroscopic Signatures. The volume of the crystal lattice is found to increase and bulk modulus to decrease for the majority of capping models (see Table 3). The single anion capping (Cl^- and OH^-) is an exception as the anion effectively bridges between two metal centers, taking less physical space than BDC, and the lattice volume decreases. The bulk moduli are all lower for the defect structures but remain within 5 GPa of pristine UiO-66.

A key question is whether the missing ligands have an observable spectroscopic signature. The simulated infrared (IR)

DOI: 10.1021/acs.jpcc.6b01659
J. Phys. Chem. C 2016, 120, 9276−9281

Table 3. Structural and Mechanical Properties of Pristine and Defective UiO-66 with Different Capping Mechanisms Following the Removal of a Single BDC Ligand

capping	volume (Å^3)	bulk modulus (GPa)
UiO-66	9120	23.04
Cl^-	9074	20.03
Cl^-/H_2O	9126	20.77
Cl^-/DMF	9132	21.15
OH^-	9092	20.19
OH^-/H_2O	9137	20.67
OH^-/DMF	9138	19.98
CH_3COO^-	9148	20.60

spectra of 1−4 missing linkers for the two lowest energy charge-capping mechanisms (acetate and Cl^-/H_2O) are presented in Figure 4. We highlight several important features

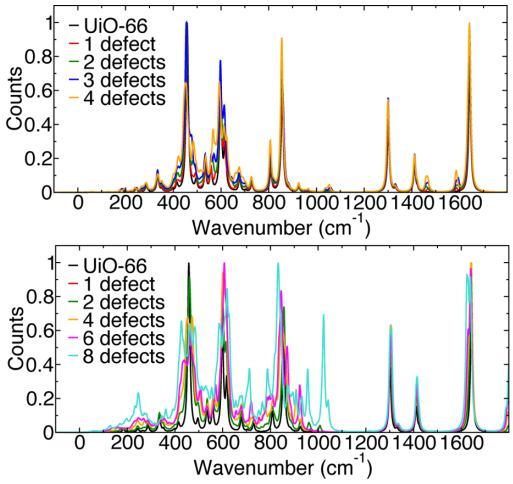

Figure 4. Simulated IR spectra for pristine and defective UiO-66 with acetate (1−4 missing BDC linkers) (top) and Cl^-/H_2O (1, 2, 4, 6, and 8 missing BDC linkers) (bottom) as the charge-capping mechanism. IR spectra are plotted between −200−1800 cm^{-1}. A broadening factor of 10 cm^{-1} was applied.

for the identification of either charge cap. First, for the acetate capping acetate peaks are evident at 1463 cm^{-1} and between 1583−1586 cm^{-1} due to the asymmetric and symmetric stretching of the C−O carboxylate bonds, respectively, which can be distinguished from the C−O carboxylate stretch of BDC, occurring between 1617 and 1650 cm^{-1}. The C−H bond stretch of acetate occurs at 2900 cm^{-1}, and the BDC C−H stretch at 2947 cm^{-1}. Additional peaks between 720−994 cm^{-1} are associated with bending and twisting of the Zr node. Shoulder peaks are associated with the loss of symmetry at the Zr node, but are difficult to distinguish. For the Cl^-/H_2O charge cap, allocating specific frequencies is more difficult. As was the case for acetate, additional peaks between 500−900 cm^{-1} are present due to the reduction in symmetry of the Zr node (as evident for eight missing linkers in Figure 4). The Zr−Cl stretch is difficult to assign to one specific mode but occurs in the same frequency range as the Zr−O stretches between 582−612 cm^{-1}. The most obvious difference for this system is the O−H bond stretch of water at 3378 cm^{-1} (see SI for the full spectral range and associated Raman spectra). The results suggest that high-resolution vibrational spectroscopy may provide the means to assign the local charge-capping mechanism and give insights into defect concentrations.

CONCLUSION

From an analysis of the defect chemistry of linker removal in UiO-66, we conclude that the lowest energy processes are for acetate and Cl^-/H_2O charge-capping mechanisms. We show that H_2O capping at high concentrations results in an ordered-defect structure consistent with the NU-1000 framework. A cluster between two acetic acid molecules and a protonated BDC linker is found to have a strong binding affinity and is a candidate product of ligand loss. The results are expected to be transferable to other UiO frameworks with relevance to a wider range of hybrid organic−inorganic solids.

ASSOCIATED CONTENT

Supporting Information

The Supporting Information is available free of charge on the ACS Publications website at DOI: 10.1021/acs.jpcc.6b01659.

Further methodological and computational details including a full breakdown of the defect free energies, IR and Raman spectra, and force field parameters. (PDF)

AUTHOR INFORMATION

Corresponding Authors

*E-mail: j.gale@curtin.edu.au. Phone: +618 9266 7800.
*E-mail: a.walsh@bath.ac.uk, Phone: +44 (0) 1225 385432.

Notes

The authors declare no competing financial interest.

ACKNOWLEDGMENTS

J.K.B is funded by the EPSRC (EP/G03768X/1). J.D.G thanks the Australian Research Council for funding under the Discovery Program, as well as the Pawsey Supercomputing Centre and NCI for the provision of computing resources. A.W. acknowledges support from the Royal Society. D.T. and K.L.S. are funded under ERC Starting Grant 277757 and J.M.S is funded under EPSRC Grant EP/K004956/1. Access to the ARCHER supercomputer was facilitated through membership of the HPC Materials Chemistry Consortium (EP/L000202). *Data access statement*: the parameter files and input configurations used in this work are available from http://dx.doi.org/10.4225/06/570D936A4B86F.

REFERENCES

(1) Ma, L.; Abney, C.; Lin, W. Enantioselective Catalysis with Homochiral Metal-Organic Frameworks. *Chem. Soc. Rev.* **2009**, *38*, 1248−1256.
(2) Liu, J.; Zhou, W.; Liu, J.; Howard, I.; Kilibarda, G.; Schlabach, S.; Coupry, D.; Addicoat, M.; Yoneda, S.; Tsutsui, Y. Photo-induced Charge-Carrier Generation in Epitaxial MOF Thin Films: High Efficiency as a Result of an Indirect Electronic Band Gap? *Angew. Chem., Int. Ed.* **2015**, *54*, 7441−7445.
(3) Arstad, B.; Fjellvåg, H.; Kongshaug, K. O.; Swang, O.; Blom, R. Amine Functionalised Metal-Organic Frameworks (MOFs) as Adsorbents for Carbon Dioxide. *Adsorption* **2008**, *14*, 755−762.
(4) Alvaro, M.; Carbonell, E.; Ferrer, B.; Llabrés i Xamena, F. X.; Garcia, H. Semiconductor Behavior of a Metal-Organic Framework (MOF). *Chem. - Eur. J.* **2007**, *13*, 5106−5112.
(5) Hwang, Y. K.; Hong, D.-Y.; Chang, J.-S.; Jhung, S. H.; Seo, Y.-K.; Kim, J.; Vimont, A.; Daturi, M.; Serre, C.; Férey, G. Amine Grafting on Coordinatively Unsaturated Metal Centers of MOFs: Consequences

DOI: 10.1021/acs.jpcc.6b01659
J. Phys. Chem. C 2016, 120, 9276−9281

for Catalysis and Metal Encapsulation. *Angew. Chem., Int. Ed.* **2008**, *47*, 4144−4148.
(6) Liu, Y.; Eubank, J. F.; Cairns, A. J.; Eckert, J.; Kravtsov, V. C.; Luebke, R.; Eddaoudi, M. Assembly of Metal-Organic Frameworks (MOFs) Based on Indium-Trimer Building Blocks: A Porous MOF with soc Topology and High Hydrogen Storage. *Angew. Chem., Int. Ed.* **2007**, *46*, 3278−3283.
(7) Cavka, J. H.; Jakobsen, S.; Olsbye, U.; Guillou, N.; Lamberti, C.; Bordiga, S.; Lillerud, K. P. A New Zirconium Inorganic Building Brick Forming Metal-Organic Frameworks with Exceptional Stability. *J. Am. Chem. Soc.* **2008**, *130*, 13850−13851.
(8) Valenzano, L.; Civalleri, B.; Chavan, S.; Bordiga, S.; Nilsen, M. H.; Jakobsen, S.; Lillerud, K. P.; Lamberti, C. Disclosing the Complex Structure of UiO-66 Metal-Organic Framework: A Synergic Combination of Experiment and Theory. *Chem. Mater.* **2011**, *23*, 1700−1718.
(9) Katz, M. J.; Brown, Z. J.; Colón, Y. J.; Siu, P. W.; Scheidt, K. A.; Snurr, R. Q.; Hupp, J. T.; Farha, O. K. A Facile Synthesis of UiO-66, UiO-67 and their Derivatives. *Chem. Commun.* **2013**, *49*, 9449−9451.
(10) Vermoortele, F.; Bueken, B.; Le Bars, G.; Van de Voorde, B.; Vandichel, M.; Houthoofd, K.; Vimont, A.; Daturi, M.; Waroquier, M.; Van Speybroeck, V. Synthesis Modulation as a Tool To Increase the Catalytic Activity of Metal-Organic Frameworks: The Unique Case of UiO-66 (Zr). *J. Am. Chem. Soc.* **2013**, *135*, 11465−11468.
(11) Wu, H.; Chua, Y. S.; Krungleviciute, V.; Tyagi, M.; Chen, P.; Yildirim, T.; Zhou, W. Unusual and Highly Tunable Missing-Linker Defects in Zirconium Metal-Organic Framework UiO-66 and Their Important Effects on Gas Adsorption. *J. Am. Chem. Soc.* **2013**, *135*, 10525−10532.
(12) Van de Voorde, B.; Stassen, I.; Bueken, B.; Vermoortele, F.; De Vos, D.; Ameloot, R.; Tan, J.-C.; Bennett, T. D. Improving the Mechanical Stability of Zirconium-based Metal-Organic Frameworks by Incorporation of Acidic Modulators. *J. Mater. Chem. A* **2015**, *3*, 1737−1742.
(13) Barin, G.; Krungleviciute, V.; Gutov, O.; Hupp, J. T.; Yildirim, T.; Farha, O. K. Defect Creation by Linker Fragmentation in Metal-Organic Frameworks and its Effects on Gas Uptake Properties. *Inorg. Chem.* **2014**, *53*, 6914−6919.
(14) Shearer, G. C.; Chavan, S.; Ethiraj, J.; Vitillo, J. G.; Svelle, S.; Olsbye, U.; Lamberti, C.; Bordiga, S.; Lillerud, K. P. Tuned to Perfection: Ironing Out the Defects in Metal-Organic Framework UiO-66. *Chem. Mater.* **2014**, *26*, 4068−4071.
(15) Planas, N.; Mondloch, J. E.; Tussupbayev, S.; Borycz, J.; Gagliardi, L.; Hupp, J. T.; Farha, O. K.; Cramer, C. J. Defining the Proton Topology of the Zr6-Based Metal-Organic Framework NU-1000. *J. Phys. Chem. Lett.* **2014**, *5*, 3716−3723.
(16) Hod, I.; Bury, W.; Karlin, D. M.; Deria, P.; Kung, C.-W.; Katz, M. J.; So, M.; Klahr, B.; Jin, D.; Chung, Y.-W. Directed Growth of Electroactive Metal-Organic Framework Thin Films Using Electrophoretic Deposition. *Adv. Mater.* **2014**, *26*, 6295−6300.
(17) Yang, D.; Odoh, S. O.; Wang, T. C.; Farha, O. K.; Hupp, J. T.; Cramer, C. J.; Gagliardi, L.; Gates, B. C. Metal-Organic Framework Nodes as Nearly Ideal Supports for Molecular Catalysts: NU-1000-and UiO-66-Supported Iridium Complexes. *J. Am. Chem. Soc.* **2015**, *137*, 7391−7396.
(18) Cadman, L. K.; Bristow, J. K.; Stubbs, N. E.; Tiana, D.; Mahon, M. F.; Walsh, A.; Burrows, A. D. Compositional Control of Pore Geometry in Multivariate Metal-Organic Frameworks: An Experimental and Computational Study. *Dalton Trans.* **2016**, *45*, 4316−4326.
(19) Bristow, J. K.; Tiana, D.; Walsh, A. Transferable Force Field for Metal-Organic Frameworks from First-Principles: BTW-FF. *J. Chem. Theory Comput.* **2014**, *10*, 4644−4652.
(20) Butler, K. T.; Hendon, C. H.; Walsh, A. Electronic Chemical Potentials of Porous Metal-Organic Frameworks. *J. Am. Chem. Soc.* **2014**, *136*, 2703−2706.
(21) Fuentes-Cabrera, M.; Nicholson, D. M.; Sumpter, B. G.; Widom, M. Electronic Structure and Properties of Isoreticular Metal-Organic Frameworks: The Case of M-IRMOF1 (M= Zn, Cd, Be, Mg, and Ca). *J. Chem. Phys.* **2005**, *123*, 124713.
(22) Torrisi, A.; Bell, R. G.; Mellot-Draznieks, C. Predicting the Impact of Functionalized Ligands on CO_2 adsorption in MOFs: A combined DFT and Grand Canonical Monte Carlo Study. *Microporous Mesoporous Mater.* **2013**, *168*, 225−238.
(23) Devautour-Vinot, S.; Maurin, G.; Serre, C.; Horcajada, P.; Paula da Cunha, D.; Guillerm, V.; de Souza Costa, E.; Taulelle, F.; Martineau, C. Structure and Dynamics of the Functionalized MOF Type UiO-66 (Zr): NMR and Dielectric Relaxation Spectroscopies Coupled with DFT Calculations. *Chem. Mater.* **2012**, *24*, 2168−2177.
(24) Gale, J. D.; Rohl, A. L. The General Utility Lattice Program (GULP). *Mol. Simul.* **2003**, *29*, 291−341.
(25) Gale, J. D. GULP: A Computer Program for the Symmetry-Adapted Simulation of Solids. *J. Chem. Soc., Faraday Trans.* **1997**, *93*, 629−637.
(26) Kresse, G.; Hafner, J. Ab initio Molecular Dynamics for Liquid Metals. *Phys. Rev. B: Condens. Matter Mater. Phys.* **1993**, *47*, 558.
(27) Perdew, J. P.; Burke, K.; Ernzerhof, M. Generalized Gradient Approximation Made Simple. *Phys. Rev. Lett.* **1996**, *77*, 3865−3868.
(28) Valiev, M.; Bylaska, E. J.; Govind, N.; Kowalski, K.; Straatsma, T. P.; Van Dam, H. J.; Wang, D.; Nieplocha, J.; Apra, E.; Windus, T. L. NWChem: A Comprehensive and Scalable Open-Source Solution for Large Scale Molecular Simulations. *Comput. Phys. Commun.* **2010**, *181*, 1477−1489.
(29) Dunning, T. H., Jr Gaussian Basis Sets for use in Correlated Molecular Calculations. I. The Atoms Boron through Neon and Hydrogen. *J. Chem. Phys.* **1989**, *90*, 1007−1023.
(30) Woon, D. E.; Dunning, T. H., Jr Gaussian Basis sets for use in Correlated Molecular Calculations. III. The Atoms Aluminum through Argon. *J. Chem. Phys.* **1993**, *98*, 1358−1371.
(31) Zhao, Y.; Truhlar, D. G. The M06 Suite of Density Functionals. *Theor. Chem. Acc.* **2008**, *120*, 215−241.
(32) Zhao, Y.; Truhlar, D. G. Density Functionals with Broad Applicability in Chemistry. *Acc. Chem. Res.* **2008**, *41*, 157−167.
(33) Bass, S.; Nathan, W.; Meighan, R.; Cole, R. Dielectric Properties of Alkyl Amides. II. Liquid Dielectric Constant and Loss. *J. Phys. Chem.* **1964**, *68*, 509−515.
(34) Lemmon, E. W.; Huber, M. L.; McLinden, M. O. *NIST Standard Reference Database 23*; 2003.
(35) Becke, A. D. Density-Functional Thermochemistry. III. The Role of Exact Exchange. *J. Chem. Phys.* **1993**, *98*, 5648−5652.
(36) Xantheas, S. S. On the Importance of the Fragment Relaxation Energy Terms in the Estimation of the Basis Set Superposition Error Correction to the Intermolecular Interaction Energy. *J. Chem. Phys.* **1996**, *104*, 8821−8824.
(37) Fleming, S.; Rohl, A. GDIS: A Visualization Program for Molecular and Periodic systems. *Z. Kristallogr. - Cryst. Mater.* **2005**, *220*, 580−584.
(38) Cliffe, M. J.; Wan, W.; Zou, X.; Chater, P. A.; Kleppe, A. K.; Tucker, M. G.; Wilhelm, H.; Funnell, N. P.; Coudert, F.-X.; Goodwin, A. L. Correlated Defect Nanoregions in a Metal-Organic Framework. *Nat. Commun.* **2014**, *5*, 4176.
(39) Ling, S.; Slater, B. Dynamic Acidity in Defective UiO-66. *Chem. Sci.* **2016**, DOI: 10.1039/C5SC04953A.

DOI: 10.1021/acs.jpcc.6b01659
J. Phys. Chem. C 2016, 120, 9276−9281

Chapter 5

Epitaxial growth of MOFs on surfaces

5.1 Paper 4 - Chemical bonding at the metal-organic framework / metal oxide interface: simulated epitaxial growth of MOF-5 on rutile TiO_2

Understanding the binding mechanisms and adhesion strengths between two interfacing surfaces, particularly when designing functional devices, such as photovoltaic cells, is crucial. The choice of which materials to interface does not only depend on their independent material properties, but also if uniform surface coverage can be achieved during growth. Different growth mechanisms can occur when growing thin films of a material on a substrate.[254,255] The first and most common is the Stranski-Krastanov mechanism, where a few uniform layers will grow on a substrate before crystal nucleation and adsorbate-adsorbate interactions dominate, leading to the nucleation of clusters. Surface roughness, if the Stranski-Krastanov mechanism was dominating crystal growth, would increase as a function of film thickness. Secondly, the Volmer-Weber mechanism, which due to dominating adsorbate-adsorbate interactions, forms rough surfaces with spontaneous nucleation forming many clusters across the substrate material. Finally, the Frank-van der Merwe mechanism for thin film growth produces atomically smooth surfaces, as in this mechanism the surface-adsorbate interactions dominate over those between adsorbates.[254,255] Ohnsorg *et al.*[256] report the growth of a thin film of HKUST-1 on modified Au surfaces. The authors use scanning probe microscopy and ellipsometry to measure the growing surface roughness and thickness, respectively, to identify the growth of HKUST-1 by the Volmer-Weber mechanism. If the Volmer-Weber mechanism is to dominate the growth of thin films of MOFs on surfaces, then initial growth will depend on the interaction of the MOF with surface adsorption sites.

The energetics of interacting a material with surface sites of a substrate, such as a metal oxide, will depend on many factors. Firstly, the lattice mismatch, which is defined as the percentage difference between the unit cell lattice parameters of two interfacing materials, must be low with values ideally $< 5\%$. Additionally, the chemical termination at each surface and where the strongest interactions between two surfaces, based on the formation of chemical bonds, will occur. Finally, the phase purity

and crystallinity of the growing thin film must be considered, with epitaxial growth a distribution of material symmetry phases may form under different synthesis conditions, leading to thin films with different materials and optical properties.

In the following paper we conduct a screening procedure for calculating lattice mismatch between two interfacing surfaces developed by Butler *et al.*[257] The screening procedure was carried out for between multiple oxides and MOF structures, and identified a low lattice mismatch between the (110) surface of TiO_2 and the (011) surface of MOF-5. A combination of first-principles and classical methods are then used to model the interface between the cleaved surfaces, and calculations include thermodynamically favourable positions of the ligands and possible reconstruction mechanisms of the oxide surface when interfaced.

5.1.1 Additional ESI

Gaussian and plane waves method

The Quickstep module in CP2k was used in the paper for structure optimisation, which uses a hybrid Gaussian and plane-waves (GPW) approach.[258] Standard approaches to conducting DFT calculations on systems are efficient but do not scale linearly with system size owing to the computation of the Coulomb energy and orthogonalisation of the wave functions. The GPW approach was developed to prevent "bottlenecks" in computation efficiency of DFT by efficient treatment of electrostatic interactions to allow linear scaling and a reduction in computation time.

The GPW approach uses Gaussian atom-centered basis sets as primary basis functions for the wave functions and plane waves for the charge density. The advantage of using Fast Fourier Transform methods with plane waves for calculation of the Hartree Coulomb energy and Kohn-Sham matrix has been discussed in the methodology section of this thesis.

The representation of the Gaussian orbital basis sets in the GPW approach for the electron density ($\rho(\mathbf{r})$) considering the density matrix element ($P^{\mu\nu}$) is given by Equation 5.1.

$$\rho(\mathbf{r}) = \sum_{\mu\nu} P^{\mu\nu}\phi_\mu(\mathbf{r})\phi_\nu(\mathbf{r}) \tag{5.1}$$

where, $\phi_\mu(\mathbf{r}) = \sum_i d_{i\mu} g_i$ with primitive Gaussian functions ($g_i(\mathbf{r})$) and contraction coefficients ($d_{i\mu}$).

The plane wave representation considering V, the volume of the unit cell and reciprocal lattice vectors ($\mathbf{G}$) is given by Equation 5.2.

$$\widetilde{\rho}(\mathbf{r}) = \frac{1}{V}\sum_{\mathbf{G}} \widetilde{\rho}(\mathbf{G}) exp(i\mathbf{G}.\mathbf{r}) \tag{5.2}$$

The Kohn-Sham energy functional under the GPW approach considering the interaction of ionic cores and electronic density using the Gaussian basis-set construct (Equation 5.1) and the plane wave construct (Equation 5.2) is given by Equation 5.3.[258]

$$
\begin{aligned}
E[\rho] = E^T[\rho + E^V[\rho] + E^H[\rho] + E^{XC}[\rho] + E^{II} \\
&= \sum_{\mu\nu} P^{\mu\nu} \left\langle \phi_\mu(\mathbf{r}) | -\frac{1}{2} \bigtriangledown^2 | \phi_\nu(\mathbf{r}) \right\rangle \\
&+ \sum_{\mu\nu} P^{\mu\nu} \left\langle \phi_\mu(\mathbf{r}) | V^{PP}_{loc}(\mathbf{r}) | \phi_\nu(\mathbf{r}) \right\rangle \\
&+ \sum_{\mu\nu} P^{\mu\nu} \left\langle \phi_\mu(\mathbf{r}) | V^{PP}_{nonloc}(\mathbf{r},\mathbf{r'}) | \phi_\nu(\mathbf{r},\mathbf{r'}) \right\rangle \\
&+ 2\pi V \sum_{\mathbf{G}} \frac{\widetilde{\rho}^*(\mathbf{G})\widetilde{\rho}(\mathbf{G})}{\mathbf{G}^2} + \int e^{xc}(\mathbf{r}) d\mathbf{r} \\
&+ \frac{1}{2} \sum_{I \neq J} \frac{Z_I Z_J}{\mathbf{R}_I - \mathbf{R}_J}
\end{aligned}
\tag{5.3}
$$

where $\mathrm{E}^T[\rho]$ is the electronic kinetic energy, $\mathrm{E}^V[\rho]$ is the electronic interaction with the cores of the ions, $\mathrm{E}^H[\rho]$ is the electronic Coulomb energy, E^{XC} the exchange correlation energy and E^{II} is the electrostatic interactions between the cores with charges, Z and positions, **R**. The local (V^{PP}_{loc}) and non-local (V^{PP}_{nonloc}) components of E^V are described by norm-conserving pseudopotentials. The norm-conserving pseudopotentials used for the paper were those of Goedecker, Teter and Hutter (GTH). The GTH pseudopotentials are parameterised using all-electron wave functions from fully relativistic calculations, and show improved accuracies for heavy atoms above other pseudopotentials.[258]

The use of plane wave pseudopotentials is wasteful of computer time and resources for models involving large vacuums such as surface slabs, but remain efficient at removing the need to model core electrons. The use of the GPW hybrid plane wave pseudopotentials and Gaussian basis sets allows efficient treatment of the core electrons, and vacuum region, by using local basis sets that do no extend across the vacuum region.

Surface slab construction

Slab models are commonly used to model surfaces and interfaces of solid-materials, and are formed of a cleaved surface with an appropriate number of layers of material such that the lower layers would represent the bulk. The constructed slab is periodic in the *x* and *y* directions with vacuum added in the *z* direction and the atomic positions have generally been optimised for the bulk structure prior to a super cell construction, from which a surface is cleaved. There are multiple considerations when constructing a surface slab including; the thermodynamic stability of the cleaved surface, if the cut has left a dipole across the material and how large the vacuum region must be to ensure any electrostatic interactions do not extend across periodic images. Once constructed, it is common practice with thinner material slabs that when optimising the surface, the atomic positions in the lowest layers are fixed such that they

remain in the bulk positions. With thicker slabs where little atomic displacement of the lowers layers would occur during optimisation, all atom positions can be relaxed.

For the following paper, the thermodynamically most stable surface of TiO_2, which is the (110) surface, was cleaved from optimised atomic positions of the bulk material. For the slab models of the surface a large vacuum region of 30 Å was used, and a full relaxation of atomic positions was adopted owing to the thickness of the material considered.

5.1.2 Coulomb energy correction

An electrostatic energy correction was required for calculating the proton transfer energy between BDC ligand and TiO_2 surface. We place a F^- anion in the centre of a cubic unit cell and calculate the internal energy as a function of inverse unit cell length, a. The internal energy of a charged unit cell with infinite dimensions can be extrapolated from the intercept of $1/a$ *vs* internal energy plot. The difference in energy of an F^- anion in the unit cell used for the BDC on TiO_2 surface calculations and the total energy of the charged unit cell with infinite dimensions is the correction per +/- 1 charge on a system (-0.408 eV). As two charges need to be accounted for (from surface and ligand charged reference states) in the correction, a factor of two is applied when calculating the final proton transfer energy. The charge correction was calculated as the difference between the infinite box limit (intercept of the plot given in Figure 5-1) and the energy of the anion in the unit cell used for the first-principles calculations of BDC on TiO_2.

Table 5.1: Total energy of F^- anion in a cubic unit cell of dimensions (a) used to calculate the electrostatic Coulomb energy correction of charged reference states.

a	$1/a$ ($Å^{-1}$)	Total energy (Ha)	Total energy (eV)
10	0.1	-24.227	-659.253
15	0.066666667	-24.205	-658.660
20	0.05	-24.194	-658.341
25	0.04	-24.186	-658.145
30	0.033333333	-24.182	-658.012
35	0.028571429	-24.178	-657.916
40	0.025	-24.175	-657.844
45	0.022222222	-24.173	-657.788
50	0.02	-24.172	-657.743

Thermodynamic cycle of proton transfer

The thermodynamic cycle considered for calculating the proton transfer energy between BDC ligand and TiO_2 surface is given in Figure 5-2. Note the inclusion of the electrostatic Coulomb energy correction.

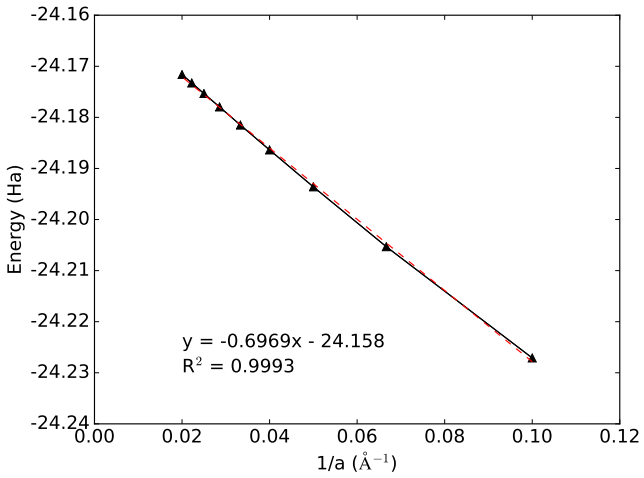

Figure 5-1: Electrostatic Coulomb energy correction plot from data given in Table 5.1.

Table 5.2: Calculation of electrostatic Coulomb energy correction from the infinite box limit as determined from data reported in Table 5.1.

Intercept (infinite box limit) energy (Ha)	-24.158
In box same size as simulations (Ha)	-24.173
Δ E (Coulomb) (Ha)	0.015
Δ E (Coulomb) (eV)	0.408

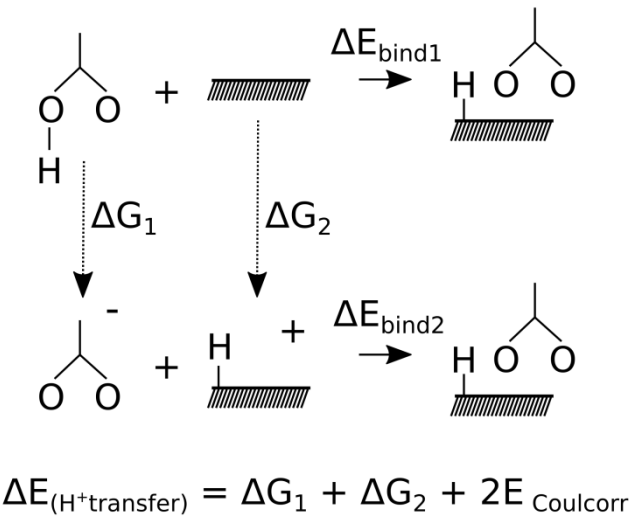

Figure 5-2: Thermodynamic cycle considered for calculating proton transfer energies between BDC and the TiO_2 surface.

5.1.3 Forcefield parameter files

The forcefield parameter files can be found as open-source resources at the following Github address: https://github.com/WMD-group/Epitaxy-MOF-5-TiO2/

5.1.4 Personal contribution

My personal contribution to the paper entitled *"Chemical bonding at the metal-organic framework / metal oxide interface: simulated epitaxial growth of MOF-5 on rutile TiO_2"* included all first-principles calculations on the (110) surface of TiO_2 and locating energy minima of the BDC ligand on the surface. I also parameterised the forcefield models for both MOF-5 and TiO_2, conducted all structure optimisations of the interfaced periodic materials and calculated the energy of adhesion between the interfaces. K. Svane assisted with surface construction prior to optimisation.

ARTICLE TYPE www. rsc.org/xxxxxx | XXXXXXXX

Chemical bonding at the metal-organic framework / metal oxide interface: simulated epitaxial growth of MOF-5 on rutile TiO_2

Jessica K. Bristow,[a] Keith T. Butler[a], Katrine L. Svane,[a], Julian D. Gale*[c] and Aron Walsh,*[a,b]

[a] Centre for Sustainable Chemical Technologies and Department of Chemistry, University of Bath, Claverton Down, Bath, BA2 7AY, UK. Tel: 01225 385432; E-mail: a.walsh@bath.ac.uk, [b] Global E^3 Institute and Department of Materials Science and Engineering, Yonsei University, Seoul 120-749, Korea, [c] Curtin Institute for Computation, Department of Chemistry, Curtin University, PO Box U1987, Perth, WA 6845, Australia. Email: j.gale@curtin.edu.au

Received Xth XXXXXXXXXX 20XX, Accepted Xth XXXXXXXXX 20XX

First published on the web Xth XXXXXXXXXX 200X

DOI: 10.1039/b000000x

Thin-film deposition of metal-organic frameworks (MOFs) is now possible, but little is known regarding the microscopic nature of hybrid heterointerfaces. We first assess optimal substrate combinations for coherent epitaxy of MOFs based on a lattice matching procedure. We then perform a detailed quantum mechanical / molecular mechanical investigation of the growth of (011) MOF-5 on (110) rutile TiO_2. The lowest energy interface configuration involves a bidentate connection between two TiO_6 polyhedra with deprotonation of terephthalic acid to a bridging oxide site. The epitaxy of MOF-5 on the surface of TiO_2 was modelled with a forcefield parametrised to quantum chemical binding energies and bond lengths. The microscopic interface structure and chemical bonding characteristics are expected to be relevant to other framework-oxide combinations.

1 Introduction

Metal-organic frameworks (MOFs) are formed of inorganic metal clusters and organic ligands, self assembled into extended porous networks. Progress in the understanding of crystallisation mechanisms [1] and methods for controlling pore geometry and morphology [2,3] has allowed the fabrication of thin film MOFs for applications including molecular sensors, smart membranes and catalytic coatings. [4,5]

There are two distinct approaches for fabricating MOF heterointerfaces. [6] The first is the deposition of a preformed MOF onto a surface, e.g. using a one-pot solvothermal reaction. The second is templated growth where the surface of a substrate can be functionalised, for example, with -thio, -COOH or -CF_3 monolayers. [7–9] The latter is considered advantageous for uniform thin-film growth since it offers selective and directional growth with a reduced number of defects at interfacing sites.

There are numerous examples of MOF interface formation in the recent literature. For example, Ameloot *et al.* demonstrated controlled thickness and crystal size of thin film growth of HKUST-1 (a Cu^{2+} paddle-wheel structure with attractive physical properties [10]) on Cu metal electrodes using electrochemical deposition. [11] In accordance with classical nucleation theory, they report decreasing MOF crystal size with an increased applied voltage due to an increased rate of crystal growth. In 2010, Yoo *et al.* reported the heterostructured layered growth of the isorecticular IRMOF-3 and MOF-5 structures on the surface of Al_2O_3. [12] Using a core/shell approach, where one MOF is seeded on top of the other, a layered structure formed of Al_2O_3 substrate/IRMOF-3/MOF-5 layers was grown. Growth was demonstrated regardless of which MOF formed the core and shell. This approach allows for the construction of complex heterostructured devices with differing porosity and functional properties throughout the material. More recently, Fischer *et al.* reported a heterostructure between HKUST-1 and [Cu_2ndc$_2$dabco] (ndc: 1,4-naphtalene dicarboxylate, dabco: 1,4-diazabicyclo(2.2.2) octane), which were grown upon a pyridyl-functionalized Au substrate. [13] The layered systems displayed enhanced adsorption affinity for small organic molecules, such as methanol, at standard conditions. A significant development has been the application of vapour phase deposition techniques: Ameloot *et al.* and Ritala *et al.* independently reported the gas phase deposition of ZIF-8 and MOF-5 onto surfaces using the chemical vapour deposition and atomic layer deposition, respectively. The optimisation of vapour phase approaches to the growth of MOF thin films would allow greater control over uniformity and thickness for device manufacturing. [14,15]

Resolving the interface structure following epitaxial growth is challenging, especially for hybrid solids that are inherently 'soft' materials. Different experimental approaches have been attempted for determining the surface termination of MOFs, including an atomic-force microscopy examination of

HKUST-1.[16] Computational approaches to predicting the termination of MOF crystals have also provided useful guidance. Schmid *et al.* used classical and first principles methods to predict the surface structure and growth mechansim of HKUST-1.[17] The calculated surface formation energies suggested that a ligand termination of the (111) surface is the lowest energy cleavage of the crystal. It should also be noted that complex defects are possible in MOFs, such as missing ligands and metal clusters during growth, further complicate surface structure characterisation.[18]

Following an initial screening procedure to identify lattice-matched MOF / substrate combinations, we report a combined classical and first principles investigation of the mechanism of epitaxy of MOF-5 on the (110) surface of rutile TiO_2. Favourable binding positions of the BDC linker forming MOF-5 are calculated with density functional theory (DFT) and used to re-parameterise an existing MOF forcefield to describe the interface. The (011) surface of MOF-5 is then interfaced with the (110) surface of TiO_2 and the resulting chemical interactions and surface reconstruction are reported.

2 Methodology

2.1 Lattice matching procedure

Screening for optimal materials combinations based on minimization of lattice mismatch was conducted to find viable combinations of MOFs and binary materials including mainly metal oxides. We employed the electronic-lattice-site (ELS) procedure.[19] The process involves cleaving all low-index surfaces of both the MOFs and substrates using the atoms object in the atomic simulation environment (ASE).[20] The mismatch of surface cell vectors ($u \times v$) can then be calculated as a percentage difference, taking into account possible orientations and supercell expansions. The definition of surface cell parameters is given by the Zur and McGill scheme of defining a set of primitive vectors of the cell such that they are independent of any rotations or reflections of the lattice, thus allowing a complete identification of compatible surfaces for epitaxial interfacing.[21,22] We define an arbitrary cut-off of 8 % mismatch, which takes into account the mechanical softness and flexibility of many hybrid frameworks.

2.2 First principles calculations

Total energy calculations were performed within the Kohn-Sham density functional theory framework using the PBEsol functional for the exchange-correlation potential with a D3 van der Waals correction in the QUICKSTEP module of the CP2K program.[23–25] PBE pseudopotentials of the analytical form of Goedecker, Teter and Hutter (GTH) were used to model the interaction between the valence electrons [Ti($2s^2 3s^2 3p^6 3d^2$), C($2s^2 2p^2$), O($2s^2 2p^4$), F($2s^2 2p^5$), and H(1s)] and the atomic cores.[26] Kohn-Sham orbitals are expanded with local Gaussian functions from the cc-TZ library for C, H, F and O with those from the DZV-GTH-PADE library for Ti.[27,28] The planewave cut-off for the auxiliary density basis set was set to 300 Ry with SCF convergence set to 1×10^{-7} Ha.

2.3 Forcefield calculations

Analytical forcefield calculations used GULP[29,30] and the VMOF forcefield[31] as parameterised for common MOFs. VMOF represents the interaction between metal and ligands by modified MM3 Buckingham potentials, as given in Equation 1, plus the Coulomb terms, and is an extension to a previous parameterised forcefield, BTW-FF.[32–34]

$$E_{ij}^{MM3} = \varepsilon_{ij}\left[A\exp\left(-B\frac{d_{ij}}{d_{ij}^0}\right) - C\left(\frac{d_{ij}^0}{d_{ij}}\right)^6\right] \qquad (1)$$

Combination rules, where $\varepsilon_{ij} = \sqrt{\varepsilon_{ii}\times\varepsilon_{jj}}$ and $d_{ij}^0 = \sqrt{d_{ii}^0 \times d_{jj}^0}$, were used for the ε_{ij} and d_{ij}^0 values of the MM3 potential, that were parameterised for each metal to reproduce the structural and mechanical properties of a subset of MOFs including: MOF-5, IRMOF-10, MOF-650, UiO-66, UiO-67, MIL-125, NOTT-300, and MOF-74.

Intramolecular bonding parameters of the ligands are taken directly from the CHARMM library and charges derived using the charge equilibrium scheme of Gasteiger.[35–37] Formal charges were used for the metal cations and oxide anions within the metal nodes; we can therefore consider the node and ligands as essentially separate components.

The total internal energy (U) expression can be written as

$$U = \sum_{bonds}\frac{1}{2}k_r(r-r_0)^2 + \sum_{angles}\frac{1}{2}k_\theta(\theta-\theta_0)^2 + \sum_{dihedrals}\frac{1}{2}k_\Psi[1+cos(n\Psi+\Psi_0)] + \frac{1}{2}\sum_i\sum_j\frac{q_i q_j e^2}{4\pi\varepsilon_0 r_{ij}}$$

where, k_r, k_θ and k_Ψ are interatomic force constants, r the distance between a pair of atoms, θ are 3-body and Ψ are 4-body angles, q represents point charges and ε_0 the vacuum permittivity.

Long-range interactions of the ligand were treated as Lennard-Jones functions with combination rules for ε and σ of each individual atom. Lennard-Jones interactions of the ligands were truncated at 12.5 Å and the cut-off of the MM3 Buckingham interactions of the metal node was set to 12.0 Å.

For the TiO_2 surface, a formal charge model was adopted, with Ti and O interacting *via* a MM3 Buckingham term as was used for the MOF metal node. Combination rules were used

for the ε_{ij} and d^0_{ij} values of the MM3 functional, which were parameterised to reproduce structural and mechanical properties of bulk rutile TiO_2.

3 Results and Discussion

3.1 Epitaxial matching

A screening procedure was executed to calculate the lattice mismatch between a range of common MOFs and inorganic materials, such as oxides and chalcogenides, with the purpose being to identify systems with small variations of the interfacing surface cell parameters (Figure 1). The procedure does not consider chemical identity, but focuses on lattice strain, calculated as the percentage difference between interfacing surface parameters. If lattice mismatch of the cleaved surfaces is calculated to exceed 8% between a "soft" MOF and comparatively hard binary material surface, is it unlikely that a uniform coverage of that MOF on the surface would be observed. Furthermore, large lattice mismatch between surface parameters is likely to introduce extended defects at interfacing sites, mechanical instability and weak chemical bonding.

The results of the epitaxial screening are summarised in Figure 1. Numerical values of lattice mismatch, surface indices and surface expansions are provided as supporting information. Several interesting trends are found. Firstly, common binary materials used as templates for surface growth, including Al_2O_3, TiO_2 and α-SiO_2, are identified to have low lattice mismatch with many MOF topologies. This includes common MOFs such as COF-1, MIL-125, DMOF-1 (orthorhombic and rhombohedral polymorphs) and MOF-649, suggesting these to be functional templating materials. Secondly, we highlight that MOF-649 and DMOF-1 with wine-rack pore topology show the greatest surface compatibility across most binary materials considered. These MOFs are good candidates for porous thin film materials. The screening procedure has also identified ZnO and ZrO_2 to be poor substrate materials for the epitaxial growth of MOFs.

Our results confirm experimental observations made by Hermes *et al.* who reported the successful growth of MOF-5 on Al_2O_3 surfaces but state that growth was not possible on α-SiO_2 wafers with the same reaction conditions.[38] There is a favourable lattice mismatch between the (011) and (110) surfaces of MOF-5 and the (010) and (100) surfaces of Al_2O_3. However, we do not find any favourable lattice planes that would interface effectively between MOF-5 and SiO_2 in accord with the experimental observations.

3.2 Epitaxial growth of MOF-5 on TiO_2

We now consider the interface between the (110) surface of TiO_2 and the (011) surface of MOF-5 in more detail as a representative system (see Figure 2). TiO_2 is a photocatalytic material and popular for its surface reactivity.[39–41] The (110) surface of TiO_2 is known to favourably bind the benzene dicarboxylate (BDC) ligands that form MOF-5.[42] MOF-5, first synthesised by Yaghi *et. al.*, is composed of BDC ligands and Zn^{2+} cations in tetrahedral coordination, with each metal node containing 4 Zn ions and 1 central inorganic oxygen anion.[43]

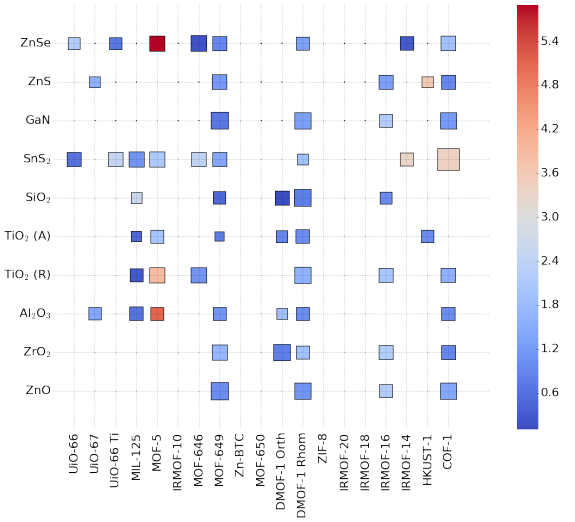

Fig. 1 Assessment of epitaxial matching between a range of metal-organic frameworks and inorganic materials. The square markers signify lattice mismatch within 8%. The size of the marker is inversely proportional to the mismatch in surface area ($u \times v$ expansion) between the interfacing surfaces. The colour of the marker reflects the lattice strain, from blue (low strain) to red (high strain). The most favourable matches therefore appear as large blue squares. The interface with the smallest mismatch is plotted for each combination. The polymorphs chosen are the experimental structures at T = 300 K, with both the anatase (A) and rutile (R) phases considered for TiO_2.

3.2.1 Carboxylate attachment on TiO_2: first principles. The (110) surface of TiO_2 was cut with a 6×3 surface expansion using GDIS.[44] The final surface slab contained 540 atoms with cell dimensions of 17.7 and 19.5 Å. The complexity of surface defects and the presence of water adlayers is extensively reported for TiO_2.[45–48] To reduce the cost and complexity of the calculations we consider the bare unreconstructed (110) surface of TiO_2 as a representative interface with MOFs. To create a 3-D periodic model, a vacuum gap of 32 Å was inserted in the z-direction. Such a large vacuum region is necessary as the length of BDC exceeds 7 Å. Once placed on the oxide surface, the gap must be sufficient that electrostatic interactions of the BDC/oxide surface do not ex-

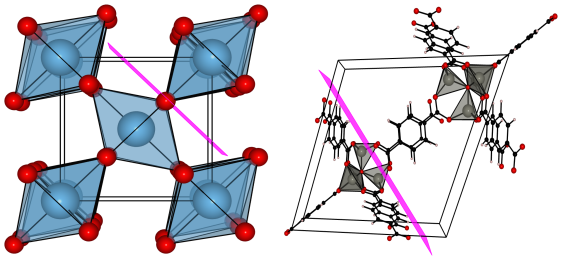

Fig. 2 Representation of the unit cell of rutile TiO_2 (left) and MOF-5 (right) with highlighted lattice planes (pink) along (110) and (011), respectively.

tend across periodic images. Multiple configurations for placing BDC on the (110) surface of TiO_2 were investigated including atomic relaxation (see Figure 3 and Table 1).

We consider six models, which we describe in terms of the initial and final configurations: **Model 1.** *Initial:* Monodentate binding configuration of BDC to one Ti polyhedron with the capping hydrogen of BDC at an appropriate distance for an oxide-H(BDC) interaction *Final:* The ligand remained in a monodentate configuration with the proton of the BDC directed at a surface oxide ion. **Model 2.** *Initial:* Monodentate binding configuration to one Ti polyhedron with the proton of BDC pointing away from the surface. *Final:* The ligand translated from being above one Ti polyhedra to approach a second one in a bidentate manner. The movement across the surface distorted the ligand into a local minimum with reduced symmetry. **Model 3.** *Initial:* Bidentate binding of BDC between two Ti polyhedra in the *x* direction with the proton initialised to point away from the surface. *Final:* A small displacement of the molecule was observed and bidentate contact with the surface was maintained. **Model 4.** *Initial:* The ligand was initialised as a bidentate connection between two Ti polyhedra in the *xy* plane with the proton initialised to point away from the surface. *Final:* Deprotonation occured as illustrated in Figure 4. A loss of bidentate coordination resulted in the proton interacting with a nearby oxide and rotation of the ligand into the same position as model 6. **Model 5.** *Initial:* Deprotonated model 2 with the hydrogen located on a three-coordinate oxygen of the surface that is located between Ti polyhedra. *Final:* A small displacement of the ligand. **Model 5 (low symmetry).** *Initial:* The same as model 5 but with symmetry breaking of the Ti-O to check for alternative local minima. *Final:* The bond lengths were very similar to model 5 with an energy lowering of only 54 meV. **Model 6.** *Initial:* Deprotonated model 2 with the hydrogen located on a two-coordinate bridging oxygen on the surface. *Final:* Minor structure relaxation. **Model 6 (low symmetry).** *Initial:* The same as model 6 but with symmetry breaking of the Ti-O to check for alternative local

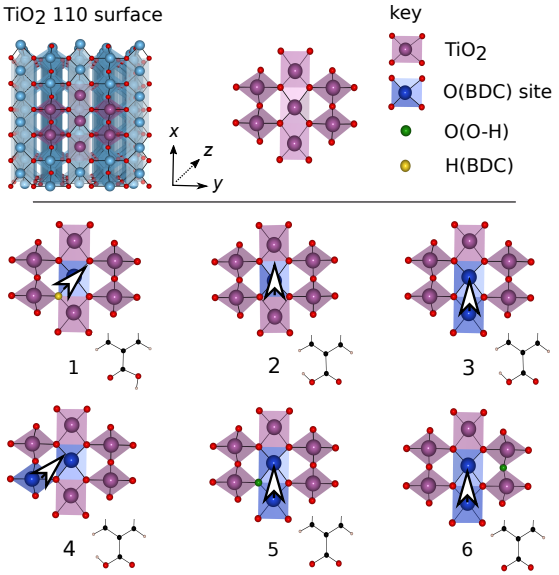

Fig. 3 Initial configurations of the BDC ligand on the (110) surface of TiO_2. Highlighted (purple) is a central region of the TiO_2 surface for depicting the relative positions of Ti polyhedra that the BDC were bound to. For each surface model we highlight (blue) the Ti polyhedra that the BDC is initialised as bound to, with the capping of the carboxylate/carboxylic acid group that was considered at this binding site (lower right of each image). Yellow highlighted oxygen atoms indicate an initial H-bonding interaction with protonated BDC and green shows the initial position of protons when considering a deprotonated ligand at the surface. Arrows across binding sites show the orientation of the BDC ligand.

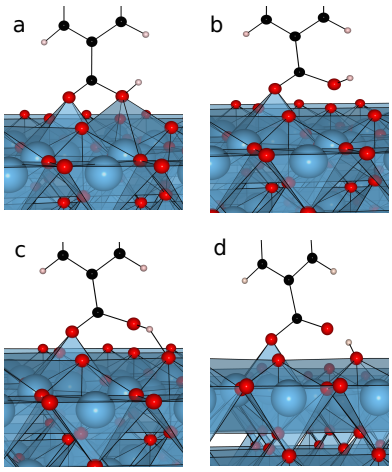

Fig. 4 Deprotonation of BDC (model 4 in Figure 3) during optimisation: (a) the initial configuration of the ligand; (b) the loss of the bonding interaction between the protonated carboxylic acid oxygen and Ti as the ligand begins to rotate; (c) the proton on the carboxylic acid oxygen beginning to interact with a bridging oxygen on the surface; (d) the proton transfer from the ligand to the surface.

minima. *Final:* The original structure was largely recovered, and no energy gain was found.

The most favourable site for BDC adsorption (Table 1) is model 6 (Figure 3) with monodentate binding and deprotonation. The high relative energies of the other configurations suggests that for an isolated ligand on the surface of TiO_2, only this ground-state configuration would be accessible.

3.2.2 Carboxylate attachment on TiO_2: forcefield.

Exploring the configurational space of the interface between MOF-5 and TiO_2 using first principles techniques is prohibitively expensive from a computational perspective. We therefore developed an analytical forcefield model to describe the interface. The starting point was an existing forcefield derived for metal-organic frameworks, VMOF, which describes the bulk properties of a wide range of metal-organic frameworks.[31] A forcefield for TiO_2 was fitted to reproduce the lattice parameters and elastic constants of bulk TiO_2 (rutile) the results of which are shown in Table 2.

The next step was to model the MOF / oxide interaction, which includes reproducing the first principles binding energies of BDC to the TiO_2 surface. For consistency, experimental lattice parameters of TiO_2 were used for both sets of calculations on the surface, with the atomic positions fully relaxed in each case. Charges in the cross-linking BDC ligand were re-fitted to reproduce the Ti-O(carb) bond lengths and bind-

Table 1 Relative energy (ΔU_R) of the six models considered for binding of BDC on TiO_2 (shown in Figure 3). The internal energy of binding (ΔU) is calculated with reference to BDC (details in SI). Note models 5 and 6 include the energy of proton transfer to the surface.

Model	ΔU_R (eV)	ΔU (eV)
1	1.231	-1.442
2	1.263	-1.410
3	1.202	-1.472
4	Transforms to model 6	
5	0.870	-1.804
5 (ls)	0.816	-1.858
6	0.000	-2.673
6 (ls)	0.005	-2.668

Table 2 Comparison of structural and mechanical properties of TiO_2 from forcefield (FF) calculations against experimental (Exp.) values. The percentage deviation in the cell parameters is given in parenthesis. The elastic constants are given in GPa, while cell lengths are in Å.

Property	Exp.	FF
a	4.587	4.421 (3.61)
b	4.587	4.421 (3.61)
c	2.954	3.068 (3.87)
C_{11}	268.0	235.3
C_{12}	175.0	178.5
C_{23}	147.0	114.6
C_{33}	484.2	403.9
C_{44}	123.8	108.6
C_{66}	190.2	178.5

ing energies of the most stable protonated (model 3) and deprotonated (model 6) configurations. The reference states, including a required Coulomb correction, are detailed in the SI. When a complete thermodynamic cycle is considered, both the binding energies and proton transfer energies calculated from DFT and FF techniques agree to within 0.1 eV.

3.2.3 MOF-5 on TiO_2: interface structure. The lattice spacing of the MOF-5 epilayer was expanded uniformly to match the more rigid TiO_2 substrate. Note that the calculated bulk moduli are 217.7 GPa for TiO_2 and 8.8 GPa for MOF-5. The uniform expansion in the x and y direction will lead to consistent strain throughout the MOF layer regardless of height of material considered, which may not be consistent with realistic growth, but is unavoidable when implementing periodic boundaries. The atom positions of the vacuum slabs of the protonated oxide and deprotonated MOF were then separately optimised using our forcefield.

The MOF-5 termination consists of two ligands that contact the surface. The ligands are perpendicular, with a difference in rotation of 90° at the surface. Although one ligand (ligand **a**) was initialised as bidentate between two Ti atoms – as identified as the lowest energy position for the isolated ligand – the other (ligand **b**) must be initialised as monodentate above one Ti cation. Only the most stable deprotonated carboxylate model was considered.

For an initial model of the interface between the surfaces of MOF-5 and TiO_2, we first consider the minimum layer thickness of MOF-5 to contain one internal pore as shown by structure 1 in the SI. During optimisation, ligand **b** significantly changes geometry. The ligand begins to tilt relative to the surface normal as the carboxylic acid head rotates. The rotation causes electrostatic repulsion between the carboxylic acid oxygen and the protonated bridging oxygen (O(O-H)) of the TiO_2 surface. As a consequence of this repulsion the O(O-H) is displaced, fulfilling the valence of a neighbouring 5-coordinate Ti site, and the carboxylic acid oxygen becomes incorporated into the surface in place of the O(O-H) bridging group. Two configurations were possible depending on the direction that the ligand initially tilts in, as determined by which side of the carboxylic acid oxygen that the proton was initialised on, with one configuration being 0.094 eV more stable than the latter. The two possible models for ligand **b** as described will be referred to as ligand **b** model 1 and 2 and are depicted in the SI. Ligand **a** remains in bidentate coordination following optimisation and little change in geometry is observed, further confirming the stability of the ground-state configuration of isolated BDC on TiO_2.

First principles calculations were conducted to verify the predicted reconstruction on three positions of the isolated ligand **b** on the surface, systems 1–3 correspond to results given in Table 3: 1. Ligand **b** on the surface prior to reconstruction; 2. Ligand **b** model 1 following surface reconstruction; 3. Ligand **b** model 2 following surface reconstruction. Comparison of relative energies (Table 3) prior to and following the reconstruction of the TiO_2 surface, confirm forcefield predictions of the described reconstruction mechanism at the site of ligand **b** adsorption. Following the reconstruction, the final configuration is the second most energetically favourable position of isolated BDC on the (110) surface of TiO_2, when compared to the identified ground-state configuration (ligand **a** position).

Table 3 First principles relative energies prior to and following the predicted reconstruction of the TiO_2 surface at the site of ligand **b** adsorption. Relative energies are given between the three configurations (Δ U) and also relative to the thermodynamic ground-state configuration ($\Delta\ U^{ground-state}$), illustrated as model 6 in Figure 3.

Position	Δ U (eV)	$\Delta\ U^{ground-state}$ (eV)
1	2.730	3.014
2	0.000	0.284
3	0.037	0.321

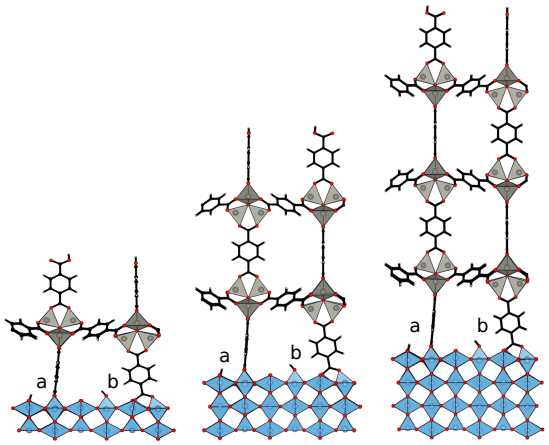

Fig. 5 Structure models considered for different layer thickness of MOF-5 and TiO_2. Ligand **a** and ligand **b** are labelled for each model. Note that each structure is periodic in the xy plane.

3.2.4 MOF-5 on TiO_2: interface energetics. Following the identification of the ground-state surface configuration of TiO_2 when interfaced with MOF-5, the strength of interaction between the layers can be assessed. Several models were constructed to simulate the simultaneous growth of the layers of MOF-5 and TiO_2 (Figure 5). From a plot of layer thickness against total internal energy (see SI), the energy of adhesion can be defined. We calculated this to be 1.43 Jm^{-2} for MOF-5

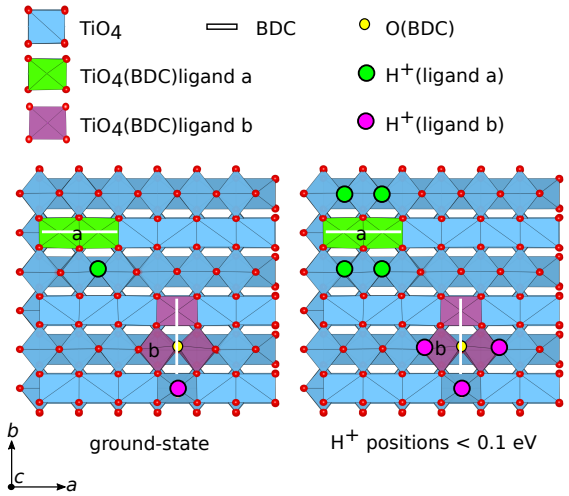

Fig. 6 The (110) surface of TiO_2 with highlighted oxygen sites where proton migration from ligand **a** (green) and ligand **b** (purple) costs < 0.1 eV as predicted by forcefield calculations. TiO_4 polyhedra are highlighted if ligand **a** (green) or ligand **b** (purple) remain bonding to the Ti sites following optimisation. At the site of ligand **b**, an oxygen atom is highlighted (yellow), which belongs to carboxylate group of ligand **b** and has become incorporated into the surface following reconstruction. Ligand orientation (white line) is given for both ligand **a** and **b**. The full structure of the MOF has been removed for clarity.

and TiO_2.

To put 1.43 Jm^{-2} into perspective, values of between between 2–5 Jm^{-2} are typical for metal/metal oxide interfaces, whilst values less than 1 Jm^{-2} are expected for weakly bound interfaces dominated by van der Waals interactions. For example, Kohyama *et al.*[49] calculate the energy of adhesion between Si-terminated SiC with Ti and Al metal surfaces to be 2.52 and 3.74 Jm^{-2}, respectively. In contrast, the interface between multi-layered graphene and SiO_2 has an energy of adhesion of 0.44 Jm^{-2}.[50] The value we report for a MOF / oxide interface therefore suggests a reasonably strong chemical binding.

3.2.5 MOF-5 on TiO_2: proton distribution. To further validate the identified ground-state configurations of the interfacing surfaces, the possibility of proton migration across neighbouring oxide sites were considered for the model of interfacing MOF-5 and TiO_2. An extensive analysis of different proton positions was conducted by migrating the protons along neighbouring oxide bridges of the TiO_2 surfaces and comparing relative energies. Owing the expense of the size of the systems considered, relative energies were calculated with the parameterised forcefield, which can reproduce the binding energy of the proton to the surface as previously predicted by first-principles calculations. The movement of the protons from ligand **a** and **b** were considered separately with configuration descriptions and relative energies reported in the SI.

We calculate for both ligand **a** and **b** that the lowest energy positions of the proton (following deprotonation of the BDC ligands), is to remain on a neighbouring oxide site. Figure 6 highlights the oxide positions surrounding ligand **a** and **b** where proton movement from the identified ground-state configurations costs < 0.1 eV. Interestingly, at the site of ligand **b** a further reconstruction of the surface is observed when substituting in a neighbouring site as highlighted (Figure 6), resulting in the newly protonated oxygen being displaced off-site and tilt of the ligand changing as it rotates into the new position at the surface in its place. The thickness of the MOF layer was found not to affect the binding mechanism of MOF-5 on the surface of TiO_2 (see SI). The same ground-state configurations is maintained for all layer thicknesses considered in this study.

4 Conclusions

A number of viable metal-organic framework / inorganic substrate combinations have been identified that could be used for epitaxial thin-film growth. We have focused on the prototype case of the (011) surface of MOF-5 on the (110) surface of rutile TiO_2, including the initial contact of the ligands, followed by the structure and thermodynamics of complete films. Ideal growth with clean termination of surfaces were considered for this initial analysis of the thermodynamics associated with the growth of MOFs on oxide surfaces. We find that following deprotonation of the BDC ligand, it is thermodynamically favourable for the TiO_2 surface to reconstruct, resulting in the incorporation of a ligand into the surface. The energy of adhesion between MOF-5 and TiO_2 surfaces is calculated to be 1.43 Jm^{-2}, which reflects the significant chemical interaction at the hybrid heterointerface.

5 Acknowledgments

J.K.B is funded by the EPSRC (Grant No. EP/G03768X/1). J.D.G thanks the Australian Research Council for funding under the Discovery Programme, as well as the Pawsey Supercomputing Centre and NCI for the provision of computing resources. A.W. acknowledges support from the Royal Society University Research Fellowship scheme. K.L.S. is funded under ERC Starting Grant 277757 and J.M.S is funded under EPSRC grant no. EP/K004956/1. The work benefited from the high performance computing facility at the University of Bath. Access to the ARCHER supercomputer was facilitated

through membership of the HPC Materials Chemistry Consortium (EP/L000202).

References

1 O. Shekhah, H. Wang, D. Zacher, R. A. Fischer and C. Wöll, *Angew. Chem. Int. Ed.*, 2009, **48**, 5038–5041.
2 L. K. Cadman, J. K. Bristow, N. E. Stubbs, D. Tiana, M. F. Mahon, A. Walsh and A. D. Burrows, *Dalton Trans.*, 2016, **45**, 4316–4326.
3 N. Stock and S. Biswas, *Chem. Rev.*, 2011, **112**, 933–969.
4 D. Zacher, O. Shekhah, C. Wöll and R. A. Fischer, *Chem. Soc. Rev.*, 2009, **38**, 1418–1429.
5 O. Shekhah, *Mater.*, 2010, **3**, 1302–1315.
6 D. Zacher, R. Schmid, C. Wöll and R. A. Fischer, *Angew. Chem. Int. Ed.*, 2011, **50**, 176–199.
7 S. Hermes, F. Schröder, R. Chelmowski, C. Wöll and R. A. Fischer, *J. Am. Chem. Soc.*, 2005, **127**, 13744–13745.
8 B. Liu, M. Ma, D. Zacher, A. Bétard, K. Yusenko, N. Metzler-Nolte, C. Woll and R. A. Fischer, *J. Am. Chem. Soc.*, 2011, **133**, 1734–1737.
9 E. Biemmi, C. Scherb and T. Bein, *J. Am. Chem. Soc.*, 2007, **129**, 8054–8055.
10 C. H. Hendon and A. Walsh, *Chem. Sci.*, 2015, **6**, 3674–3683.
11 R. Ameloot, L. Stappers, J. Fransaer, L. Alaerts, B. F. Sels and D. E. De Vos, *Chem. Mater.*, 2009, **21**, 2580–2582.
12 Y. Yoo and H.-K. Jeong, *Cryst. Growth Des.*, 2010, **10**, 1283–1288.
13 M. Tu and R. A. Fischer, *J. Mater. Chem. A*, 2014, **2**, 2018–2022.
14 L. D. Salmi, M. J. Heikkilä, E. Puukilainen, T. Sajavaara, D. Grosso and M. Ritala, *Microporous Mesoporous Mater.*, 2013, **182**, 147–154.
15 I. Stassen, M. Styles, G. Grenci, H. Van Gorp, W. Vanderlinden, S. De Feyter, P. Falcaro, D. De Vos, P. Vereecken and R. Ameloot, *Nat. Mater.*, 2015, **15**, 304–310.
16 M. Shöâeè, J. R. Agger, M. W. Anderson and M. P. Attfield, *CrystEngComm*, 2008, **10**, 646–648.
17 S. Amirjalayer, M. Tafipolsky and R. Schmid, *J. Phys. Chem. Lett.*, 2014, **5**, 3206–3210.
18 J. K. Bristow, K. L. Svane, D. Tiana, J. M. Skelton, J. D. Gale and A. Walsh, *J. Phys. Chem. C*, 2016, **120**, 9276–9281.
19 K. T. Butler, Y. Kumagai, F. Oba and A. Walsh, *J. Mater. Chem. C*, 2016, **4**, 1149–1158.
20 S. R. Bahn and K. W. Jacobsen, *Comput. Sci. Eng.*, 2002, **4**, 56–66.
21 A. Zur and T. McGill, *J. Appl. Phys.*, 1984, **55**, 378–386.
22 A. Zur, T. McGill and M.-A. Nicolet, *J. Appl. Phys.*, 1985, **57**, 600–603.
23 J. VandeVondele, M. Krack, F. Mohamed, M. Parrinello, T. Chassaing and J. Hutter, *Comput. Phys. Commun.*, 2005, **167**, 103–128.
24 J. P. Perdew, A. Ruzsinszky, G. I. Csonka, O. A. Vydrov, G. E. Scuseria, L. A. Constantin, X. Zhou and K. Burke, *Phys. Rev. Lett.*, 2008, **100**, 136406.
25 S. Grimme, J. Antony, S. Ehrlich and H. Krieg, *J. Chem. Phys.*, 2010, **132**, 154104.
26 M. Krack, *Theor. Chem. Acc.*, 2005, **114**, 145–152.
27 K. A. Peterson and T. H. Dunning Jr, *J. Chem. Phys.*, 2002, **117**, 10548–10560.
28 T. H. Dunning Jr, *J. Chem. Phys*, 1970, **53**, 2823–2833.
29 J. D. Gale, *J. Chem. Soc. Faraday Trans.*, 1997, **93**, 629–637.
30 J. D. Gale and A. L. Rohl, *Mol. Simulat.*, 2003, **29**, 291–341.
31 J. K. Bristow, J. M. Skelton, K. L. Svane, A. Walsh and J. D. Gale, *arXiv preprint arXiv:1607.07285*, 2016.
32 J. K. Bristow, D. Tiana and A. Walsh, *J. Chem. Theory Comput.*, 2014, **10**, 4644–4652.
33 N. L. Allinger, Y. H. Yuh and J. H. Lii, *J. Am. Chem. Soc.*, 1989, **111**, 8551–8566.
34 N. L. Allinger, F. Li and L. Yan, *J. Comput. Chem.*, 1990, **11**, 848–867.
35 B. R. Brooks, C. L. Brooks, A. D. MacKerell, L. Nilsson, R. J. Petrella, B. Roux, Y. Won, G. Archontis, C. Bartels and S. Boresch, *J. Comput. Chem.*, 2009, **30**, 1545–1614.
36 J. Gasteiger and M. Marsili, *Tetrahedron*, 1980, **36**, 3219–3228.
37 J. Gasteiger and M. Marsili, *Tetrahedron Lett.*, 1978, **19**, 3181–3184.
38 S. Hermes, D. Zacher, A. Baunemann, C. Wöll and R. A. Fischer, *Chem. Mater.*, 2007, **19**, 2168–2173.
39 N. Negishi, K. Takeuchi and T. Ibusuki, *J. Mater. Sci.*, 1998, **33**, 5789–5794.
40 D. O. Scanlon, C. W. Dunnill, J. Buckeridge, S. A. Shevlin, A. J. Logsdail, S. M. Woodley, C. R. A. Catlow, M. J. Powell, R. G. Palgrave, I. P. Parkin *et al.*, *Nat. Mater.*, 2013, **12**, 798–801.
41 J. Buckeridge, K. T. Butler, C. R. A. Catlow, A. J. Logsdail, D. O. Scanlon, S. A. Shevlin, S. M. Woodley, A. A. Sokol and A. Walsh, *Chem. Mater.*, 2015, **27**, 3844–3851.
42 A. Tekiel, J. S. Prauzner-Bechcicki, S. Godlewski, J. Budzioch and M. Szymonski, *J. Phys. Chem. C*, 2008, **112**, 12606–12609.
43 S. S. Kaye, A. Dailly, O. M. Yaghi and J. R. Long, *J. Am. Chem. Soc.*, 2007, **129**, 14176–14177.
44 S. Fleming and A. Rohl, *Z. Kristallogr.*, 2005, **220**, 580–584.
45 C. Zhang and P. J. Lindan, *J. Chem. Phys.*, 2003, **118**, 4620–4630.
46 J.-M. Pan, B. Maschhoff, U. Diebold and T. Madey, *J. Vac. Sci. Technol.*, 1992, **10**, 2470–2476.
47 K. Onda, B. Li, J. Zhao, K. D. Jordan, J. Yang and H. Petek, *Science*, 2005, **308**, 1154–1158.
48 B. J. Morgan and G. W. Watson, *J. Phys. Chem. C*, 2009, **113**, 7322–7328.
49 M. Kohyama and J. Hoekstra, *Phys. Rev. B*, 2000, **61**, 2672.
50 S. P. Koenig, N. G. Boddeti, M. L. Dunn and J. S. Bunch, *Nat. Nanotechnol.*, 2011, **6**, 543–546.

Chapter 6

Modulating the pore shape of MOFs

6.1 Paper 5 - Compositional control of pore geometry in multivariate metal–organic frameworks: an experimental and computational study

Controlling the materials properties of MOFs extends further than optical absorption or mechanical hardness often tuned for inorganic materials. Other properties such as pore shape and chemical interactions within the pore can be tuned by changing the composition of the frameworks. In the following paper we report how varying the concentration of halogen (X) substituents on the ligands comprising a Zn^{2+}/BDC(1-X)/DABCO MOF named DMOF-1, changes the ground state pore shape. Varying the favoured pore shape means changing the ground state symmetry of the MOF, which can be appropriate for many applications including responsive drug delivery and reversible gas absorption. In the following paper, we conduct calculations to support experimental work, to firstly identify the ground state pore shape with increasing concentration of Cl, Br and I substituents. We then further calculate the energy profiles for converting between different pore shapes using the nudged elastic band method, and finally analyse the non-covalent interactions in the system to explain the variation in observed ground state pore shape.

Non-covalent interactions (as depicted between 2 example molecules in Figure 6-1), originate from dispersive interactions between instantaneous-instantaneous, and induced-instantaneous dipoles due to spontaneous polarisation of atoms in molecules.[259] In the following paper we show non-covalent interactions control the pore shape of the different compositions of halogen substituted DMOF-1, which demonstrates the importance of non-covalent interactions and the control they have on final material properties, particularly in MOFs.

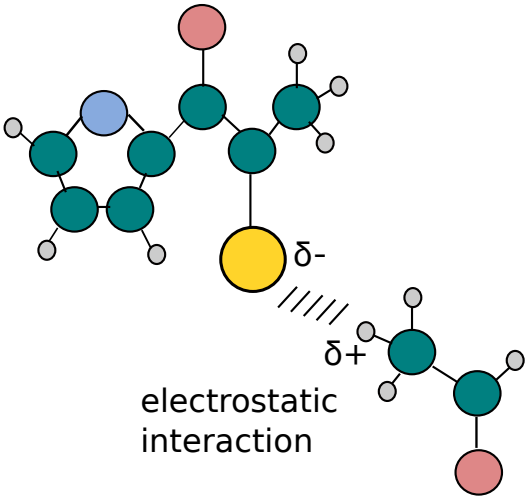

Figure 6-1: Schematic of an electrostatic interaction between two organic molecules

6.1.1 Additional ESI

The climbing image solid-state nudged elastic band method

The nudged elastic band (NEB) method is used to calculate the minimum energy reaction pathways (MEP) between two relaxed configurations.[260] A linear interpolation along a path between initial and final configurations allows the generation of images, which represent intermediate configurations. The NEB forces (F_i^{NEB}) on each image (i) are given by:

$$F_i^{NEB} = F_i^{s||} + F_i^{\nabla\perp} \tag{6.1}$$

where, $F_i^{s||}$ is the spring force parallel to the path and $F_i^{\nabla\perp}$ is the force due to the gradient of the potential, which is calculated from the potential force (F_i^{∇}) and a up-winding tangent in a positive gradient direction ($\hat{\tau}_i$):

$$F_i^{\nabla\perp} = F_i^{\nabla} - (F_i^{\nabla}.\hat{\tau}_i)\hat{\tau}_i \tag{6.2}$$

Spring constants are then added along the path to ensure even spacing between the generated images during relaxation, considering the vector on each image ($\mathbf{R}_i$):

$$F_i^{s||} = k(|\mathbf{R}_{i+1} - \mathbf{R}_i| - |\mathbf{R}_i - \mathbf{R}_{i-1}|)\hat{\tau}_i \tag{6.3}$$

The relaxation of each image along the path allows the MEP between initial and final configuration to be calculated. The climbing image (CI) NEB is an extension used to find "true" saddle-points, which represent transition points on the potential energy surface. During a CI-NEB calculation the highest

energy image is considered to be the transition state. Parallel forces from applied spring constants (Equation 6.3) are not applied to this image, allowing the spacing between neighbouring images to differ and the configuration to fully relax by maximising the perpendicular forces (Equation 6.2).[260]

$$\mathbf{v}_1 = (h_{1x}, 0, 0) \tag{6.4}$$

$$\mathbf{v}_2 = (h_{2x}, h_{2y}, 0) \tag{6.5}$$

$$\mathbf{v}_3 = (h_{3x}, h_{3y}, h_{3z}) \tag{6.6}$$

In solid-state (SS) NEB calculations, a final consideration required is the variation in volume of the unit cell along the calculated MEP. Any unit cell (h), can be considered as 3 vectors, $\mathbf{v}_1$ (Equation 6.4), $\mathbf{v}_2$ (Equation 6.5) and $\mathbf{v}_3$ (Equation 6.6) and 6 degrees of freedom in a triangular matrix:

$$\begin{pmatrix} h_{1x} & 0 & 0 \\ h_{2x} & h_{2y} & 0 \\ h_{3x} & h_{3y} & h_{3z} \end{pmatrix}$$

The changes in unit cell volume are then accounted for by Hooke's law as a function of strain on the system:

$$(h^{def} - h) = Y^{-1}(h.\sigma) \tag{6.7}$$

where, h^{def} is the change in unit cell lattice vectors, Y is the Young's modulus, and σ is the stress tensor. Further considerations for coupling the scaled unit cell volumes and atomic positions are required.[260]

The SS-CI-NEB is an approach that allows accurate MEP between two known configurations to be calculated, and is particularly useful for obtaining energy pathways during phase changes of materials, providing that the number of atoms in the unit cell remain the same along the pathway. In the following paper the CI-SS-NEB method is used to calculation energy pathways between different symmetries of DMOF-1 with varying concentrations of halogen substituents.

6.1.2 Personal contribution

My personal contribution to the paper entitled *"Compositional control of pore geometry in multivariate metal-organic frameworks: an experimental and computational study"* included calculating the ground state pore topology of each MOF with differing substituent and calculating energy profiles between the different topologies with a nudged elastic band approach. D. Tiana calculated the non-covalent

interaction plots using a topological analysis with DFT. L. Cadman, N. Stubbs and M. Mahon did all experimental synthesis, characterisation and analysis on the structures.

6.1.3 Access statement

Dalton Transactions

PAPER

View Article Online
View Journal | View Issue

Cite this: *Dalton Trans.*, 2016, **45**, 4316

Compositional control of pore geometry in multivariate metal–organic frameworks: an experimental and computational study†

Laura K. Cadman, Jessica K. Bristow, Naomi E. Stubbs, Davide Tiana, Mary F. Mahon,* Aron Walsh* and Andrew D. Burrows*

Received 15th October 2015,
Accepted 2nd December 2015

DOI: 10.1039/c5dt04045k

www.rsc.org/dalton

A new approach is reported for tailoring the pore geometry in five series of multivariate metal–organic frameworks (MOFs) based on the structure $[Zn_2(bdc)_2(dabco)]$ (bdc = 1,4-benzenedicarboxylate, dabco = 1,8-diazabicyclooctane), DMOF-1. A doping procedure has been adopted to form series of MOFs containing varying linker ratios. The series under investigation are $[Zn_2(bdc)_{2-x}(bdc\text{-}Br)_x(dabco)]\cdot n$DMF **1** (bdc-Br = 2-bromo-1,4-benzenedicarboxylate), $[Zn_2(bdc)_{2-x}(bdc\text{-}I)_x(dabco)]\cdot n$DMF **2** (bdc-I = 2-iodo-1,4-benzenedicarboxylate), $[Zn_2(bdc)_{2-x}(bdc\text{-}NO_2)_x(dabco)]\cdot n$DMF **3** ($bdc\text{-}NO_2$ = 2-nitro-1,4-benzenedicarboxylate), $[Zn_2(bdc)_{2-x}(bdc\text{-}NH_2)_x(dabco)]\cdot n$DMF **4** ($bdc\text{-}NH_2$ = 2-amino-1,4-benzenedicarboxylate) and $[Zn_2(bdc\text{-}Br)_{2-x}(bdc\text{-}I)_x(dabco)]\cdot n$DMF **5**. Series **1–3** demonstrate a functionality-dependent pore geometry transition from the square, open pores of DMOF-1 to rhomboidal, narrow pores with increasing proportion of the 2-substituted bdc linker, with the rhomboidal-pore MOFs also showing a temperature-dependent phase change. In contrast, all members of series **4** and **5** have uniform pore geometries. In series **4** this is a square pore topology, whilst series **5** exhibits the rhomboidal pore form. Computational analyses reveal that the pore size and shape in systems **1** and **2** is altered through non-covalent interactions between the organic linkers within the framework, and that this can be controlled by the ligand functionality and ratio. This approach affords the potential to tailor pore geometry and shape within MOFs through judicious choice of ligand ratios.

Introduction

Metal–organic frameworks (MOFs) have structures that contain extended co-ordination networks of metal centres connected by bridging organic ligands.[1,2] Materials chemistry has seen a rapid growth in the study of MOFs in recent years due largely to their potential for porosity and the extensive range of applications, such as gas storage,[3] separations[4] and drug delivery,[5] that derive from this.

Making changes to the structure and geometry of the bridging ligand is a powerful route to optimising pore size and shape.[6] The IRMOF series, for example, consists of MOFs of the general formula $[Zn_4OL_3]$ where L is a linear dicarboxylate.[7] The pore size of the MOF can be increased through extension of L, or decreased by introducing a substituent onto L that projects into the pores. To illustrate the utility of this, analysis of the IRMOF series allowed identification of the MOF with optimum pore size for methane adsorption.[7] The lengthening of organic linkers can lead to less stable frameworks and on some occasions result in different topologies or interpenetration.

Multivariate MOFs (MTV-MOFs), mixed-component MOFs in which two or more linkers play the same structural role, allow for the incorporation of multiple functionalities into the structure whilst maintaining the framework topology.[8–10] Here we present a route to the tuning of pore geometry in DMOF-1 type structures of the general formula $[Zn_2L_2(dabco)]$ (L = dicarboxylate, dabco = 1,8-diazabicyclooctane) in which two linkers of the same length, but differing in the functional groups attached to the aromatic ring, are used in the synthesis.

DMOF-1 is a zinc-based pillared MOF of the form $[Zn_2(bdc)_2(dabco)]$ (bdc = 1,4-benzenedicarboxylate).[11,12] The as-synthesised form of the MOF contains a cubic framework with square pores in which the bdc linkers are bent away slightly from the square grid, and solvent molecules (DMF, H_2O) are present as guests within the pores. The framework geometry is maintained upon removal of the included solvent,

Department of Chemistry, University of Bath, Claverton Down, Bath BA2 7AY, UK. E-mail: a.d.burrows@bath.ac.uk

†Electronic supplementary information (ESI) available: Syntheses, characterisation and computational details. CCDC 1401468–1401475 and 1431185. For ESI and crystallographic data in CIF or other electronic format see DOI: 10.1039/c5dt04045k

though the activated MOF contains linear bdc linkers and a regular square grid. The framework also displays guest-induced flexibility, resulting in a compressed structure upon the inclusion of benzene into the pores.

Flexible MOFs have received increasing attention due to their interesting properties.[13,14] For example, they often display reversible structural alterations in response to solvent changes, temperature or pressure. Several studies have shown that replacing the bdc ligands in DMOF-1 with another dicarboxylate can result in alterations of the pore size and shape, similar to the guest-induced behaviour (Fig. 1).[6,15–17]

Given the success in replacing the bdc linker in DMOF-1 with structurally similar dicarboxylate ligands,[15,18,19] a synthetic strategy was developed to investigate the potential for forming mixed-ligand frameworks related to this material. Multivariate analogues of DMOF-1 have been prepared previously, either through use of mixtures of dicarboxylic acids in the synthesis[6,12] or incomplete post-synthetic modification of [Zn(bdc-NH_2)$_2$(dabco)] (bdc-NH_2 = 2-amino-1,4-benzenedicarboxylate).[15] However, the effect of the linker ratio on the pore geometry has, to the best of our knowledge, not previously been studied. Here we report a systematic approach through which pore compression can be enhanced and pore size control can be achieved. A multivariate approach is adopted to fine tune the structures and properties of several series of MOFs relating to the DMOF-1 framework. A second dicarboxylic acid which is functionally substituted at the *ortho*-position on the benzene ring, referred to generically as H_2bdc-X, was introduced into the reaction mixture in varying ratios of H_2bdc : H_2bdc-X. By employing this doping procedure, MOF libraries of the form [Zn_2(bdc)$_{2-x}$(bdc-Br)$_x$(dabco)]·*n*DMF **1** (bdc-Br = 2-bromo-1,4-benzenedicarboxylate), [Zn_2(bdc)$_{2-x}$(bdc-I)$_x$(dabco)]·*n*DMF **2** (bdc-I = 2-iodo-1,4-benzenedicarboxylate), [Zn_2(bdc)$_{2-x}$(bdc-NO_2)$_x$(dabco)]·*n*DMF (bdc-NO_2 = 2-nitro-1,4-benzenedicarboxylate) **3** and [Zn_2(bdc)$_{2-x}$(bdc-NH_2)$_x$(dabco)]·*n*DMF **4** were prepared and characterised. In a similar manner, the series [Zn_2(bdc-Br)$_{2-x}$(bdc-I)$_x$(dabco)]·*n*DMF **5** was prepared through the use of different ratios of H_2bdc-Br and H_2bdc-I in the reaction mixture.

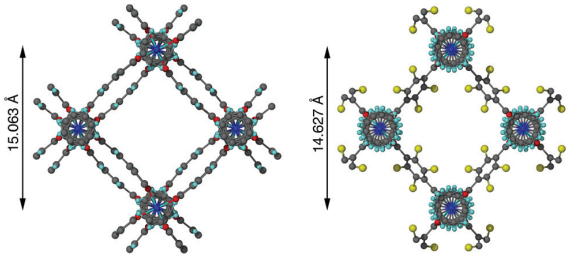

Fig. 1 Pore structure of [Zn_2(bdc)$_2$(dabco)]·4DMF·0.5H_2O (left) and [Zn_2(bdc-Br)$_2$(dabco)] (right), the latter showing a slight diagonal compression of the pore with the addition of bromine substituents into the framework. The bromine atom in [Zn_2(bdc-Br)$_2$(dabco)] is disordered over four positions.

Results and discussion

Synthesis and composition

The reaction of $Zn(NO_3)_2$·6H_2O with dabco and mixtures of dicarboxylic acids in varying ratios in DMF at 120 °C for 3 days afforded crystalline products for all members of series **1–5**. All products were formed in good yields of approximately 60–80%. For members of series **1**, **3** and **5**, colourless block crystals were produced, whereas the compounds in series **2** yielded colourless needles and those in series **4** gave orange-brown block crystals. The composition of all compounds in series **1–5** were determined using ^{1}H NMR spectroscopy on acid-digested samples of the dried MOFs. In addition to studying bulk samples, NMR spectra were also recorded on one individual acid-digested crystal for select members of series **1**, **3**, **4** and **5**. These ^{1}H NMR spectra showed the presence of both bdc and bdc-X ligands in each sample, demonstrating the successful formation of multivariate MOFs as opposed to physical mixtures containing two discrete phases.

The integral analyses from the spectra taken of both bulk and individual crystal samples of series **1**, **3** and **4** showed that all members of these series had a ligand ratio composition similar to that present in the reaction mixture, thus demonstrating that there were no significant ligand preferences and that the composition can be controlled through the relative reactant concentrations. This is in contrast to observations on the IRMOF system, for which there were significant differences between the ratios of linkers used in the reaction mixture and those observed in the products.[9,10]

Series **1**, **3** and **4** showed little compositional variation within the bulk phase itself, with a comparison of the integrals from individual crystal samples to those of the bulk products indicating only small variations between samples from the same batch (<3% of the mean value quoted).

In contrast, analysis of the integrals in the ^{1}H NMR spectra of series **2** and **5** revealed evidence of strong ligand preferences. In both of these series the bdc-I ligand is preferentially excluded in favour of the other dicarboxylate. In series **2** this resulted in an incorporation of up to 20% more bdc into the framework than was present in the reaction mixture, and in series **5** there was up to 24% more bdc-Br in the framework than was expected from the reaction mixture (Fig. 2).

X-ray diffraction analysis of [Zn_2(bdc)$_{2-x}$(bdc-Br)$_x$(dabco)]·*n*DMF 1

All members of series **1** gave powder XRD patterns containing the same general features, suggesting all compounds possess similar framework topologies. A closer inspection revealed the presence of two unique phases, which can be identified in the PXRD patterns through differences in their peak positions (Fig. 3). Above a bdc-Br content of 54%, peaks at 2θ 8.4° and 16.7° shift to lower values. These subtle alterations in the PXRD patterns suggest that the products with a higher bdc-Br content contain structural differences (concurrent with altered unit cell parameters) to those with lower bdc-Br content. The PXRD patterns from the samples with 39% and 54% bdc-Br

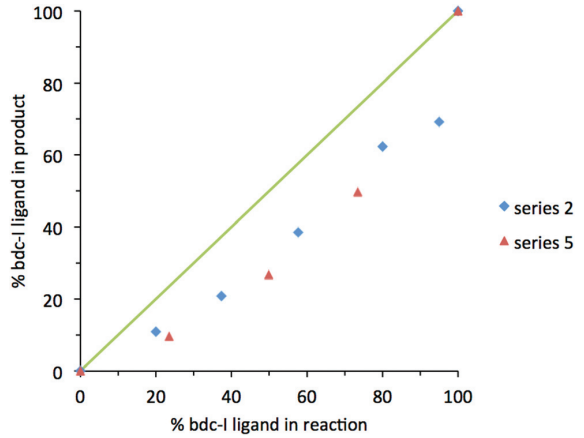

Fig. 2 The percentage inclusion of bdc-I into $[Zn_2(bdc)_{2-x}(bdc\text{-}I)_x(dabco)]\cdot n$DMF **2** and $[Zn_2(bdc\text{-}Br)_{2-x}(bdc\text{-}I)_x(dabco)]\cdot n$DMF **5**, plotted against the percentage bdc-I in the reaction mixture.

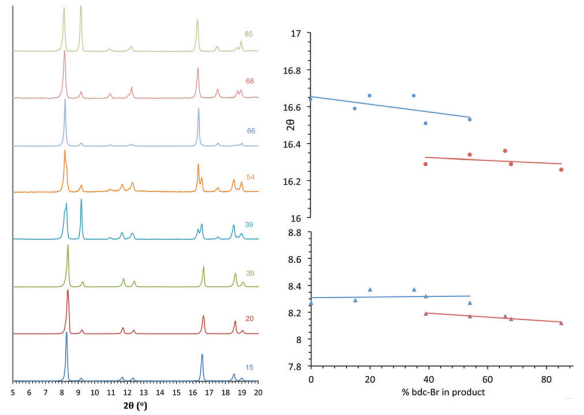

Fig. 3 PXRD patterns of the compounds $[Zn_2(bdc)_{2-x}(bdc\text{-}Br)_x(dabco)]\cdot n$DMF **1**, with the number shown against each powder pattern denoting the % bdc-Br in the sample. The plot of 2θ against % bdc-Br shows the key peaks which shift with the change in pore topology.

show elements of the traces from both pore types (Fig. 3), suggesting that both phases are present in these samples.

Four of the ligand ratios used yielded crystals that were suitable for single crystal X-ray diffraction, and these compounds were structurally characterised as $[Zn_2(bdc)(bdc\text{-}Br)(dabco)]\cdot$DMF **1a**, $[Zn_2(bdc)_{0.8}(bdc\text{-}Br)_{1.2}(dabco)]\cdot$DMF **1b**, $[Zn_2(bdc)_{0.4}(bdc\text{-}Br)_{1.6}(dabco)]$ **1c** and $[Zn_2(bdc)_{0.3}(bdc\text{-}Br)_{1.7}(dabco)]$ **1d**. The crystal structures of all contain the expected DMOF-1 framework topology, consistent with PXRD results. Thus the structures all contain paddlewheel units formed from two Zn(II) centres bridged by four carboxylate groups and with nitrogen donors from dabco ligands occupying the axial sites. The bridging dicarboxylate and dabco ligands link these secondary building units (SBUs) into three-dimensional networks. In all four structures, the bromine atoms exhibited positional disorder over the four available positions of the benzene ring.

A clear difference in the crystal structures is observed between the lower bdc-Br content structures **1a** and **1b** and the higher bdc-Br content structures **1c** and **1d**. Compounds **1a** and **1b** crystallise in a tetragonal space group and display a distorted square grid topology (Fig. 4a), similar to that observed in the solvated DMOF-1 structure. For both of these structures the dicarboxylate linker is bent, arching away from a linear arrangement and causing a distortion to the regular square grid topology of the framework. These distortions alternate into and out of the pore between each layer of the framework leading to square channels throughout the structure (Fig. 4b).

In contrast to **1a** and **1b**, compounds **1c** and **1d** crystallise in an orthorhombic space group and display pores of a rhomboidal, narrow geometry (Fig. 4c). A comparison of the frameworks of **1c** and **1d** to that of $[Zn_2(bdc\text{-}Br)_2(dabco)]$[19] show that the pores in the mixed-ligand structures are compressed to a higher degree than in the single ligand parent (Table 1).

The change in pore size and shape in series **1** with increased bdc-Br content is accompanied by a loss of the dicarboxylate distortion shown in **1a** and **1b**. The subtle changes observed in the experimental PXRD patterns from low to high bdc-Br content reflect changes in the unit cell parameters that occur with the change in pore geometry. Further analysis of these structures has been addressed by a computational study (*vide infra*).

In contrast to most of the MOFs in this paper, the experimental powder X-ray diffraction patterns of **1c** and **1d** showed a number of differences in the positions of the peaks to those in the X-ray powder diffraction patterns simulated from the

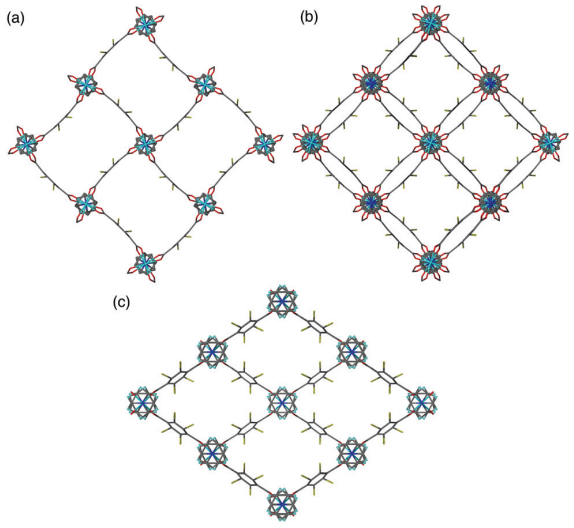

Fig. 4 (a) The individual distorted square pores in $[Zn_2(bdc)(bdc\text{-}Br)(dabco)]\cdot$DMF **1a**, (b) square channels in $[Zn_2(bdc)(bdc\text{-}Br)(dabco)]\cdot$DMF **1a** viewed over multiple layers, (c) the rhomboidal pores in $[Zn_2(bdc)_{0.4}(bdc\text{-}Br)_{1.6}(dabco)]$ **1c**.

Table 1 Zn···Zn distances in single and mixed-ligand systems of $[Zn_2(bdc)_{2-x}(bdc\text{-}Br)_x(dabco)]$ **1**

Structure	Pore shape	Shortest pore diagonal Zn···Zn (Å)
$[Zn_2(bdc)_2(dabco)]\cdot 4DMF\cdot 0.5H_2O$ (DMOF-1)[11]	Distorted square	15.063
[Zn2(bdc)(bdc-Br)(dabco)]·DMF **1a**	Distorted square	14.988
$[Zn2(bdc)_{0.8}(bdc\text{-}Br)_{1.2}(dabco)]\cdot DMF$ **1b**	Distorted square	14.976
$[Zn2(bdc)_{0.4}(bdc\text{-}Br)_{1.6}(dabco)]$ **1c**	Rhomboidal	12.759
$[Zn2(bdc)_{0.3}(bdc\text{-}Br)_{1.7}(dabco)]$ **1d**	Rhomboidal	12.858
$[Zn_2(bdc)_{0.48}(bdc\text{-}Br)_{1.52}(dabco)]$ **1c′**	Rhomboidal	14.229
$[Zn_2(bdc\text{-}Br)_2(dabco)]$[19]	Rhomboidal	14.627

single crystal studies. These differences were suspected of being related to the difference in temperature at which the diffraction patterns were generated – the experimental pattern was collected at ambient temperature whereas the single crystal X-ray diffraction data were collected at 150 K. To test this theory, the single crystal data for **1c** was re-collected at ambient temperature (**1c′**). While the overall topology of **1c′** is similar to that of **1c**, crystallising in an orthorhombic space group and presenting rhomboidal pores, significant changes in the unit cell parameters were observed. The compression of the pores is more acute in **1c** than in **1c′** (Table 1) accounting for the changes in unit cell parameters observed. After the room temperature data collection, the crystal of **1c′** was cooled to 150 K and the unit cell parameters collected at that temperature matched those of **1c**. The reversible unit cell parameter shift from **1c** to **1c′** leads to a movement of peaks in the generated diffraction pattern, and the experimental patterns recorded for the bulk samples of **1c** and **1d** at room temperature match well to that simulated from the single crystal structure of **1c′** (Fig. S24†). The slight difference in bdc : bdc-Br ratio between **1c** and **1c′** is insignificant, and a consequence of different crystals being used in the analyses and the softness in determining site occupancy factors against a backdrop of the disorder noted.

X-ray analysis of $[Zn_2(bdc)_{2-x}(bdc\text{-}I)_x(dabco)]\cdot n$DMF 2

Similar structural trends to those found in series **1** are observed in $[Zn_2(bdc)_{2-x}(bdc\text{-}I)_x(dabco)]\cdot n$DMF **2**. All members of series **2** display powder diffraction patterns with the same gross features as those in DMOF-1, suggesting all multivariate species are isoreticular. As with series **1** there is a transition point within the PXRD patterns indicating a change from one crystal system to another (Fig. 5). This transition is characterised through peak position shifts similar to those observed in the brominated series and can therefore be identified as a change in the pore geometry of the framework from square to rhomboidal.

The bdc : bdc-I ratio in the products of series **2** were determined by bulk NMR spectroscopy. Integral analysis shows a clear preference for bdc inclusion into the product framework

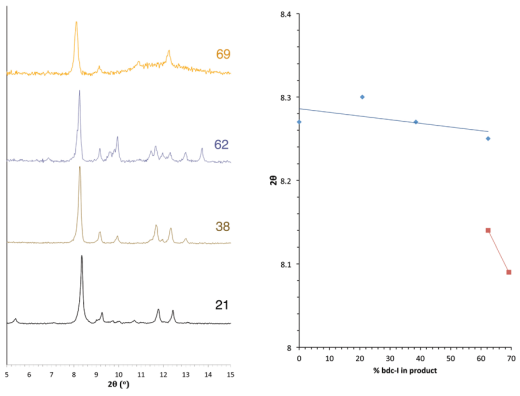

Fig. 5 PXRD patterns of the compounds $[Zn_2(bdc)_{2-x}(bdc\text{-}I)_x(dabco)]\cdot n$DMF **2** with the number shown against each powder pattern denoting the % bdc-I in the sample. The plot of 2θ against % bdc-I shows the key peak which shifts with the change in pore topology.

at the expense of the bdc-I ligand, and is consistent for all products of series **2**. Due to the strong ligand preferences observed, the square pore to rhomboidal pore transition does not occur until loadings of approximately 90% in the reaction mixture; equivalent to 60% bdc-I in the MOF. Taking the ratio of bdc : bdc-I in the framework into account, the shift from square to rhomboidal pore geometries occurs at approximately the same product stoichiometry for series **1** and series **2**. The small size and needle-like nature of the crystals from series **2** meant that single crystal X-ray diffraction was not possible for any of the compounds in this series.

X-ray diffraction analysis of $[Zn_2(bdc)_{2-x}(bdc\text{-}NO_2)_x(dabco)]\cdot n$DMF 3

The PXRD patterns from $[Zn_2(bdc)_{2-x}(bdc\text{-}NO_2)_x(dabco)]\cdot n$DMF **3** show a similar trend to those observed in the bdc-Br and bdc-I analogues, **1** and **2**. Products which contain a stoichiometry of >60% bdc-NO_2 give diffraction patterns with a shift of peaks along with the loss and appearance of others (Fig. 6) when compared with those with low bdc-NO_2 content.

These changes are consistent with the premise that a change in the pore geometries and lattice parameters are occurring. In the sample containing 59% bdc-NO_2, the PXRD pattern clearly shows the presence of both square-pore and rhomboidal-pore phases of the MOF (Fig. 6).

Single crystal X-ray analysis was carried out on $[Zn_2(bdc)_{1.2}(bdc\text{-}NO_2)_{0.8}(dabco)]\cdot 2.5$DMF **3a** confirming this compound contains a distorted square pore framework (Fig. 7), similar to those of **1a** and **1b** and consistent with the PXRD data. Single crystal X-ray diffraction of compound $[Zn_2(bdc)_{0.6}(bdc\text{-}NO_2)_{1.4}(dabco)]\cdot n$DMF **3b** was also carried out and it showed unit cell parameters similar to those for **1c** and **1d**, indicating that the rhomboidal pore form of this species is accessible. As data quality for **3b** were poor, with disorder precluding any additional insight into the factors affecting pore

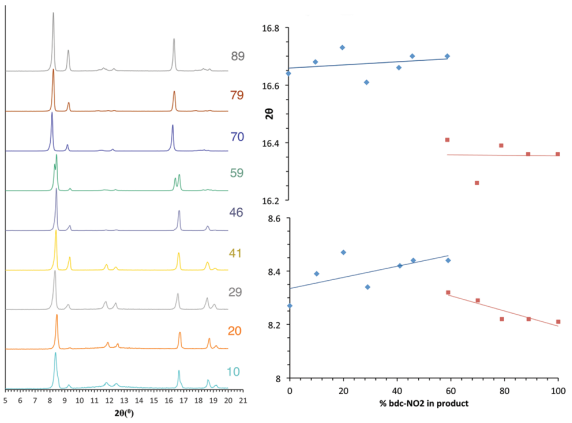

Fig. 6 PXRD patterns of the compounds $[Zn_2(bdc)_{2-x}(bdc\text{-}NO_2)_x(dabco)]\cdot n$DMF **3** with the number shown against each powder pattern denoting the % bdc-NO_2 in the sample. The plot of 2θ against % bdc-NO_2 shows the key peaks which shift with the change in pore topology.

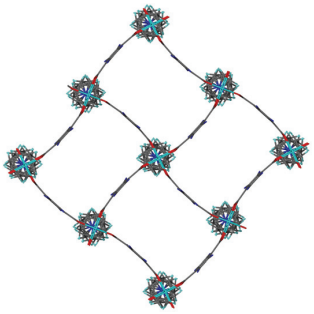

Fig. 7 Structure of the network in $[Zn_2(bdc)_{1.2}(bdc\text{-}NO_2)_{0.8}(dabco)]\cdot 2.5$DMF **3a** showing a view of one layer of the framework as viewed along the *c*-axis, demonstrating the distorted bdc linkers.

geometry, this crystal structure has not been presented herein (see ESI†).

In contrast to series **1** and **2**, a second transition in series **3** is observed at 100% bdc-NO_2 content *i.e.* $[Zn_2(bdc\text{-}NO_2)_2(dabco)]$ which crystallises in a tetragonal crystal lattice with square pore geometry.[18] This means that rhomboidal pores with bdc-NO_2 are only possible in a multivariate system, and furthermore the multivariate approach allows the attainment of pore geometries containing particular functional groups that cannot otherwise be accessed.

X-ray diffraction analysis of $[Zn_2(bdc)_{2-x}(bdc\text{-}NH_2)_x(dabco)]\cdot n$DMF 4

In contrast to series **1–3**, the PXRD patterns for compounds of series $[Zn_2(bdc)_{2-x}(bdc\text{-}NH_2)_x(dabco)]\cdot n$DMF **4** show no evidence for a transition between structures containing square and rhomboidal pores (Fig. S19†). Instead, all of the frameworks display powder diffraction patterns that correspond to the square pore form. Further evidence is provided by single crystal analyses completed upon $[Zn_2(bdc)_{1.6}(bdc\text{-}NH_2)_{0.4}(dabco)]\cdot 2.6$DMF **4a** and $[Zn_2(bdc)_{0.2}(bdc\text{-}NH_2)_{1.8}(dabco)]\cdot 1.5$DMF **4b**. Both of these MOFs show similar connectivity and topology to that of DMOF-1, and display distorted square pores, despite significantly different loadings of the bdc-NH_2 ligand in the framework.

Whilst a comparison to series **1–3** might lead to the assumption that both **4a** and **4b** would crystallise in tetragonal settings, there is a change in space group from tetragonal in the case of **4a** to monoclinic in the case of **4b**. The structure of **4b** is overall very similar to that of **4a** but shows a minor deviation in the alignment of the crystal sheets as viewed along the *b*-axis causing a distortion of the neighbouring dabco units (Fig. 8). This corresponds in the β angle shifting away from the required 90° of the tetragonal species, to 94.727(2)°.

X-ray diffraction analysis of $[Zn_2(bdc\text{-}Br)_{2-x}(bdc\text{-}I)_x(dabco)]\cdot n$DMF 5

The series $[Zn_2(bdc\text{-}Br)_{2-x}(bdc\text{-}I)_x(dabco)]\cdot n$DMF **5** was formed through varying the ratios of the two substituted ligands bdc-Br and bdc-I. As with series **1–4**, the formations of the multivariate products were identified through ^{1}H NMR spectroscopy. PXRD analysis of the products showed similarities to that of DMOF-1, indicating that isoreticular structures had been formed. No evidence for a transition between structural types was observed (Fig. S20†).

The products from a reaction mixture ratio of 50% H_2bdc-Br and H_2bdc-I yielded crystals suitable for single crystal X-ray diffraction. The crystal structure was solved in an orthorhombic space group and identified as $[Zn_2(bdc\text{-}Br)_{1.4}(bdc\text{-}I)_{0.6}(dabco)]\cdot 2.6$DMF **5a**. The structure shows the presence of rhomboidal pores, similar to those observed in **1c** and **1d**. Unlike the mixed bdc/bdc-Br and bdc/bdc-I series, **1** and **2** respectively, the compounds in series **5** always contain 100% halogenated ligands, but with varying ratios of bdc-Br and bdc-I. The lack of any changes in the peak positions within the PXRD patterns of **5** suggests that all species from this series crystallise in the rhomboidal pore form. This is consistent with findings from compounds with high loadings of bdc-Br and bdc-I from series **1** and **2**.

Materials modelling

Given the changes observed in pore geometry with composition in compounds from series **1–3** and the contrasting lack of changes observed in series **4** and **5**, atomistic simulations were undertaken in order to gain insight into these observations.

Further to assessing the energy difference between different phases, we also probed potential transitions between the structures in order to gain insight into the dynamic stability. Solid-state nudged elastic band (SS-NEB) calculations between symmetry representative structures were performed using VASP at the DFT/PBEsol level of theory.[20–24] The saddle point in potential energy obtained between two stable polymorphs (within SS-NEB) can be used to predict the activation energy associated

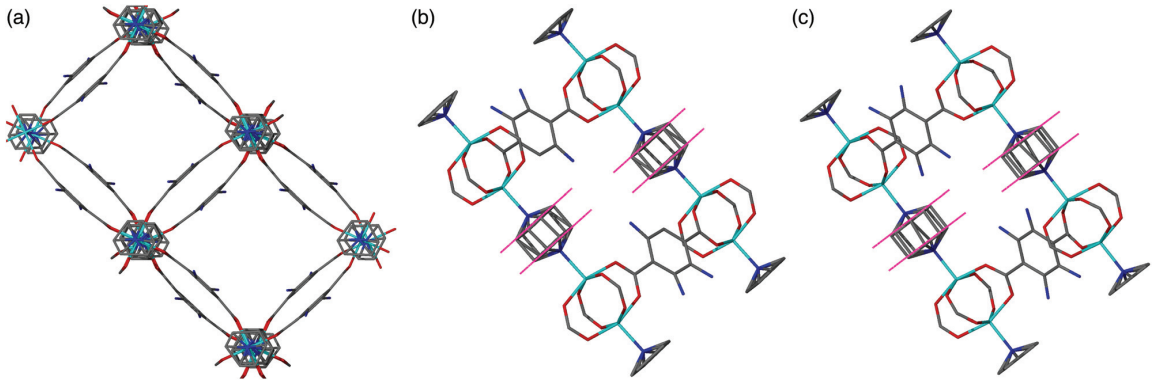

Fig. 8 (a) Structure of the distorted square pore form of $[Zn_2(bdc)_{0.2}(bdc\text{-}NH_2)_{1.8}(dabco)]\cdot 1.5DMF$ **4b** as viewed down the *c*-axis. (b) View of **4b** along the *b*-axis showing the offset nature of the neighbouring dabco ligands. (c) View of $[Zn_2(bdc)_{1.6}(bdc\text{-}NH_2)_{0.4}(dabco)]\cdot 2.6DMF$ **4a** along the *b*-axis showing the neighbouring dabco ligands in-line with one another. In all cases included solvent molecules and hydrogen atoms have been removed for clarity.

with the possible structural transformation. Full computational details can be found in the ESI.†

Two different 100% halogenated structures were modelled for series **1** and **2**. The first halogenated model has Br/I substituted alternatively on each side of neighbouring aromatic rings (A), resulting in 50% of the halogens within each neighbouring pore. The second model has halogen substitution with the same overall concentration but with the halogens on neighbouring rings located within the same pore (S) (Fig. 9). These models allow us to assess the effect of local halogen orientation and concentration, which may influence the phase stability.

Three pore topologies were considered: perfect square, distorted square and rhomboid for each halogen substituent and un-substituted (100% bdc) framework. The relative energies of each topology with respect to the distorted pore structures are given in Table 2, with calculated activation energies between each phase.

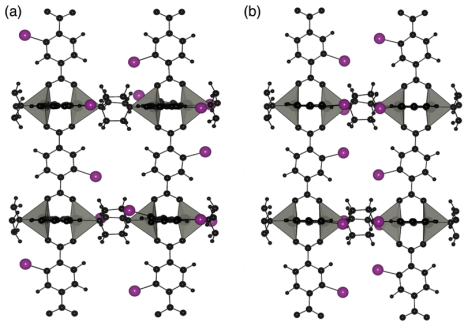

Fig. 9 Halogen substitution positions modelled in DMOF-1. (a) Substitution within alternating pores (A) and (b) substitution in the same pore (S), with the halogen atoms shown in purple.

Calculated relative energies (Table 2) of the structures support the observed behaviours of the frameworks with higher concentrations of halogenated-bdc (*i.e.* in series **1** and **2**). In particular, the relative energy between the square and rhomboidal pore structures is lowest for the 100% bdc structure whereas the perfect square pore structure becomes less accessible with increasing halogen content, supporting the experimental observation that with increasing halogen content the square pore structure is not formed.

When considering the relative energies between square and rhomboid structures with 100% bdc, 100% bdc-Br (A) or 100% bdc-I (A), the rhomboid form is the higher energy configuration. In contrast, for either the 100% bdc-Br (S) or 100% bdc-I (S), where there is a high concentration of Br in half of the pores, the rhomboidal form is more stable. This observation suggests that above a certain concentration of halogen within a pore, there is a thermodynamic driving force for the formation of the narrow, rhomboidal pore framework.

Potential energy profiles showing the activation energies between structures (as given in Table 2) for the three hypothetical structural transformations are depicted in Fig. 10 to further evaluate the thermodynamic stabilities of each structure. Three structural transitions were considered:

Transition 1: 'Distorted square' to 'square' pore structure. This defines activation energy $E_{act}(1)$ required to remove the structural distortion following solvent evacuation.

Transition 2: 'Distorted square' to 'rhomboid' pore structure. This defines activation energy $E_{act}(2)$ for the compression of the pores observed in some mixed-ligand structures.

Transition 3: 'Perfect square' to 'rhomboid' pore structure. This defines activation energy $E_{act}(3)$ associated with compressing the structure from a higher symmetry square pore form. It is also associated with MOF 'breathing' and structural flexibility.

The energy profiles further support the observed behaviour of the frameworks. Each structure is locally stable and

Table 2 Relative total energies between perfect square, distorted square and narrow pore structures in kJ mol^{-1}. Note that the reported energy of each structure is relative to the distorted pore structure of DMOF-1. Activation energies reported for Transition 1 are from the distorted to perfect square, from distorted to the rhomboid pore structure for Transition 2 and from square to rhomboid pore structure for Transition 3

Ligand	Perfect square pore	Distorted square pore	Rhomboidal pore	$E_{act}(1)$/kJ mol^{-1}	$E_{act}(2)$/kJ mol^{-1}	$E_{act}(3)$/kJ mol^{-1}
bdc	52.1	0	−8.2	18.5	−0.1	—
bdc-Br (A)	−34.8	0	−10.8	42.7	−0.2	37.8
bdc-Br (S)	−29.4	0	−68.5	37.4	—	14.6
bdc-I (A)	−65.7	0	−32.6	49.2	2.1	67.0
bdc-I (S)	23.0	0	−51.8	69.2	3.1	22.0

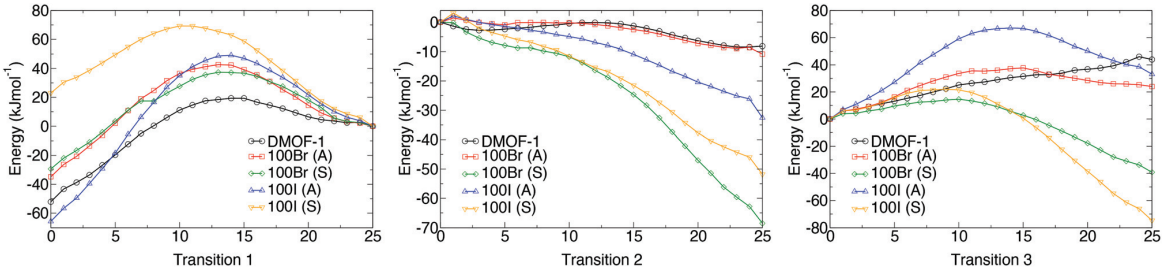

Fig. 10 The potential energy surfaces associated with the three structural transformations with varying halide concentration, as predicted from nudged elastic band calculations (DFT/PBEsol). Transition 1 (left) is for a perfect square to distorted square structure, Transition 2 (centre) relates to a distorted square to rhomboid structure and Transition 3 (right) corresponds to a square to rhomboid pore structure. Structures labelled A have the halogens on neighbouring rings projecting into alternating pores whereas structures labelled S have the halogens on neighbouring rings projecting in to the same pores.

dynamic conversion between pore topologies would not be possible for structures with halogen substituents. Interestingly, for the 100% bdc structure, no activation barrier between square and rhomboid pore topology is evident. This supports the capability of the 100% bdc structure to 'breathe' with applied external stimulus such as a temperature or pressure.

We also consider the change in chemical interactions with increasing halogen concentration within the pore. Non-covalent interaction (NCI) analysis allows the visualisation of charge density within a chemical system that is not attributed to formal covalent bonding.[25–28] Two interactions were found to be of importance for the structural behaviour of DMOF-1. Firstly, attractive dispersive interactions between the carboxylate oxygen atoms and the hydrogen atoms on the dabco ligand are present. This interaction is present regardless of the substituent on the bdc ligand and could be a driving force for the COO–Zn–COO angle to change in DMOF-1, subsequently contributing to reversible structural 'breathing'. We show here that the relative energies of the different pore topologies are consistent with experimental observations. The calculated activation energies confirm that the structures are not interconvertible and a single pore topology is thermodynamically favorable for all systems, supporting the X-ray analyses.

Secondly, the preference for a rhomboidal pore structure for the halogenated mixed-ligand DMOF-1 structures can be explained by the dispersive interactions between the halogen atom and the hydrogen atom on the dabco ligand. Fig. 11 depicts this interaction between Br and H in the 100% bdc-Br (S) system. With increasing concentration of halogen, the number of these interactions increases and this provides the thermodynamic driving force for the observed behaviour. As

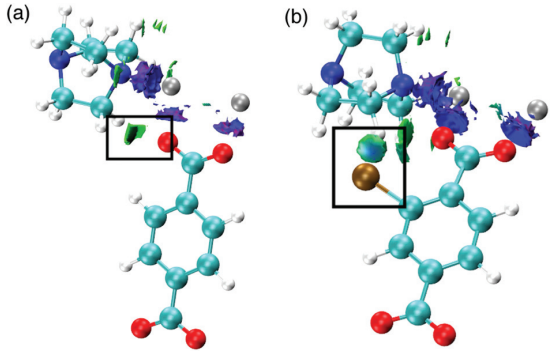

Fig. 11 Non-covalent interactions (a) in the node of DMOF-1 determined from topological analysis of DFT calculations and (b) between H and Br in DMOF-1–Br. The depicted density represents repulsive interactions between the paired Zn metals (blue) and attractive interactions as highlighted between the carboxylate O and Zn atoms (green). Also shown are attractive interactions between the carboxylate O and H-(dabco).

the halogen–halogen distances within the pore are greater than 6 Å in series **1**, this rules out halogen–halogen interactions as a contributing factor to pore compression. Indeed, these interactions were also not evident in the NCI analysis. Further support can be found in series **3** and **4**, with NO_2 and NH_2 groups as substituents on the bdc ligand. At 100% concentration of substituent on each aromatic ring these structures do not collapse into rhomboidal geometry, but remain in a square pore topology. For the amino-containing framework **4**, H(NH_2)–H(dabco) only weak interactions are present that would not provide enough attractive force to drive the structure to collapse. For the case of series **3**, the analysis of observed pore topologies is more complex. During geometry optimisation, a rotation of the NO_2 substituent renders the non-covalent interactions diffuse and weak due to the lone pair repulsion between the O(NO_2)–O(carboxylate). The relative energies of pore topologies with high concentration of NO_2 are sensitive to the extent of rotation and are therefore not reported.

Structural stability of series 1–5

Previous reports have shown that the DMOF-1 structure is susceptible to hydrolysis from atmospheric water leading to the collapse of the framework over time.[29] Studies were therefore undertaken on selected members of series **1–5** to determine if the addition of a second bdc-X ligand affected the stability in air. A similar protocol has been used to assess the structural stability of MOF-177.[30]

Compounds $[Zn_2(bdc)(bdc\text{-}Br)(dabco)]\cdot$DMF **1a**, $[Zn_2(bdc)_{1.5}(bdc\text{-}I)_{0.5}(dabco)]\cdot n$DMF **2a**, $[Zn_2(bdc)_{1.2}(bdc\text{-}NO_2)_{0.8}(dabco)]\cdot 2.5$DMF **3a**, $[Zn_2(bdc)_{1.16}(bdc\text{-}NH_2)_{0.84}(dabco)]\cdot n$DMF **4c** and $[Zn_2(bdc\text{-}Br)_{1.4}(bdc\text{-}I)_{0.6}(dabco)]\cdot 2.6$DMF **5a** were monitored by powder X-ray diffraction at one week intervals over several weeks. DMOF-1 was also monitored under the same conditions as a control sample. Compounds **2a**, **4c** and **5a** showed slightly increased framework stabilities in air relative to DMOF-1, with all three compounds showing significant structural changes after one week and a total collapse in crystallinity after 2–3 weeks.

Powder X-ray diffraction of **3a** showed no change in the structure of the framework after one week. As with **2a** and **4c**, this represents an increase in stability compared to DMOF-1, although complete loss of crystallinity in **3a** was observed after three weeks of air exposure. In contrast, the diffraction pattern of compound **1a** remained unchanged for over four weeks of air exposure, suggesting that the framework has considerably greater structural stability in air than the parent DMOF-1. Although powder X-ray diffraction studies will not reveal the presence of amorphous decomposition phases, the similar signal to noise ratios in the PXRD patterns of **1a** over time suggest the possibility of the bulk of the material decomposing to an amorphous product leaving only a small amount of crystalline product is unlikely.

The stability of $[Zn_2(bdc\text{-}Br)_2(dabco)]$ was similarly monitored for comparison. Although the framework stability of this compound was greater than that of DMOF-1 with no alterations to the diffraction pattern for up to two weeks, it is significantly lower than **1a**. Multivariate MOFs, such as **1a**, therefore can allow access to more air- or moisture-stable structures than those of the single-linker structures. These results are summarized graphically in Fig. 12.

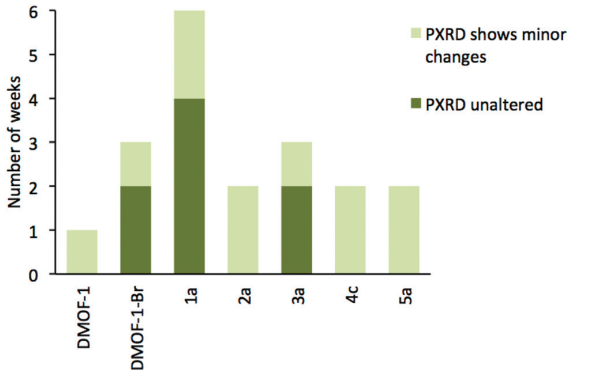

Fig. 12 Structural stability tests of selected compounds as monitored by PXRD. Minor changes to the PXRD patterns include peak broadening and the appearance of additional peaks, while the main peaks remain present.

Experimental

All chemicals used were commercially sourced (Sigma-Aldrich) unless otherwise stated, and were used without purification. DMOF-1 and its multivariate analogues were prepared using similar syntheses to that previously reported with modifications to the dicarboxylic acid ratios as detailed in the ESI.† The synthetic procedure for compounds in series **1–4** involved the combination of H_2bdc and H_2bdc-X along with dabco and $Zn(NO_3)_2\cdot 6H_2O$ in DMF. Each reaction mixture was sonicated to aid dissolution before being sealed and heated at 120 °C for 3 days. For each of series **1**, **3** and **4**, nine compounds were synthesised by varying the compositional factor, x in $[Zn_2(bdc)_{2-x}(bdc\text{-}X)_x(dabco)]$. Series **2** contained four compounds and series **5** contained three compounds. Characterisation was carried out using ^{1}H NMR spectroscopy, powder X-ray diffraction and single crystal X-ray crystallography (see ESI†).

Individual crystal samples for ^{1}H NMR spectroscopy used only one signal crystal of the compound, with the sample prepared in a similar manner to the bulk samples. The bulk samples were first dried at 120 °C before being digested using an acid-based digestion solution of DMSO-d_6 and DCl (see ESI†). Individual crystal samples were air dried prior to being digested.

Single crystal X-ray analysis were carried out on compounds **1a–d**, **1c′**, **3a**, **4a**, **4b** and **5a** with details of the data collections and refinements given in Table 3. Further details of these analyses are provided in the ESI.†

Representative samples from series **1–5** were selected for framework stability experiments. The samples were air dried

Table 3 Data collection and refinement details for compounds **1a–d**, **1c′**, **3a**, **4a**, **4b** and **5a**

Compound	**1a**	**1b**	**1c**	**1d**	**1c′**	**3a**	**4a**	**4b**	**5a**
Chemical formula	$C_{25}H_{36}O_9N_3BrZn_2$	$C_{25}H_{25.8}O_9N_3Br_{1.2}Zn_2$	$C_{22}H_{18.4}O_8N_2Br_{1.6}Zn_2$	$C_{22}H_{18.4}O_8N_2Br_{1.6}Zn_2$	$C_{22}H_{18.48}O_8N_2Br_{1.52}Zn_2$	$C_{29.5}H_{36.7}O_{12.1}N_{5.3}Zn_2$	$C_{29.8}H_{38.6}O_{10.6}N_5Zn_2$	$C_{22}H_{21.8}O_8N_{3.8}Zn_2$	$C_{29.8}H_{36.2}O_{10.6}N_{4.6}I_{0.6}Br_{1.4}Zn_2$
Formula Mass	723.14	738.92	697.38	705.27	691.07	789.88	767.19	598.17	947.19
Temperature/K	150(2)	150(2)	150(2)	150(2)	298(2)	150(2)	150(2)	150(2)	150(2)
Crystal system	Tetragonal	Tetragonal	Orthorhombic	Orthorhombic	Orthorhombic	Tetragonal	Tetragonal	Monoclinic	Orthorhombic
Space group	*P*4/*ncc*	*P*4/*ncc*	*Ammm*	*Ammm*	*Ammm*	*I*4/*mcm*	*P*4/*ncc*	*I*2/*a*	*Pncb*
a/Å	14.9880(4)	14.9760(4)	9.6280(2)	9.6230(3)	9.6342(14)	15.0210(4)	14.9813(3)	15.3434(4)	9.6270(3)
b/Å	14.9880(4)	14.9760(4)	12.7590(2)	12.8580(6)	16.488(3)	15.0210(4)	14.9813(3)	14.7669(3)	13.2670(4)
c/Å	19.2400(5)	19.2380(6)	17.5720(3)	17.4800(8)	14.229(3)	19.2220(8)	19.2011(6)	19.2363(4)	17.2190(5)
α/°	90	90	90	90	90	90	90	90	90
β/°	90	90	90	90	90	90	90	94.7265(19)	90
γ/°	90	90	90	90	90	90	90	90	90
Unit cell volume/Å^3	4322.1(3)	4314.7(3)	2158.61(7)	2162.84(16)	2260.2(8)	4337.1(3)	4309.5(2)	4343.63(17)	2199.24(11)
No. of formula units per unit cell, *Z*	4	4	2	2	2	4	4	4	2
No. of reflections measured	71 851	20 056	19 984	15 147	2827	39 254	14 611	23 630	31 992
No. of independent reflections	1901	1904	1399	1403	1229	1356	2088	4259	1953
R_{int}	0.0967	0.0561	0.0437	0.0752	0.0532	0.1208	0.0789	0.0526	0.0996
Final R_1 values ($I > 2\sigma(I)$)	0.0917	0.0967	0.0653	0.0735	0.0905	0.0529	0.0650	0.0523	0.0950
Final w$R(F^2)$ values ($I > 2\sigma(I)$)	0.2620	0.2472	0.1840	0.2074	0.2471	0.1299	0.1891	0.1624	0.2457
Final R_1 values (all data)	0.1212	0.1109	0.0697	0.0786	0.0981	0.0806	0.0810	0.0595	0.1186
Final w$R(F^2)$ values (all data)	0.2795	0.2558	0.1897	0.2131	0.2562	0.1483	0.2081	0.1702	0.2667

and kept open to the atmosphere under ambient conditions. Monitoring of the framework crystallinity was conducted using powder X-ray diffraction at one week intervals over a period of six weeks.

Computational methods, based on density functional theory (DFT), are detailed in the ESI.†

Conclusions

Multivariate MOFs based on the structure of DMOF-1 and containing varying ratios of different dicarboxylate ligands have been successfully synthesised and characterised. The series $[Zn_2(bdc)_{2-x}(bdc\text{-}Br)_x(dabco)]\cdot n$DMF **1**, $[Zn_2(bdc)_{2-x}(bdc\text{-}NO_2)_x(dabco)]\cdot n$DMF **3** and $[Zn_2(bdc)_{2-x}(bdc\text{-}NH_2)_x(dabco)]\cdot n$DMF **4** show the incorporation of ligands into the product framework in the same ratio as that present in the reaction mixture. Both series $[Zn_2(bdc)_{2-x}(bdc\text{-}I)_x(dabco)]\cdot n$DMF **2** and $[Zn_2(bdc\text{-}Br)_{2-x}(bdc\text{-}I)_x(dabco)]\cdot n$DMF **5** demonstrate a strong ligand preference with the bdc-I ligand being preferentially excluded during framework formation.

The systematic approach to mixed-ligand MOF formation has demonstrated that by variation of dicarboxylic acid ratios in the reaction mixture the pore topology of the framework can be controlled. Computational studies on series $[Zn_2(bdc)_{2-x}(bdc\text{-}Br)_x(dabco)]\cdot n$DMF **1** have shown that above a certain halogen concentration there is a thermodynamic driving force for pore compression. However, at very high concentrations of halogen within the pore, the activation energy for this transition is lowered. These results support the experimental findings of a lower pore compression in $[Zn_2(bdc\text{-}Br)_2(dabco)]$ than in the multivariate MOFs. The correlation of pore geometry to the ligand ratio opens up the possibility of pore size and shape tuning through reaction stoichiometry control. Pore geometries which may only otherwise be accessed *via* solvent changes or complete substitution of the ligand can therefore be formed through the use of a multivariate approach.

This approach allows the potential for pore shape alterations without the loss of desirable properties introduced through ligand choices. These pore transitions are dependent upon the functionality of the substituent, as demonstrated by series $[Zn_2(bdc)_{2-x}(bdc\text{-}NH_2)_x(dabco)]\cdot n$DMF **4** and $[Zn_2(bdc\text{-}Br)_{2-x}(bdc\text{-}I)_x(dabco)]\cdot n$DMF **5** which show no pore transitions.

The multivariate MOFs of series **1**, **2**, **3** and **4** are more stable to air than DMOF-1. In the specific case of $[Zn_2(bdc)(bdc\text{-}Br)(dabco)]\cdot$DMF **1a**, the compound shows enhanced stability over both $[Zn_2(bdc)_2(dabco)]$ and $[Zn_2(bdc\text{-}Br)_2(dabco)]$, demonstrating that multivariate species can have properties which extend beyond the combination of the corresponding single ligand systems.

Acknowledgements

L.K.C. is funded by an EPSRC studentship. J.K.B. is funded by the EPRSC Doctoral Training Centre for Sustainable Chemical Technologies at the University of Bath (Grant No. EP/G03768X/1). D.T. was funded under ERC starting grant 277757. A.W. acknowledges support from the Royal Society and EPSRC Grant No. EP/K004956/1. The work benefits from the high performance computing facility at the University of Bath. Access to ARCHER supercomputer was facilitated through membership of the HPC materials Chemistry Consortium (EPSRC Grant No. EP/L000202). The authors thank Dr A. Otero de la Roza for useful discussions and Dr J. Lowe for NMR spectroscopic advice.

Notes and references

1 H. Furukawa, K. E. Cordova, M. O'Keeffe and O. M. Yaghi, *Science*, 2013, **341**, 1230444.
2 S. Horike, S. Shimomura and S. Kitagawa, *Nat. Chem.*, 2009, **1**, 695.
3 M. P. Suh, H. J. Park, T. K. Prasad and D.-W. Lim, *Chem. Rev.*, 2012, **112**, 782.
4 J.-R. Li, J. Sculley and H.-C. Zhou, *Chem. Rev.*, 2012, **112**, 869.
5 P. Horcajada, R. Gref, T. Baati, P. K. Allan, G. Maurin, P. Couvreur, G. Férey, R. E. Morris and C. Serre, *Chem. Rev.*, 2012, **112**, 1232.
6 S. Henke, A. Schneemann, A. Wütscher and R. A. Fischer, *J. Am. Chem. Soc.*, 2012, **134**, 9464.
7 M. Eddaoudi, J. Kim, N. Rosi, D. Vodak, J. Wachter, M. O'Keeffe and O. M. Yaghi, *Science*, 2002, **295**, 469.
8 A. D. Burrows, *CrystEngComm*, 2011, **13**, 3623.
9 H. Deng, C. J. Doonan, H. Furukawa, R. B. Ferreira, J. Towne, C. B. Knobler, B. Wang and O. M. Yaghi, *Science*, 2010, **327**, 846.
10 A. D. Burrows, L. C. Fisher, C. Richardson and S. P. Rigby, *Chem. Commun.*, 2011, **47**, 3380.
11 D. N. Dybtsev, H. Chun and K. Kim, *Angew. Chem., Int. Ed.*, 2004, **43**, 5033.
12 H. Chun, D. N. Dybtsev, H. Kim and K. Kim, *Chem. – Eur. J.*, 2005, **11**, 3521.
13 T. Loiseau, C. Serre, C. Huguenard, G. Fink, F. Taulelle, M. Henry, T. Bataille and G. Férey, *Chem. – Eur. J.*, 2004, **10**, 1373.
14 P. Horcajada, F. Salles, S. Wuttke, T. Devic, D. Heurtaux, G. Maurin, A. Vimont, M. Daturi, O. David, E. Magnier, N. Stock, Y. Filinchuk, D. Popov, C. Riekel, G. Férey and C. Serre, *J. Am. Chem. Soc.*, 2011, **133**, 17839.
15 Z. Wang and S. M. Cohen, *J. Am. Chem. Soc.*, 2009, **131**, 16675.
16 S. Henke, D. C. F. Wieland, M. Meilikhov, M. Paulus, C. Sternemann, K. Yusenko and R. A. Fischer, *CrystEngComm*, 2011, **13**, 6399.
17 S. Henke, A. Schneemann, S. Kapoor, R. Winter and R. A. Fischer, *J. Mater. Chem.*, 2012, **22**, 909.
18 K. Uemura, F. Onishi, Y. Yamasaki and H. Kita, *J. Solid State Chem.*, 2009, **182**, 2852.

19 K. Uemura, Y. Yamasaki, F. Onishi, H. Kita and M. Ebihara, *Inorg. Chem.*, 2010, **49**, 10133.
20 P. E. Blöchl, *Phys. Rev. B: Condens. Matter*, 1994, **50**, 17953.
21 G. Henkelman and H. Jónsson, *J. Chem. Phys.*, 2000, **113**, 9978.
22 G. Henkelman, B. P. Uberuaga and H. Jónsson, *J. Chem. Phys.*, 2000, **113**, 9901.
23 J. P. Perdew, K. Burke and M. Ernzerhof, *Phys. Rev. Lett.*, 1996, **77**, 3865.
24 K. J. Caspersen and E. A. Carter, *Proc. Natl. Acad. Sci. U. S. A.*, 2005, **102**, 6738.
25 J. Contreras-Garcia, E. R. Johnson, S. Keinan, R. Chaudret, J. P. Piquemal, D. N. Beratan and W. Yang, *J. Chem. Theory Comput.*, 2011, **7**, 625.
26 W. Humphrey, A. Dalke and K. Schulten, *J. Mol. Graphics*, 1996, **14**, 33.
27 A. Otero de la Roza, M. A. Blanco, A. M. Pendás and V. Luaña, *Comput. Phys. Commun.*, 2009, **180**, 157.
28 A. Otero de la Roza, E. R. Johnson and V. Luaña, *Comput. Phys. Commun.*, 2014, **185**, 1007.
29 H. Jasuja, N. C. Burtch, Y.-G. Huang, Y. Cai and K. S. Walton, *Langmuir*, 2013, **29**, 633.
30 D. Saha and S. Deng, *J. Phys. Chem. Lett.*, 2010, **1**, 73.

6.2 Paper 6 - Compositional control of pore geometry through steric interactions in a multivariate metal-organic framework series

The following paper entitled "Compositional control of pore geometry through steric interactions in a multivariate metal-organic framework series" is a continuation to paper 5. Instead of halogen substituents on the BDC ligands, paper 6 instead considers the substitution of different concentrations of 1,4-naphthalene dicarboxylate on the BDC ligands. The non-covalent interactions between NDC substituent and H(DABCO) ligand are analysed and the nudged elastic band method used to calculate the energy difference between pore shapes with differing concentrations of BDC:BDC-NDC.

6.2.1 Personal contribution

My personal contribution to the paper entitled *"Compositional control of pore geometry through steric interactions in a multivariate metal-organic framework series"* included calculating the ground state pore topology of each MOF with differing concentration of NDC and calculating energy profiles between the different topologies with a nudged elastic band approach. D. Tiana calculated the non-covalent interaction plots using a topological analysis with DFT. L. Cadman, N. Stubbs and M. Mahon did all experimental synthesis, characterisation and analysis on the structures.

Journal Name

ARTICLE

Compositional control of pore geometry through steric interactions in a multivariate metal-organic framework series

Received 00th January 20xx,
Accepted 00th January 20xx

DOI: 10.1039/x0xx00000x

www.rsc.org/

L.K. Cadman, J.K. Bristow, H. Wright, D. Tiana, M.F. Mahon,[a] A. Walsh and A.D. Burrows[c]

A multi-compoent series of metal-organic frameworks is reported in which control of steric bulk within the framework results in pore geometry and size tailoring. The series contains two dicarboxylate ligands of similar structural roles; [Zn2(bdc)2-x(ndc)x(dabco)].xDMF, where bdc = 1,4-benzene dicarboxylate, ndc = 1,4-naphthalene dicarboxylate and dabco = 1,8-diazabicyclooctane. The series displays transitions from open, square pores to rhomboidal, narrow pores as the ndc content within the framework is incrementally increased. A second transition returning to open, square pores is observed at ndc content >70% in the structure. Computational anaylsis revelas this structural transition is due to the steric interactions present upon increased ndc content in the MOFs.

Introduction

Metal-organic frameworks (MOFs) are a class of porous materials which have been attracting much attention due to their simplistic synthesis,[1, 2] desirable properties[3-7] and potential for control and structural design.[8] Of these, systems which contain more than one type of ligand have gained significant interest.[8-11] Many of these multi-ligand MOFs contain ligands which are structurally different to one another such as UMCM-1; $[Zn_4O(bdc)(btb)_{4/3}]$ which contains an extended tricarboxylate ligand; btb (4,4',4'',-Benzene-1,3,5-triyl-tris(benzoic acid) and a smaller dicarboxylate ligand; bdc (benzene dicarboxylate).[12] Other classes of multi-ligand MOFs contain ligands which play similar structural roles within the framework. These have been termed multi-component MOFs and allow for the ratio of ligands to be varied, opening up the possibility for property tuning through ligand ratio control.[13] Previous examples of these multi-component MOFs include several based around the structure of MOF-5 $[Zn_4O(bdc)_3]$ in which a second, functionalised bdc-X ligand is introduced to the framework.[9, 11, 14]

We have previously reported the successful tailoring of pore shape and size in multi-component series' based on the DMOF-1 framework; $[Zn_2(bdc)_2(dabco)]$.[15] A second dicarboxylic acid which is functionally substituted at the ortho-position on the benzene ring, referred to generically as H_2bdc-X, was introduced into the reaction mixture in varying ratios of H_2bdc:H_2bdc-X. The product composition was controlled through reaction stoichiometry and the resulting frameworks were of the form $[Zn_2(bdc)_{2-x}(bdc\text{-}X)_x(dabco)]$.nDMF where X=Br, I, NO_2 or NH_2. The systems were shown to have a functionally dependent effect on the pore shape and size, with increasing amounts of halide and nitro functionally substituted ligands (H_2bdc-Br, H_2bdc-I and H_2bdc-NO_2) causing the pores of the resulting framework to change from an open, square form to a narrow, rhomboidal form. Ligands with an amino group substitution (H_2bdc-NH_2) showed no change to the pore shape with varying concentration of the ligand in the framework. Computational studies revealed that these pore effects are a result of non-covalent interactions between the functional group in the ortho-position of the dicarboxylate ligand, and the hydrogen on the dabco ligand. These effects are particularly pronounced for the halide substituted dicarboxylic acids. For the amino-containing frameworks these non-covalent interactions are weak and do not provide enough attractive force to drive the pore structure to collapse.

Here we report a similar mixed-ligand strategy to that previously described.[15] Based around the DMOF-1 system, a second dicarboxylic acid was employed in the reaction synthesis alongside the benzene dicarboxylic acid (H_2bdc) in varying amounts. The second ligand used in this case is 1,4-naphthalenedicarboxylic acid (H_2ndc). The single ligand system $[Zn_2(ndc)_2(dabco)]$ has been reported.[16, 17] This method successfully synthesised nine new MOFs of the general composition $[Zn_2(bdc)_{2-x}(ndc)_x(dabco)]$.nDMF. Analysis of the products was then carried out with a combination of ^{1}H NMR spectroscopy, powder X-ray diffraction (PXRD), single crystal X-ray diffraction and computational studies to determine the effects of varying the amount of the naphthalene dicarboxylate ligand incorporation into the framework.

[a] Address here.
[b] Address here.
[c] Address here.

† Footnotes relating to the title and/or authors should appear here.
Electronic Supplementary Information (ESI) available: [details of any supplementary information available should be included here]. See DOI: 10.1039/x0xx00000x

Experimental

Synthesis of the compounds $[Zn_2(bdc)_{2-x}(ndc)_x(dabco)].nDMF$ were carried out using similar reaction conditions to those reported for that of DMOF-1.[18] $Zn(NO_3)_2.6H_2O$ (0.6 mmol) was added to H_2bdc and H_2ndc (0.6 mmol of combined dicarboxylate ligand content in varying ratios) and dabco (0.3 mmol) in 8 ml anhydrous DMF. The reactants were sealed in a vial and heated to 120°C for 60 hours. The reaction yielded colourless block crystals which were filtered whilst hot to remove unreacted starting materials. The product was then washed with hot DMF and allowed to cool to room temperature.

Results and discussion

Nine members of the mixed-ligand series $[Zn_2(bdc)_{2-x}(ndc)_x(dabco)]n$*x*DMF were successfully synthesised by varying the ratio of H_2bdc and H_2ndc ligands in the reaction mixture from 1:9 through to 9:1. The compositions of the products formed are given in the ESI.

The compositions of all products were determined through ^1H NMR on acid digested bulk samples. To ensure that products were mixed-component systems and not a physical mixture of two single ligand systems, ^1H NMR spectroscopy was also conducted on individual crystals to determine the presence of both ligands (fig 1). This method involved taking one individual crystal from each sample and digesting it using a DCl/d_6-DMSO solution. This was repeated on multiple crystals from the same bulk sample to determine compositional variation in the products. Three crystals from each product were digested and analysed by ^1H NMR, with the exception of $[Zn_2(bdc)_{1.8}(ndc)_{0.2}(dabco)].nDMF$ and $[Zn_2(bdc)_{1.6}(ndc)_{0.4}(dabco)].nDMF$ as these crystals were too small to successfully isolate.

^1H NMR spectroscopy on digested individual crystals from all seven samples show the presence of both H_2bdc and H_2ndc ligands confirming the formation of mixed-component species. The integral analysis of spectra on bulk samples showed similar ligand content to that of the reaction mixture, indicating that there is no preferential inclusion of one dicarboxylate ligand over the other into the framework. A comparison of the individual crystal ^1H NMR spectra and the corresponding bulk spectra for each product showed a similar content of each dicarboxylate ligand indicating that little compositional variation was present within each sample (fig 1).

Structural characterisations of all products were carried out through powder X-ray diffraction (PXRD). All products gave PXRD patterns containing similar general features suggesting that all mixed-ligand products possess similar framework topologies to one another (fig 2). A comparison to the powder diffraction trace generated from the single crystal structure of DMOF-1 confirms that it is topologically similar to that of the mixed-ligand products. A change in relative intensity of some peaks in products with a ndc content of 50% and 70% can be explained by differences in solvent in the pores.

A closer inspection of the powder diffraction patterns shows three distinct phases which are identified through peak position changes between the patterns. At low ndc content <20% the peak positions resemble those of DMOF-1, at a ndc content between 29% and 70% the peak positions occur at a lower 2θ value and at ndc >70% the peak positions shift gradually back to a higher 2θ. A similar effect was observed in the previously reported structures $[Zn_2(bdc)_{2-x}(bdc\text{-}X)_x(dabco)].nDMF$ and was found to correspond to a change in the pore shape and size of the products formed.

To identify whether similar effects are occurring in this series, two structures, one from each of the phases, were analysed through single crystal X-ray diffraction. These are identified as $[Zn_2(bdc)_{1.01}(1,4\text{-}ndc)_{0.99}(dabco)]\cdot 2.3DMF$ **1a** and $[Zn_2(bdc)_{0.23}(1,4\text{-}ndc)_{1.77}(dabco)]\cdot 1.6DMF$ **1b**.

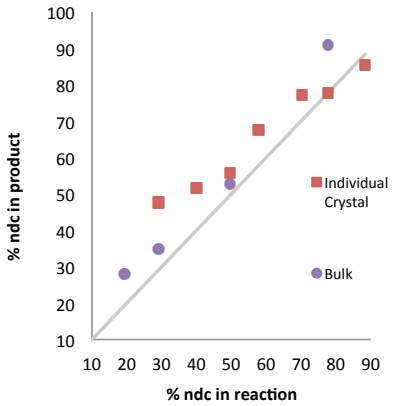

Fig 1 – The inclusion of 1,4-ndc into $[Zn_2(bdc)_{2-x}(1,4\text{-}ndc)_x(dabco)].x$DMF products

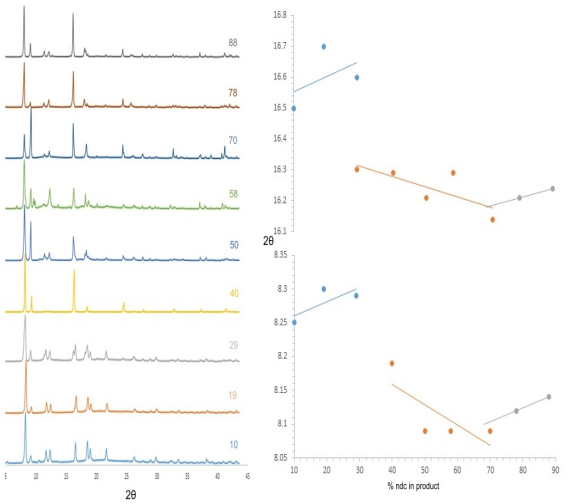

Fig 2. PXRD patterns of the as-synthesised compounds $[Zn_2(bdc)_{2-x}(ndc)_x(dabco)].nDMF$

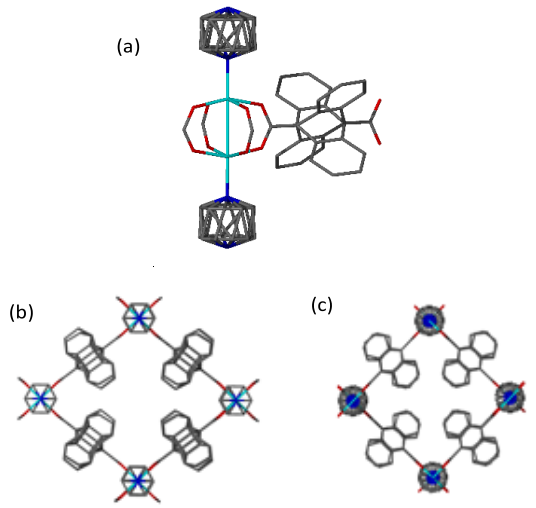

Fig 3 – (a) SBU of $[Zn_2(bdc)_{0.23}(1,4\text{-ndc})_{1.77}(dabco)]\cdot 1.6DMF$ **1b**, showing the disordered naphthalene ligand. Hydrogen atoms have been removed for clarity. (b) view down the c-axis of $[Zn_2(bdc)_{1.01}(1,4\text{-ndc})_{0.99}(dabco)]\cdot 2.3DMF$ **1a** showing the rhomboidal pore structure. (c) view along the c-axis of $[Zn_2(bdc)_{0.23}(1,4\text{-ndc})_{1.77}(dabco)]\cdot 1.6DMF$ **1b** showing the square pore structure. In both (b) and (c) the naphthalene ligand is disordered over several positions and hydrogen atoms have been removed for clarity.

Both structures present topologically similar frameworks to that of DMOF-1 which supports the PXRD findings. The structures present a 3-dimensional grid-like structure in which zinc paddlewheel SBU's are bridged by four dicarboxylate ligands (fig 3). These SBUs are joined together in 2-dimenisonal sheets which are then connected by pillaring dabco ligands to form the overall 3-dimensional structure. In all cases, severe disorder of the dicarboxylate ligands is present. Both the bdc and 1,4-ndc ligands are disordered over all four-positions around the paddlewheel and the naphthalene ring is further disordered over multiple positions (fig 3a).

There are prominent structural differences between the two structures of **1a** and **1b**. In the case of **1a** the grid-like structure crystallises in an orthorhombic crystal system and has compressed, rhomboidal shaped pores (fig 3b). Such compressed pore structures have been shown to form in mixed-ligand systems of DMOF-1 as previously reported. The structure of **1b** crystallises in a tetragonal crystal system and has open, square pores (fig 3c) similar to those observed in the single ligand system $[Zn_2(1,4\text{-ndc})_2(dabco)]$ and DMOF-1. These findings show that similar pore geometry and size control can be achieved through the formation of a multi-component system containing the naphthalene dicarboxylate ligand, as is observed in the systems with a functional group substituent on the ring. The three phases observed in the PXRD patterns can therefore be categorised as square-rhomboidal-square pore shape transitions.

Computational studies were conducted on $[Zn_2(bdc)_2(dabo)]$, $[Zn_2(bdc)(ndc)(dabo)]$, **7a** and $[Zn_2(ndc)_2(dabo)]$. Relative total energies are given in table 1 and show that the final symmetry and pore shape of the structure is dependent upon ndc concentration within the framework. At 50% ndc concentration we show the rhombohedral pore structure to be more stable. In stark contrast, at 100% ndc content the structure is shown to favour a square pore framework. These results confirm the observations from experimental studies.

Table 1 - Energy relative to the orthorhombic structure (KJmol-1)

	Content of 1,4-ndc		
	0%	50%	100%
Rhomboidal Pore	52.2	-60.4	51.3
Square Pore	0.0	0.0	0.0

The explanation for this stability trend is due to the physical steric size of the ndc ligand. In all cases at both 50% and 100% concentration of ndc, the ligand twists within the structure. The twisting occurs to allow the additional side ring fused to the main body of the aromatic dicarboxylate unit to reside within the pore of the MOF, thus reducing destabilizing steric interactions. As the content of the ndc within the framework increases, the larger pore structure, with open square pores has a lower total energy.

Previous computational studies have shown that the structural symmetry changes observed in $[Zn_2(bdc)_{2-x}(bdc\text{-}X)_x(dabco)]$ were due to non-covalent interactions between the substituent atom and the hydrogen on the dabco.[15] Here we are considering possible interactions in the pore involving naphthalene groups. Non covalent interaction (NCI) analysis has shown no significant interaction between H(ndc)-H(dabco), supporting the conclusion that these interactions would not account for the calculated energy differences between symmetries. We therefore conclude the observed pore shape changes with ndc content to be purely due to steric interactions.

Conclusions

Multivariate MOFs based of the general form $[Zn_2(bdc)_{2-x}(ndc)_x(dabco)]\cdot nDMF$ **1** and containing varying ratios of the two dicarboxylate ligands have been successfully synthesised and characterised. The series contains nine multi-component structures which have similar ligand ratios to those present in the reaction mixture, allowing effective compositional control.

The systematic synthesis of series **1** has demonstrated that by varying the bdc:ndc ratio the pore size and shape of the resulting MOF can be tailored and controlled. A low content of <20% ndc and high contents of ≥77% ndc produce a square pore framework similar to that of the known single ligand structures $[Zn_2(bdc)_2(dabo)]$ and $[Zn_2(ndc)_2(dabo)]$. The structures with a ndc content of >20% and <77% present a rhomboidal, narrow pore structure. Computational studies have supported experimental findings for this system showing

that these observed structural changes result from steric interactions within the pores.

This correlation of pore geometry to ligand ratio in DMOF-1 systems containing sterically hindered ligands presents striking evidence for the possibility of pore size and shape tuning in multi-component systems through reaction stoichiometry control.

Acknowledgements

L.K.C. is funded by an EPSRC studentship. J.K.B. is funded by the EPRSC Doctoral Training Centre for Sustainable Chemical Technologies at the University of Bath (Grant No. EP/G03768X/1). D.T. was funded under ERC starting grant 277757. A.W. acknowledges support from the Royal Society and EPSRC Grant No. EP/K004956/1. The work benefits from the high performance computing facility at the University of Bath. Access to ARCHER supercomputer was facilitated through membership of the HPC materials Chemistry Consortium (EPSRC Grant No. EP/L000202).Consortium (EPSRC Grant No. EP/L000202). The authors Dr J. Lowe for NMR spectroscopic advice.

Notes and references

Crystallographic data for compounds **1a** and **1b** are shown in the table below

Compound reference	**1a**	**1b**
Chemical formula	C3.25 H2.70 N0.25 O Zn0.25	C3.65 H2.95 N0.25 O Zn0.25
Formula Mass	77.6	82.66
Crystal system	Orthorhombic	Tetragonal
Space group	Cmmm	P4/nbm
a/Å	13.9230(3)	15.4550(3)
b/Å	16.7920(3)	15.4550(3)
c/Å	9.6660(2)	9.6660(2)
α/°	90°	90°
β/°	90°	90°
γ/°	90°	90°
Unit cell volume/Å^3	2259.86(8)	2308.79(8)
No. of formula units per unit cell, *Z*	16	16
No. of reflections measured	16618	32572
No. of independent reflections	1457	1397
R_{int}	0.0385	0.0596
Final R_1 values ($I > 2\sigma(I)$)	0.0460	0.0556
Final $wR(F^2)$ values ($I > 2\sigma(I)$)	0.1300	0.1547
Final R_1 values (all data)	0.0483	0.0770
Final $wR(F^2)$ values (all data)	0.1338	0.1798

1. R. Robson, *Dalton transactions*, 2008, 5113-5131.
2. J. L. C. Rowsell and O. M. Yaghi, *Microporous and Mesoporous Materials*, 2004, **73**, 3-14.
3. J. R. Li, J. Sculley and H. C. Zhou, *Chem Rev*, 2012, **112**, 869-932.
4. E. Coronado and G. Minguez Espallargas, *Chem Soc Rev*, 2013, **42**, 1525-1539.
5. D. E. Williams and N. B. Shustova, *Chemistry*, 2015, 21, 15474-15479.
6. M. Mani-Biswas and T. Cagin, *Computational and Theoretical Chemistry*, 2012, **987**, 42-56.
7. N. A. Khan, Z. Hasan and S. H. Jhung, *J Hazard Mater*, 2013, **244-245**, 444-456.
8. J. K. Mohamed Eddaoudi, Nathaniel Rosi,, J. W. David Vodak, Michael O'Keeffe, and O. M. Yaghi, *Science*, 2002, **295**, 469-472.
9. H. Deng, C. J. Doonan, H. Furukawa, R. B. Ferreira, J. Towne, C. B. Knobler, B. Wang and O. M. Yaghi, *Science*, 2010, **327**, 846-850.
10. A. D. Burrows, L. C. Fisher, C. Richardson and S. P. Rigby, *Chem Commun (Camb)*, 2011, **47**, 3380-3382.
11. K. Koh, A. G. Wong-Foy and A. J. Matzger, *Chem Commun (Camb)*, 2009, 6162-6164.
12. K. Koh, A. G. Wong-Foy and A. J. Matzger, *Angew Chem Int Ed Engl*, 2008, **47**, 677-680.
13. A. D. Burrows, *CrystEngComm*, 2011, **13**, 3623.
14. W. Kleist, F. Jutz, M. Maciejewski and A. Baiker, *European Journal of Inorganic Chemistry*, 2009, 3552-3561.
15. L. K. Cadman, J. K. Bristow, N. E. Stubbs, D. Tiana, M. F. Mahon, A. Walsh and A. D. Burrows, *Dalton transactions*, 2016, **45**, 4316-4326.
16. H. Chun, D. N. Dybtsev, H. Kim and K. Kim, *Chemistry*, 2005, **11**, 3521-3529.
17. K. Uemura, Y. Komagawa, Y. Yamasaki and H. Kita, *Desalination*, 2008, **234**, 1-8.
18. D. N. Dybtsev, H. Chun and K. Kim, *Angew Chem Int Ed Engl*, 2004, **43**, 5033-5036.

Chapter 7

Summary and the future for metal-organic frameworks

7.1 Conclusions and future work

7.1.1 Chapter 3: transferable forcefields for MOFs

The parameterisation of two transferable forcefield models derived for metal-organic frameworks were discussed in chapter 1. The reproduction of vibrational properties is a critical consideration for MOFs, which possess soft-modes that may lead to subtle structural distortions. The harmonic approximation is known to only be accurate when the geometry is close to the global minimum structure. The consideration of temperature and pressure effects on MOFs, especially when calculating temperature dependent vibrational properties, questions the accuracy and applicability of the harmonic approximation. Using the quasi-harmonic approximation in paper 2 has allowed the consideration of volume expansion with temperature as an anharmonic effect on the vibration properties calculated. Extending the harmonic approximation is advantageous for materials such as MOFs to ensure the accuracy of accurately reproducing the soft-modes of the systems. The forcefields offer a means for a large-scale screening procedure of the thermodynamic properties of MOFs.

Future work for the forcefields would include accounting for the magnetic spin state on the metal cations using the atomic overlap model, which is already integrated into the GULP programme.[261] The inclusion of angular functions to the purely radial MM3 Buckingham and Coulomb function, allows non-spherical cations to be calculated and subsequent distortions, *e.g.* Jahn-Teller effect can be modelled.

Other future work includes fitting non-bonding forcefield parameters in the same manner as was reported in paper 2 in the VMOF forcefield, to reproduce temperature and pressure response of flexible frameworks. MIL-53 is an example of a flexible framework, which undergoes "breathing" motions and phase changes, where the ground state pore shape changes with temperature and pressure varia-

tion.[262,263] The sensitivity of flexible frameworks to the vibrational frequencies, in particular the soft-modes, is severe. Using a forcefield such as VMOF, which has been derived to accurately reproduce soft-modes of MOF frameworks would be advantageous for accurately reproducing the breathing and phase changes profiles with applied stimulus.

7.1.2 Chapter 4: defects and disorder in MOFs

The formation of missing ligand defects and their distributions in the framework, UiO-66 (Zr^{4+}/BDC), were discussed in chapter 2. A combination of first-principles and classical calculations were used in paper 3. The defect formation energies of the missing ligand defect as a function of concentration and relative defect location in the framework were calculated. When removing one BDC ligand from UiO-66, 4 Zr cations are left under-coordinated and the system has a +2 charge. The most favourable charge capping mechanism following the removal of the ligand was identified to be with two acetate anions in bidentate coordination. The second most favourable charge capping mechanism was 2(Cl^{-}/H_2O), where the water molecule reduces metal center reactivity as the Cl^{-} anion is only singly coordinated to Zr. All symmetry inequivalent relative locations from two and three ligand removals were calculated. The calculated defect free energies for each symmetry unique configuration predict the missing ligand defects would cluster locally to each other and at a non-dilute concentration in the system.

Future work would involve calculating the defect formation energy of missing metals as well as missing ligands in the structure of UiO-66. Goodwin *et al.* report the characterisation of nano-regions of clustered Schottky defects with rocksalt symmetry, which would suggest complimentary metal and ligand vacancies in the UiO-66 structure.[264] Other future work would include calculating the free energies of formation of the missing ligand defect in other structures that have more functional properties, for example in MIL-125(Ti^{4+}/BDC), which is a photocatalyst. Reaction rates and product yield may be modulated by introduction of the missing ligand defect. Additionally, phase transitions may be possible in other materials with a high concentrations of defects leading to a large structure prediction challenge.

7.1.3 Chapter 5: simulated epitaxial growth of MOFs on surfaces

Epitaxial growth of MOFs on oxide surfaces was discussed in chapter 3. The prediction of favourable surfaces to interface between MOFs and inorganic binary substrates is important for directing the experimental growth of uniform and dense thin films. A simple screening procedure was carried out in paper 4, where lattice mismatch percentages of cleaved surfaces of MOF and inorganic binary substrates, mainly metal oxides, were reported. The screening procedure identified the interface between the (110) surface of the rutile structured TiO_2 and the (011) surface of MOF-5. The interfacial energetics predicted a favourable reconstruction of the oxide, originating from the ligand carboxylate group repelling a bridging oxide anion on the oxide surface. Following surface reconstruction, the ligand became incorporated into the surface after displacing an oxide anion. Surface reconstruction is difficult to

characterise with experimental techniques, but would control the adhesion mechanism and energetics between the two surfaces. The prediction of surface reconstruction of an interface involving a MOF with a substrate is therefore important to understand observed surface growth coverage and uniformity. Finally, the energy of adhesion between the interfacing surfaces of MOF-5 and TiO_2 was calculated to be of reasonable strength.

Future work for the epitaxy of MOFs on oxide surfaces would first involve improving the initial screening procedure to include atom identity when identifying favourable surfaces to be interfaced. The inclusion of atom identity would allow favourable chemical binding sites to be predicted. The approach of Butler *et. al.*, as was used for the lattice mismatching, is capable of considering atom identity, by using the electronegativity of the ions in the systems to identify favourable bonding sites. The complexity of knowing the favourable termination for cleaving the surfaces of MOFs, has currently prevented us from applying this approach for atom identity inclusion to the screening procedure. Further calculations would be required on all possible cleaved surfaces, across a broad range of compositions and topologies of MOFs, before assumptions could be made to include atom identity in screening methods including atom identities.

Other future work for the epitaxy of MOFs on surfaces, would be to screen across a variety of oxide surface and MOFs to calculate if the observed reconstruction of the TiO_2 surface when interfaced with MOF-5, would also be favourable for other interfacing systems. Furthermore, additional calculations could be conducted to predict if intrinsic defects at the surface, such as an oxygen vacancy or missing ligand defect, would be more energetically favourable following the surface reconstruction. If these points were addressed then more general predictions on the interface stability and purity could be made.

7.1.4 Chapter 6: modulating the pore shape of MOFs

Finally, two papers describing the the modulation of the pore shapes of MOFs were discussed, the first being a method to control the pore shape by varying the concentration of halogen substituent on the ligands forming DMOF-1, and the second using a bulky side substituent; NDC. X-Ray diffraction was used to characterise the space-group and unit cell dimensions of synthesised DMOF-1(Zn^{2+}/DABCO/ (BDC:BDC-X)), where X = Cl, Br, or I, and DMOF-1(Zn^{2+}/DABCO/ (BDC:BDC-NDC)) frameworks. In paper 5 it was found that pore compression to produce a framework with rhombohedral symmetry and diamond shaped pore, was thermodynamically favourable at higher halogen (BDC-X) concentrations. At lower concentrations of halogen, a framework with monoclinic symmetry with a square pore is thermodynamically favourable. Using geometry optimisation and nudged elastic band calculations, the energy difference in either topology was calculated, which confirmed experimental observations, that at a high halogen concentration the ground state pore topology changed to favour rhomboid symmetry. Non-covalent interaction analysis attributed this observation of change in ground state pore topology to long-range dispersive interactions between halogen anions and protons on the DABCO ligands. At

a given concentration, the number of interactions were sufficient to cause an internal pressure around the pore edges, such that compression of the pore shape was favourable.

In paper 6, the square pore form of DMOF-1(Zn^{2+}/DABCO/(BDC:BDC-NDC)) was calculated and experimentally observed to be favourable for low ($< 20\%$) concentrations and high ($> 77\%$) concentrations of NDC in the framework structures, whilst compression favourable for intermediate concentrations. We calculate the non-covalent interactions between NDC and H(DABCO) to again be the thermodynamic driving force for pore compression. However, at high concentrations the steric interactions between NDC groups within the pores of the MOFs overcome the effects of the non-covalent interactions and the non-compressed, square-pore form becomes thermodynamically favourable.

Future work would involve varying the ligand identity in DMOF-1, other than BDC/BDC-X/BDC-NDC, to try and increase substituent-H(DABCO) interactions to observe if any more severe phase changes occur, or if a different crystal product with different chemical composition would be favoured. Other future work would include making the compression more functional, for example replacing the BDC ligand with a redox active ligands, for which pore compression and phase changes may result in modulation of the fundamental band gap.

7.2 Closing remarks

Working with both forcefields and MOFs requires a great deal of patience and determination, working with MOF forcefields has therefore been an emotional rollercoaster, full of many failures before producing successful results. Although the technology of MOFs has advance rapidly even during the duration of my PhD, it seems there is always an "if" or a "but" when it comes to finding a large industrial scale application for MOFs other than gas absorption and catalysis, which were developed decades ago for these materials. MOFs do, however, possess complex chemical functionality and a vast amount of potential for small-scale applications. It is therefore my prediction for MOFs that opposing the current research focus on MOFs for finding a "magic" framework capable of changing the world as we know it, the current lesser focus on internal absorption of functional and active molecules, using the framework as an inert cage, will begin to dominate research literature on these unique and quirky materials.

Bibliography

[1] S. Arrhenius, *Philos. Mag.*, 1896, **41**, 237–276.

[2] C. D. Keeling, T. P. Whorf, M. Wahlen and J. v. d. Plicht, *Nature*, 1995, **375**, 666–670.

[3] R. R. Nemani, C. D. Keeling, H. Hashimoto, W. M. Jolly, S. C. Piper, C. J. Tucker, R. B. Myneni and S. W. Running, *Science*, 2003, **300**, 1560–1563.

[4] NASA Orbital Debris Program Office (accessed 29/07/16): http://orbitaldebris.jsc.nasa.gov/photogallery/beehives.html.

[5] LondonBioPackaging website (accessed 20/07/16): http://www.londonbiopackaging.com/about-our-products/waste-disposal/.

[6] D. Hoornweg and P. Bhada-Tata, *What a waste: a global review of solid waste management*, 2012.

[7] Basics notions about solids (accessed 29/07/16): http://www.porous-35.com/electrochemistry-semiconductors-3.html.

[8] A. H. Wilson, *Proc. R. Soc. A.*, 1931, **133**, 458–491.

[9] A. Luque and A. Martí, *Phys. Rev. Lett.*, 1997, **78**, 5014.

[10] A. Wilson, *Proc. R. Soc. A.*, 1931, **134**, 277–287.

[11] A. M. Stoneham, *Theory of defects in solids: electronic structure of defects in insulators and semiconductors*, Oxford University Press, 2001.

[12] R. Bube, *Electronic properties of crystalline solids: an introduction to fundamentals*, Elsevier, 2012.

[13] A. Luque, A. Martí, N. López, E. Antolín, E. Cánovas, C. Stanley, C. Farmer, L. Caballero, L. Cuadra and J. Balenzategui, *Appl. Phys. Lett.*, 2005, **87**, 083505.

[14] W. Shockley and H. J. Queisser, *J. Appl. Phys.*, 1961, **32**, 510–519.

[15] D. M. Chapin, C. Fuller and G. Pearson, *J. Appl. Phys.*, 1954, **25**, 676–677.

[16] R. Schaetzl and M. L. Thompson, *Soils*, Cambridge University Press, 2015.

[17] S. L. Brantley and N. P. Mellott, *Am. Mineral.*, 2000, **85**, 1767–1783.

[18] M. H. Hey, *Mineralogical Mag.*, 1930, **22**, 422–437.

[19] J. Smith, *Adv. Chem. Ser.*, 1971, **101**, 171–200.

[20] P. J. Smeets, J. S. Woertink, B. F. Sels, E. I. Solomon and R. A. Schoonheydt, *Inorg. Chem.*, 2010, **49**, 3573–3583.

[21] M. Briend-Faure, O. Cornu, D. Delafosse, R. Monque and M. Peltre, *Appl. Catal.*, 1988, **38**, 71–87.

[22] W. C. Yoo, S. Kumar, Z. Wang, N. S. Ergang, W. Fan, G. N. Karanikolos, A. V. McCormick, R. L. Penn, M. Tsapatsis and A. Stein, *Angew. Chem. Int. Ed.*, 2008, **47**, 9096–9099.

[23] D. K. Murray, T. Howard, P. W. Goguen, T. R. Krawietz and J. F. Haw, *J. Am. Chem. Soc.*, 1994, **116**, 6354–6360.

[24] P. H. Kasai, R. Bishop Jr and D. McLeod Jr, *J. Phys. Chem.*, 1978, **82**, 279–285.

[25] D. R. Rolison, *Chem. Rev.*, 1990, **90**, 867–878.

[26] A. Walcarius, *Anal. Chim. Acta*, 1999, **384**, 1–16.

[27] Z. Wang, A. Mitra, H. Wang, L. Huang and Y. Yan, *Adv. Mater.*, 2001, **13**, 1463–1466.

[28] M. A. Snyder and M. Tsapatsis, *Angew. Chem. Int. Ed.*, 2007, **46**, 7560–7573.

[29] J. Coronas and J. Santamaria, *Chem. Eng. Sci.*, 2004, **59**, 4879–4885.

[30] F. Pechar and D. Rykl, *Chem. Pap.*, 1985, **39**, 369–377.

[31] S.-b. Liu, J.-F. Wu, L.-J. Ma, T.-C. Tsai and I. Wang, *J. Catal.*, 1991, **132**, 432–439.

[32] X. Feng, X. Ding and D. Jiang, *Chem. Soc. Rev.*, 2012, **41**, 6010–6022.

[33] A. P. Cote, A. I. Benin, N. W. Ockwig, M. O'Keeffe, A. J. Matzger and O. M. Yaghi, *Science*, 2005, **310**, 1166–1170.

[34] H. Furukawa and O. M. Yaghi, *J. Am. Chem. Soc.*, 2009, **131**, 8875–8883.

[35] S.-Y. Ding, J. Gao, Q. Wang, Y. Zhang, W.-G. Song, C.-Y. Su and W. Wang, *J. Am. Chem. Soc.*, 2011, **133**, 19816–19822.

[36] N. Giri, M. G. Del Pópolo, G. Melaugh, R. L. Greenaway, K. Rätzke, T. Koschine, L. Pison, M. F. C. Gomes, A. I. Cooper and S. L. James, *Nature*, 2015, **527**, 216–220.

[37] A. Kitaigorodsky, *Molecular crystals and molecules*, Elsevier, 2012, vol. 29, p. 133.

[38] D. J. Harding, W. Phonsri, P. Harding, I. A. Gass, K. S. Murray, B. Moubaraki, J. D. Cashion, L. Liu and S. G. Telfer, *Chem. Commun.*, 2013, **49**, 6340–6342.

[39] D. J. Harding, W. Phonsri, P. Harding, K. S. Murray, B. Moubaraki and G. N. Jameson, *Dalton Trans.*, 2015, **44**, 15079–15082.

[40] L. E. Kreno, K. Leong, O. K. Farha, M. Allendorf, R. P. Van Duyne and J. T. Hupp, *Chem. Rev.*, 2011, **112**, 1105–1125.

[41] R. Griffith, *J. Chem. Phys.*, 1943, **11**, 499–505.

[42] N. L. Rosi, J. Eckert, M. Eddaoudi, D. T. Vodak, J. Kim, M. O'Keeffe and O. M. Yaghi, *Science*, 2003, **300**, 1127–1129.

[43] H. Li, M. Eddaoudi, M. OKeeffe and O. M. Yaghi, *Nature*, 1999, **402**, 276–279.

[44] H. A. Jahn and E. Teller, Proc. R. Soc. A., 1937, pp. 220–235.

[45] C. H. Hendon and A. Walsh, *Chem. Sci.*, 2015, **6**, 3674–3683.

[46] F. Zhang, X. Zou, X. Gao, S. Fan, F. Sun, H. Ren and G. Zhu, *Adv. Funct. Mater.*, 2012, **22**, 3583–3590.

[47] C. K. Brozek and M. Dinca, *J. Am. Chem. Soc.*, 2013, **135**, 12886–12891.

[48] N. S. Venkataramanan, R. Sahara, H. Mizuseki and Y. Kawazoe, *Int. J. Mol. Sci.*, 2009, **10**, 1601–1608.

[49] C. H. Hendon, D. Tiana, M. Fontecave, C. Sanchez, L. Darras, C. Sassoye, L. Rozes, C. Mellot-Draznieks and A. Walsh, *J. Am. Chem. Soc.*, 2013, **135**, 10942–10945.

[50] J. Gascon, M. D. Hernández-Alonso, A. R. Almeida, G. P. van Klink, F. Kapteijn and G. Mul, *ChemSusChem*, 2008, **1**, 981–983.

[51] A. Torrisi, C. Mellot-Draznieks and R. G. Bell, *J. Chem. Phys.*, 2010, **132**, 044705.

[52] A. Torrisi, C. Mellot-Draznieks and R. G. Bell, *J. Chem. Phys.*, 2009, **130**, 194703.

[53] T. Wu, L. Shen, M. Luebbers, C. Hu, Q. Chen, Z. Ni and R. I. Masel, *Chem. Commun.*, 2010, **46**, 6120–6122.

[54] N. Stock and S. Biswas, *Chem. Rev.*, 2011, **112**, 933–969.

[55] O. Delgado-Friedrichs, M. OKeeffe and O. M. Yaghi, *Phys. Chem. Chem. Phys.*, 2007, **9**, 1035–1043.

[56] H. Furukawa, K. E. Cordova, M. OKeeffe and O. M. Yaghi, *Science*, 2013, **341**, 1230444.

[57] M. OKeeffe, M. A. Peskov, S. J. Ramsden and O. M. Yaghi, *Acc. Chem. Res.*, 2008, **41**, 1782–1789.

[58] N. W. Ockwig, O. Delgado-Friedrichs, M. OKeeffe and O. M. Yaghi, *Acc. Chem. Res.*, 2005, **38**, 176–182.

[59] J. Zhang, S. Chen, A. Zingiryan and X. Bu, *J. Am. Chem. Soc.*, 2008, **130**, 17246–17247.

[60] Q. Shi, Z. Chen, Z. Song, J. Li and J. Dong, *Angew. Chem. Int. Ed.*, 2011, **123**, 698–701.

[61] W.-Y. Gao, Y. Chen, Y. Niu, K. Williams, L. Cash, P. J. Perez, L. Wojtas, J. Cai, Y.-S. Chen and S. Ma, *Angew. Chem. Int. Ed.*, 2014, **53**, 2615–2619.

[62] C. Heering, I. Boldog, V. Vasylyeva, J. Sanchiz and C. Janiak, *CrystEngComm*, 2013, **15**, 9757–9768.

[63] X. Song, S. Jeong, D. Kim and M. S. Lah, *CrystEngComm*, 2012, **14**, 5753–5756.

[64] D.-X. Xue, A. J. Cairns, Y. Belmabkhout, L. Wojtas, Y. Liu, M. H. Alkordi and M. Eddaoudi, *J. Am. Chem. Soc.*, 2013, **135**, 7660–7667.

[65] H. Chun and N. Jin, *Bull. Korean Chem. Soc.*, 2009, **30**, 1405.

[66] http://rcsr.net/nets (accessed 08/08/16): Reticular Chemistry Structure Resource.

[67] Z. Hu and D. Zhao, *Dalton Trans.*, 2015, **44**, 19018–19040.

[68] A. Mallick, B. Garai, M. A. Addicoat, P. S. Petkov, T. Heine and R. Banerjee, *Chem. Sci.*, 2015, **6**, 1420–1425.

[69] L. K. Cadman, J. K. Bristow, N. E. Stubbs, D. Tiana, M. F. Mahon, A. Walsh and A. D. Burrows, *Dalton Trans.*, 2016, **45**, 43164326.

[70] Y. Horiuchi, T. Toyao, M. Saito, K. Mochizuki, M. Iwata, H. Higashimura, M. Anpo and M. Matsuoka, *J. Phys. Chem. C*, 2012, **116**, 20848–20853.

[71] H. Wu, Y. S. Chua, V. Krungleviciute, M. Tyagi, P. Chen, T. Yildirim and W. Zhou, *J. Am. Chem. Soc.*, 2013, **135**, 10525–10532.

[72] A. Ferguson, L. Liu, S. J. Tapperwijn, D. Perl, F.-X. Coudert, S. Van Cleuvenbergen, T. Verbiest, M. A. van der Veen and S. G. Telfer, *Nat. Chem.*, 2016, **8**, 250–257.

[73] J. S. Grosch and F. Paesani, *J. Am. Chem. Soc.*, 2012, **134**, 4207–4215.

[74] F. Salles, A. Ghoufi, G. Maurin, R. G. Bell, C. Mellot-Draznieks and G. Férey, *Angew. Chem.*, 2008, **120**, 8615–8619.

[75] M. de Miguel, F. Ragon, T. Devic, C. Serre, P. Horcajada and H. García, *ChemPhysChem*, 2012, **13**, 3651–3654.

[76] M. J. Katz, Z. J. Brown, Y. J. Colón, P. W. Siu, K. A. Scheidt, R. Q. Snurr, J. T. Hupp and O. K. Farha, *Chem. Commun.*, 2013, **49**, 9449–9451.

[77] F. Vermoortele, B. Bueken, G. Le Bars, B. Van de Voorde, M. Vandichel, K. Houthoofd, A. Vimont, M. Daturi, M. Waroquier, V. Van Speybroeck *et al.*, *J. Am. Chem. Soc.*, 2013, **135**, 11465–11468.

[78] S. Øien, D. Wragg, H. Reinsch, S. Svelle, S. Bordiga, C. Lamberti and K. P. Lillerud, *Cryst. Growth Des.*, 2014, **14**, 5370–5372.

[79] F. Ragon, B. Campo, Q. Yang, C. Martineau, A. D. Wiersum, A. Lago, V. Guillerm, C. Hemsley, J. F. Eubank, M. Vishnuvarthan *et al.*, *J. Mater. Chem. A.*, 2015, **3**, 3294–3309.

[80] M. Shöâeè, J. R. Agger, M. W. Anderson and M. P. Attfield, *CrystEngComm*, 2008, **10**, 646–648.

[81] S. Amirjalayer, M. Tafipolsky and R. Schmid, *J. Phys. Chem. Lett.*, 2014, **5**, 3206–3210.

[82] H. Gliemann and C. Wöll, *Mater. Today*, 2012, **15**, 110–116.

[83] W. P. Deleu, I. Stassen, D. Jonckheere, R. Ameloot and D. E. De Vos, *J. Mater. Chem. A.*, 2016, **4**, 9519–9525.

[84] D. Zacher, A. Baunemann, S. Hermes and R. A. Fischer, *J. Mater. Chem.*, 2007, **17**, 2785–2792.

[85] Y. Liu, Z. Ng, E. A. Khan, H.-K. Jeong, C.-b. Ching and Z. Lai, *Micropor. Mesopor. Mater.*, 2009, **118**, 296–301.

[86] J. Gascon, S. Aguado and F. Kapteijn, *Micropor. Mesopor. Mater.*, 2008, **113**, 132–138.

[87] A. Summerfield, I. Cebula, M. Schroder and P. H. Beton, *J. Phys. Chem. C*, 2015, **119**, 23544–23551.

[88] N. Campagnol, T. Van Assche, T. Boudewijns, J. Denayer, K. Binnemans, D. De Vos and J. Fransaer, *J. Mater. Chem. A.*, 2013, **1**, 5827–5830.

[89] R. Ameloot, L. Stappers, J. Fransaer, L. Alaerts, B. F. Sels and D. E. De Vos, *Chem. Mater.*, 2009, **21**, 2580–2582.

[90] J.-L. Zhuang, D. Ceglarek, S. Pethuraj and A. Terfort, *Adv. Funct. Mater.*, 2011, **21**, 1442–1447.

[91] C. Carbonell, I. Imaz and D. Maspoch, *J. Am. Chem. Soc.*, 2011, **133**, 2144–2147.

[92] J.-L. Zhuang, D. Ar, X.-J. Yu, J.-X. Liu and A. Terfort, *Adv. Mater.*, 2013, **25**, 4631–4635.

[93] I. Stassen, M. Styles, G. Grenci, H. Van Gorp, W. Vanderlinden, S. De Feyter, P. Falcaro, D. De Vos, P. Vereecken and R. Ameloot, *Nat. Mater.*, 2016, **15**, 304–310.

[94] L. D. Salmi, M. J. Heikkilä, E. Puukilainen, T. Sajavaara, D. Grosso and M. Ritala, *Micropor. Mesopor. Mat.*, 2013, **182**, 147–154.

[95] S. Hermes, F. Schröder, R. Chelmowski, C. Wöll and R. A. Fischer, *J. Am. Chem. Soc.*, 2005, **127**, 13744–13745.

[96] D. Braga, *Angew. Chem. Int. Ed.*, 2003, **42**, 5544–5546.

[97] M. Fujita, Y. J. Kwon, S. Washizu and K. Ogura, *J. Am. Chem. Soc.*, 1994, **116**, 1151–1152.

[98] L. Ma, C. Abney and W. Lin, *Chem. Soc. Rev.*, 2009, **38**, 1248–1256.

[99] J. Lee, O. K. Farha, J. Roberts, K. A. Scheidt, S. T. Nguyen and J. T. Hupp, *Chem. Soc. Rev.*, 2009, **38**, 1450–1459.

[100] I. Luz, F. Llabrés i Xamena and A. Corma, *J. Catal.*, 2010, **276**, 134–140.

[101] Y. K. Hwang, D.-Y. Hong, J.-S. Chang, S. H. Jhung, Y.-K. Seo, J. Kim, A. Vimont, M. Daturi, C. Serre and G. Férey, *Angew. Chem. Int. Ed.*, 2008, **47**, 4144–4148.

[102] I. Luz, F. Llabrés i Xamena and A. Corma, *J. Catal.*, 2012, **285**, 285–291.

[103] D. Jiang, T. Mallat, F. Krumeich and A. Baiker, *J. Catal.*, 2008, **257**, 390–395.

[104] M. H. Alkordi, Y. Liu, R. W. Larsen, J. F. Eubank and M. Eddaoudi, *J. Am. Chem. Soc.*, 2008, **130**, 12639–12641.

[105] B. Gomez-Lor, E. Gutierrez-Puebla, M. Iglesias, M. Monge, C. Ruiz-Valero and N. Snejko, *Inorg. Chem.*, 2002, **41**, 2429–2432.

[106] U. Ravon, M. E. Domine, C. Gaudillère, A. Desmartin-Chomel and D. Farrusseng, *New J. Chem.*, 2008, **32**, 937–940.

[107] C. Prestipino, L. Regli, J. Vitillo, F. Bonino, A. Damin, C. Lamberti, A. Zecchina, P. Solari, K. Kongshaug and S. Bordiga, *Chem. Mater.*, 2006, **18**, 1337–1346.

[108] T. Ezuhara, K. Endo and Y. Aoyama, *J. Am. Chem. Soc.*, 1999, **121**, 3279–3283.

[109] R. Vaidhyanathan, S. S. Iremonger, G. K. Shimizu, P. G. Boyd, S. Alavi and T. K. Woo, *Science*, 2010, **330**, 650–653.

[110] J. L. Rowsell, E. C. Spencer, J. Eckert, J. A. Howard and O. M. Yaghi, *Science*, 2005, **309**, 1350–1354.

[111] Y. Liu, C. Brown, D. Neumann, V. Peterson and C. Kepert, *J. Alloys Compd.*, 2007, **446**, 385–388.

[112] W. Zhou and T. Yildirim, *Phys. Rev. B*, 2006, **74**, 1803011–1803014.

[113] J. L. Rowsell, J. Eckert and O. M. Yaghi, *J. Am. Chem. Soc.*, 2005, **127**, 14904–14910.

[114] C. M. Brown, Y. Liu, T. Yildirim, V. K. Peterson and C. J. Kepert, *Nanotechnology*, 2009, **20**, 2040251–2040262.

[115] J. L. Rowsell and O. M. Yaghi, *Angew. Chem. Int. Ed.*, 2005, **44**, 4670–4679.

[116] D. Saha, Z. Bao, F. Jia and S. Deng, *Environ. Sci. Technol.*, 2010, **44**, 1820–1826.

[117] D. Britt, H. Furukawa, B. Wang, T. G. Glover and O. M. Yaghi, *Proc. Natl. Acad. Sci. U.S.A.*, 2009, **106**, 20637–20640.

[118] P. Nugent, Y. Belmabkhout, S. D. Burd, A. J. Cairns, R. Luebke, K. Forrest, T. Pham, S. Ma, B. Space, L. Wojtas *et al.*, *Nature*, 2013, **495**, 80–84.

[119] S. Choi, T. Watanabe, T.-H. Bae, D. S. Sholl and C. W. Jones, *J. Phys. Chem. Lett.*, 2012, **3**, 1136–1141.

[120] P. Horcajada, T. Chalati, C. Serre, B. Gillet, C. Sebrie, T. Baati, J. F. Eubank, D. Heurtaux, P. Clayette, C. Kreuz *et al.*, *Nat. Mater.*, 2010, **9**, 172–178.

[121] K. M. Taylor-Pashow, J. D. Rocca, Z. Xie, S. Tran and W. Lin, *J. Am. Chem. Soc.*, 2009, **131**, 14261–14263.

[122] A. C. McKinlay, R. E. Morris, P. Horcajada, G. Férey, R. Gref, P. Couvreur and C. Serre, *Angew. Chem. Int. Ed.*, 2010, **49**, 6260–6266.

[123] A. Layre, P. Couvreur, H. Chacun, J. Richard, C. Passirani, D. Requier, J. Benoit and R. Gref, *J. Control. Release*, 2006, **111**, 271–280.

[124] R. C. Huxford, J. Della Rocca and W. Lin, *Curr. Open. Chem. Biol.*, 2010, **14**, 262–268.

[125] Y. Kobayashi, B. Jacobs, M. D. Allendorf and J. R. Long, *Chem. Mater.*, 2010, **22**, 4120–4122.

[126] D. Tiana, C. H. Hendon, A. Walsh and T. P. Vaid, *Phys. Chem. Chem. Phys.*, 2014, **3**, 14463–14472.

[127] D. Sheberla, L. Sun, M. A. Blood-Forsythe, S. Er, C. R. Wade, C. K. Brozek, A. Aspuru-Guzik and M. Dinca, *J. Am. Chem. Soc.*, 2014, **136**, 8859–8862.

[128] K.-H. Low, V. Roy, S. S.-Y. Chui, S. L.-F. Chan and C.-M. Che, *Chem. Commun.*, 2010, **46**, 7328–7330.

[129] S.-L. Cai, Y.-B. Zhang, A. B. Pun, B. He, J. Yang, F. M. Toma, I. D. Sharp, O. M. Yaghi, J. Fan, S.-R. Zheng *et al.*, *Chem. Sci.*, 2014, **5**, 4693–4700.

[130] A. A. Talin, A. Centrone, A. C. Ford, M. E. Foster, V. Stavila, P. Haney, R. A. Kinney, V. Szalai, F. El Gabaly, H. P. Yoon *et al.*, *Science*, 2014, **343**, 66–69.

[131] J. Fraxedas, S. Molas, A. Figueras, I. Jiménez, R. Gago, P. Auban-Senzier and M. Goffman, *J. Solid State Chem.*, 2002, **168**, 384–389.

[132] A. Figueras, J. Caro, J. Fraxedas and V. Laukhin, *Synth. Met.*, 1999, **102**, 1611–1612.

[133] J. Kim, H.-Y. Cho and W.-S. Ahn, *Catal. Surv. Asia.*, 2012, **16**, 106–119.

[134] C. Zheng, H. F. Greer, C.-Y. Chiang and W. Zhou, *CrystEngComm*, 2014, **16**, 1064–1070.

[135] S. S. Kaye, A. Dailly, O. M. Yaghi and J. R. Long, *J. Am. Chem. Soc.*, 2007, **129**, 14176–14177.

[136] J. A. Greathouse and M. D. Allendorf, *J. Am. Chem. Soc.*, 2006, **128**, 10678–10679.

[137] MOF Technologies website (accessed 29/07/16): http://www.moftechnologies.com/our-technology.html.

[138] Zheng Ni, Masel Richard I, 2006, Rapid metal organic framework molecule synthesis method, US Patent US20090131643 A1.

[139] W. Heitler and F. London, *Z. Phys.*, 1927, **44**, 455–472.

[140] L. Pauling, *Chem. Rev.*, 1928, **5**, 173–213.

[141] C. W. Scherr, *J. Chem. Phys.*, 1955, **23**, 569–578.

[142] J. D. Bolcer and R. B. Hermann, *Rev. Comp. Ch., Vol. 5*, 1994, 1–63.

[143] H. Eyring, *J. Chem. Phys.*, 1935, **3**, 107–115.

[144] S. Glasstone, H. Eyring and K. J. Laidler, *The theory of rate processes*, McGraw-Hill, 1941.

[145] K. J. Laidler and M. C. King, *J. Phys. Chem.*, 1983, **87**, 2657–2664.

[146] C. J. Cramer, *Essentials of computational chemistry: theories and models*, John Wiley & Sons, 2013.

[147] R. L. Hilderbrandt, *Comput. Chem.*, 1977, **1**, 179–186.

[148] E. Schrödinger, *Phys. Rev.*, 1926, **28**, 1049.

[149] M. Born and R. Oppenheimer, *Ann. Phys.*, 1927, **389**, 457–484.

[150] M. Born, *Quantum*, 1927, **2**, 4.

[151] D. R. Hartree, Math. Proc. Cambridge, 1928, pp. 89–110.

[152] D. R. Hartree, Math. Proc. Cambridge, 1928, pp. 111–132.

[153] V. Fock, *Z. Phys*, 1928, **49**, 323–338.

[154] J. P. Perdew, M. Ernzerhof, A. Zupan and K. Burke, *J. Chem. Phys.*, 1998, **108**, 1522–1531.

[155] P. Hohenberg and W. Kohn, *Phys. Rev.*, 1964, **136**, B864.

[156] J. P. Perdew and M. Levy, *Phys. Rev. Lett.*, 1983, **51**, 1884.

[157] J. P. Perdew, A. Ruzsinszky, J. Tao, V. N. Staroverov, G. E. Scuseria and G. I. Csonka, *J. Chem. Phys.*, 2005, **123**, 062201.

[158] J. P. Perdew, K. Burke and M. Ernzerhof, *Phys. Rev. Lett.*, 1996, **77**, 3865.

[159] J. P. Perdew and W. Yue, *Phys. Rev. B.*, 1986, **33**, 8800.

[160] J. P. Perdew, A. Ruzsinszky, G. I. Csonka, O. A. Vydrov, G. E. Scuseria, L. A. Constantin, X. Zhou and K. Burke, *Phys. Rev. Lett.*, 2008, **100**, 136406.

[161] L. He, F. Liu, G. Hautier, M. J. Oliveira, M. A. Marques, F. D. Vila, J. Rehr, G.-M. Rignanese and A. Zhou, *Phys. Rev. B.*, 2014, **89**, 064305.

[162] M. De La Pierre, R. Orlando, L. Maschio, K. Doll, P. Ugliengo and R. Dovesi, *J. Comput. Chem.*, 2011, **32**, 1775–1784.

[163] J. P. Perdew and K. Schmidt, AIP Conf. Proc., 2001, pp. 1–20.

[164] N. Troullier and J. L. Martins, *Phys. Rev. B*, 1991, **43**, 1993.

[165] P. E. Blöchl, *Phys. Rev. B*, 1994, **50**, 17953.

[166] J. Ziman, *Phys. Today*, 1961, **14**, 64–66.

[167] F. Bloch, *Phys. Today*, 1976, **29**, 23–27.

[168] J. Chu and A. Sher, *Physics and properties of narrow gap semiconductors*, Springer, 2008.

[169] M. Mohraz and L. L. Lohr, *Int. J. Quantum Chem.*, 1976, **10**, 811–835.

[170] A. Kiejna, G. Kresse, J. Rogal, A. De Sarkar, K. Reuter and M. Scheffler, *Phys. Rev. B.*, 2006, **73**, 035404.

[171] D. A. Pearlman, D. A. Case, J. W. Caldwell, W. S. Ross, T. E. Cheatham III, S. DeBolt, D. Ferguson, G. Seibel and P. Kollman, *Comput. Phys. Commun.*, 1995, **91**, 1–41.

[172] J. E. Jones, Proc. R. Soc. A., 1924, pp. 463–477.

[173] R. A. Buckingham, Proc. R. Soc. A., 1938, pp. 264–283.

[174] N. L. Allinger, Y. H. Yuh and J. H. Lii, *J. Am. Chem. Soc.*, 1989, **111**, 8551–8566.

[175] N. L. Allinger, F. Li and L. Yan, *J. Comput. Chem.*, 1990, **11**, 848–867.

[176] J. R. Maple, U. Dinur and A. T. Hagler, *Proc. Natl. Acad. Sci. USA*, 1988, **85**, 5350–5354.

[177] R. Walsh, *Acc. Chem. Res.*, 1981, **14**, 246–252.

[178] S. J. Blanksby and G. B. Ellison, *Acc. Chem. Res.*, 2003, **36**, 255–263.

[179] G. Lewis and C. Catlow, *J. Phys. C.*, 1985, **18**, 1149.

[180] W. D. Cornell, P. Cieplak, C. I. Bayly, I. R. Gould, K. M. Merz, D. M. Ferguson, D. C. Spellmeyer, T. Fox, J. W. Caldwell and P. A. Kollman, *J. Am. Chem. Soc.*, 1995, **117**, 5179–5197.

[181] S. L. Mayo, B. D. Olafson and W. A. Goddard, *J. Phys. Chem.*, 1990, **94**, 8897–8909.

[182] A. K. Rappé, C. J. Casewit, K. Colwell, W. Goddard III and W. Skiff, *J. Am. Chem. Soc.*, 1992, **114**, 10024–10035.

[183] M. O'Keefe and N. Brese, *J. Am. Chem. Soc.*, 1991, **113**, 3226–3229.

[184] A. K. Rappe and W. A. Goddard III, *J. Phys. Chem.*, 1991, **95**, 3358–3363.

[185] A. R. Leach, *Molecular modelling: principles and applications*, Pearson Education, 2001.

[186] M. A. Addicoat, N. Vankova, I. F. Akter and T. Heine, *J. Chem. Theory Comput.*, 2014, **10**, 880–891.

[187] S. Bureekaew, S. Amirjalayer, M. Tafipolsky, C. Spickermann, T. K. Roy and R. Schmid, *Phys. Status Solidi (B)*, 2013, **250**, 1128–1141.

[188] C. Campaná, B. Mussard and T. K. Woo, *J. Chem. Theory Comput.*, 2009, **5**, 2866–2878.

[189] L. Vanduyfhuys, S. Vandenbrande, T. Verstraelen, R. Schmid, M. Waroquier and V. Van Speybroeck, *J. Comput. Chem.*, 2015, **36**, 1015–1027.

[190] F. L. Hirshfeld, *Theor. Chim. Acta.*, 1977, **44**, 129–138.

[191] C. I. Bayly, P. Cieplak, W. Cornell and P. A. Kollman, *J. Phys. Chem.*, 1993, **97**, 10269–10280.

[192] J. P. Dürholt, R. Galvelis and R. Schmid, *Dalton Trans.*, 2016, **45**, 4370–4379.

[193] E. L. First and C. A. Floudas, *Microporous Mesoporous Mater.*, 2013, **165**, 32–39.

[194] D. J. Evans and B. L. Holian, *J. Chem. Phys.*, 1985, **83**, 4069–4074.

[195] S. Nose, *J. Phys.: Condens. Matter*, 1990, **2**, SA115.

[196] S. Nose, *J. Chem. Phys.*, 1984, **81**, 511–519.

[197] G. J. Martyna, D. J. Tobias and M. L. Klein, *J. Chem. Phys.*, 1994, **101**, 4177–4189.

[198] A. Lamura, G. Gompper, T. Ihle and D. Kroll, *EPL*, 2001, **56**, 319.

[199] S. Elliott, *The physics and chemistry of solids*, Wiley, 1998.

[200] G. J. Martyna and M. E. Tuckerman, *J. Chem. Phys.*, 1999, **110**, 2810–2821.

[201] M. L. Cohen and T. Bergstresser, *Phys. Rev.*, 1966, **141**, 789.

[202] M. I. Aroyo, A. Kirov, C. Capillas, J. Perez-Mato and H. Wondratschek, *Acta Crystallogr. Sect. A.*, 2006, **62**, 115–128.

[203] X.-B. Li, P. Guo, T.-F. Cao, H. Liu, W.-M. Lau and L.-M. Liu, *Sci. Rep.*, 2014, **5**, 10848–10848.

[204] G. Kresse and J. Hafner, *Phys. Rev. B*, 1993, **47**, 558.

[205] S. Kivelson and C. Gelatt Jr, *Phys. Rev. B*, 1979, **19**, 5160.

[206] G. Dresselhaus, *J. Phys. Chem. Solids*, 1956, **1**, 14–22.

[207] R. M. Martin, *Electronic structure: basic theory and practical methods*, Cambridge university press, 2004, p. 96.

[208] MIT News, Explained:phonons (accessed 07/08/16): http://news.mit.edu/2010/explained-phonons-0706.

[209] M. M. Cohen, *Introduction to the quantum theory of semiconductors*, Gordon and Breach Science Publishers, 1972.

[210] C. Bhandari and G. Verma, *Phys. Rev.*, 1965, **140**, A2101.

[211] R. A. Wheeler, H. Dong and S. E. Boesch, *ChemPhysChem*, 2003, **4**, 382–384.

[212] R. A. Broglia, G. Colò, G. Onida and H. E. Roman, in *Solid State Physics of Finite Systems*, Springer, 2004, pp. 105–130.

[213] G. P. Srivastava, *The physics of phonons*, CRC Press, 1990.

[214] J. Gale, *GULP: User Manual, Royal Institution and Imperial College, London*, 1992, **1994**, year.

[215] J. Gale, *GULP manual*, 1998.

[216] K. Kunc and R. M. Martin, *Phys. Rev. Lett.*, 1982, **48**, 406.

[217] G. Ackland, M. Warren and S. Clark, *J. Phys. Condens. Matter.*, 1997, **9**, 7861.

[218] P. Giannozzi, S. De Gironcoli, P. Pavone and S. Baroni, *Phys. Rev. B.*, 1991, **43**, 7231.

[219] X. Gonze, *Phys. Rev. A.*, 1995, **52**, 1086.

[220] R. P. Feynman, *Phys. Rev.*, 1939, **56**, 340.

[221] A. Jain, S. P. Ong, G. Hautier, W. Chen, W. D. Richards, S. Dacek, S. Cholia, D. Gunter, D. Skinner, G. Ceder *et al.*, *Apl. Mater.*, 2013, **1**, 011002.

[222] F. H. Allen, *Acta Crystallogr. Sect. A*, 2002, **58**, 380–388.

[223] J. E. Saal, S. Kirklin, M. Aykol, B. Meredig and C. Wolverton, *JOM*, 2013, **65**, 1501–1509.

[224] C. E. Wilmer, O. K. Farha, Y.-S. Bae, J. T. Hupp and R. Q. Snurr, *Energy & Environ. Sci.*, 2012, **5**, 9849–9856.

[225] C. E. Wilmer, M. Leaf, C. Y. Lee, O. K. Farha, B. G. Hauser, J. T. Hupp and R. Q. Snurr, *Nat. Chem.*, 2012, **4**, 83–89.

[226] J. G. McDaniel and J. Schmidt, *J. Phys. Chem. C.*, 2012, **116**, 14031–14039.

[227] J. K. Bristow, D. Tiana and A. Walsh, *Journal of chemical theory and computation*, 2014, **10**, 4644–4652.

[228] R. Bader, A. Larouche, C. Gatti, M. Carroll, P. MacDougall and K. Wiberg, *J. Chem. Phys.*, 1987, **87**, 1142–1152.

[229] R. F. Bader, M. T. Carroll, J. R. Cheeseman and C. Chang, *J. Am. Chem. Soc.*, 1987, **109**, 7968–7979.

[230] J. Evans, T. Mary, T. Vogt, M. Subramanian and A. Sleight, *Chem. Mater.*, 1996, **8**, 2809–2823.

[231] T. Mary, J. Evans, T. Vogt and A. Sleight, *Science*, 1996, **272**, 90.

[232] S. S. Han and W. A. Goddard, *J. Phys. Chem. C.*, 2007, **111**, 15185–15191.

[233] R. Patil and E. Subbarao, *J. Appl. Crystallogr.*, 1969, **2**, 281–288.

[234] S. Sawada and G. Shirane, *J. Phys. Soc. Jpn.*, 1949, **4**, 52–56.

[235] G. Shirane and A. Takeda, *J. Phys. Soc. Jpn.*, 1952, **7**, 1–4.

[236] M. P. Attfield, *Chem. Commun.*, 1998, 601–602.

[237] N. Khosrovani and A. Sleight, *Int. J. Inorg. Mater.*, 1999, **1**, 3–10.

[238] P. Tschaufeser and S. Parker, *J. Phys. Chem.*, 1995, **99**, 10609–10615.

[239] D. Dubbeldam, K. S. Walton, D. E. Ellis and R. Q. Snurr, *Angew. Chem.*, 2007, **119**, 4580–4583.

[240] N. Lock, Y. Wu, M. Christensen, L. J. Cameron, V. K. Peterson, A. J. Bridgeman, C. J. Kepert and B. B. Iversen, *J. Phys. Chem. C.*, 2010, **114**, 16181–16186.

[241] W. Zhou, H. Wu, T. Yildirim, J. R. Simpson and A. H. Walker, *Phys. Rev. B.*, 2008, **78**, 054114.

[242] C. Yang, X. Wang and M. A. Omary, *Angew. Chem.*, 2009, **121**, 2538–2543.

[243] R. F. Bader, *Atoms in molecules*, Wiley Online Library, 1990.

[244] R. Bader and T. Nguyen-Dang, *Adv. Quantum Chem.*, 1981, **14**, 63–124.

[245] F. W. Biegler-könig, R. F. Bader and T.-H. Tang, *J. Comput. Chem.*, 1982, **3**, 317–328.

[246] J. Gasteiger and M. Marsili, *Tetrahedron*, 1980, **36**, 3219–3228.

[247] J. W. Ponder and F. M. Richards, *J. Comput. Chem.*, 1987, **8**, 1016–1024.

[248] J. D. Gale, *Journal of the Chemical Society, Faraday Transactions*, 1997, **93**, 629–637.

[249] J. D. Gale and A. L. Rohl, *Mol. Simul.*, 2003, **29**, 291–341.

[250] W. L. Jorgensen, J. Chandrasekhar, J. D. Madura, R. W. Impey and M. L. Klein, *J. Chem. Phys.*, 1983, **79**, 926–935.

[251] E. Neria, S. Fischer and M. Karplus, *J. Chem. Phys.*, 1996, **105**, 1902–1921.

[252] P. A. Kollman, I. Massova, C. Reyes, B. Kuhn, S. Huo, L. Chong, M. Lee, T. Lee, Y. Duan, W. Wang *et al.*, *Acc. Chem. Res.*, 2000, **33**, 889–897.

[253] A. Klamt and G. Schüürmann, *J. Chem. Soc., Perkin Trans. 2*, 1993, 799–805.

[254] R. Koch, *J. Phys. Condens. Matter*, 1994, **6**, 9519.

[255] Z. Zhang and M. G. Lagally, *Science*, 1997, **276**, 377–383.

[256] M. L. Ohnsorg, C. K. Beaudoin and M. E. Anderson, *Langmuir*, 2015, **31**, 6114–6121.

[257] K. T. Butler, Y. Kumagai, F. Oba and A. Walsh, *J. Mater. Chem. C.*, 2016, **4**, 1149–1158.

[258] J. VandeVondele, M. Krack, F. Mohamed, M. Parrinello, T. Chassaing and J. Hutter, *Comput. Phys. Commun.*, 2005, **167**, 103–128.

[259] F. London, *Trans. Faraday Soc.*, 1937, **33**, 8b–26.

[260] G. Henkelman, B. P. Uberuaga and H. Jónsson, *J. Chem. Phys.*, 2000, **113**, 9901–9904.

[261] S. M. Woodley, P. D. Battle, C. R. A. Catlow and J. D. Gale, *J. Phys. Chem. B.*, 2001, **105**, 6824–6830.

[262] A. M. Walker, B. Civalleri, B. Slater, C. Mellot-Draznieks, F. Corà, C. M. Zicovich-Wilson, G. Román-Pérez, J. M. Soler and J. D. Gale, *Angew. Chem. Int. Ed.*, 2010, **49**, 7501–7503.

[263] Y. Liu, J.-H. Her, A. Dailly, A. J. Ramirez-Cuesta, D. A. Neumann and C. M. Brown, *J. Am. Chem. Soc.*, 2008, **130**, 11813–11818.

[264] M. J. Cliffe, W. Wan, X. Zou, P. A. Chater, A. K. Kleppe, M. G. Tucker, H. Wilhelm, N. P. Funnell, F.-X. Coudert and A. L. Goodwin, *Nat. Commun.*, 2014, **5**, 4176.